

AD-A084 940

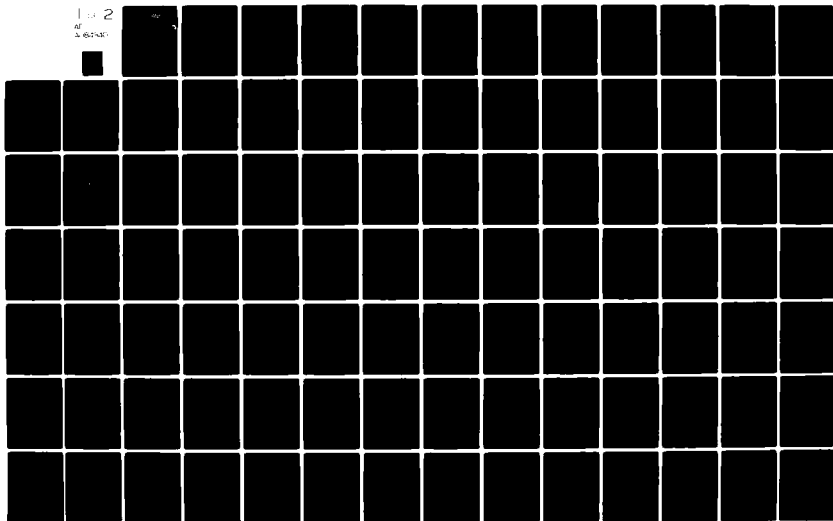
LOCKHEED MISSILES AND SPACE CO INC PALO ALTO CA PALO --ETC F/8 17/5
MULTIDIMENSIONAL TIME DEPENDENT STRUCTURE AND MECHANISMS FOR NO--ETC(U)
AUG 79 J B KUMER F19628-76-C-0209

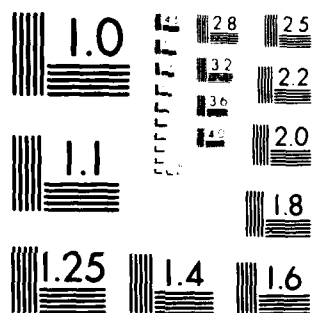
UNCLASSIFIED

AF6L -TR-79-0224

NL

1 of 2
AD
5-652501





MICROCOPY RESOLUTION TEST CHART
NATIONAL BUREAU OF STANDARDS-1963-A

ADA084940

This research was conducted by the
under contract with the
Evaluation.

AIR FORCE RESEARCH AND DEVELOPMENT
AIR FORCE SYSTEMS COMMAND
UNITED STATES AIR FORCE
HANSCOM AFB, MASSACHUSETTS 01900

| 19 REPORT DOCUMENTATION PAGE | | READ INSTRUCTIONS BEFORE COMPLETING FORM | |
|--|--------------------------------------|--|--|
| 1. REPORT NUMBER (18) AFGL-TR-79-0224 | 2. GOVT ACCESSION NO. AD-A084 940 | 3. RECIPIENT'S CATALOG NUMBER | |
| 4. TITLE (and Subtitle) (6) Multidimensional Time Dependent Structure and Mechanisms for Non-LTE CO ₂ Infrared Emissions and 4.3μm Aurora MICROMETERS | | 5. TYPE OF REPORT & PERIOD COVERED (9) Final Report, 1 Jun 76-6-1-76 to 7-31-79 31 Jul 79 | |
| 7. AUTHOR(s) (10) J. B. Kumer | | 8. CONTRACT OR GRANT NUMBER(s) (15) F19628-76-C-0209 | |
| 9. PERFORMING ORGANIZATION NAME AND ADDRESS Electro-Optics Laboratory, Dept. 52-54, Bldg. 202 Lockheed Palo Alto Research Laboratory, 3251 Hanover Street, Palo Alto, CA 94304 | | 10. PROGRAM ELEMENT, PROJECT, TASK AREA & WORK UNIT NUMBERS CDNA26AG | |
| 11. CONTROLLING OFFICE NAME AND ADDRESS Air Force Geophysics Laboratory Hanscom Air Force Base, MA 01731 Monitor/Edward T. P. Lee/OPR | | 12. REPORT DATE (11) 31 Aug 1979 | |
| 14. MONITORING AGENCY NAME & ADDRESS (if different from Controlling Office) | | 13. NUMBER OF PAGES (12) 192 | |
| | | 15. SECURITY CLASS. (of this report) Unclassified 15a. DECLASSIFICATION DOWNGRADING SCHEDULE | |
| 16. DISTRIBUTION STATEMENT (of this Report) Approved for public release; distribution unlimited (16) CDNA, I25AAXH, (17) 26, Z639 | | | |
| 17. DISTRIBUTION STATEMENT (of the abstract entered in Block 20, if different from Report) | | | |
| 18. SUPPLEMENTARY NOTES This research was sponsored by the Defense Nuclear Agency (DNA) under Subtask I25AAXHZ639, Work Unit 04 entitled "IR Data Evaluation". | | | |
| 19. ABSTRACT (Continue on reverse side if necessary; and identify by block number) aurora, infrared, radiance, structure, nadir, earthlimb, nuclear, airglow, LWIR window, 4.3μm wavelength, 2.7μm wavelength, solid etalon, interferometer, sensor, scanner, atmospheric CO ₂ , fluorescence, prompt auroral mechanism, time dependence, multi-dimensional time dependent radiation transport. | | | |
| 20. ABSTRACT (Continue on reverse side if necessary; and identify by block number) The effort was concerned with development of a two dimensional time dependent radiation transport model of the CO ₂ 4.3μm aurora. Predictions of spatial structure in auroral nadir radiance, and experimental concepts for verification were addressed. Nadir radiance gradients in the CO ₂ 4.3μm aurora are predicted to be comparable to those in the 2.7μm aurora even though the DC component of the former is ≈10 times the brighter. A rocket borne arc over flown cryogenically cooled tilting etalon spectrometer in series with a CO ₂ absorption cell wheel is shown to be the optimum experiment to provide verification. The modelling facility | | | |

#20 Continued

is also used to estimate the 4.3 μ m signal levels that might be observed in the electron gun mother-sensor module daughter spatial EXCEDE experiment and to delineate emission mechanisms for that experiment. A detailed investigation of the CO₂ 4.3 μ m zenith radiance data obtained under undisturbed night time conditions on 4/11/74 revealed compelling evidence for the existence of an OH airglow related mechanism $\text{OH}(v) + \text{N}_2 \rightarrow \text{OH}(v-1) + \text{N}_2^*$ followed by $\text{N}_2^* + \text{CO}_2 \rightleftharpoons \text{N}_2 + \text{CO}_2^*$ (001) followed by partial radiation trapping $\text{CO}_2^*(001) \rightleftharpoons \text{CO}_2 + h\nu$ 4.3 μ m for producing structured CO₂ 4.3 μ m radiance under undisturbed night time conditions. Detailed LWIR CO₂ emission earthlimb synthetic spectra that are pumped by structured mechanisms such as aurora, airglow and fluorescence are also presented. The model is also applied to very high sensitivity auroral 4.3 μ m zenith radiance data obtained 10/26/78. These data are shown to provide evidence for a prompt 4.3 μ m auroral component that is $\approx 0.3\%$ energy efficient and appears to be quenched strongly with decreasing altitude.

| | |
|---------------|-------------------------------------|
| Accession For | |
| NTIS G441 | <input checked="" type="checkbox"/> |
| NSC TAB | <input type="checkbox"/> |
| Unannounced | <input type="checkbox"/> |
| Justification | |
| By | |
| Distribution/ | |
| Availability | |
| Dist. | Available/or special |
| A | |

TABLE OF CONTENTS

| Section | Page |
|---|------|
| 1.0 INTRODUCTION | 5 |
| 2.0 THE TWO DIMENSIONAL TIME DEPENDENT CO ₂ 4.3μm AURORA, RESULTS AND IMPLICATIONS | 7 |
| 2.1 Introduction | 7 |
| 2.2 Details of the Calculation | 7 |
| 2.3 Results | 7 |
| 2.4 Implications | 21 |
| 3.0 EXPERIMENTAL VERIFICATION OF THE LATERAL PHOTON TRANSPORT SMOOTHING EFFECT IN THE CO ₂ 4.3μm AURORA | 22 |
| 3.1 Introduction | 22 |
| 3.2 Details of the Requirement to Use CO ₂ Absorption Cells | 24 |
| 3.3 The Broad Band Filtered Radiometer Concept | 32 |
| 3.4 The Narrow Band Solid Etalon Fabry Perof Tilting Filtered Radiometer Concept | 35 |
| 3.5 HIRIS Concept | 42 |
| 3.6 Arc Underfly Concept | 43 |
| 3.7 An NBTFR 2.7μm Arc Overfly Concept | 44 |
| 3.8 Conclusions | 46 |
| 4.0 APPLICATION TO PLANNING FOR SPATIAL EXCEDE | 48 |
| 5.0 EVIDENCE FOR AN OH \rightarrow N ₂ CO ₂ (v ₃) + CO ₂ + hv(4.3μm) MECHANISM FOR 4.3μm AIRGLOW | 54 |
| 6.0 ESTIMATES OF CO ₂ HOT BAND EARTHLIMB EMISSION IN THE LWIR REGION | 71 |
| 6.1 Introduction | 71 |
| 6.2 Auroral Processes | 71 |
| 6.3 Solar Processes | 73 |
| 6.4 Airglow Processes | 74 |
| 6.5 Summary and Results | 74 |

TABLE OF CONTENTS (Cont.)

| Section | | Page |
|---------|--|------|
| 7.0 | EVIDENCE FOR PROMPT 4.3 μ m AURORAL EMISSION | 78 |
| 8.0 | CONCLUSIONS | 81 |
| 9.0 | REFERENCES | 87 |

APPENDICES

| | | |
|----|---|-----|
| A: | THE APPROXIMATE 3D FORMULATION | 90 |
| B: | NOMINAL ARC MODEL | 91 |
| C: | PROCEDURE FOR RAPID CONVERGENCE | 95 |
| D: | CALCULATIONS FOR SPATIAL EXCEED | 98 |
| E: | ESTIMATED SYNTHETIC SPECTRA | 115 |
| F: | VUFOILS SHOWN AT THE 1979 SPRING MEETING OF THE AGU | 164 |
| G: | CALCULATION OF CELL WHEEL INTERCHANGE WEIGHTING FUNCTIONS | 182 |
| H: | ARC OVERFLY NADIR VIEWING HIRIS NESR CALCULATION | 184 |
| I: | CONTRACTUALLY SUPPORTED PUBLICATIONS | 185 |
| J: | DISTRIBUTION LIST | 186 |

1.0 INTRODUCTION

Space based military optical surveillance systems to perform a variety of missions are currently under consideration. An important consideration of the design of such a system is the choice of spectral region. Reliable characterization and modeling of extremes in natural backgrounds, and of the expected nuclear perturbation, is necessary to optimally choose a spectral region. Here we report an effort to model field data on infrared auroral and natural background obtained mainly by rocket borne sensors in the 4.3, 2.7 and LWIR spectral regions, to predict effects on structure, and to conceive field experiments to most effectively enhance the data base.

Specifically our effort was concerned with development of a two dimensional time dependent radiation transport model of the CO_2 4.3 μm aurora. Predictions of spatial structure in auroral nadir radiance, and experimental concepts for verification were addressed. Nadir radiance gradients in the CO_2 4.3 μm aurora are predicted to be comparable to those in the 2.7 μm aurora even though the DC component of the former is ≈ 10 times the brighter. A rocket borne arc over flown cryogenically cooled tilting etalon spectrometer in series with a CO_2 absorption cell wheel is shown to be the optimum experiment to provide verification. The modelling facility is also used to estimate the 4.3 μm signal levels that might be observed in the electron gun mother- sensor module daughter spatial EXCEDE experiment and to delineate emission mechanisms for that experiment. A detailed investigation of the CO_2 4.3 μm zenith radiance data obtained under undisturbed night time conditions on 4/11/74 revealed

compelling evidence for the existence of an OH airglow related mechanism
 $\text{OH}(v) + \text{N}_2 \rightarrow \text{OH}(v-1) + \text{N}_2^*$ followed by $\text{N}_2^* + \text{CO}_2 \rightarrow \text{N}_2 + \text{CO}_2(001)$ followed by
 partial radiation trapping $\text{CO}_2(001) \rightarrow \text{CO}_2 + h\nu\ 4.3\mu\text{m}$ for producing structured
 $\text{CO}_2\ 4.3\mu\text{m}$ radiance under undisturbed night time conditions. Detailed window
 LWIR CO_2 emission earthlimb synthetic spectra that are pumped by structural
 mechanisms such as aurora, airglow and fluorescence are also presented. The
 model is also applied to very high sensitivity auroral $4.3\mu\text{m}$ zenith radiance
 data obtained 10/26/78. These data are shown to provide evidence for a prompt
 $4.3\mu\text{m}$ auroral component that is 0.3% energy efficient and appears to be
 quenched strongly with decreasing altitude.

2.0 THE TWO DIMENSIONAL TIME DEPENDENT CO₂ 4.3μm AURORA, RESULTS AND IMPLICATIONS

2.1 Introduction

Earlier studies (Kumer 1974, 1977a) have established that excitation of N₂ by precipitating particles followed by $N_2 + CO_2 \xrightarrow{VV} N_2 + CO_2(001)$ followed by $CO_2(001) \rightarrow CO_2 + h\nu (4.3\mu m)$ is the principal mechanism for generating the 4.3μm aurora.

These studies have also shown that multiple scattering of the CO₂ emission ($CO_2(001) \rightarrow CO_2 + h\nu (4.3\mu m)$) significantly impacts the temporal and altitude dependence of the 4.3μm aurora. Thus we would also expect that multiple scattering would tend to broaden the 4.3μm arc with respect to the 3914A arc. To calculate this effect it is necessary to solve a 2 dimensional time dependent radiation transport integral equation. We have done this in application to a nominal arc model in which the arc is assumed to have stabilized in magnetic latitude for 2 minutes. The arc is assumed to have been moving at 3 km/min in a direction away from the pole prior to stabilization time. The e fold half width for energy deposition is assumed to be ~6.5 km. Our calculation shows that for a position 20 km away from arc center in the direction of motion that lateral radiation transport increases the 4.3μm nadir radiance by approximately a factor 50 over what one would predict if lateral transport were neglected.

Details of the calculation follow. The discussion is also given in a paper by Kumer (1978).

2.2 Details of the Calculation

Two spatial coordinates are used to specify the arc geometry, namely, the altitude z and the distance x measured in the north-south direction from the

arc center (north is +). The arc is assumed to extend indefinitely in the y direction (East-West). The exact 2D radiation transport equation takes the form

$$S_{2D}(z, x) = S_0(z, x) + \int dx' dz' H_{2D}(z, z'; |x-x'|) \sigma[CO_2]_z \Omega(z') S_{2D}(z', x') \quad (2-1)$$

The quantities S , S_0 , Ω , $[CO_2]$ and E are defined by Kumer and James (1974), which will be referred to as KJ. The 2D Green's function is given by

$$H_{2D} = \int_{-\infty}^{\infty} dy' H_b(\sigma\eta) / 4\pi r'^2,$$

where

$$r' = (x - x')^2 + (z - z')^2 + y'^2,$$

H_b and σ are defined in KJ, $\vec{r}' - \vec{r}$ is a vector from the point $\vec{r} = (x, 0, z)$ of photon absorption to the point $\vec{r}' = (x', y', z')$ of the photon emission, η is the column density of CO_2 molecules along the vector $\vec{r} - \vec{r}'$. It is useful to note that

$$H_{2D} = H_{2D}(\sigma |N - N'|, |x - x'|),$$

where

$$N = \int_z^{\infty} dz_1 [CO_2]_{z_1} \text{ and } N' = \int_{z'}^{\infty} dz_1 [CO_2]_{z_1}.$$

Thus, given some distribution for the inhomogeneous terms $S_0(z, x)$ (the initial excitation rate), we solve Eqn. (2-1) to obtain the exact two-dimensional solution $S_{2D}(z, x)$.

In this study we solved the problem in two ways; first by solving the exact, two-dimensional (2D) integral radiative transport equation numerically. To obtain this solution by iteration requires five nested loops in the computer. We also solve the problem by introducing an approximate 1D radiative transport integral equation which applies for each altitude mesh point z_j . This second method requires four nested loops if the 1D equations are solved by iteration for a particular arc geometry. If the inverse $G_z = (1 - H_z)^{-1}$ is obtained at each z_j , then 3 nested loops are required to obtain a solution for any particular arc. This second approach may be applied to a large variety of arc geometries.

We show that the approximate method yields results that are very close to what is achieved if the exact method is employed. For many purposes, the accuracy of the approximate method may be practically sufficient when weighed against (i) the extra computer-time cost of obtaining an exact result or (ii) cases where inaccuracy in the data do not warrant a costly, exact solution.

First we discuss the iterative technique to achieve an exact solution to Eqn. (2-1). The computation proceeds most rapidly (and economically) if we use a first guess trial solution $S_{2D}^0(z,x)$ that is as realistic as possible. An excellent trial solution $S_{2D}^A(z,x)$ may be attained in a 2-step process as follows.

The first step is to obtain the plane-parallel solution $S_{1D}(z, x)$ which applies for each mesh point x by solving the 1-dimensional plane-parallel transport equations

$$S_{1D}(\sigma N, x) = S_0(\sigma N, x) + \int \sigma dN' H_{bp}(|N - N'| \sigma) \Omega(N') S_{1D}(\sigma N', x), \quad (2-2)$$

where we have replaced the coordinate z by $N = \int_z^\infty dz' [CO_2]_{z'}$, and the notation follows that in E.J. The details of lateral transport are not accounted for in executing the procedure which generates $S_{1D}(\sigma N, x)$; therefore, the x dependence will be incorrect. However, since $H_{bp} = \int_{-\infty}^\infty dx H_{2D}$, it is easy to see by integrating eq. (1) and (2) by $\int_{-\infty}^\infty dx$ that

$$\int_{-\infty}^\infty dx S_{1D}(\sigma N, x) = \int_{-\infty}^\infty dx S_{2D}(\sigma N, x)$$

is an identity; due to lateral transport,

$$\left| \frac{d}{dx} S_{1D}(\sigma N, x) \right| > \left| \frac{d}{dx} S_{2D}(\sigma N, x) \right|$$

will hold rigorously.

The next step is to generate an approximation $S_{2D}^A(\sigma N, x)$ that is the solution of an approximate 1 dimensional integral transport equation for each mesh

point σN_j associated with z_j . That is,

$$S_{2D}^A(\sigma N, x) = S_O^A(\sigma N, x) + \Omega(\sigma N) \int dx' H_{2D}^A(\sigma N, |x-x'|) S_{2D}^A(\sigma N, x'), \quad (2-3a)$$

$$S_O^A(\sigma N, x) = (1 - \Omega(1-E)) S_{1D}(\sigma N, x), \quad (2-3b)$$

where H_{2D}^A is given by

$$H_{2D}^A = \int \sigma dN^* H_{2D} \quad (2-4)$$

and, since $\int dx H_{2D}^A = 1 - E$ the identity

$$\int_{-\infty}^{\infty} dx S_{2D} = \int_{-\infty}^{\infty} dx S_{1D} = \int_{-\infty}^{\infty} dx S_{2D}^A \quad (2-5)$$

may be obtained by integrating eq.(2-3) by $\int dx$. The identity

$$\int dN S_{2D} = \int dN S_{2D}^A \quad (2-6)$$

may be obtained by integrating eqns. (2-1) and (2-3) by $\int \sigma dN$ and by using the identity $\int \sigma dN S_O \equiv \int \sigma dN S_{1D}(1-\Omega(1-E))$. The identities (2-5) and (2-6) are useful in checking on the accuracy of numerical computations of S_{1D} , S_{2D}^A and S_{2D} . The analogous equations and identities for the 3-dimensional case are given in Appendix A.

It is not predictable how $|\frac{d}{dx} S_{2D}^A|$ will compare with $|\frac{d}{dx} S_{2D}|$.

In Fig.(2-1) we show $S_O(z, x)/\sigma [CO_2]_z \equiv S_O(\sigma N, z)$ which is utilized to describe initial auroral excitation of $CO_2(001)$ in a nominal auroral arc as described in

Appendix B below. These functions are given for the highest mesh points,

$z = 92.5, 95.1, 98.8, 107.2,$ and 140 km. The full sets of 26 z mesh points and 31 x mesh points are given in Table 2-1.

Table 2-1
z, σ_N AND x MESH POINTS USED IN TIDE CALCULATION
DESCRIBED HEREIN

(Note that $.1400 + 03 = 0.14 \times 10^5$)

| z (km) | σ_N | x (km) |
|----------|------------|--------|
| .1400+03 | .1897+00 | -100.0 |
| .1072+03 | .8318+01 | -90.0 |
| .9884+02 | .4173+02 | -80.0 |
| .9508+02 | .9378+02 | -70.0 |
| .9252+02 | .1526+03 | -60.0 |
| .9096+02 | .2046+03 | -50.0 |
| .9018+02 | .2380+03 | -40.0 |
| .8818+02 | .3330+03 | -30.0 |
| .8384+02 | .6813+03 | -20.0 |
| .8022+02 | .1224+04 | -15.0 |
| .7168+02 | .1837+04 | -10.0 |
| .7605+02 | .2379+04 | -5.0 |
| .7520+02 | .2728+04 | .0 |
| .7385+02 | .3361+04 | 5.0 |
| .7060+02 | .5556+04 | 10.0 |
| .6659+02 | .8975+04 | 15.0 |
| .6345+02 | .1264+05 | 20.0 |
| .6137+02 | .1626+05 | 30.0 |
| .6026+02 | .1845+05 | 40.0 |
| .5935+02 | .2059+05 | 50.0 |
| .5719+02 | .2698+05 | 60.0 |
| .5467+02 | .3695+05 | 70.0 |
| .5254+02 | .4819+05 | 80.0 |
| .5103+02 | .5816+05 | 90.0 |
| .5020+02 | .6475+05 | 100.0 |
| .5000+02 | .6614+05 | 110.0 |
| | | 120.0 |
| | | 150.0 |
| | | 180.0 |
| | | 210.0 |
| | | 240.0 |

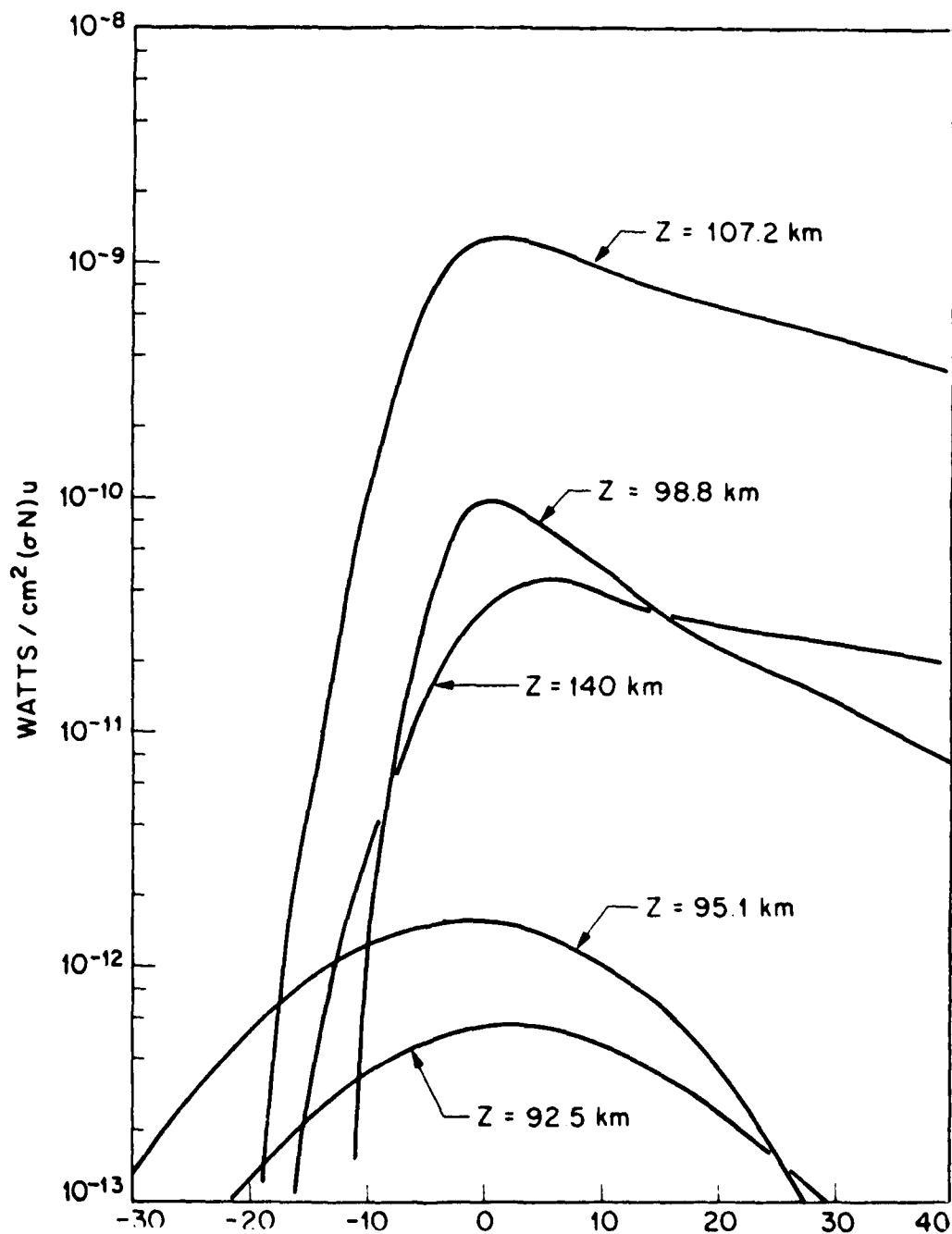


Fig. 2-1(a) Values for $S_0(z, \lambda)$ for $z = 140, 107.2, 98.8, 95.1$ and 92.5 km are shown on the interval $-30 \leq \lambda \leq 40$ km

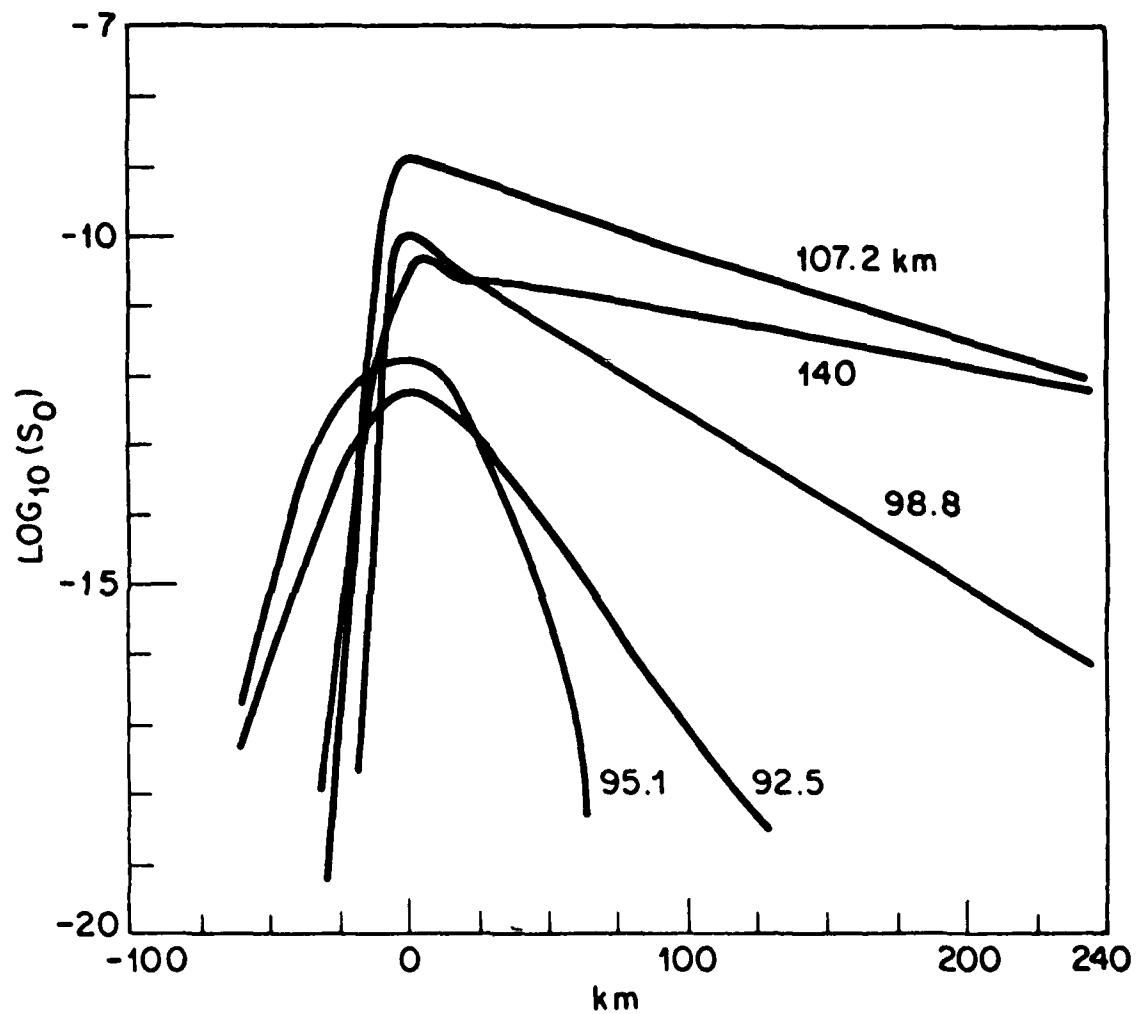


Fig. 2-1(b) As in Fig. 2-1(a), Except That the x Interval is Expanded to the Scale $-100 \leq x \leq 240$ km

On Fig. 2-2 we plot $S_0(\sigma N, x)$ vs. x for $z = 95.1$ and 107.2 km; for $z = 107.2$ km, we plot $S_{1D}(\sigma N, x)$, $S_{2D}^A(\sigma N, x)$ and $S_{2D}(\sigma N, x)$.

The S_{2D} is the result of solving eq. 2-1 by iteration. The solution S_{2D}^A of eq. 2-3 was used as the trial solution. Thirty iterations were required to achieve convergence. Convergence was accelerated by a technique described in Appendix C. The identity 2-5 is satisfied with sufficient accuracy (within 1/2%) to promote confidence that there is no major logical or numerical error in the computation. The integrations in eqs. (2-1), (2-3) and (2-5) were performed over the range $-100 < x < 240$ km. Outside this range, we assumed $S(x_L) = S(-100 \text{ km})$ for $x_L \leq -100$ km and $S(x_b) = S(240 \text{ km})$ for $x_b \geq 240$ km. Since $S_0(\sigma N, x)$ is a maximum at $x = 0$, it follows that the integral of S_{1D} over the range $x = -100$ to 240 km should be slightly larger than the integral of S_{2D} or S_{2D}^A on the same interval. This we found to be the case by about 1/2%.

From Fig. 2-2 one sees that, for $z = 107.2$ km,

$$\left| \frac{d}{dx} S_{2D} \right| > \left| \frac{d}{dx} S_{2D}^A \right| \quad (2-7)$$

holds for all x . The "tail" in S_{1D} for $x \leq -20$ km is the result of broadened values which occur in the nominal arc model for $S_0(\sigma N, x)$ in the region $85 \leq z \leq 97$ km. Essentially the same kinds of results are plotted for $z = 95.1$ km in Fig. 2-3. Again the identity 2-5 is satisfied within 0.67%. For $z = 95.1$ km, we find that

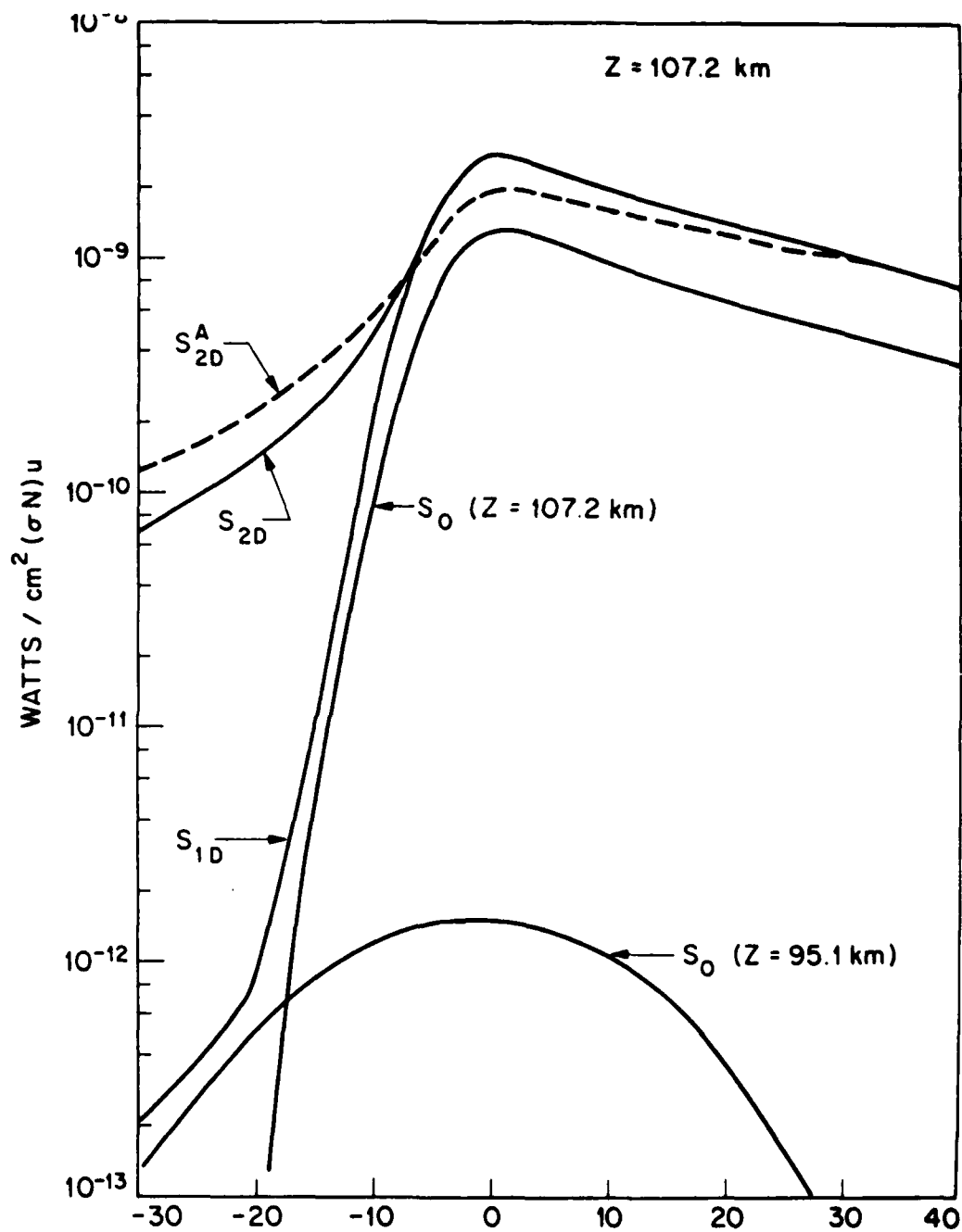


Fig. 2-2 The Quantities S_{1D} , S_{2D}^A , S_{2D} and S_0 for $z = 107.2$ km are shown on the Interval $-30 < x < 40$ km; S_0 for $z = 95.1$ km is also shown

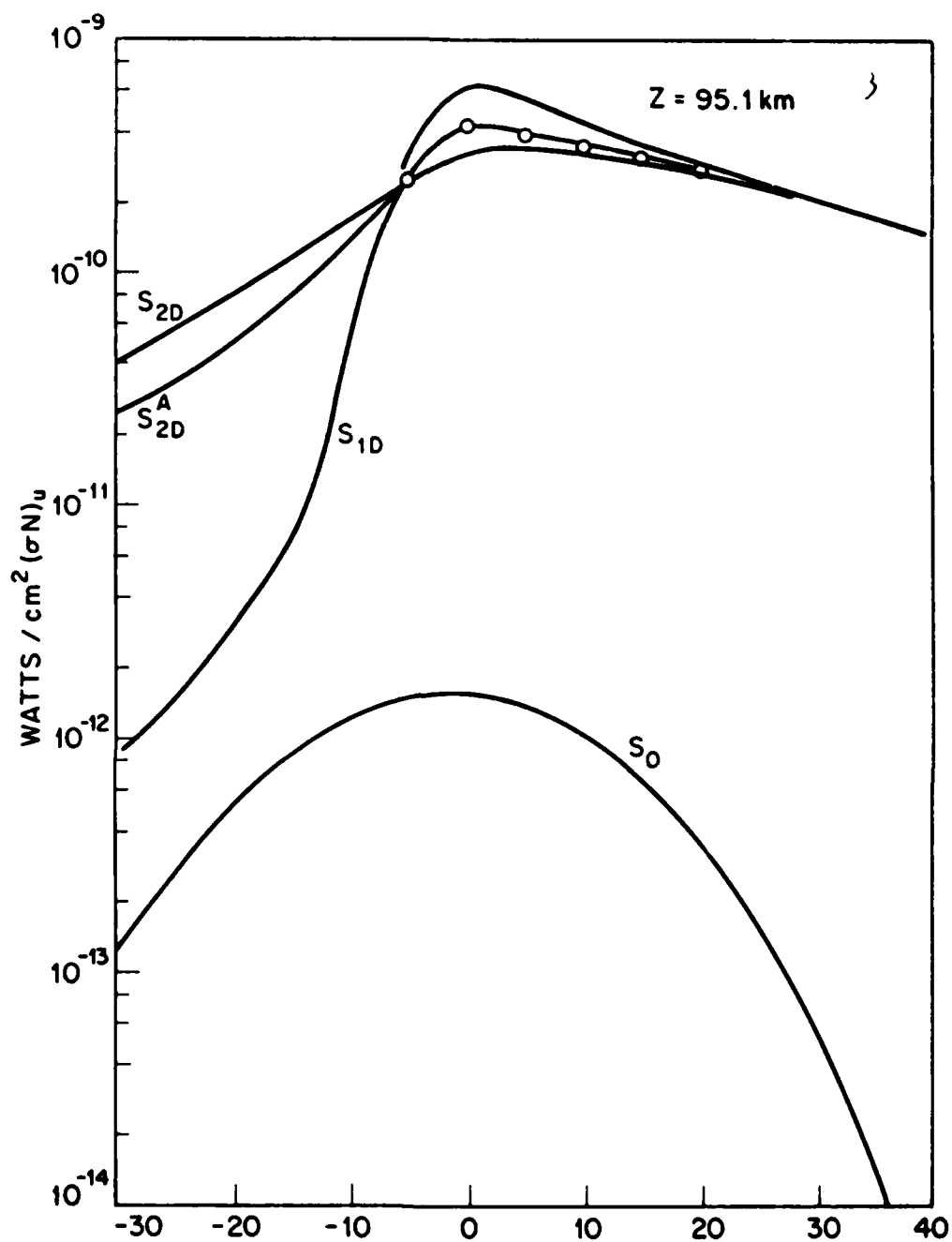


Fig. 2-3 The Quantities S_{1D} , S_{2D}^A , S_{2D} and S_0 are Shown

$$\left| \frac{d}{dx} S_{2D} \right| < \left| \frac{d}{dx} S_{2D}^A \right|. \quad (2-8)$$

In fact, the inequality(2-8) is true for all z mesh points except $z = 107.2$ km.

The simple qualitative explanation for this behaviour is (i) that H_{2D}^A is computed on the assumption that $\frac{d}{dz} S(z,x) = 0$ and (ii) that there is just one maximum in the quantities $S_0(z,x)$ and in $\int dx S_0(z,x)$ and that this maximum occurs at $z = 107.2$ km.

2.3 Results

On Fig.2-4 we show nadir radiance as a function of x as calculated from the various solutions $S(\sigma N, x)$ cited above via

$$4\pi R(x) = \sigma \int_0^{\sigma N_L} dN' T_b(\sigma N') S(\sigma N', x) \Omega(N') \quad (2-9)$$

where $N_L = \int_{z_L}^{\infty} dz' [CO_2]_{z'}$, and $z_L = 50$ km. On Fig.2-4 it is seen that $R_{2D} \approx R_{2D}^A$ (the agreement is within 5% or better on the region of x shown on Fig.2-4).

Consideration of the identity 2-6 shows there will always be at least one node in the quantity $S_{2D} - S_{2D}^A$ on the interval $0 < \sigma N < \sigma N_L$ and, correspondingly, there should be at least one node in the quantity $\Omega T(S_{2D} - S_{2D}^A)$ on this interval. This would tend to create similarity in the values R_{2D} and R_{2D}^A . For the $4.3 \mu m$ arc model that we consider in this paper, there are 2 nodes in $\Omega T(S_{2D} - S_{2D}^A)$ which occur on either side of the maximum in S_{2D} . This should further increase the similarity of R_{2D} and R_{2D}^A . Thus, one might indeed expect the close similarity between R_{2D} and R_{2D}^A which is shown on Fig. 2-4.

These results suggest that the use of the approximation eq. 2-3 to obtain approximate plane parallel multidimensional radiation transport solutions may be sufficiently accurate for some purposes.

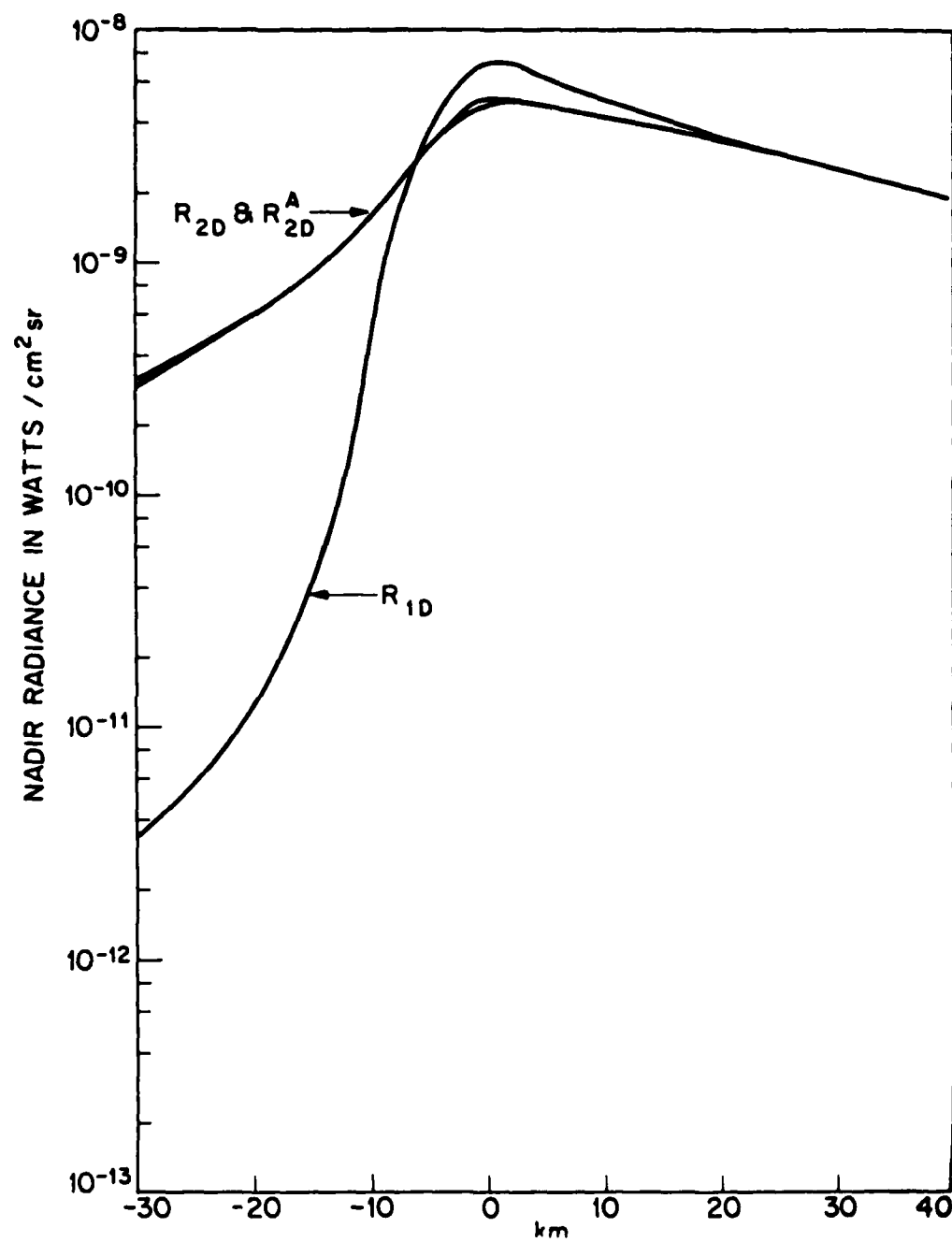


Fig. 2-4 The Quantities R_{1D} , R_{2D}^A and R_{2D} are Shown.

2.4 Implications

Lateral gradients in the nadir radiance R_{1D} that is predicted if lateral transport is neglected are seen to be considerably steeper for all values of x than for the predictions R_{2D} or R_{2D}^A which include the effects of lateral transport. The effect of lateral transport is predicted to smoothout lateral gradients. This effect should be very important in the nuclear case. The effect should be quantitatively confirmed experimentally in order to provide accurate assessment of the performance of advanced nadir viewing scanner sensors operating against the auroral, or nuclear, background.

3.0 Experimental Verification of the Lateral Photon Transport Smoothing Effect in the CO_2 4.3 μm Aurora

3.1 Introduction

In this chapter we provide quantitative analysis for several alternate rocket borne experiments to verify that the effect of lateral radiation transport of CO_2 4.3 μm photons in the earth's optically thick upper atmosphere renders the lateral gradients in the CO_2 4.3 μm auroral nadir radiance no more severe than the lateral gradients in auroral 2.7 μm nadir radiance even though the DC level of the CO_2 4.3 μm auroral radiance may be as much as 10 times that of the 2.7 μm aurora in steady state conditions. Verification of this point is important for assessing high altitude nuclear degradation of the performance of advanced nadir viewing scanner systems due to high altitude nuclear mechanisms such as x-ray, β -patch, and debris patch deposition which are similar to the aurora.

Pursuing this goal, we considered 4 distinct experimental concepts applicable for the 4.3 μm region, and briefly considered a 2.7 μm experimental concept too. Most of these concepts involved firing a rocket over an auroral arc and viewing the aurora in the nadir in order to measure lateral structure in auroral nadir radiance in the 4.3 and 2.7 μm spectral regions. Nadir viewing 4.3 μm concepts included a Broad Band Filtered Radiometer (BBFR), a narrow band tilting 10 transmission channel picket fence filtered radiometer (NBTFR) and the use of HIRIS. In each case the instruments are to be used with a wheel of CO_2 absorption cells in order to provide the added high resolution $\approx 6 \times 10^{-3} \text{ cm}^{-1}$ near the centers of the CO_2 lines that is necessary to discriminate CO_2 4.3 μm narrow line auroral nadir radiance from the earth nadir radiance background. It turns out that 0.2 to 0.5 cm^{-1} resolution between the lines is also necessary in order to suppress deleterious effects of the broad band LTE thermal stratospheric contribution to the earth's 4.3 μm nadir radiance background. This requirement is sufficient to rule out the BBFR for use in the desired arc overfly experiment. The NBTFR and HIRIS easily satisfy this 0.2 to 0.5 cm^{-1} spectral requirement. The HIRIS however turns out to be less sensitive than is required for a successful experiment. The detailed quantitative analysis presented below in Sections 3.4 and 3.5 shows that the HIRIS signal/noise ≈ 1 in the spatial wing region of the nominal arc

(approximately 15 km or more south of arc center). However, verification of the lateral smoothing effect of radiation transport on the CO_2 4.3 μm auroral arc requires accurate measurement in the spatial wing of the arc. It is shown that the required accuracy may indeed be provided by the NBTFR which can achieve signal/noise of approximately 30 in the spatial wing region of the nominal arc.

The optimum design NBTFR uses liquid Nitrogen (LN_2) cooled optics including the tilting filters, and LN_2 cooled baffling. This reduces the NEP of the .71 cm diameter InSb detector to $\approx 3.0 \times 10^{-14} \text{ w}/\sqrt{\text{Hz}}$, nearly the inherent LN_2 cooled detector noise limit. The narrow band filter is a 4" diameter Silicon (index of refraction ≈ 3.4) substrated Fabry Perot etalon designed so that the centers of 10 of its transmission channels roughly coincide with the lines p8, p10, ..., p26 of the $^{12}\text{C}^{16}\text{O}_2$ 001 \rightarrow 000 band. A 300 A blocker filter allows just the 10 channels to be transmitted. The narrow band filter is designed so that the transmission channel full width half maximum FWHM $\approx 0.21 \text{ cm}^{-1}$ (i.e., 4A) for an FOV with the 1/2 cone angle $\alpha = 2^\circ$. The throughput of the optimum NBTFR is $\approx .062 \text{ cm}^2 \text{ sr}$ for an overall optics transmission of $\approx 20\%$. The NER $\approx 5.0 \times 10^{-13} \text{ w}/\text{cm}^2 \text{ sr}$. Spectral scanning between the CO_2 line centers is achieved by tilting the filter. High spectral resolution of $\approx 6 \times 10^{-3} \text{ cm}^{-1}$ near the CO_2 line center is of course achieved by utilization of the CO_2 absorption cells. Two similar NBTFR instruments that employ LN_2 cooled optics and tilting filter have been developed under DoD contracts DAAK40-75-C-0417 and F3615-77-C-1190 for deployment in the Q hatch of the U2.

An arc underfly verification experiment was given some consideration. Our impressions on this concept are: 1) It has the advantage that a simple instrument may be used for zenith viewing against the cold sky background however, due to intervening atmospheric CO_2 absorption of auroral CO_2 4.3 μm emission it is probably necessary to use CO_2 cells in order to accurately detect weak CO_2 4.3 μm zenith auroral signals from rocket altitudes as low as 85 km. 2) It has three disadvantages; 1) the rocket spends less time in the altitude range where useful data may be obtained therefore, decreasing the

probability that phenomena will be observed; ii) the overfly can simultaneously monitor energy input by optical measurements and by measurements of the precipitating auroral particles; iii) the overfly measurements are obtained in the nadir mode which is exactly similar to the viewing mode of the advanced scanner systems that the data will support, zenith data obtained in the underfly experiment will not share this advantage, as it may be. As part of our study we also verified that an optimum NBTFR could be used effectively in an arc overfly experiment to verify that lateral gradients in the $2.7\mu\text{m}$ auroral nadir radiance are indeed as sharp and dramatic as what one would expect from an essentially prompt, optically thin auroral emission.

3.2 Details of the Requirement to Use CO_2 Absorption Cells

We address the problem of devising a field experiment to verify that lateral gradients in the CO_2 $4.3\mu\text{m}$ auroral nadir radiance are no more severe than the $2.7\mu\text{m}$ nadir radiance even though the DC level of the CO_2 $4.3\mu\text{m}$ auroral radiance may be as much as 10 times that of the $2.7\mu\text{m}$ aurora in steady state conditions. Auroral nadir radiance calculations at 2.7 and $4.3\mu\text{m}$ for a nominal arc as described in Appendix B are shown in Fig. 3-1. The lateral gradients in the auroral CO_2 $4.3\mu\text{m}$ nadir radiance are seen to actually be less than in the auroral $2.7\mu\text{m}$ nadir radiance even though the CO_2 auroral $4.3\mu\text{m}$ nadir radiance level is considerably larger than at $2.7\mu\text{m}$. The nominal 30 kR 3914A aurora moves in to lateral position $x = 0$ from the north at a rate 3 km/min and then is assumed to stabilize for 2 minutes. The long time constant ($\gtrsim 5\text{ min}$) for auroral CO_2 $4.3\mu\text{m}$ emission tends to smooth the $4.3\mu\text{m}$ lateral nadir radiance gradients north of $x = 0$. This long time dependence for the CO_2 $4.3\mu\text{m}$ aurora has been established by data obtained in the DNA/AFGL auroral measurements programs and by the detailed analysis of these data. The smoothing of the $4.3\mu\text{m}$ nadir radiance south of $x = 0$ (i.e., for $x < 0$) is predicted to be the result of lateral radiation transport. This effect has not as yet been verified experimentally. The work described in this section is aimed at the quantitative analysis of various experiments which might be performed in order to verify the CO_2 $4.3\mu\text{m}$ lateral nadir radiance radiation transport smoothing effect which is depicted on Fig. 3-1. Since this effect is such an important consideration for advanced sensors, it is clear that some kind of experimental verification is necessary.

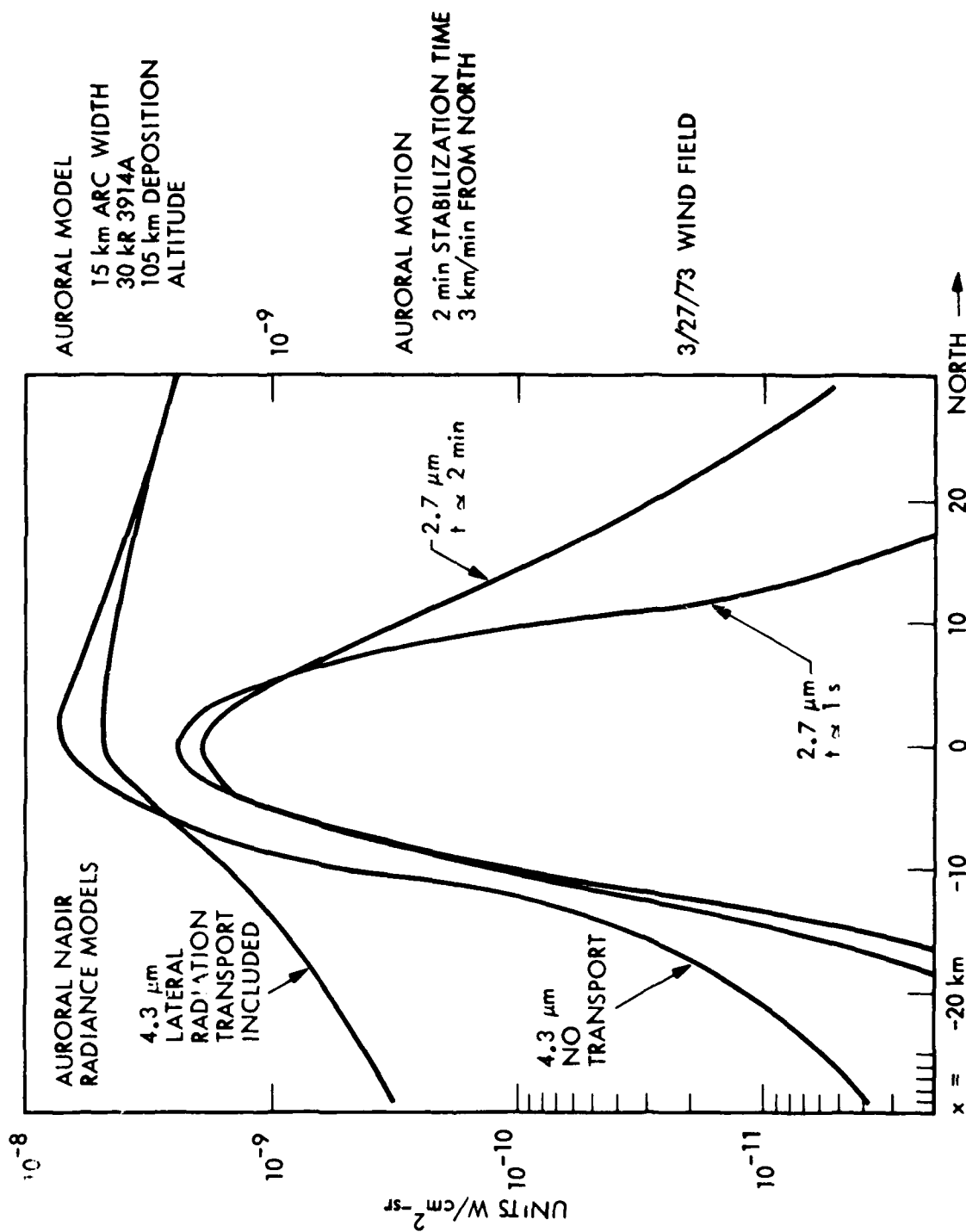


Figure 3-1 The Predicted Lateral Radiation Transport Smoothing Effect on CO_2 $4.3\mu\text{m}$ Auroral Nadir Radiance is Shown.

The verification will not be simple in an arc overfly nadir viewing experiment due to the earth background. This point is illustrated by Fig. 3-2. Auroral nadir radiance at 2.7 and 4.3 μm appropriate for a 10 kR 3914A steady state auroral arc are compared with a night time 1962 U.S. Standard Atmosphere nadir radiance background calculation (at low resolution $\approx 0.01 \mu\text{m}$) on Fig. The background levels expected to obtain at 2.7 and 4.3 μm for a somewhat more realistic 65°N winter atmosphere (PKR in winter) are also crudely drawn in as dashed lines on Fig. 3-2. Explicitly, the point made on Fig. 3-2 is that it will be difficult to distinguish the auroral nadir radiance from the earth background nadir radiance if resolution like 0.01 μm is used. It is also clear that this is particularly true with regard to nadir measurement of the 4.3 μm radiance.

The problem has a potential solution if the nadir radiance is viewed in high resolution. This point is illustrated by Fig. 3-3. Fig. 3-3 shows an estimate for the detailed spectral structure in the 4.3 μm nadir radiance which is calculated for auroral conditions similar to those obtained in the well documented (AFGL-TR-77-0157) 3/24/73 break up.

There are 3 distinct features in the detailed CO_2 4.3 μm nadir radiance spectrum, auroral R_A , stratopause R_p , and stratospheric R_s .
 $R_A : R_p : R_s = 1.9 : 7.8 : 40$. The features on Fig. 3-3 are easy to understand qualitatively. On Fig. 3-4 we show the CO_2 ν_3 vibrational temperature altitude profile appropriate for the 3/24/73 event and on Fig. 3-5 we show the altitude z where optical depth = 1 for a given displacement in cm^{-1} from line center. It is apparent that R_A is a non-LTE result of auroral enhancement in CO_2 ν_3 vibration temperature which occurs in the altitude region $z \gtrsim 75$ km and which peaks near 90 km, that R_p is due to the LTE ν_3 vibration temperature stratopause maximum which occurs near the $z \approx 50$ km region, and that R_s results from pressure broadened emission between the line centers in the stratosphere in the altitude region $z \lesssim 35$ km. The detailed spectrum on Fig. 3-3 shows that resolution $6 \times 10^{-3} \text{ cm}^{-1}$ or better is required to discriminate the CO_2 4.3 μm aurora from the stratopause and stratospheric backgrounds.

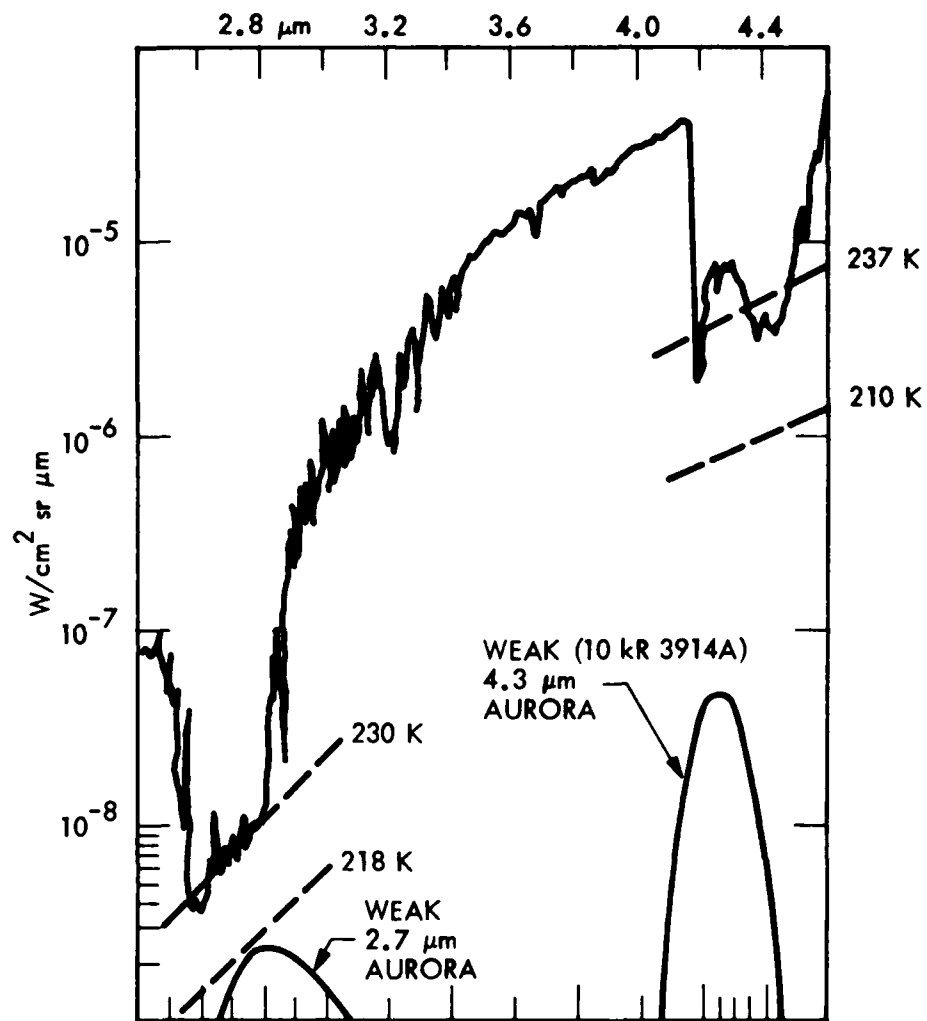


Figure 3-2 Low Spectral Resolution Comparison of Typical Nadir Background Against a Weak Auroral Case.

TWO LINE MODEL FOR ESTIMATING DETAILED NADIR SPECTRAL
STRUCTURE IN THE 4.3 μm REGION

DEFINE $R_i = \int dw R_i(W)$ THEN:

$$\begin{aligned} R_A &= 1.9 \times 10^{-9} \text{ W/cm}^2 \text{ sr} \\ R_P &= 7.8 \times 10^{-9} \text{ W/cm}^2 \text{ sr} \\ R_S &= 40.0 \times 10^{-9} \text{ W/cm}^2 \text{ sr} \end{aligned}$$

$$R_A / \Sigma R \approx 0.03$$

RESOLUTION OF $\approx 6 \times 10^{-3} \text{ cm}^{-1}$
IS NECESSARY TO OBSERVE 4.3 μm
AURORA (NADIR VIEWING)

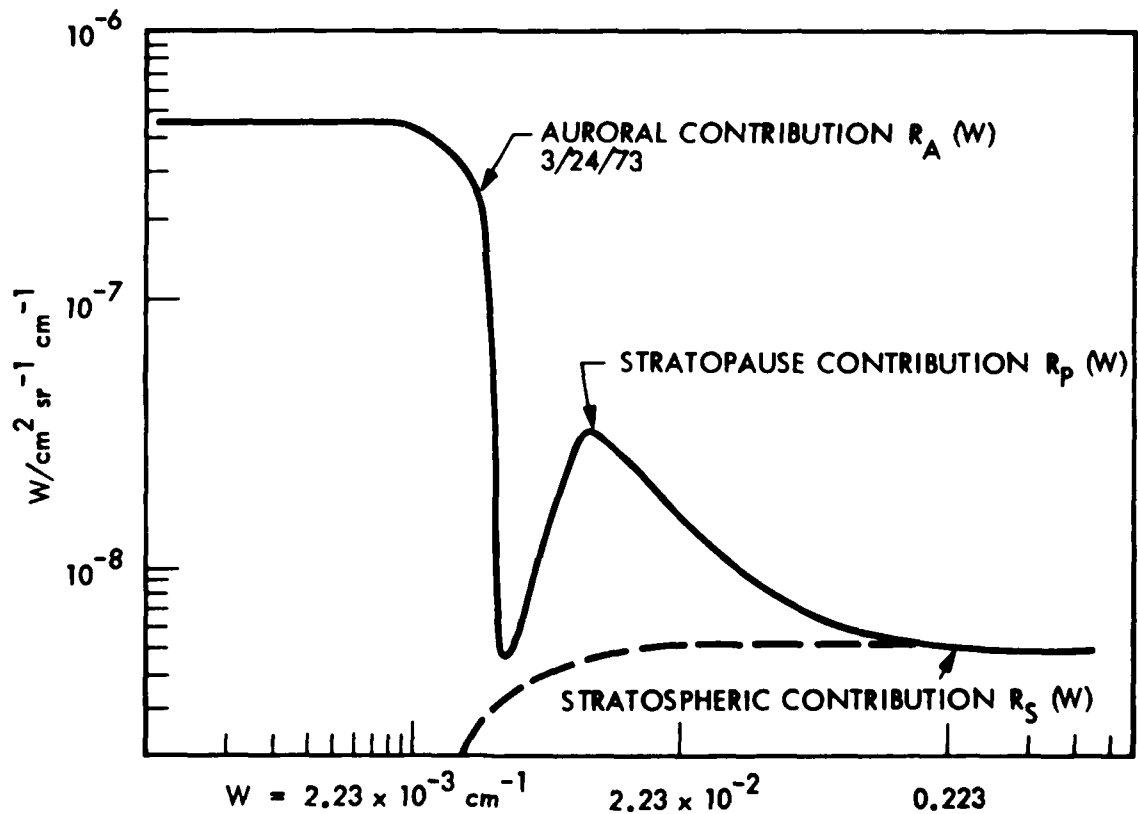


Figure 3-3 Detailed Nadir Viewing Spectral Structure in a Strong CO_2 Line Near 4.3 μm .

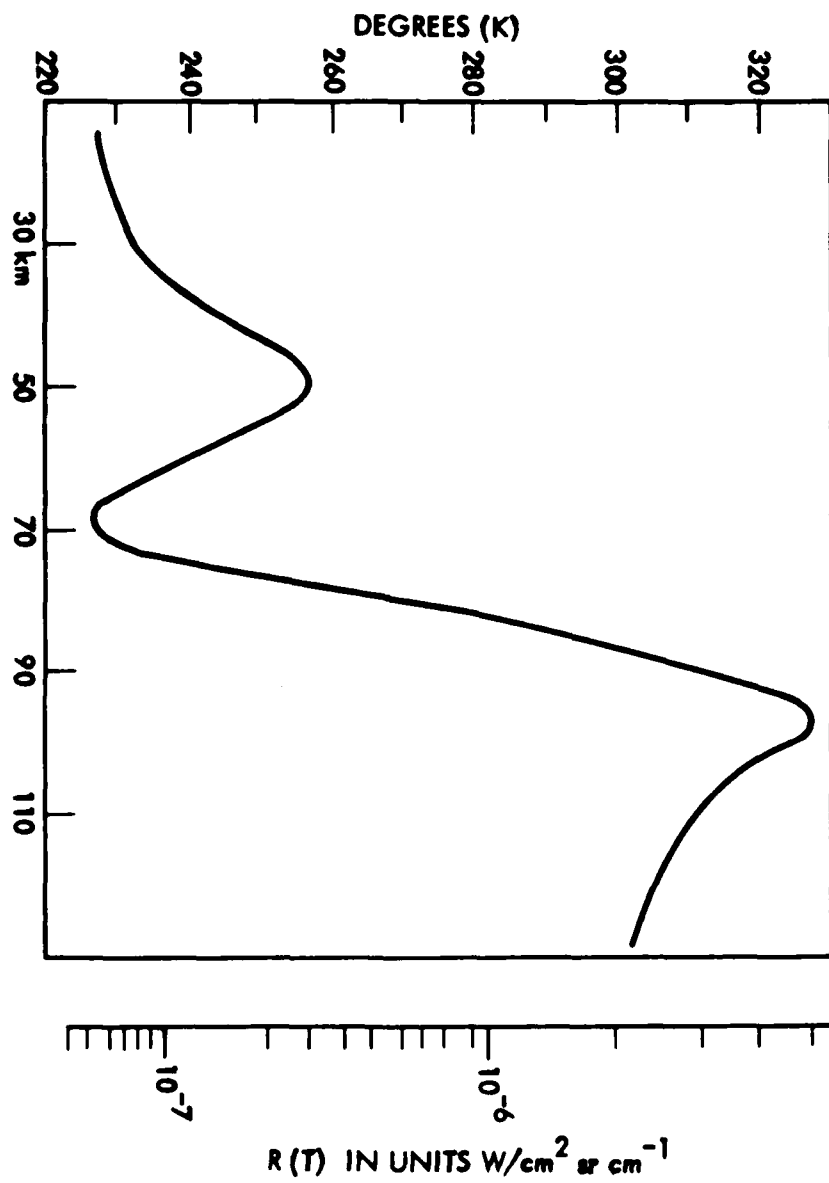


Figure 3-4 The CO_2 v_3 Temperature Profile Appropriate For the 3/24/73 Aurora.

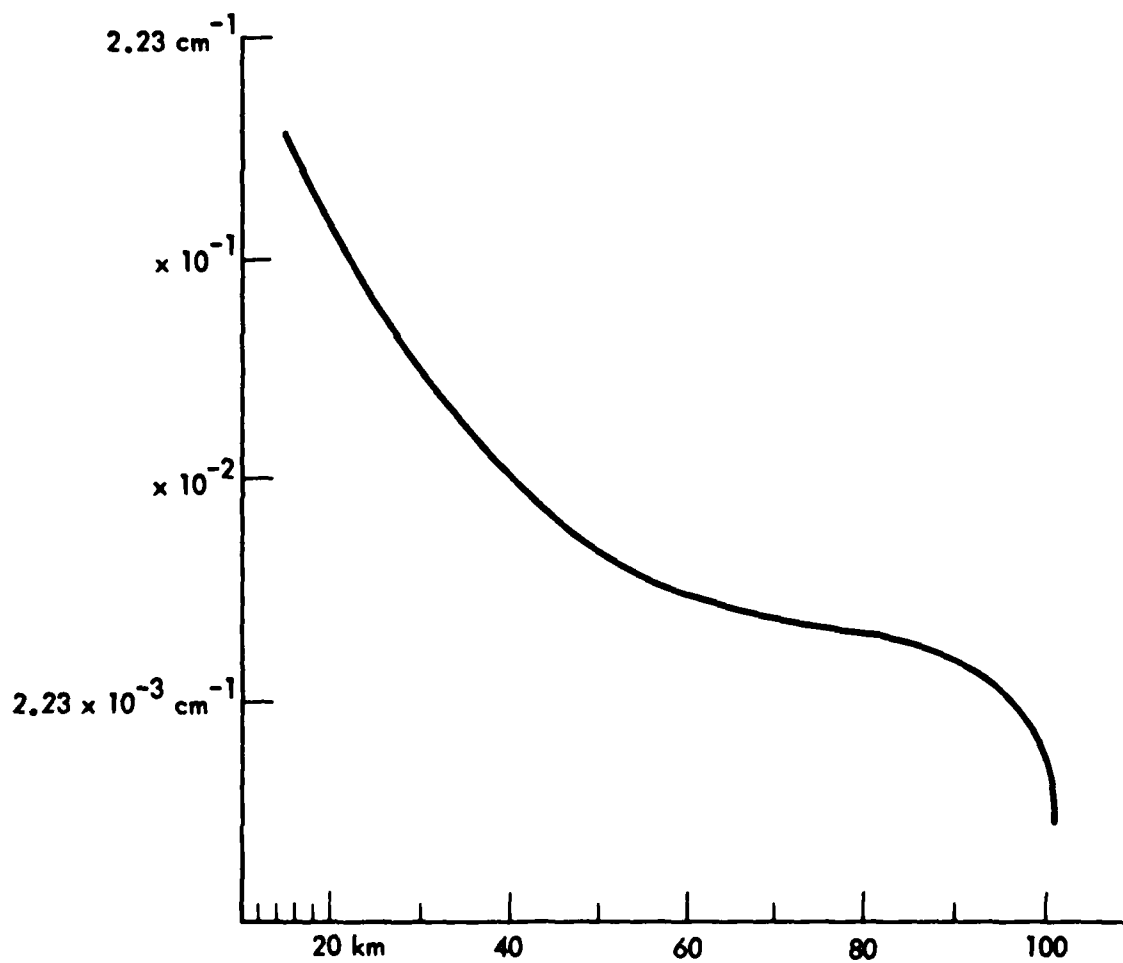


Figure 3-5 Altitude $z(w)$ For Which $\tau(z,w) = 1$ is Plotted Here.

The only way to achieve this kind of resolution with state-of-the-art technology involves utilization of CO₂ absorption cells. The cells may be used as an adjunct resolution element by positioning them in front of a broad band (.2 μm) filtered radiometer, (BBFR) or a narrow band (4A = .21 cm⁻¹) picket fence filter tilting radiometer, (NBTFR) or a HIRIS-like (resolution = 0.5 cm⁻¹ 9A) interferometer.

The CO₂ cells may be used to discriminate the auroral signal as follows. We can use two cells, one at vacuum and another with an amount of CO₂ selected to absorb the auroral component of CO₂ 4.3 μm nadir radiance shown on Fig.3-3. The change in signal R^{ij} on interchange of the two cells is the auroral nadir radiance component. The interchange of the two cells allows for weighting the auroral CO₂ 4.3 μm volume emission as a function of altitude as is currently done in the analogous NASA Nimbus 5 nadir sounding measurement of 15 μm CO₂ volume emission via "The Infrared Temperature Profile Radiometer (ITPR) Experiment" which is described by Smith et al. in the NASA Number 5 User's Guide, 1972. The change in signal R^{ij} on cell interchange is given by an integral over the product of the cell interchange weighting functions W^{ij} and the CO₂ volume emission Ω S via

$$R^{ij} = \frac{1}{4\pi} \int dz \quad W^{ij}(z) \Omega(z) S(z).$$

The physics details of the calculation of the cell interchange weighting functions W^{ij} are given in Appendix G. The highlight of the calculation is that variation in the atmospheric line and bandshapes due to altitude dependent atmospheric temperature variation, and pressure variations, are accounted for in detail.

3.3 The Broad Band Filtered Radiometer Concept

Some results for the W^{ij} are shown on Fig. 3-6 for 10 cm length cells with various CO_2 and broadener gas (B_r) partial pressures, and with various Lorentz line broadening parameters as listed on Fig. 3-6. These sounding functions W^{ij} were calculated for a broad band (4.19 to 4.38 μm) filtered radiometer, but they can also be used to gain insight as to requirements of resolution and sensitivity for more sophisticated instrumentation such as the narrow band picket fence tilting filtered radiometer, or a HIRIS like instrument.

On Fig. 3-7 we show the auroral contribution $R_A^{12} = \frac{1}{4\pi} \int dz w^{12} \Omega S_A$ that would be measured in an auroral arc overfly experiment which utilizes a 4.19 to 4.38 μm broad band filtered radiometer (BBFR) and cells 1 and 2 from Fig. 3-6.

On first consideration it might seem that the use of CO_2 absorption cells with the BBFR would be adequate to verify the lateral transport smoothing effect on CO_2 4.3 μm auroral nadir radiance in an arc overfly experiment. There are serious problems with the BBFR arc overfly experiment however. These problems are caused by the fact that the broad band filter does not spectrally discriminate against the large stratospheric nadir radiance background. By inspection of Fig. 3-7 one sees that for $x \leq -15$ km it is necessary to be able to accurately discriminate and measure the auroral contribution to nadir radiance in order to verify the CO_2 4.3 μm lateral transport gradient smoothing effect. In this critical region the auroral contribution R_A^{12} is quite small however, $R_A^{12} \leq 2.75 \times 10^{-10}$ w/cm²sr in the region $x \lesssim -15$ km. The stratospheric DC contribution R_s to the nadir radiance observed via the BBFR will at the least be about $R_s \simeq 2 \times 10^{-7}$ w/cm²sr (see Fig. 3-2 above), about 3 orders of magnitude larger than the auroral nadir radiance we wish to detect.

The large stratospheric DC signal can cause problems in the detection of

| CELL NO. | PRESSURE (atm) | | LORENTZ PARAMETER |
|----------|-----------------------|-----------------------|-----------------------|
| | CO ₂ | Br | |
| 1 | 0 | 0 | 0 |
| 2 | 4.52×10^{-6} | 0 | 2.04×10^{-4} |
| 3 | 3.27×10^{-5} | 1.63×10^{-4} | 6.29×10^{-3} |
| 4 | 6.54×10^{-5} | 0 | 2.96×10^{-3} |

4.19 TO 4.38 μm SOUNDING FUNCTIONS
FOR 4 CELLS, 10 cm LONG, CHARACTERISTICS
ARE

$$R^{ij} = \int dz W^{ij} \Omega S$$

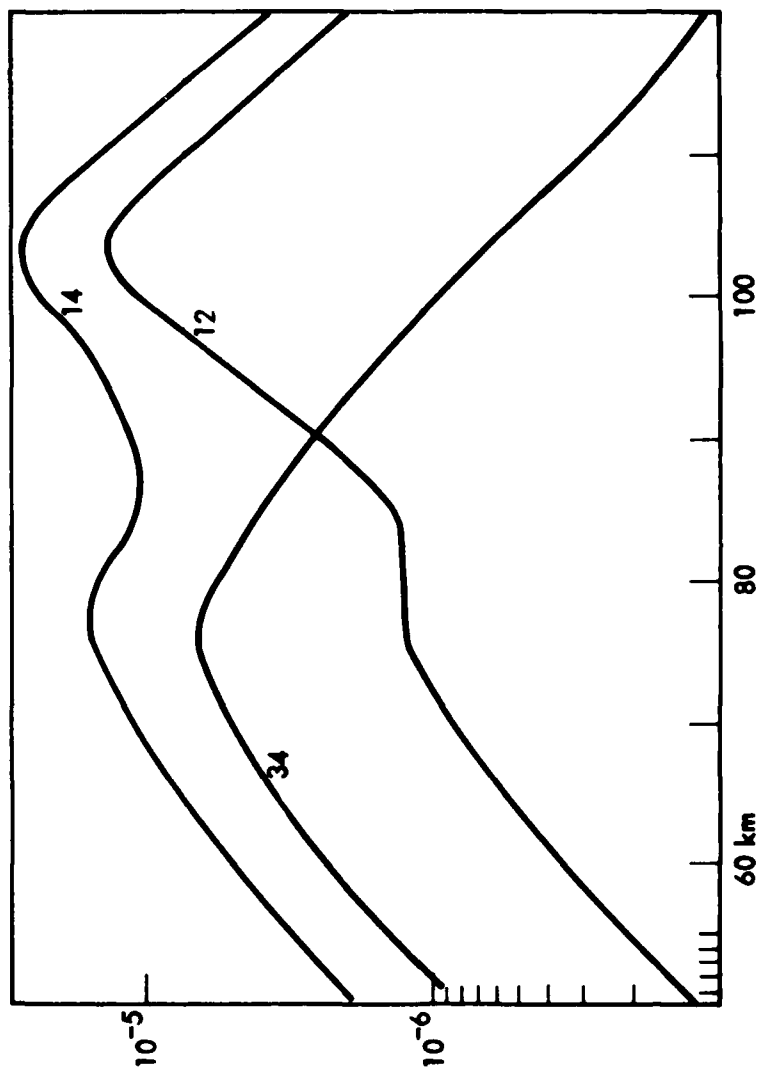


Figure 3-6 Preliminary Results W^{ij} for the Sounding Functions Which May be Achieved by Interchange of Cells Listed Above.

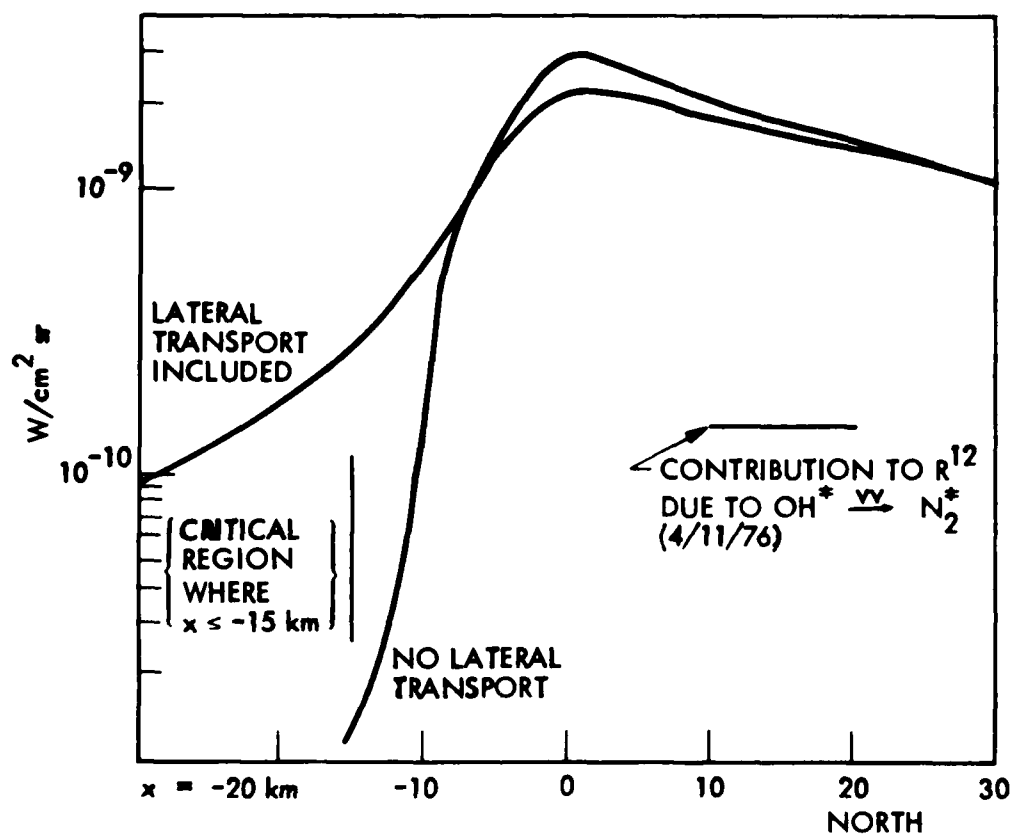


Figure 3-7 Calculations of R_A^{12} With, and Without, Including the Lateral Radiation Transport Smoothing Effect.

R_A^{12} in two ways. First, data on lateral variations in the stratospheric component of $4.3 \mu\text{m}$ nadir radiance which were obtained in the RM19 satellite experiment suggest that if the timing of cell interchange is slow (of the order 1/2 sec. or slower) the lateral structure in the stratospheric temperature can cause fluctuations of the order of 10^{-2} the DC signal per cell interchange and this will be more than enough to mask the auroral signal R_A^{12} in the critical lateral region $x \lesssim -15 \text{ km}$. Secondly, although the design goal would be to construct the cells 1 and 2 with identical transmission properties, it may well be that small deviations from this design goal could cause signal changes of the order 10^{-3} of the stratospheric background on cell interchange. Of course preflight calibration of the transmission properties could help to alleviate this problem. In order to solve both of these problems it is necessary to have, in addition to the CO_2 absorption cells which can provide a resolution capability of a few times 10^{-3} cm^{-1} near line center, an additional resolution capability of $.2$ to $.5 \text{ cm}^{-1}$ (4 to 10 A) between the lines in order to discriminate against the stratospheric contribution to nadir radiance and thereby track and account for the lateral fluctuations in the stratospheric component, and also to provide in flight calibration of the transmission characteristics of the individual cells.

3.4 The Narrow Band Solid Etalon Fabry Perot Tilting Filtered Radiometer Concept

With this purpose in mind let us next consider the use of CO_2 absorption cells and a 10 channel narrow band solid etalon Fabry Perot tilting filtered radiometer (NBTFR). We cite a similar conceptual instrument described by Kumer and Roche (Arc Overfly Nadir Radiance Experiment for the Multi II, Technical Brief, LMSC D457106, May 1975). A sketch of the design for an improved version of the NBTFR for use in the arc overfly experiment is shown on Fig. 3-8. This instrument is considerably improved over the previous conceptual design which is given in the 1975 Kumer and Roche technical brief in that the detector and all of the optics including the narrow band tilting filter to the right hand side of the lens L1 are to be liquid Nitrogen (LN_2) cooled. Similar designs for LN_2 cooled optics and tilting narrow band filters have been developed under DoD support in two background measurements programs, namely HICAMP (contract No. DAAK40-75-C-0417) and DBAR (contract No. F3615-77-C-1190). The instrumentation developed under these programs are

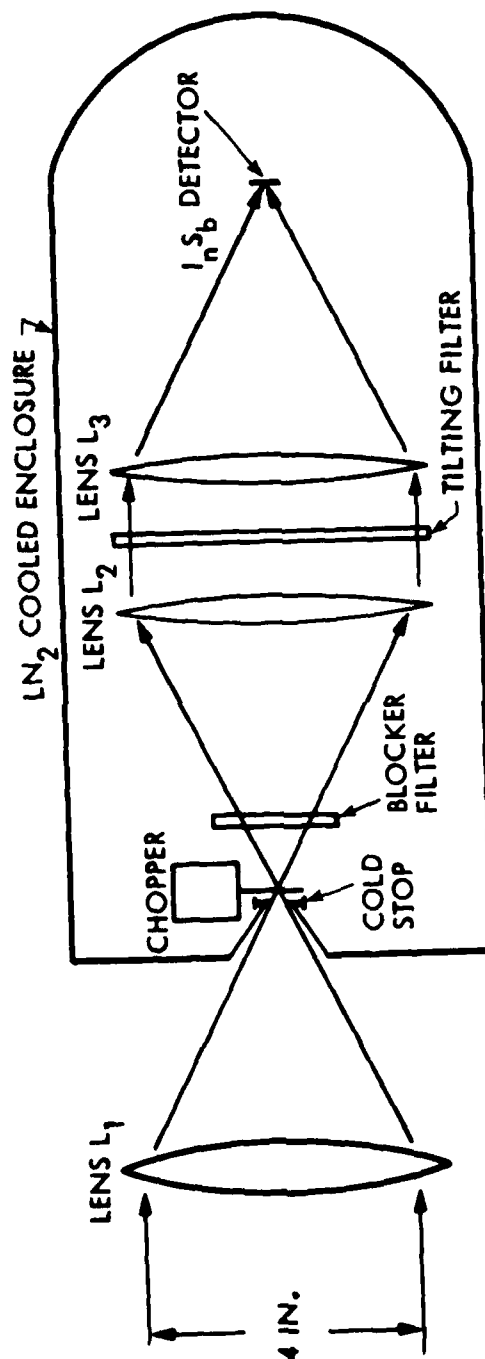


Figure 3-8 Schematic of LN₂ Cooled Optics and Tilting Filter. For Cooled baffling the dewar may be extended past L1. The lenses are F1. The detector diameter is 0.71 cm to obtain $\alpha = 2^\circ$.

utilized in a nadir mode from high flying aircraft. The technology for NBTFR LN_2 cooled optics including tilting filter has been fabricated and is currently in the debugging process under the auspices of these programs. This will considerably reduce the expense and the risk of application of similar technology to the arc overfly experiment.

An advantage of LN_2 cooled optics including tilting narrow band filter for the arc overfly experiment is the suppression of photon noise which results from nadir viewing of the earth through the narrow band filter. The contribution to NEP due to the 250°K earth viewed through the cold narrow band filter, which transmits 10 channels of width 0.2 cm^{-1} each, is about $1.5 \times 10^{-14} \text{ w}/\sqrt{\text{Hz}}$. The inherent InSb 0.71 cm for 77°K detector noise contribution to NEP is about $2 \times 10^{-14} \text{ w}/\sqrt{\text{Hz}}$. For the discussion that follows we use $\text{NEP} = 3 \times 10^{-14} \text{ w}/\sqrt{\text{Hz}}$ due to the combined effects of nadir viewing photon noise and of inherent detector noise.

In the Kumer and Roche Technical Brief (1975) it was shown that it is possible to build a solid Fabry Perot filter with a 10 channel transmission spectrum such that the centers of the transmission channels are aligned with the $10^{12} \text{C } ^{16}\text{O}_2$ $001 \rightarrow 000$ band lines P8 through P26 well enough so that the net transmission is equivalent to 7 completely transmitted lines. To achieve this transmission with an Si substrate (index of refraction $\simeq 3.4$) it must be manufactured with a thickness tolerance of ± 1 part in 10^3 , or about $\pm 1 \text{ um}$. In telephone conversation 12-5-77 with Perkin Elmer representative Ed Strauss indicated that manufacture of an Si substrate within this tolerance can readily be achieved. Use of the Si substrate rather than quartz (index of refraction $\simeq 1.6$) allows for expanding the FOV up to $\frac{1}{2}$ full cone angle $\alpha = 2^\circ$. With $\alpha = 2^\circ$ the full width half maximum (FWHM_{00}) of the transmission channels is broadened by a factor $\sqrt{2}$ from the design value of $2 \sqrt{2} \text{ A}$

for normal incidence collimated light to $\text{FWHM}_{20} = 4\lambda$ for normal incidence of the conical bundle of light with $\alpha = 2^\circ$. This follows from the centroid blue shift formula for small angles θ for the Fabry Perot filter, namely $\delta\lambda_\theta \cong \lambda_0 \theta^2 / 2n^2$ where $\lambda_0 \cong 4.3 \times 10^4 \text{ \AA}$ and an index of refraction $n \cong 3.4$ for an Si substrate. For the $\frac{1}{2}$ cone angle α normally incident bundle of light $\text{FWHM}_\alpha \cong \sqrt{\text{FWHM}_{20}^2 + \delta\lambda_\alpha^2}$. Thus use of an Si substrate rather than quartz improves throughput by a factor 4 but it also increases detector area by a factor 4 therefore, NER is improved by just a factor 2.

Rapid filter tilting may be utilized to track and discriminate against lateral spatial fluctuations in the stratospheric DC signal and also to provide in flight calibration of the transmission characteristics of the cells. Each tilt scan should be programmed so that about $2/3$ of the tilt scan time period τ is used to displace the centers of the transmission spectra from -4λ to $+4\lambda$ with respect to the band line centers, thus giving an effective line center match up dwell time of about $1/3 \tau$. The remaining $2/3 \tau$ should be used to obtain a rapid tilt scan through $1/2$ of a free spectral range λ_s in order to detect and account for temporal changes in the stratospheric spectral nadir radiance which will result from sensing lateral variation in the atmospheric temperature profile as the result of the lateral rocket motion. A tilt scan period of about $1/10$ second can readily be achieved. If the 4 cells listed on Figure 3-6 are used, with interchange each $1/2$ sec. (take 0.1 sec for interchange and 0.4 sec dwell time for each cell) then the effective on line dwell time for any pair of cells during a complete 2 second cell wheel rotation period will be $2 \times .4 \times (1/4) \times (1/3) \text{ sec} = .067 \text{ sec}$. If the lateral rocket motion is $\leq 1 \text{ km/sec}$ then the corresponding lateral spatial resolution is $\leq 2 \text{ km}$. If rocket apogee occurs more than 30 km above the centroid altitude ($2 \approx 105 \text{ km}$) for W^{12} one might consider telescoping the NBFTR in order to simultaneously retain both the $\sigma = 2^\circ 1/2$ cone angle advantage for increased throughput and the 2 km lateral spatial resolution (since $30 \text{ km} \times (4 \pi/180) \approx 2 \text{ km}$).

Let us estimate the accuracy to which we can obtain the CO_2 auroral $4.3 \mu\text{m}$ nadir radiance component by use the NBFTR of Fig. 3-8 sequenced as to tilt scan and cell interchange as described above. As cited above the 10 channel picket fence filter will provide 100% transmission for the equivalent radiance of slightly more than 7 of the narrow CO_2 $4.3 \mu\text{m}$ auroral nadir

radiance lines. Information provided on page 79 of the report (AFCRL-TR-74-0334) by Kumer indicates that there are about 40 strong lines in the auroral component of CO_2 4.3 μm nadir radiance. By inspection of Fig. 3-7, we see that the auroral nadir radiance signal R_L^{12} in a single line on interchange of cells 1 and 2 can be reasonably estimated by $R_L^{12} = R_A^{12}/40$. In order to detect the CO_2 4.3 μm nadir radiance in the crucial lateral transport dominated region $x \leq -15\text{km}$ it is necessary that the NBTFR $\text{NER} \ll 7R_L^{12}$ in that region. The throughput φ of the NBTFR is given by $\varphi = \text{Top} (\pi\alpha^2) (\pi r^2)$ where $\text{Top} \approx 20\%$, α is the FOV 1/2 cone angle 2° , and r is the aperture radius 2"; $\varphi = .062 \text{ cm}^2 \text{ sr}$. The NEP is approximately $3 \times 10^{-14} \text{ w}/\sqrt{\text{Hz}}$ hence the NER for a 1 second dwell time is $\text{NER} \approx \text{NEP}/\varphi \approx 5 \times 10^{-13} \text{ w}/\text{cm}^2 \text{ sr}/\sqrt{\text{Hz}}$. During the complete 2 second cell interchange and tilt scan sequence there are just $2 \times .067$ seconds of on line dwell time available for any pair of cells so that the NER^{12} for interchange of cells 1 and 2 during the 2 second interchange and tile scan sequence is $\text{NER}^{12} \approx 1.3 \times 10^{-12} \text{ w}/\text{cm}^2 \text{ sr}$. At $x = -15 \text{ km}$, $R_A^{12} \approx 2.75 \times 10^{-10} \text{ w}/\text{cm}^2 \text{ sr}$ and $7R_L^{12}/40 \approx 4.8 \times 10^{-11} \text{ w}/\text{cm}^2 \text{ sr}$. Hence in the crucial region $x \leq -15 \text{ km}$ the auroral signal to noise S_A/N which can be obtained by use of the NBTFR sketched on Fig. 3-8 along with the 4 CO_2 cells listed on Fig. 3-6, sequenced as to tile scan and cell interchange in 2 second intervals as described above, is $S_A/N \leq 7R_L^{12}/\text{NER}^{12} \approx 37$ for $x \leq -15 \text{ km}$. By inspection of Fig. 3-7 we see that S_A/N retains a hefty value $S_A/N \approx 12.6$ at $x = -30 \text{ km}$. Thus, with 2 km lateral resolution in the region $-30 \text{ km} < x < -15 \text{ km}$ we can obtain 15 data points with signal to noise in the range $12.6 \leq S_A/N \leq 37$. This kind of S_A/N in the critical region $-30 \leq x \leq -15 \text{ km}$ should provide for unambiguous verification of the smoothing effect of lateral radiation transport on lateral

gradients in the auroral CO_2 $4.3\mu\text{m}$ nadir radiance. It also becomes clear that a footprint as large as 8 km will not degrade the verification, hence the NBTFR need not necessarily be telescoped in order to obtain useful data, even for viewing from apogee as high as 200 km.

We see from Fig. 3-7 that nadir radiance due to the mechanism $\text{OH} \xrightarrow{\text{V}}$ $\text{N}_2 \xrightarrow{\text{V}}$ $\text{CO}_2 (\text{V}_3) \rightarrow \text{CO}_2 + h\nu_{4.3\mu\text{m}}$ will begin to rival that of auroral CO_2 $4.3\mu\text{m}$ emission in contribution to the measured signal R_M^{12} for x in the region $x \leq -30\text{km}$. The use of cells 3 and 4 however, will provide enough added discrimination against the OH mechanism so that its contribution R_{OH}^{12} to the measured signal R_M^{12} can be assessed by analysis of the measured signals R_M^{14} and R_M^{34} and the auroral component of R_M^{12} can be recovered via $R_A^{12} = R_M^{12} - R_{\text{OH}}^{12}$.

To conclude our discussion of the use of the NBTFR along with CO_2 absorption cells in order to verify the lateral radiation transport smoothing effect on lateral gradients in the CO_2 $4.3\mu\text{m}$ auroral nadir radiance we note that our requirement that $\text{NER}^{12} < 7R_L^{12}$ is satisfied so well in the critical region $x \leq -15\text{km}$ that we can in fact consider relaxation of the LN_2 cooled black baffling requirements. The added advantage of including cells 3 and 4 for discrimination against the stratopause and the $\text{OH}(\text{V}) \xrightarrow{\text{V}}$ $\text{N}_2 \xrightarrow{\text{V}}$ $\text{CO}_2 (\text{V}_3) \rightarrow \text{CO}_2 + h\nu_{4.3\mu\text{m}}$ nadir radiance components, as well as the filter tilting discrimination against the stratospheric components and the in flight capability for filter tilting cell transmission characteristics calibration, dictate that the NBTFR shown on Fig. 3-8 and used in conjunction with the CO_2 absorption cells described on Fig. 3-6 is eminently feasible for verification of the important lateral radiation transport smoothing effect on lateral gradients in the CO_2 $4.3\mu\text{m}$ auroral (and therefore for the similar high altitude nuclear mechanisms) nadir radiance.

3.5 HIRIS Concept

Next let us consider the use of HIRIS in conjunction with CO_2 absorption cells to verify the lateral radiation transport smoothing effect on lateral gradients in auroral CO_2 $4.3\mu\text{m}$ nadir radiance. It will be necessary to include a 4.21 to $4.32\mu\text{m}$ LN_2 cooled filter in the HIRIS optics in order to minimize the earth shine photon fluctuation contribution to HIRIS NESR and to simultaneously transmit the 40 strong auroral nadir radiance lines. Resolution of 0.5 cm^{-1} need be employed to discriminate and track stratospheric nadir radiance fluctuations and to provide in-flight calibration of cell transmission characteristics. For the purpose of estimating S_{HA}/N the auroral signal to noise that may be achieved in the critical region $x \leq -15\text{ km}$ by using the HIRIS we use the HIRIS parameters listed on page 7 of the report AFGL-OP-TM-02 by A. T. Stair, J. W. Rogers and W. R. Williamson (1976), and we get NESR $\approx 9 \times 10^{-10}\text{ w/cm}^2\text{ sr cm}^{-1}$ for HIRIS viewing the 250°K earth through an LN cooled 4.21 to $4.32\mu\text{m}$ filter. Details of the estimate are given in Appendix H. The auroral signal per CO_2 auroral nadir line radiance is $\approx R_L^{12}/.5\text{ cm}^{-1} \approx 1.38 \times 10^{-11}\text{ w/cm}^2\text{ sr cm}^{-1}$ at $x = -15\text{ km}$. Thus, even if all 40 lines in the band pass are considered, the HIRIS signal to noise S_{HA}/N at the critical region $x \approx -15\text{ km}$ is $S_{\text{HA}}/N \approx 1$. Hence, we see the use of a HIRIS type instrument in conjunction with CO_2 cells would not provide adequate performance to verify the lateral smoothing effect of radiation transport in the spatial wing ($x \approx -15\text{ km}$) of the CO_2 $4.3\mu\text{m}$ aurora.

The telescoped HIRIS is a very versatile instrument. For example it could be used in a step and stare nadir viewing mode throughout the entire infrared spectral region in a long term satellite borne experiment that would be extremely useful for obtaining comprehensive high spectral resolution AVD background definition. In that perspective it would not be prudent to risk non-recovery of the HIRIS in a short term arc overfly experiment. This is especially compelling in view of the fact that the highly specific NBTFR is a less expensive instrument (from the non-recovery risk point of view) that is considerably more sensitive than the HIRIS for verification of the lateral radiation transport smoothing effects on the lateral CO_2 $4.3 \mu\text{m}$ auroral nadir radiance gradients.

3.6 Arc Underfly Concept

An arc underfly experiment might be useful to consider as an alternate approach for providing verification of the lateral radiation transport smoothing effect on lateral gradients in CO_2 $4.3 \mu\text{m}$ auroral nadir radiance. The obvious advantage is that viewing the aurora in the zenith sidesteps the nadir viewing problem of discriminating the auroral emission from the earth background. However, now the aurora must be viewed through large optical depths unless the sensor is at 90 to 95 km altitude or higher. On the other hand, once the rocket gets too high (110 km) the auroral signal becomes both weak and difficult to interpret. Some of the disadvantages of this kind of experiment are as follows.

Due to the presence of the OH(V) mechanism for the CO_2 $4.3 \mu\text{m}$ emission maximum which occurs near 85 km, and to the large optical depth of atmospheric CO_2 through which the aurora must be viewed, it appears that auroral zenith signals of the strength found in the critical region $x \leq -15$ km will not be detectable from rocket altitude $Z_R \lesssim 85$ km, even if CO_2 cells are used to attempt to sound the altitude distribution of CO_2 $4.3 \mu\text{m}$ volume emission above the rocket. We further believe that data obtained from rocket altitude above 105 km will also be too weak and uncertain to be useful in the $x \leq -15$ km region. Thus useful data might be obtained for about 130 sec as the rocket altitude Z_R varies from 85 to apogee (105 km) and then back to 85 km. By

comparison, in an overfly NBTFR experiment the rocket can be programmed to reach apogee at 220 km and will obtain useful data for 320 seconds. Thus in the overfly experiment chances for observing the arc in the critical region $-40^\circ \times -15^\circ$ are considerably enhanced over those of the arc underfly experiment. Another advantage of the arc overfly experiment is that energy deposition can be monitored both optically (by nadir measurements in the N_2 LBH system for example) and also by observing the precipitating auroral particles. Finally, the nadir viewing arc overfly concept is more appealing esthetically since the advanced earth disc scanner systems for which the data will provide support, will also be used in a nadir viewing mode.

Thus we conclude that the arc underfly experiment appears to be considerably less desirable than an arc overfly experiment which utilizes the NBTFR as described above for the purpose of verification of the smoothing effect in the lateral CO_2 $4.3 \mu m$ nadir radiance gradient which results from lateral transport.

3.7 An NBTFR $2.7 \mu m$ Arc Overfly Concept

Finally, we should address the verification of relatively sharp lateral gradients in auroral $2.7 \mu m$ nadir radiance. The $2.7 \mu m$ instrument discussed by Kumer and Roche (1975) can be improved in NER by a factor $\times 1/6$ by use of the improved NBTFR technology discussed above, namely LN_2 cooled optics and tilting filter and the use of an Si substrate for the narrow band filter. On the other hand the $2.7 \mu m$ auroral signal in the Kumer and Roche Technical Brief (1975) is over estimated by a factor 3 since an energy efficiency 2% was used rather than 0.7% which now appears more realistic in view of recent independent determinations from a large number of sources as reported at the April 1979 DNA/AFGL, HAES Infrared Data Review Meeting. The net effect is that sensitivity to the $2.7 \mu m$ auroral nadir radiance that is a factor $\times 2$ better than depicted in the Kumer and Roche article can be achieved with a NBTFR. Performance with this sensitivity for an arc similar to that overflown on 3/27/73 in the Ice Cap program is illustrated on Fig. 3-9.

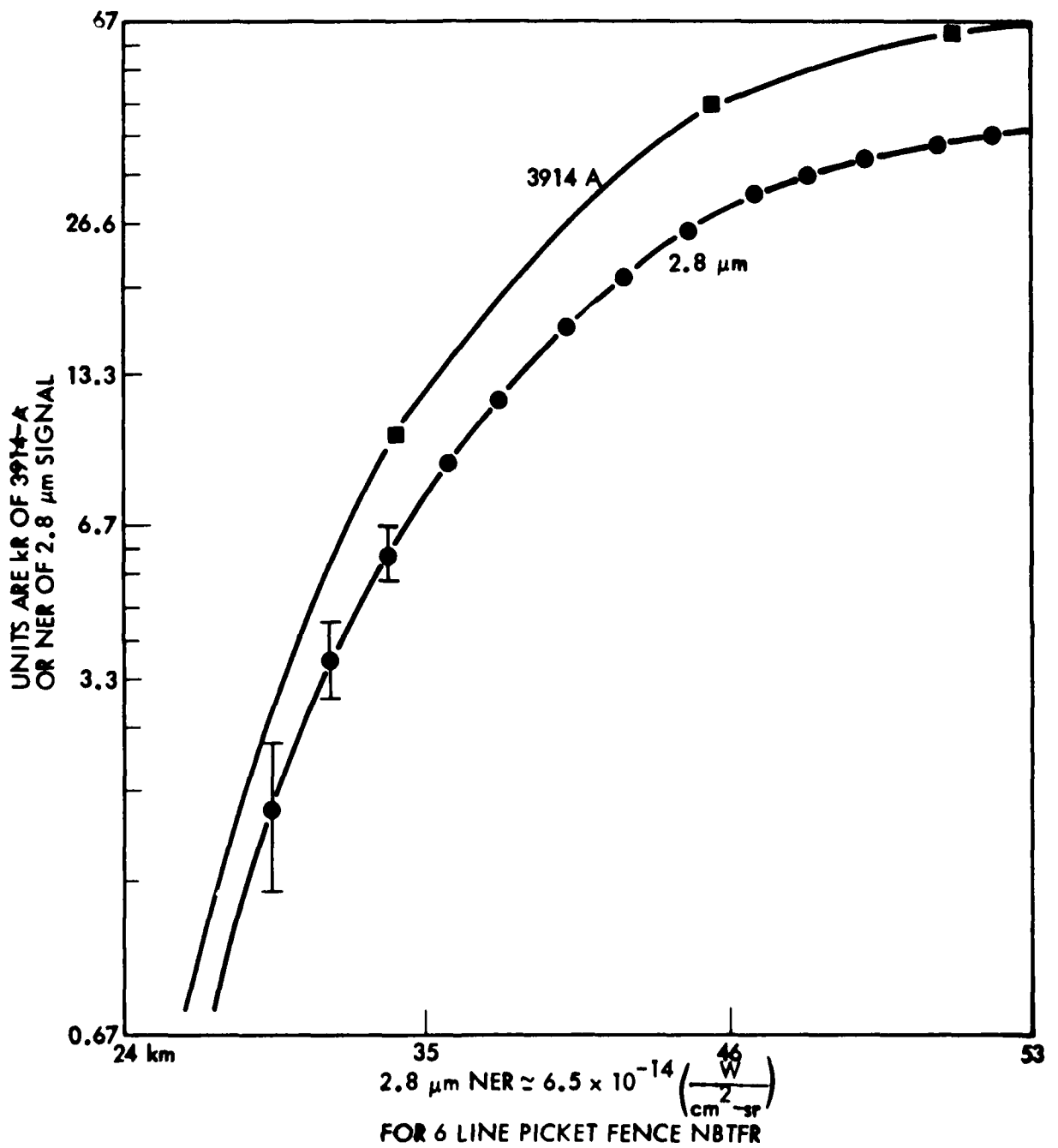


Figure 3-9 Illustrates Anticipated Performance of an Optimized 2.8 μm NBTFR on Overflight of an Arc Modelled After the 3/27/73 Arc Encountered in the ICECAP Program.

3.8 Conclusions

We have considered 4 distinct experimental concepts to verify that the effect of lateral radiation transport of CO_2 4.3 μm photons in the earth's optically thick upper atmosphere renders the lateral gradients in the CO_2 4.3 μm auroral nadir radiance no more severe than the lateral gradients in auroral 2.7 μm nadir radiance even though the DC level of the CO_2 4.3 μm auroral radiance may be as much as 10 times that of the 2.7 μm aurora in steady state conditions. Most of these concepts involved firing a rocketborne sensor over an auroral arc and viewing the aurora in the nadir in order to measure lateral structure in auroral nadir radiance in the 4.3 and 2.7 μm spectral regions. Nadir viewing 4.3 μm concepts included a Broad Band Filtered Radiometer (BBFR), a narrow band tilting 10 transmission channel picket fence filtered radiometer (NBTFR) and the use of HIRIS. In each case the instruments are to be used with a wheel of CO_2 absorption cells in order to provide the added high resolution $\sim 6 \times 10^{-3} \text{ cm}^{-1}$ near the centers of the CO_2 lines that is necessary to discriminate CO_2 4.3 μm narrow line auroral nadir radiance from the earth nadir radiance background. It is also necessary to have 0.2 to 0.5 cm^{-1} resolution between the lines in order to suppress deleterious effects of the broad band LTE thermal stratospheric contribution to the earth's 4.3 μm nadir radiance background. This requirement is sufficient to rule out the BBFR for use in the desired arc overfly experiment. The NBTFR and HIRIS easily satisfy this 0.2 to 0.5 cm^{-1} spectral requirement. The HIRIS however turns out to be significantly less sensitive and more costly than the optimum design NBTFR.

The optimum design NBTFR uses liquid Nitrogen (LN_2) cooled optics including the tilting filters, and LN_2 cooled baffling. This reduces the NEP of the .71 cm diameter InSb detector to $\approx 3 \times 10^{-14} \text{ W}/\sqrt{\text{Hz}}$, nearly the inherent LN_2 cooled InSb detector noise limit. The narrow band filter is a 4" diameter Silicon (index of refraction ≈ 3.4) substrated Fabry Perot etalon designed so that the centers of 10 of its transmission channels roughly coincide with the lines p8, p10, ..., p26 of the $^{12}\text{C}^{16}\text{O}_2$ 001 \rightarrow 000 band. A 300 Å blocker filter allows just the 10 channels to be transmitted. The narrow band filter is

designed so that the transmission channel full width half maximum FWHM 0.21 cm^{-1} (i.e., 4A) for an FOV with the 1/2 cone angle $= 2^\circ$. The through put of the optimum NBTFR is $.031 \text{ cm}^2 \text{ sr}$ for an overall optics transmission of 10%. The $\text{NER} = 7.10 \times 10^{-13} \text{ w/cm}^2 \text{ sr}$. Spectral scanning between the CO_2 line centers is achieved by tilting the filter. High spectral resolution of $6 \times 10^{-3} \text{ cm}^{-1}$ near the CO_2 line center is achieved by utilization of the CO_2 absorption cells.

An arc underfly verification experiment was also considered and rejected on the basis that; i) the rocket spends less time in the altitude range where useful data may be obtained therefore decreasing the probability that phenomena will be observed; ii) the overfly can simultaneously monitor energy input by optical measurements and by measurements of the precipitating auroral particles; iii) the overfly measurements are obtained in the nadir mode which is exactly similar to the viewing mode of the advanced scanner sensors that the data will support, zenith data obtained in the underfly experiment will not share this advantage.

As part of our study we also verified that an optimum NBTFR could be used effectively in an arc overfly experiment to verify that lateral gradients in the 2.7 μ auroral nadir radiance are indeed as sharp and dramatic as one would expect from an essentially prompt, optically thin auroral emission.

4.0 APPLICATION TO PLANNING FOR SPATIAL EXCEDE

In this chapter we generate estimates for the $4.3 \mu\text{m}$ signal levels that we expect to see in the EXCEDE mother-daughter spatial experiment as described to us by Bob O'Neill. In this experiment the mother vehicle will carry the electron gun and provide at altitude $z = 90 \text{ km}$ a 120 kw dosed region. Observations will be performed from the nearby daughter vehicle. For the purpose of calculation, the dosed region can be approximated by a magnetic field aligned rectangle of 70 m length L parallel to the magnetic field and a 20 m width D which is perpendicular to the magnetic field but parallel to the horizontal component of rocket velocity. The rectangle is assumed to have a one cm depth. The rectangle has velocity component $V = 600 \text{ m/sec}$ in the direction perpendicular to the magnetic field.

On fig.4-1 we show a schematic of the instantaneous deposition region (IDR) and adjacent regions as viewed from the daughter vehicle which is presumed to be moving parallel to the EXCEDE electron gun. Adjacent regions are the predosed region (PR), the advanced transport region (ATR) and the lower transport region (LTR). We shall see below that transport rather than predosing dominates $4.3 \mu\text{m}$ radiance due to prompt electron beam induced direct excitation of CO_2 in the ν_3 state. We call this $4.3 \mu\text{m}$ excitation mechanism I. In discussion of mechanism I we refer to the predosed region (PR) as the predosed transport region (PDR).

We expect 4 obvious components of $4.3 \mu\text{m}$ radiation to be present. The first mechanism (Mechanism I) is prompt electron beam induced direct excitation of CO_2 (ν_3). Mechanism I will produce a component R^{I} that will radiatively relax at $A \approx 419/\text{sec}$, the deposition rectangle will move one D perpendicular to the field line with a frequency $V/D \approx 30/\text{sec}$ so this component will be essentially prompt. A 2nd component R^{II} will result from prompt electron beam induced excitation of N_2^+ followed by the reactions

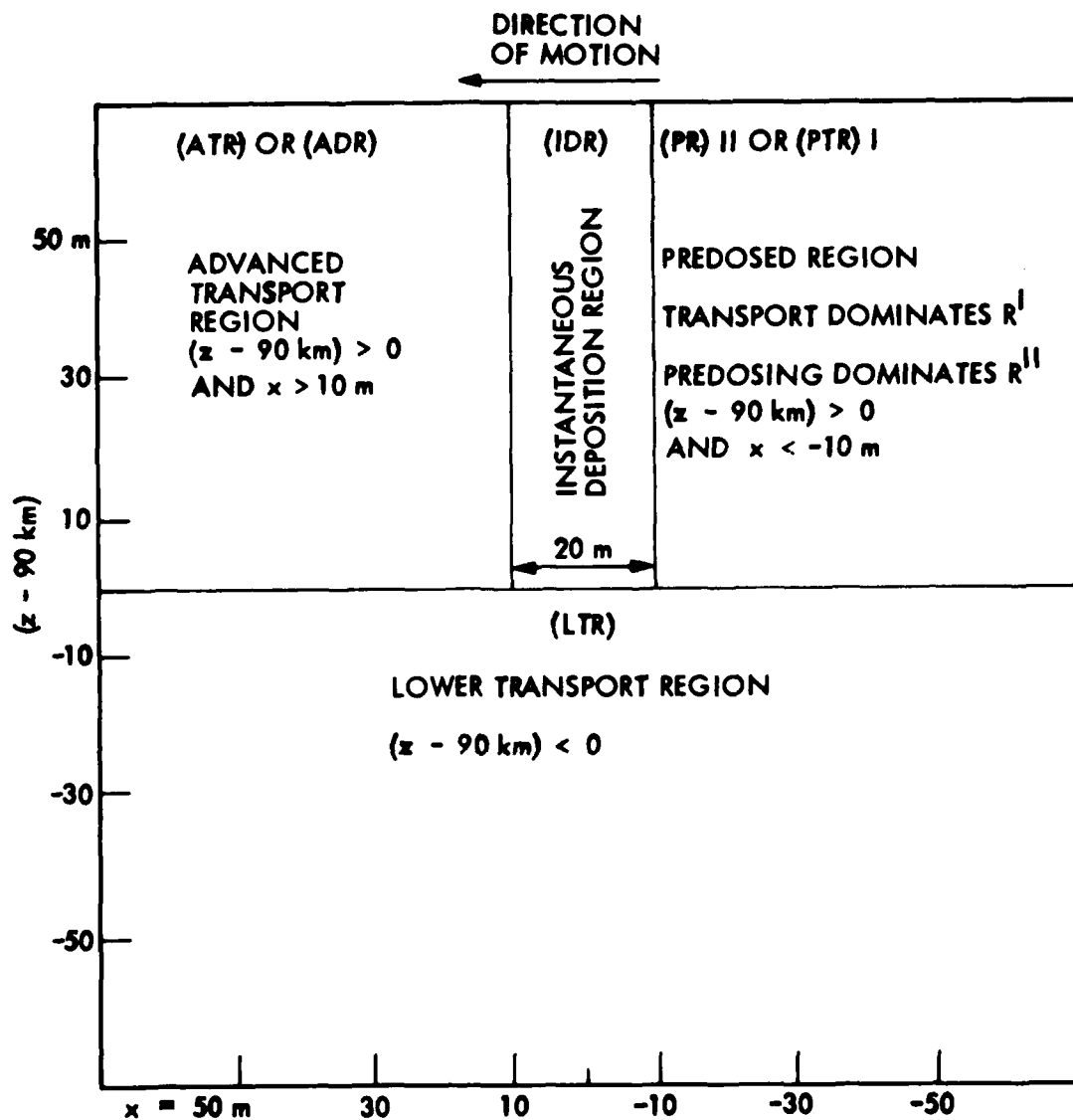
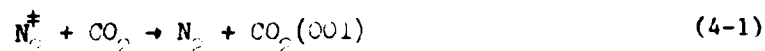
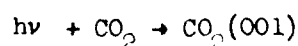


Figure 4-1 A Schematic of the Instantaneous Deposition Region and Adjacent Regions as Seen From the Daughter Vehicle.



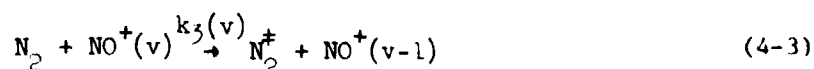
This second mechanism (Mechanism II) will leave a long DC tail behind the deposition region because the time constant for reaction (4-1) is of the order of a minute at 90 km altitude.

Radiation transport



will also cause a glow outside of the dosed and predosed regions. Both mechanisms I and II will contribute to the glow in the transport region but, as we shall see below, mechanism II will dominate.

We also considered another component R_{NO^+} , namely 4.3 μm emission from NO^+ produced in vibrationally excited states. At 90 km altitude this NO^+ emission will be heavily quenched by N_2 so that it will be essentially prompt. To generate the contribution R_{NO^+} from $\text{NO}^+(v) \rightarrow \text{NO}^+(v-1) + h\nu$ we followed Tarr and Archer (DNA 3297F) in assuming a production ϵ_{NO^+} of 5 photons per NO^+ produced, we used rates $k_3(v)$ for



inferred from the data for $k_3(1)$ given by Gordietz et. al. (1978) and from calculations of $k_3(v)/k_3(1)$ as listed in

DNA3297F, and we used Einstein coefficients A_{v-1}^v for $\text{NO}^+(v) \rightarrow \text{NO}^+(v-1) + h\nu$ taken from Frank Billingsleys publications. The results we generated on this

basis indicated that R_{NO^+} would dominate heavily in the region IDR. However, Herb Mitchell reports (private communication) that in earlier electron gun experiments the ratio of $4.3 \mu m$ to $3914A$ remains constant over the altitude region $80 < z < 120$ km. N_2^+ $3914A$ emission should not be quenched in this region but R_{NO^+} should be heavily quenched, i.e., $A_{v-1}^v / (A_{v-1}^v + k_3(v)[N_2]) \approx 1/2$ for $z > 120$ km. Thus in order for the constant ratio $3914A/4.3 \mu m$ to obtain in the region $80 < z < 120$ km it must be that R_{NO^+} is not dominant. For this to occur would mean that either $\epsilon_{NO^+} < 5$, $k_3(1)$ is greater than given by Gordietz et. al., A_{v-1}^v is less than calculated by Billingsley, or any combination of the above.

For our purpose we have generated estimates R_{NO^+} on the data base cited above (ϵ_{NO^+} and $k_3(v)/k_3(1)$ from DNA 5007F, $k_3(1)$ from Gordietz et. al., and A_{v-1}^v from Billingsley). The EXCEDE mother-daughter experiment may prove these estimates to be considerably erroneous. This will indicate deficiencies in the data base, rather than in the methods we use to estimate R_{NO^+} from the data base.

Finally there is the ambient background CO_2 $4.3 \mu m$ emission to consider. At ∞ km this will be dominated by the $OH^+ \xrightarrow{VV} N_2^+ \xrightarrow{VV} CO_2(001) \rightarrow CO_2 + hv$ mechanism. Then it can be quite variable. This mechanism for high altitude CO_2 emission is discussed in a paper by Kumer et al. (1978).

Results are summarized in Table 1. Clearly R_{NO^+} dominates the region IDR

Table 4-1. Entries in units 10^{-9} watts/cm² sr unless ratios are involved.

| Mechanism → Region | I | II | NO ⁺ (v) | Am- bient | R (total EXCEED) | R _T /ambient* | radiance change over ΔZ ≈ 70 m in the region LTR |
|-----------------------|----|---------|---|--------------|---------------------|--------------------------|--|
| IDR | 22 | 4 to 28 | 300 | .65 to 2 | 838 | 1300 | N/A |
| PR | 1 | 28 | decays like e ⁻ (x/1.5m) | .65 to 2 | 28 | 43 | N/A |
| Sum of PR Regl as | 1 | 4.5 | 0 | .65 to 2 | 5.5 | 8.5 | 0.5 to 2.0 |

* Ambient is taken to be 0.65×10^{-9} watts/cm² sr (Off mechanism, 4/11/74).

N/A Not Applicable.

and R^{II} dominates the transport regions and the region PR. From the data in IDR we can get ϵ_{NO^+} since $\epsilon_{NO^+} \propto R_{NO^+}$, from data in the region PR we can get ϵ_{N_2} , the efficiency for prompt high energetic electron collision induced excitation of N_2^+ by means other than vv transfer from $NO^+(v)$ since $\epsilon_{N_2} + \epsilon_{NO^+} \propto R^{II}$. Finally we may get some information on ϵ_{CO_2} , the prompt high energetic electron collision induced efficiency for producing $CO_2(v_3)$ via $e + CO_2 \rightarrow e + CO_2(v_3)$ from data in the transport region since in these regions $R^I/R^{II} \simeq 0.000$ based on the efficiencies we have assumed in order to generate these preliminary estimates.

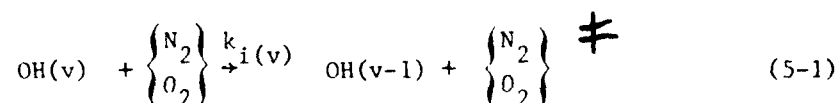
Details of the calculation of the estimates in table 4.1 are given in Appendix D.

5.0 EVIDENCE FOR AN $\text{OH} \xrightarrow{\nu\nu} \text{N}_2 \xrightarrow{\nu\nu} \text{CO}_2(\nu_3) \rightarrow \text{CO}_2 + h\nu$ (4.3 μm) Mechanism for 4.3 μm Airglow

5.1 Introduction

In the previous work by Kumer and James (1974) and Kumer (1974) it had been assumed that the only important undisturbed night time mechanisms in the altitude region $z \geq 50$ km for producing CO_2 excited in the ν_3 normal mode of vibration were (i) excitation by thermal collisions and (ii) excitation by the radiative absorption of 4.3 μm earthshine by CO_2 . The radiative decay of $\text{CO}_2(\nu_3)$ results in emission near 4.3 μm . Therefore, measurements of the undisturbed night time atmospheric 4.3 μm zenith radiance for altitudes $z \geq 50$ km might be used to test if these are indeed the only important mechanisms for producing $\text{CO}_2(\nu_3)$ in undisturbed night time conditions.

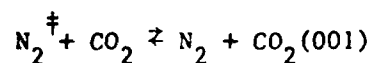
Since 1974 preliminary 4.3 μm zenith radiance data sets obtained 27 April 1973, 25 February 1974, 11 April 1974, 6 March 1975, and 12 March 1975 have shown evidence (Kumer, HAES Report No. 57, 1976) for a non-auroral feature near 85 km which cannot easily be explained on the basis of mechanisms (i) and (ii). The consistent appearance of this feature in the 4.3 μm zenith radiance data near 85 km, and the large values for the rate constants $k_i(\nu)$ ($i = 1$ for N_2 , $i = 2$ for O_2) for the reactions



which have been reported by Streit and Johnston (1976), had stimulated a preliminary study (Kumer, 1976) to investigate the mechanism



followed by near resonant vv transfer back and forth between N_2 and CO_2



and 4.3 μm radiation trapping



as the source of the feature which is observed near 80 to 85 km altitude. In this chapter we show in detail how this mechanism explains the presence of the feature which occurs near 85 km in the data set obtained on 11 April 1974. The work this chapter covers has been published in J. Geophys. Res. (Kumer, et al, 1978).

5.2 ANALYSIS

One of the goals for the 1974 auroral measurements program was to obtain a 4.3 μm zenith radiance profile under quiet conditions so that there would be no significant auroral component in the data thus obtained. The evening of 11 April 1974 was free of auroral activity so the "quiet conditions" rocket was launched that evening. The 4.3 μm zenith radiance data are shown by curve D on Figure 5-1. These data were obtained with a rocket-borne liquid nitrogen cooled CVF spectrometer, the description of which has been given by Stair et al., (1973) and Wyatt and Frodsham (1977). Spectra thus obtained showed an emission feature near 4.3 μm which may be identified as $CO_2 v_3$ band emission. A preliminary version of these data were reported by Stair et al. (1975) and the final version of these data are reported by Wheeler et al., (1976). Data above 92 km are lost since the signal is smaller than instrument noise for $z > 92$ km.

The curve A which is also shown on Figure 5-1 is a calculation which accounts for just the two traditional nighttime mechanisms (Kumer and James, 1974) for the excitation of $CO_2 (v_3)$, namely (i) vibrational excitation by thermal collisions and (ii) absorption of 4.3 μm earthshine by CO_2 . In order to perform this calculation it is necessary that we use the most accurate model for the atmospheric temperature and pressure on the evening of 11 April 1974 that can be constructed on the basis of whatever pertinent data are

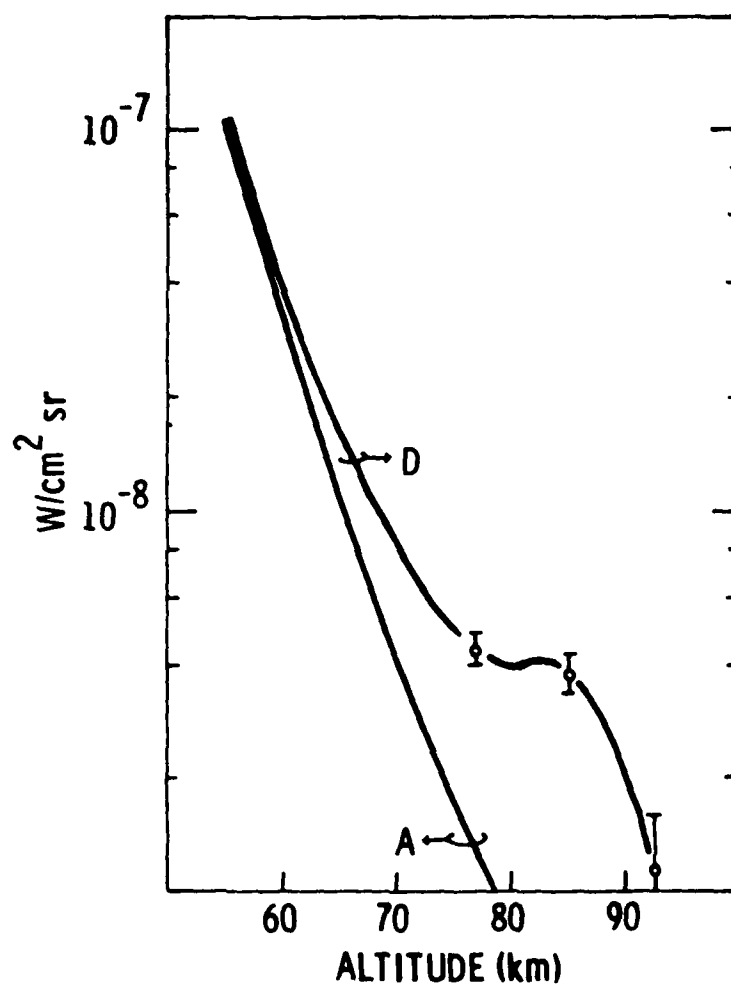


Fig. 5-1. The 4/11/74 4.3 μm zenith radiance data are shown by curve D. Error bars indicate the uncertainty. Curve A shows a 4.3 μm zenith radiance calculation that is based on the traditional night-time $\text{CO}_2(\nu_3)$ excitation mechanisms (i) and (ii) which are discussed in the text, and on our nominal atmospheric model which is also described in the text.

available. Up to 60 km altitude our model is based on the U.S. Army Atmospheric Sciences Laboratory meteorological rocket data which were obtained in a sounding rocket experiment launched from the Poker Flat Range (PKR) on the evening of 11 April 1974. These data were provided by R. O. Olsen (1976). Above 60 km we joined this data smoothly to a data point at 87 km which is interpolated from OH airglow rotational temperature determined (Ware, private communication 1978) from interferometric data obtained on 4/9/84 and 4/13/74 via ground based instrumentation located near PKR. No such data were available from the 10th to the 12th due to clouds and snowstorm activity. Thus we interpolate the mesopause temperature $T \approx 203 \pm 25^\circ\text{K}$ to apply for 4/11/74 on the basis of these preliminary data supplied by Ware:

| time(UT) | date | OH rotational temperature |
|----------|---------|---------------------------|
| 3:30 | 4/9/74 | 205.9 |
| 8:33 | 4/9/74 | 194.0 |
| 11:00 | 4/13/74 | 207.6 |

The large uncertainty we assign to the interpolated mesopause temperature data point accounts for large daily and hourly variations (Ware et al., 1976; and Noxon, 1978) in airglow rotational temperature, and presumably in mesopause temperature as well. The temperature profile $T_N(z)$ for our nominal model atmosphere which is constructed on the basis of available data as explained above is shown on Figure 5-2.

We use the nominal temperature model $T_N(z)$ and the mechanisms (i) thermal collisions and (ii) $4.3 \mu\text{m}$ earthshine absorption in order to generate the calculation of $4.3 \mu\text{m}$ zenith radiance which is shown by curve A on Figure 5-1. The calculation and data (curve D on Figure 5-1 are within a factor 0.78 agreement below $z \approx 60$ km altitude. Considering that the overall calibration of the CVF is about $\pm 25\%$, and also considering that an overall change of 2.5°K in the temperature profile can cause a 10% change in $4.3 \mu\text{m}$ zenith radiance, the agreement for $z \leq 60$ km between the data and calculations as shown on Figure 5-1 is quite good. Centered at about 85 km there seems to be a contribution of

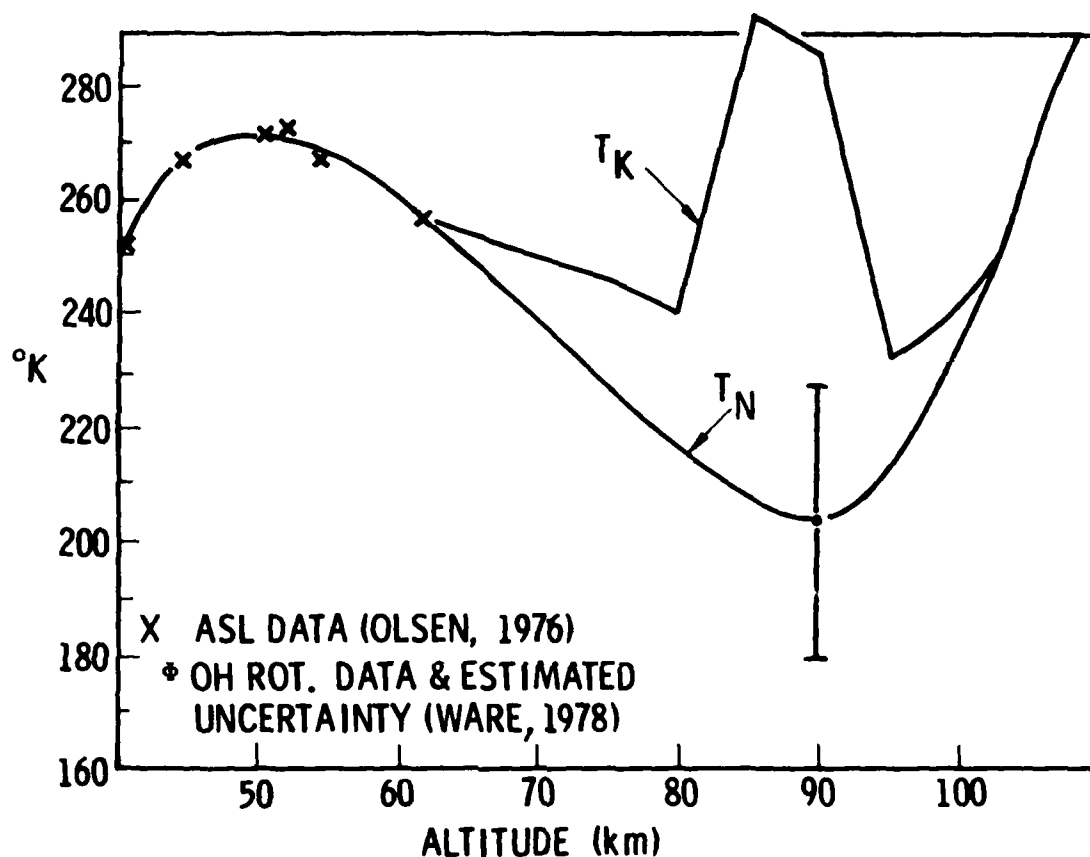


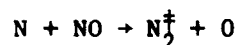
Fig. 5-2. The curve labelled T_N is our nominal atmospheric temperature profile. The nominal model is based on ASL sounding rocket data (R. O. Olsen, private communication 1976) and OH airglow rotational temperature (Ware, 1978). The unrealistic temperature model labelled T_K is required to fit the 4/11/74 4.3 μ m zenith radiance data via a calculation based on mechanisms (i) and (ii).

approximately $4 \times 10^{-9} \text{ w cm}^{-2} \text{ sr}^{-1}$ $4.3 \mu\text{m}$ zenith radiance data that can not be explained by our nominal model atmosphere and the traditional night-time $\text{CO}_2(\nu_3)$ excitation mechanisms (i) and (ii).

In addition to our nominal temperature profile $T_N(z)$ we show another temperature model $T_K(z)$ on fig. 5-2. This temperature model is required if just the mechanisms (i) and (ii) are used to generate a calculation that will fit the data D on Figure 5-1. We believe it is very unlikely that a temperature profile anything at all like $T_K(z)$ actually existed on 4/11/74. The mesopause temperature data provided by Ware for 4/9/74 and 4/13/74 tend to substantiate our contention.

We do however, believe that our model $T_N(z)$ is reasonably realistic. If this is the case then there must be some $\text{CO}_2(\nu_3)$ excitation mechanism, in addition to mechanisms (i) and (ii), which is operative in the 80 to 85 km region.

We considered and rejected several mechanisms that might account for the additional excitation. For example, energy deposition in the 80 to 85 km region by hard particle precipitation would be accompanied by visible emissions. These were not observed. Or, excitation of N_2^+ via the reaction



would require unrealistically large night time densities of N in order to provide the required source.

The only mechanism promising enough to warrant discussion here is the OH^+ driven mechanism, that is production of N_2 via reaction (5-1) where the $\text{OH}(\nu)$ is initially produced via



or



There are two reasons for considering this mechanism: (a) The 85 km peak altitude requirement could be nearly satisfied by reaction (5-1).

altitude profile for OH^\dagger emission typically peaks near 85 km, (Baker et al., 1977). We expect then that the altitude where peak quenching of OH^\dagger occurs would be somewhat lower than 85 km. (b) The total power/cm² produced by reactions (5-3) and (5-4) exceeds the power/cm² (apparently of the order $4\pi \times 4 \times 10^{-9}$ watts/cm²) which is required to explain the "knee" which occurs near 85 km in the 11 April 1974 data.

There are numerous measurements of OH airglow volume emission rates available in the literature (Baker et al., 1977). To investigate the $\text{OH}(v) + \text{N}_2 \rightarrow \text{N}_2^\dagger + \text{OH}(v-1)$ hypothesis we arbitrarily selected a measured airglow OH $\Delta v = 2$ volume emission rate versus altitude $\epsilon_{72}(v=2, z)$ reported in the literature by Rogers et al., (1973). The subscript 72 refers to the date these data were obtained and differentiates them from a 2 cd data set obtained in 1975 that we discuss later in this paper. The volume emission rate $\epsilon_{72}(z)$ published by Rogers et al., was measured on 6 March 1972 by a rocket-borne radiometer with a passband that transmits the OH $\Delta v = 2$ sequence bands $4 \rightarrow 2$, $3 \rightarrow 1$, and $2 \rightarrow 0$. To estimate the corresponding altitude dependent N_2^\dagger production rate $\text{QN}_2^\dagger(z)$ we set $\text{QN}_2^\dagger(z) = \epsilon_{72}(z) < k_1/A > [\text{N}_2]$. The calculation of $< k_1/A >$ requires a knowledge of the rate constants for reactions (5-1) and (5-3). For the purpose of our discussion we will label these rate constants k_1 , k_2 , and k_3 (k_1 and k_2 refer to reaction (5-1), they are defined above). A knowledge of the Einstein coefficients $A_{v''}^{v'}$ for radiative decay of $\text{OH}(v')$ to $\text{OH}(v'')$ is also required. For our calculation we used the $A_{v''}^{v'}$ calculated by Mies (1974). Mies' calculation is based on experimental data obtained by Murphy (1971).

In the initial analysis we present here we shall neglect production of $\text{OH}(v)$ excitations by the $\text{HO}_2 + \text{O}$ reaction. This is justified since we know that $\text{O}_3 + \text{H} \rightarrow \text{OH}(v) + \text{O}_2$ contributes significantly to production of the night time OH airglow, the role of $\text{HO}_2 + \text{O}$ in contributing to $\text{OH}(v)$ excitation is less clearly defined. For reaction (5-3) we used the relative $\text{OH}(v)$ formation rates $k_3(9):k_3(8):k_3(7):k_3(6) = 0.54:0.29:0.10:0.07$ and $k_3(v \leq 5) = 0$ as determined by Good (1976) from the data of Charters et al., (1976).

Quenching rates of $\text{OH}(v)$ by N_2 and O_2 for $4 \leq v \leq 9$ are given by Streit and Johnson (1976). We should note that Streit and Johnson were not able to determine if the generally exothermic reaction 5-1 proceeds by vibration transfer vv accompanied by partition of the balance of the energy into translation

and rotation vtr or whether it is purely vtr. We will proceed under the assumption that reaction 5-1 is vv and that excess energy is balanced via vtr. We designate the rate constants for vv excitation of N_2^+ for reaction 5-1 by $k_1(v)$. For O_2 the process is not relevant to this discussion, we designate the rates $k_2(v)$. We show the $k_1(v)$ and $k_2(v)$ that we used for this calculation on Fig. 5-3. If we use the smallest imaginable values $k_1(v) = 0$ for $i = 1$ and 2 and for $v \leq 3$ we get $E_{VV} = \int dz QN_2^+ = 0.08 \text{ ergs/cm}^2 \text{ sec}$, and if we use the largest reasonably imaginable values $k_1(v) = 10^{-13} \text{ cm}^3/\text{sec}$ for $i = 1$ and 2 and for $v \leq 3$ we get $E_{VV} = 0.19 \text{ ergs/cm}^2 \text{ sec}$. If we use reasonable intermediate extrapolations as shown on Fig. 5-3 for the $k_1(v)$ for $i = 1$ and 2 and for $v \leq 3$ we get $E_{VV} = 0.11 \text{ ergs/cm}^2 \text{ sec}$. The z dependence of $QN_2^+(z)$ was not affected appreciably by the extrapolation assumptions. This point is illustrated by Fig. 5-4 where the profile $QN_2^+(\oplus)$ which applies for $k_1(v) = 10^{-13}/\text{sec}$ for $v \leq 3$, the profile QN_2^+ which applies for $k_1(v)$ for $v \leq 3$ extrapolated as shown on Fig. 5-3 and the profile $QN_2^+(-)$ which applies for $k_1(v) = 0$ for $v \leq 3$ are presented.

For our calculation, we shall use QN_2^+ which we designate by $QN_{2,72}^+$ in the remainder of our paper. This will be sufficient for our purpose of demonstrating that the mechanism initiated by reaction (5-1) is a solid candidate for explanation of the enhanced $4.3 \mu\text{m}$ zenith radiance observed on 4/11/74 in the 80 to 85 km altitude region.

For the reaction



we use $k_5 = 3.3 \times 10^{-11} \text{ cm}^3/\text{sec}$ (Westenberg et al., 1970). Although k_5 may have a small v dependence (Rogers et al., 1973) this is not particularly important for our problem since reaction (5-5) quenches the low lying $OH(v)$ levels most efficiently where as reaction (5-1) produces N_2^+ mainly from the upper levels $v \geq 4$ as shown by Fig. 3-4.

Other quantities necessary for the calculation of $\langle k_1/A \rangle$ include the O and N_2 number densities, $[O]$ and $[N_2]$ respectively. We obtained these from the DNA Handbook (Blank et al., 1974). The volume emission rate ϵ_{72} in the bands $4 \rightarrow 2$, $3 \rightarrow 1$, and $1 \rightarrow 0$ which was reported by Rogers et al, is also shown on

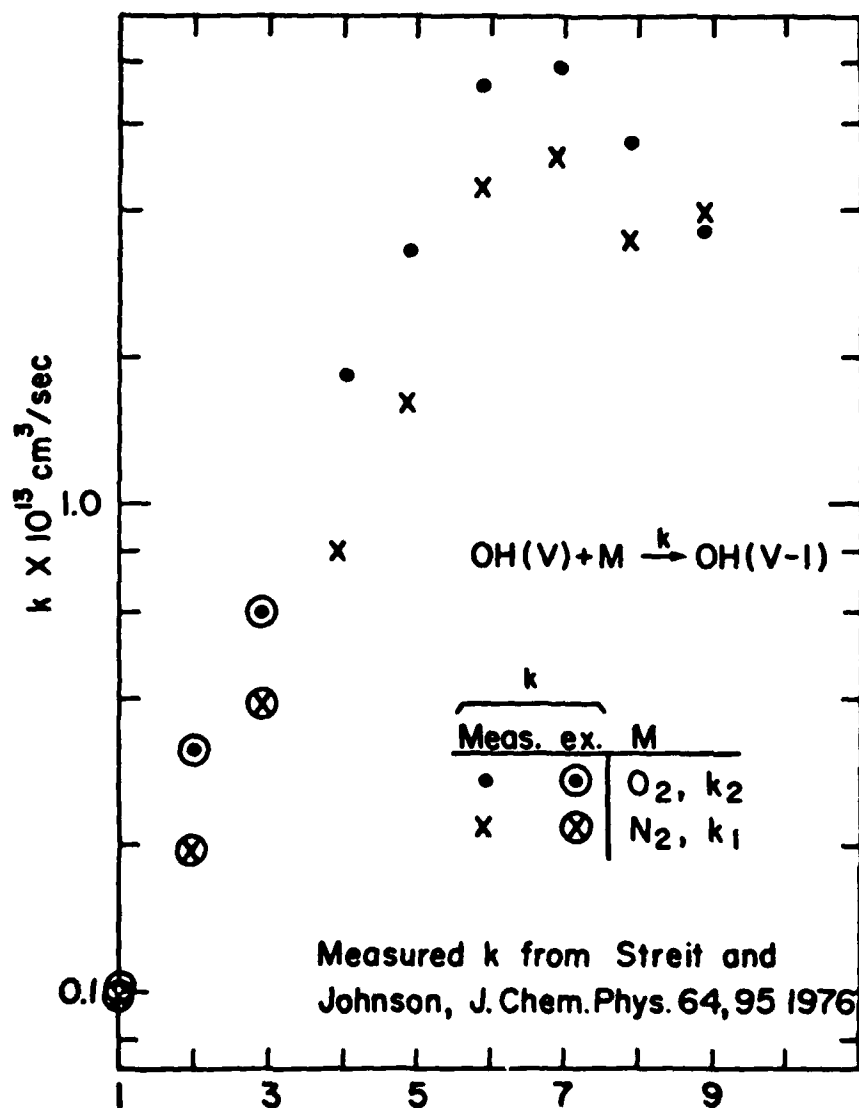


Fig. 5-3. The data for $k_1(v)$ for $i = 1$ and 2 and for $4 \leq v \leq 9$ from Streit and Johnston (1976) are shown here. Reasonable extrapolation for $v < 4$ are also shown. Effects of variations in the extrapolated values are discussed in the text.

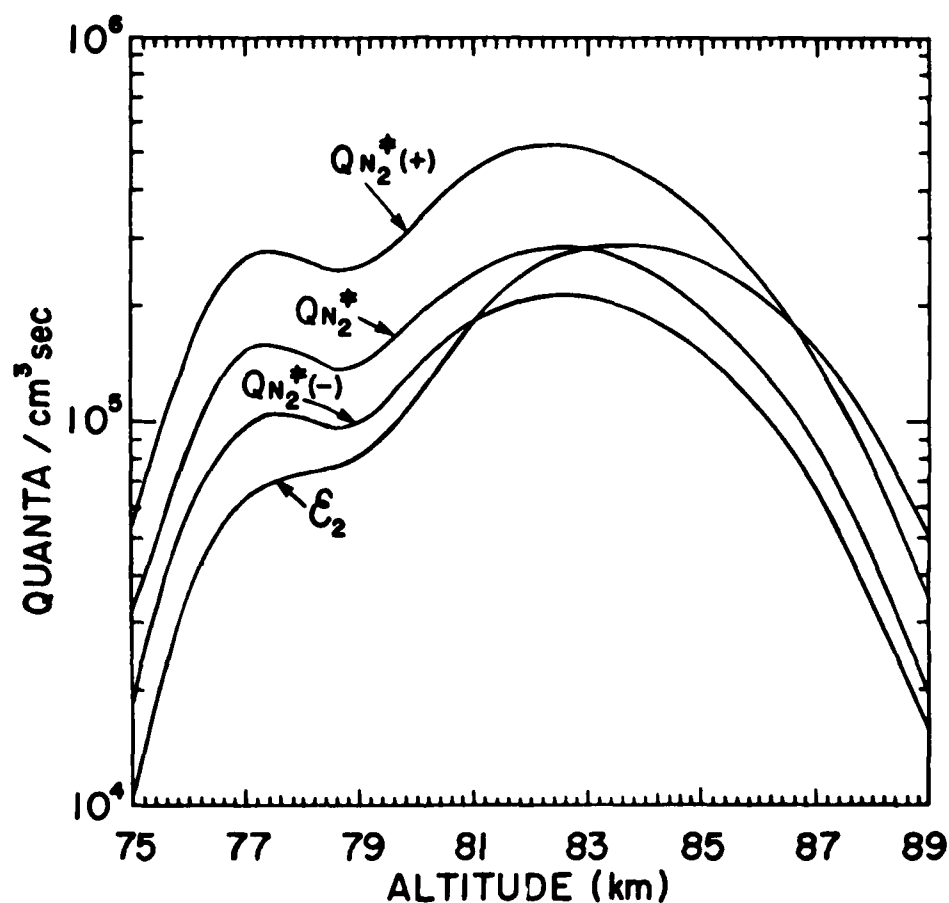


Fig. 5-4. The 6 March 1972 measured (Rogers et al) altitude profile ϵ_{72} of volume emission in the bands $4 \rightarrow 2$, $3 \rightarrow 1$, and $2 \rightarrow 0$, and the inferred vibration transfer $\text{OH}(v) \xrightarrow{v'v'} \text{N}_2^+$ rate QN_2^+ are shown in this figure. The rates $\text{QN}_2^+(+)$, QN_2^+ and $\text{QN}_2^+(-)$ are computed on three different assumptions for the value of the rate constants $k_1(v)$ for $v \leq 3$. We consider the rate QN_2^+ to be the most reasonable of the three.

Fig. 5-4. The calculation of $\langle k_1/A \rangle$ which is appropriate for estimating the transfer rate of vibration from OH(v) to N_2^+ from the volume emission rate $\epsilon_{72}(z)$ measured in bands 4+2, 3+1 and 2+0 by Rogers et al. (1973) proceeds as follows.

$$\langle k_1/A \rangle [N_2] = \sum_{v=1}^9 n_v k_1(v) [N_2] / \sum_{v=2}^4 n_v A_{v-2}^v$$

where the $n_v = [OH(v)]$ are the relative populations of OH(v). For $v = 9$

$$n_v = k_3(v) / (A^v + Q_{TV}) \quad (5-6)$$

where $Q_{TV} = Q_{mv} + k_5 [O]$, $Q_{mv} = k_1(v)[N_2] + k_2(v)[O_2]$ and where $A^v = \sum_{v' < v} A_{v',v}^{v'}$. For successively smaller values of v the n_v are given by

$$n_v = \left(k_3(v) + Q_{m(v+1)} n_{v+1} + \sum_{v' > v} n_{v'} A_{v,v'}^{v'} \right) / (A^v + Q_{TV}) \quad (5-7)$$

Standard $CO_2(v_3)$ radiation transport methods (Kumer and James, 1974; Kumer, 1977a) may be used to compute the CO_2 4.3 μm zenith radiance profile R_{OH72} that would be generated by a source of N_2^+ given by $QN_{2,72}^*$. The earth's atmosphere is optically thick for CO_2 4.3 μm in the 80 to 100 km region. For this reason there is a maximum in the zenith radiance profile that occurs several km below the maximum in $QN_{2,72}^*$.

The altitude of the maximum in the OH airglow layer is known to vary considerably from one measurement to another (Baker et al., 1977). It would be fortuitous if we could achieve a good fit to the data (curve D on Fig. 5-1) linear combination of the radiance due to mechanism (i) and (ii) (Curve A on Fig. 5-1) and the radiance R_{OH72} computed from a particular set of OH volume

emission data, such as the data $\epsilon_{72}(z)$ reported by Rogers et al. The maximum in the Rogers et al., OH volume emission data occurs at a relatively low altitude $z = 84$ km. We selected a 2 cd set of OH volume emission data $\epsilon_{75}(z)$ with maximum occurring at relatively high altitude $z = 89$ km, these data were obtained 3/4/75 (Baker et al., 1977). These data were obtained in the 8+6 and 7+5 bands. The vibration transfer rate $QN_{2,75}^+$ to N_2 is given by

$$QN_{2,75}^+ = \epsilon_{75} \sum_{v=1}^9 n_v k_1(v) [N_2] / \sum_{v=7,8} n_v A_{v-2}^v$$

and $\int dz QN_{2,75}^+ = 0.0374$ ergs/cm² sec. The radiance R_{OH75} may be computed from $QN_{2,75}^+$ as discussed above.

A least squares best fit to the data D of radiance curves A, R_{OH72} and R_{OH75} is shown on Fig. 5-5. The linear combination $1.28A + 0.816 R_{OH72} + 1.84 R_{OH75}$ is required to achieve the fit shown on Fig. 5-5. The coefficient of curve A indicates the absolute calibration of the instrument should be modified to reduce the quoted value of the data (curve D on Fig. 5-1) by a factor 1/1.28. This is well within the $\pm 25\%$ quoted accuracy in absolute calibration. The "recalibration" is justified since we expect our calculation and the data to match in the altitude region $z \lesssim 60$ km where the kinetic temperature driven mechanisms (i) and (ii) dominate, and where we have ASL met. rocket sounding data on atmospheric temperature. The total column vibrational transfer of energy E_{VV} from OH^+ to N_2^+ then is given by

$$E_{VV} = (0.816 \times \int dz QN_{2,72}^+ + 1.84 \times \int dz QN_{2,75}^+) / 1.28$$

$$= .12 \text{ ergs/cm}^2 \text{ sec.}$$

The $\pm 25^\circ$ uncertainty in mesopause temperature that is indicated on fig. 5-2 causes an associated contribution to uncertainty in the recalibration factor of approximately 15% and to uncertainty in E_{VV} of approximately $\pm 17\%$.

Also we should note that the 9+8 and 8+7 OH bands are centered near 4.47 and 4.14 μ m. Volume emission $\epsilon_{v''}^v$ in a given band may be calculated via

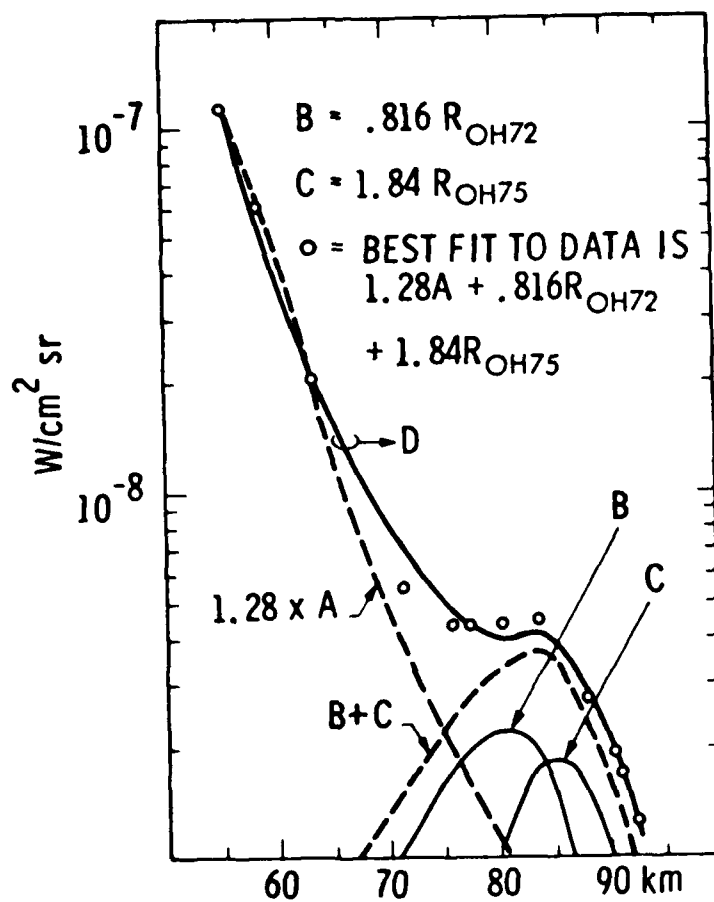


Fig. 5-5. A least squares fit to the data D which is given by $1.28A + 0.816 R_{OH72} + 1.84 R_{OH75}$ is shown on this figure.

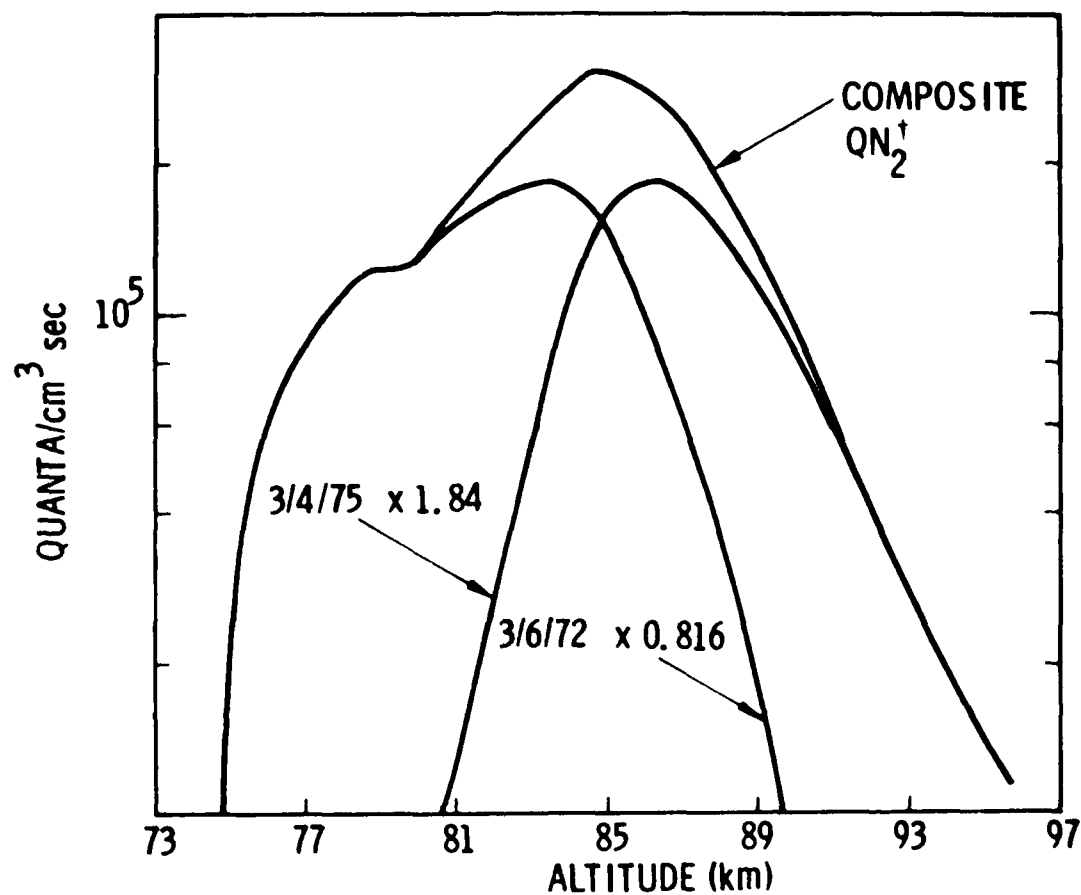


Fig. 5-6. The composite QN_2^+ which gives the fit to the data as shown on Figure 5-5. The composite is a linear combination of the QN_2^+ inferred from OH volume emissions ϵ_{72} and ϵ_{75} that were measured on 6 March 1972 and 4 March 1975. The coefficients are 0.816 and 1.84 respectively.

$$\epsilon_{v''}^{v'} = \left\{ .816 \epsilon_{72} \eta_{v'} A_{v''}^{v'} / \sum_{v=2}^4 \eta_v A_v^v + 1.84 \epsilon_{75} \eta_{v'} A_{v''}^{v'} / \sum_{v=7,8} v A_{v-2}^v \right\} / 1.28$$

The calculations shows that $\int dz QN_2^{\dagger} / \int dz (\epsilon_8^9 + \epsilon_7^8) \approx 16.4$ hence direct OH emission near $4.3 \mu\text{m}$ is not significant compared to the $\text{CO}_2(\nu_3)$ emission which results from vibration transfer from $\text{OH}(v)$ to N_2 . The fact that OH $v \rightarrow v-1$ bands which lie between the 2.7 and $4.3 \mu\text{m}$ features are not observed in the CVF spectra supports this conclusion.

On Fig. 5-7 we show how the $\text{OH}^{\dagger} \xrightarrow{v\nu} \text{N}_2$ mechanism affects the 11 April 1974 night time vibrational temperatures of the CO_2 001 state T_{001} and of N_2 T_{N_2} . The solid curve is nominal atmospheric kinetic temperature model T_N . The dash dot curve shows that T_{N_2} and T_{001} are identical for altitudes $z \lesssim 75 \text{ km}$. At $z \gtrsim 72 \text{ km}$ the dash cot curves split into a component which is due to mechanisms (i) and (ii) but which neglects the $\text{OH}^{\dagger} \xrightarrow{v\nu} \text{N}_2$ mechanism, and another component which is due to mechanisms (i) and (ii) and the $\text{OH}^{\dagger} \xrightarrow{v\nu} \text{N}_2$ mechanism. It is apparent that the $\text{OH}^{\dagger} \xrightarrow{v\nu} \text{N}_2$ mechanism dominates the T_{N_2} and T_{001} in the region $z \gtrsim 73 \text{ km}$.

We show Fig. 5-7 to demonstrate how the inclusion of the $\text{OH}^{\dagger} \xrightarrow{v\nu} \text{N}_2$ mechanism would modify the calculational results for night time vibrational temperatures from that given by Kumer and James (1974). The corresponding modification in the quiet night time weak $\text{CO}_2 \nu_3$ band vibrational temperatures may be calculated by methods given by Kumer (1977b).

5.3 CONCLUSIONS

We conclude that the feature near 85 km which is observed in the 11 April 1974 $4.3 \mu\text{m}$ zenith radiance data is a manifestation of the $\text{OH}^{\dagger} \xrightarrow{v\nu} \text{N}_2$ mechanism. A columnar transfer of $0.12 \pm 0.025 \text{ ergs/cm}^2 \text{ sec}$ of vibration energy from OH^{\dagger} to N_2^{\dagger} is required to explain the feature. A carefully planned experiment utilizing rocket-borne measurements of OH emission and CO_2 4.3 and $15 \mu\text{m}$ zenith radiance coordinated with simultaneous and independent measurements of

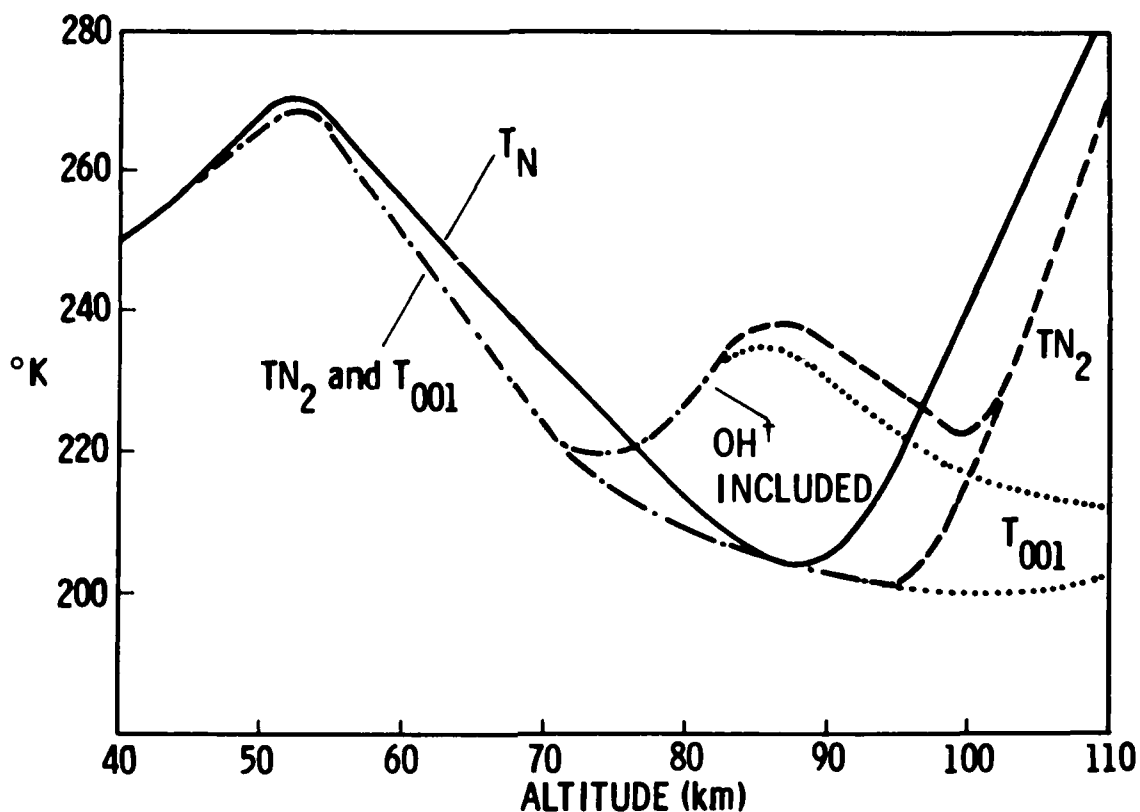


Fig. 5-7. The solid curve is our nominal model atmospheric kinetic temperature T_N for 11 April 1974. The dash-dot curves are the coupled N_2 and $CO_2(001)$ vibrational temperatures T_{N_2} and T_{001} . The dash-dot curves break into two components for $z \geq 72$ km. The mechanisms (i) and (ii) were used in the computation of both the dash-dot curves but the $OH^+ \rightarrow N_2$ mechanism was included in the computation of the upper curve but not in the computation of the lower curve. The T_{N_2} and T_{001} decouple at $z \gtrsim 84$ km and $z \gtrsim 95$ km in the two cases. The T_{N_2} are the dashed curves, the T_{001} the dotted curves. This figure illustrates the dominance of the $OH^+ \rightarrow N_2$ mechanism on the vibrational temperatures T_{001} and T_{N_2} above $z \approx 72$ km.

atmospheric temperature up to 90 km altitude (by ASL sounding rockets, Nimbus 6 PMR atmospheric temperature sounder and ground-based OH rotational temperature measurements for example), could be used to verify the role of the mechanism $\text{OH}^+ \xrightarrow{\text{VV}} \text{N}_2^+$ in the formation of 4.3 μm emission in the altitude region $z \geq 80$ km.

5.4 ACKNOWLEDGEMENTS

The ASL sounding rocket data provided R. O. Olsen and the unpublished preliminary OH airglow rotational temperature data provided by Gene Ware added considerably to our effort. Excellent suggestions by R. J. McNeal and R. S. Stolarski added considerably to the quality of our work.

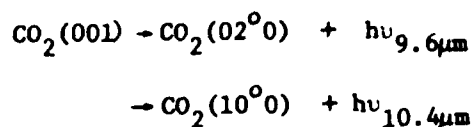
6.0 ESTIMATES OF CO₂ HOT BAND EARTHLIMB EMISSION IN THE LWIR REGION

6.1 Introduction

Sensitive earthlimb and ATH sensors are under consideration. Even weak background emissions might impact the performance of such sensors. In this chapter we report estimates for the CO₂ LWIR spectral radiance which results from auroral, solar, and airglow pumping of excited states of CO₂.

6.2 Auroral Processes

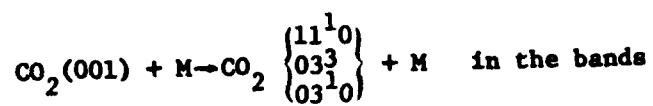
The CO₂(001) will be produced in the aurora by $N_2^+ + CO_2 \rightarrow CO_2(001)$. This is followed by LWIR emission in the CO₂ laser lines via



Subsequent emission will also occur in the CO₂ LWIR bands $2\nu_1' + \nu_2' \rightarrow 2\nu_1'' + \nu_2'' = 2\lambda_1$.

| ν_1' | ν_2'' | ν_3' | ν_1'' | ν_2'' | ν_3'' | $\frac{\lambda (\mu m)}{\text{Origins}}$ |
|-------------------|-----------|----------|-------------------|-----------|-----------|--|
| 02 ² 0 | → | | 01 ³ 0 | | | 15 |
| 10 ⁰ 0 | → | | 01 ³ 0 | | | 13.87 |
| 02 ⁰ 0 | → | | 01 ³ 0 | | | 16.18 |

In addition LWIR may be produced by



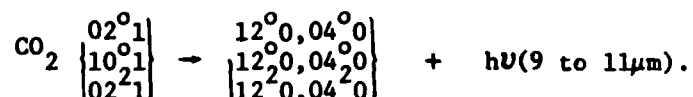
$2\nu'_1 + \nu'_2 \rightarrow 2\nu''_1 + \nu''_2 = 3 \rightarrow 2$, these bands are

| $\nu'_1 \quad \nu'_2 \quad \nu'_3 \rightarrow \nu''_1 \quad \nu''_2 \quad \nu''_3$ | $\lambda (\mu\text{m})$ Origins |
|--|------------------------------------|
| $11^1 0 \quad \quad \quad 02^2 0$ | 13.48 |
| $11^1 0 \quad \quad \quad 02^0 0$ | 12.63 |
| $11^1 0 \quad \quad \quad 10^0 0$ | 14.52 |

| $\nu_1' \nu_2' \nu_3' \rightarrow \nu_1'' \nu_2'' \nu_3''$ | $\lambda(\mu\text{m})$ Origins |
|--|-----------------------------------|
| $03^3 0 \rightarrow 02^2 0$ | 15.03 |
| $03^1 0 \rightarrow 02^2 0$ | 16.74 |
| $03^1 0 \rightarrow 02^0 0$ | 15.45 |
| $03^1 0 \rightarrow 10^0 0$ | 18.37 |

6.3 Solar Processes

In the solar case the $\text{CO}_2(001)$ is produced by absorption of $4.3\mu\text{m}$ sunlight by CO_2 . The CO_2 LWIR is produced from the $\text{CO}_2(001)$ as discussed above. In addition $\text{CO}_2(10^0 1)$ and $\text{CO}_2(02^0 1)$ may be produced by absorption of $2.7\mu\text{m}$ sunlight. CO_2 LWIR is generated from these states by laser radiation..



The lower states of the laser transition form the upper state for LWIR transition $2\nu_1' + \nu_2' \rightarrow 2\nu_1'' + \nu_2'' = 4 \rightarrow 3$. Some of the most notable of these transitions are listed below

| | λ |
|-----------------------------|-----------|
| $20^0 0 \rightarrow 03^1 0$ | 11.56 |
| $04^0 0 \rightarrow 11^1 0$ | 21.21 . |

Also, the mechanism $M + \text{CO}_2 \begin{Bmatrix} 021 \\ 101 \end{Bmatrix} \rightarrow M + \text{CO}_2 \begin{Bmatrix} 2\nu_1' + \nu_2' = 5, \nu_3' = 0 \end{Bmatrix}$ will produce LWIR in the transition $2\nu_1' + \nu_2' \rightarrow 2\nu_1'' + \nu_2'' = 5 \rightarrow 4$, notable of these are

| | $\lambda(\mu\text{m})$ Origins |
|-----------------------------|-----------------------------------|
| $13^3 0 \rightarrow 04^2 0$ | 11.66 |
| $05^3 0 \rightarrow 12^2 0$ | 20.84 |

6.4 Airglow Processes

In the night time airglow $\text{CO}_2(001)$ is produced by vibration transfer $\text{OH}(\nu) + \text{N}_2 \xrightarrow{\text{V}} \text{N}_2 + \text{CO}_2 \xrightarrow{\text{V}} \text{CO}_2(001)$, LWIR results from the $\text{CO}_2(001)$ by processes discussed above.

6.5 Summary and Results

In summary, we have pointed out 6 distinct groups of CO_2 LWIR band complexes that may be pumped by the aurora, sunlight, or the OH airglow. Below we shall designate the total limb radiance in a given band complex by R_n . The subscript n designates the band complex as follows:

| <u>Subscript</u> | <u>Process and Band Complex</u> |
|------------------|---|
| 1 | $2 \nu'_1 + \nu'_2 \rightarrow 2 \nu''_1 + \nu''_2 = 2 \rightarrow 1$ |
| 2 | " $= 3 \rightarrow 2$ |
| 3 | " $4 \rightarrow 3$ |
| 4 | " $5 \rightarrow 4$ |
| 5 | $h\nu_{2.7} + \text{CO}_2 \rightarrow \begin{smallmatrix} 101 \\ 021 \end{smallmatrix} \rightarrow \begin{smallmatrix} 120 \\ 210 \end{smallmatrix} + \text{laser radiation, 9 to 11 } \mu\text{m}$ |
| 6 | $001 \rightarrow \begin{smallmatrix} 020 \\ 100 \end{smallmatrix}$ " |

It is possible to use the altitude profiles of vibrational temperature of the CO_2 upper states 00^01 , 02^01 , 02^21 , and 10^01 in order to estimate CO_2 LWIR limb radiances in the band complexes $n = 1$ to 6. In order to calculate the limb radiance estimates we used CO_2 ν_3 vibrational temperatures $T_v(z)$ that we have calculated for the March 24, 1973 auroral breakup, these are shown in Table 6-1. For the 60° solar zenith sunlit case we use the $T_v(z)$ published in the Kumer (1977b) paper and for the airglow case we use $T_{001}(z)$ as shown on Fig. 5-7 in the previous chapter. The limb radiance R in an optically thin band is approximately given by

$$R = \frac{1}{4\pi} \int ds A[\text{CO}_2] e^{-T_o/T_v(z)}$$

where the integral is along a limb viewing path s , A is the Einstein radiative decay coefficient of the upper state, $[CO_2]$ the CO_2 number density, $T_v(z)$ the vibrational temperature in the upper state, and $T_0 = hc E'/k$ where E' is the vibrational energy of the upper state in units cm^{-1} . The band complex $2 \rightarrow 1$ is optically thick and requires a more complicated computation

$$R_1 = \frac{1}{4\pi} \int \sigma [CO_2] ds T(\sigma N(s)) A e^{-T_0/T(v)}.$$

The assumption is made that the sub levels in a given complex of levels $2 \nu_1 + \nu_2$ are populated according to local thermodynamic equilibrium (LTE). This is probably not the actual case, more research is needed to determine the population distribution within a given complex of levels since this determines the spectral distribution of the CO_2 LWIR limb radiance. For present purposes we will use the estimates based on the LTE assumption in order to get some idea of the CO_2 LWIR limb radiance in window regions that is due to solar, auroral, and airglow pumping. The estimated radiance in each band complex that is due to each of these mechanisms is given in Table 6-2.

It is possible to use these estimates for R_n in order to generate synthetic LWIR limb spectra for tangent altitudes 80, 90, and 100 km. These spectra are generated at a CVF-like resolution of $.01 \lambda$ in the 10 to $14.5 \mu m$ and in the 16.5 to $20 \mu m$ region, and spectra with $0.5 cm^{-1}$ HIRIS-like resolution are generated in the region of the Q branches of selected bands. These spectra are generated by line by line methods described by Kumer in HAES Report No. 70 (1977). Line positions and strengths from the McClatchey tape are utilized. The synthetic spectra are shown in Appendix E.

TABLE 6-1

24 March 1973 Kinetic (T_K), N_2 Vibrational (T_{N_2}) and CO_2 ν_3 Vibrational (T_J)Temperatures Versus Altitude. The index J designates the 4.3 μ m band upperstate $\nu_1 \nu_2 \nu_3$ as explained in the paper by Kumer (1977a).

| Z (km) | T_K | T_{N_2} | T_J | | | | | | | | | |
|-----------|-------|-----------|-------|-------|-------|-------|-------|-------|-------|-------|-------|-------|
| | | | 1 | 2 | 3 | 4 | 5 | 6 | 7 | 8 | 9 | 10 |
| 100.0 | 556.4 | 570.1 | 297.9 | 232.5 | 233.5 | 238.3 | 232.1 | 243.3 | 245.7 | 247.2 | 237.8 | 239.6 |
| 107.9 | 276.9 | 503.0 | 313.0 | 285.3 | 284.7 | 282.4 | 285.3 | 279.1 | 277.0 | 275.5 | 282.7 | 281.7 |
| 99.6 | 217.7 | 420.7 | 325.9 | 293.0 | 291.8 | 288.9 | 292.6 | 285.1 | 282.7 | 280.8 | 289.1 | 288.0 |
| 95.2 | 203.8 | 372.9 | 326.9 | 290.3 | 288.6 | 285.6 | 289.5 | 282.0 | 279.8 | 278.1 | 285.6 | 284.6 |
| 92.6 | 200.6 | 342.8 | 321.8 | 281.7 | 279.7 | 276.9 | 280.7 | 274.1 | 272.5 | 271.3 | 276.9 | 276.1 |
| 91.0 | 199.0 | 326.8 | 316.9 | 278.1 | 275.8 | 273.2 | 277.0 | 270.7 | 269.4 | 268.4 | 273.0 | 272.4 |
| 90.2 | 198.2 | 322.4 | 314.6 | 277.1 | 274.7 | 272.0 | 276.0 | 269.7 | 268.4 | 267.5 | 271.8 | 271.2 |
| 88.1 | 199.1 | 310.7 | 308.1 | 275.3 | 272.5 | 269.8 | 274.2 | 267.7 | 266.6 | 265.8 | 269.5 | 269.0 |
| 83.7 | 203.1 | 288.0 | 288.1 | 267.4 | 264.3 | 261.8 | 267.2 | 260.6 | 260.2 | 259.9 | 261.3 | 261.1 |
| 80.2 | 208.7 | 270.7 | 271.0 | 257.2 | 254.4 | 252.6 | 257.9 | 252.5 | 252.8 | 253.1 | 251.9 | 252.0 |
| 77.7 | 211.8 | 258.8 | 259.0 | 248.0 | 245.7 | 244.8 | 248.8 | 245.7 | 246.7 | 247.5 | 243.9 | 244.4 |
| 76.0 | 213.7 | 251.4 | 251.6 | 241.9 | 240.2 | 239.9 | 242.7 | 241.5 | 242.9 | 244.0 | 239.0 | 239.6 |
| 75.2 | 214.8 | 248.0 | 248.1 | 239.1 | 237.6 | 237.6 | 239.8 | 239.5 | 241.1 | 242.3 | 236.7 | 237.4 |
| 73.8 | 216.6 | 242.5 | 242.6 | 234.6 | 233.5 | 234.0 | 235.1 | 236.4 | 238.2 | 239.6 | 233.1 | 234.0 |
| 70.6 | 221.2 | 231.4 | 231.4 | 227.1 | 226.8 | 228.1 | 227.3 | 230.8 | 232.9 | 234.5 | 227.1 | 228.1 |
| 66.6 | 229.0 | 228.7 | 228.7 | 227.4 | 227.3 | 228.2 | 227.5 | 230.0 | 231.4 | 232.6 | 227.5 | 228.1 |
| 69.4 | 235.6 | 232.4 | 232.4 | 232.1 | 232.1 | 232.3 | 232.1 | 233.2 | 233.9 | 234.6 | 231.9 | 232.2 |
| 61.4 | 240.0 | 236.5 | 236.5 | 236.4 | 236.4 | 236.4 | 236.4 | 236.8 | 237.2 | 237.5 | 236.1 | 236.2 |
| 60.3 | 242.4 | 238.9 | 238.9 | 238.9 | 238.8 | 238.8 | 238.9 | 239.0 | 239.3 | 239.5 | 238.6 | 238.7 |
| 59.4 | 243.9 | 240.6 | 240.6 | 240.5 | 240.5 | 240.5 | 240.5 | 240.6 | 240.7 | 240.9 | 240.3 | 240.3 |
| 57.2 | 247.1 | 244.4 | 244.4 | 244.3 | 244.3 | 244.3 | 244.3 | 244.2 | 244.2 | 244.3 | 244.1 | 244.1 |
| 54.7 | 250.8 | 248.7 | 248.7 | 248.7 | 248.7 | 248.6 | 248.7 | 248.5 | 248.4 | 248.4 | 248.6 | 248.9 |
| 52.6 | 254.1 | 252.3 | 252.3 | 252.3 | 252.3 | 252.2 | 252.3 | 252.1 | 252.0 | 251.9 | 252.2 | 252.2 |
| 51.0 | 256.4 | 254.8 | 254.8 | 254.8 | 254.8 | 254.8 | 254.8 | 254.6 | 254.6 | 254.5 | 254.8 | 254.7 |
| 48.2 | 257.7 | 256.3 | 256.3 | 256.3 | 256.3 | 256.2 | 256.3 | 256.1 | 256.0 | 255.9 | 256.2 | 256.2 |
| 48.0 | 258.0 | 257.7 | 257.7 | 257.7 | 257.6 | 257.6 | 257.7 | 257.5 | 257.4 | 257.3 | 257.6 | 257.6 |

Table 6-2
LIMB RADIANCE ESTIMATES

(1) Auroral (representative of 24 March 1973 breakup)

| Z(km) | R_1 | R_2 | R_3 | R_4 | R_5 | R_6 |
|-------|--------------|--------------|-------|-------|-------|-------------|
| 80 | 2.09^{-8*} | 1.2^{-8} | | | | 1.34^{-8} |
| 90 | 8.6^{-9} | 1.67^{-9} | | | | 1.04^{-8} |
| 100 | 1.9^{-9} | 7.02^{-11} | | | | 2.75^{-9} |

(2) Solar (60° solar zenith)

| Z | R_1 | R_2 | R_3 | R_4 | R_5 | R_6 |
|-----|-------------|--------------|--------------|--------------|--------------|-------------|
| 80 | 2.49^{-7} | 4.25^{-8} | 4.61^{-10} | 2.65^{-10} | 2.94^{-10} | 4.7^{-8} |
| 90 | 9.96^{-8} | 1.54^{-9} | 1.91^{-10} | 2.73^{-11} | 2.31^{-10} | 8.41^{-9} |
| 100 | 2.56^{-8} | 1.62^{-11} | 3.19^{-11} | 1.18^{-12} | 4.61^{-11} | 1.34^{-9} |

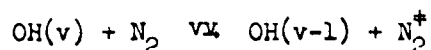
(3) Airglow (representative of 11 April 1974 $4.3 \mu\text{m}$ data)

| Z | R_1 | R_2 | R_3 | R_4 | R_5 | R_6 |
|-----|--------------|--------------|-------|-------|-------|--------------|
| 80 | 4.17^{-9} | 2.39^{-9} | | | | 2.67^{-9} |
| 90 | 5.27^{-10} | 1.02^{-10} | | | | 6.37^{-10} |
| 100 | 5.87^{-11} | 2.17^{-12} | | | | 8.48^{-11} |

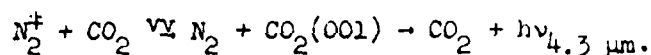
* 2.08^{-8} here means $2.09 \times 10^{-8} \text{ w cm}^2 \text{ ster}$ is the auroral limb radiance in the complex of 2 → 1 bands.

7.0 EVIDENCE FOR A PROMPT 4.3 μ m AURORAL EMISSION

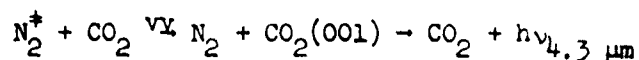
A rocket carrying a two channel liquid nitrogen cooled radiometer at 2.7 and 4.3 μ m and a photometer at 4278 Å was launched 10/26/78 at the Poker Flat Research Range, Alaska, for the Defense Nuclear Agency. The radiometers sensitivity was about a factor X50 better than had been previously used for any rocket borne observations of aurora at 2.7 and 4.3 μ m. An auroral arc (IBC II⁺) moved about ten minutes before launch from an overhead position at the launch area to a stable position about 50 km to the north. Comparison of the 4.3 μ m radiance on rocket ascent and descent at altitudes below 85 km show similar profiles that can be identified with the OH airglow mechanism



followed by



From 90 to about 105 km the ascent zenith radiances are nearly an order of magnitude brighter than on rocket descent. The ascent 90 to 105 km altitude region was heavily predosed in comparison with the corresponding region on descent. The higher ascent values of 4.3 μ m zenith radiance are consistent with the well documented (Kumer, 1977a), long time response 4.3 μ m auroral mechanism



where the N_2^+ is initially produced by the electron precipitation.

At altitudes above about 100 km for both ascent and descent the 4.3 μ m zenith radiance data show structure and values that suggest a second, nearly "prompt" auroral mechanism. This structure is clearly evident at radiance levels well below the NER of previous instrumentation.

The apparent energy efficiency for the mechanism is $\epsilon \approx 0.3\%$ (or 1.1×10^{-10} w/cm² ster at 4.3 μ m per kR at 4278 Å) for altitude $Z \gtrsim 115$ km. The data indicate that the effective value of ϵ decreases rapidly with decreasing altitude in the region $100 < Z < 115$ km, thus suggesting a strong quenching effect in this altitude region.

A preliminary analysis of these data has been presented at the DNA IR review meeting held 10-12 April 1979 at the Air Force Geophysics Laboratory and is summarized in the document AFGL-TM-18. A slightly more sophisticated presentation of this material was given May 28 - June 1 at the Annual Spring Meeting of American Geophysical Union. Vufoils shown at this presentation are included as Appendix F. This presentation is currently being written up for submission for publication in J. Geophys. Res. An important goal of future field experiments and data evaluation is of course to attempt to confirm and to identify the mechanism for the "prompt" 4.3 μ m aurora so that it may be included in nuclear IR predictive codes such as ROSCOE. Future rocket borne auroral experiments should employ high spectral resolution to identify the emitting specie, and should be designed to provide information on the altitude dependence of the effective 4.3 μ m fluorescent efficiency. The ground based support should be designed to complement the rocket data in achieving this latter goal as well as to provide input for a reasonably

accurate determination of the time response of the nearly prompt mechanism. Calibrated ground based all sky red (6300 \AA) and blue (4278 \AA) filtered TV data is ideal for this purpose.

We also suggest that detailed radiation transport analysis in application to the 25 February 1974 side looking radiometer data may reveal confirming evidence for the existence of a nearly prompt mechanism. It is possible that a 2 dimensional analysis of the 24 February 1974 side looking data might also distinguish the contribution of the dominant slow CO_2 $4.3\mu\text{m}$ aurora from that of the nearly "prompt" mechanism.

8.0 CONCLUSIONS

Methods to deal with the time dependent two dimensional radiation transport in the CO_2 4.3 μm auroral arc were developed and applied to a nominal aurora in the presence of a wind field. The nominal auroral arc moved in from the north at 3 km/min, and then stabilized for two minutes. The calculations showed that lateral gradients in the nadir radiance that are predicted if lateral transport is neglected are considerably steeper than for the predictions which do include the effects of lateral transport. The predicted smoothing effect of lateral radiation transport of CO_2 4.3 μm photons in the earth's optically thick upper atmosphere is dramatic enough so that it renders the lateral gradients in the CO_2 4.3 μm auroral nadir radiance no more severe than the lateral gradients in auroral 2.7 μm nadir radiance even though the DC level of the CO_2 4.3 μm auroral radiance may be as much as 10 times that of the 2.7 μm aurora in steady state conditions.

This point is important for assessing high altitude nuclear degradation of the performance of advanced nadir viewing scanning sensors due to high altitude nuclear mechanisms such as x-ray, β -patch, and debris patch deposition which are similar to the aurora. To provide verification we considered 4 distinct experimental concepts applicable for the 4.3 μm region, and briefly considered a 2.7 μm experimental concept too. Most of these concepts involved firing a rocket over an auroral arc and viewing the aurora in the nadir in order to measure lateral structure in auroral nadir radiance in the 4.3 and 2.7 μm spectral regions. Nadir viewing 4.3 μm concepts included a broad band filtered radiometer (BBFR), a narrow band tilting 10 transmission channel picket fence

filtered radiometer (NBTR) and the use of HIRIS. In each case the instruments are to be used with a wheel of CO_2 absorption cells in order to provide the added high resolution $\sim 6 \times 10^{-3} \text{ cm}^{-1}$ near the centers of the CO_2 lines that is necessary to discriminate CO_2 4.3 μm narrow line auroral nadir radiance from the earth nadir radiance background. Also, 0.2 to 0.5 cm^{-1} resolution between the lines is necessary in order to suppress deleterious effects of the broad band LTE thermal stratospheric contribution to the earth's 4.3 μm nadir radiance background. This requirement is sufficient to rule out the BBTR for use in the desired arc overfly experiment. The NBTR and HIRIS easily satisfy this 0.2 to 0.5 cm^{-1} spectral requirement. It turns out that viewing the 250° earth degrades the HIRIS sensitivity to the point that verification of the lateral radiation transport smoothing effect on the CO_2 4.3 μm aurora in the spatial wing of the nominal arc is marginal. However, since the NBTR views the 250°K earth through a 77°K filter with total band pass of $\sim 2 \text{ cm}^{-1}$ near to 4.3 μm , sensitivity is not degraded appreciably beyond the inherent InSb detector noise limit at 77°K and therefore verification by means of the NBTR sensor appears to be eminently feasible.

The optimum design NBTR uses liquid Nitrogen (LN_2) cooled optics including the tilting filters, and LN_2 cooled baffling. This reduces the NEP of the .71 cm diameter In Sb detector to $\approx 3 \times 10^{-14} \text{ W}/\sqrt{\text{Hz}}$, nearly the inherent LN_2 cooled detector noise limit. The narrow band filter is a 4" diameter Silicon (index of refraction ≈ 3.4) substrated Fabry Perot etalon designed so that the centers of 10 of its transmission channels roughly coincide with the lines p8, p10, ..., p26 of the $^{12}\text{C}^{16}\text{O}_2$ 001 + 000 band. A 300A blocker filter allows just the 10 channels to be

transmitted. The narrow band filter is designed so that the transmission channel full width half maximum FWHM $\approx 0.21 \text{ cm}^{-1}$ (i.e., 4A) for an FOV with the 1/2 cone angle $\alpha = 2^\circ$. The through put of the optimum NBTFR is $\approx .062 \text{ cm}^2 \text{ sr}$ for an overall optics transmission of $\approx 20\%$. The NER $\approx 5.0 \times 10^{-13} \text{ w/cm}^2 \text{ sr}$. Spectral scanning between the CO_2 line centers is achieved by tilting the filter. High spectral resolution of $\approx 6 \times 10^{-3} \text{ cm}^{-1}$ near the CO_2 line center is achieved by utilization of the CO_2 absorption cells.

As part of the study it was also verified that an optimum NBTFR could be used effectively in an arc overfly experiment to verify that lateral gradients in the $2.7\mu\text{m}$ auroral nadir radiance are indeed as sharp and dramatic as one would expect from an essentially prompt, optically thin auroral emission.

Estimates for the spatial structure to be observed by the sensor module on the spatial EXCEDE daughter vehicle on viewing the electron gun discharge at the mother vehicle at 90 km altitude were also generated. These suggest that prompt emission by NO^+ might be expected to dominate the region of instantaneous energy deposition but that the long lived mechanism $\text{N}_2^+ + \text{CO}_2 \rightarrow \text{CO}_2(001) + \text{CO}_2 + h\nu 4.3\mu\text{m}$ will dominate the predosed regions. Also it is estimated that radiation transport into regions that are adjacent to the region of instantaneous deposit and to the predosed region will be strong enough to produce a signal above background. Data that will be obtained in these so called transport regions can serve as a guide for the development of a numerically effective CO_2 $4.3\mu\text{m}$ 3 dimensional radiation transport facility for application to the nuclear case (highly structured β deposition region).

Analysis of a feature near 85 km which is observed in the 11 April 1974 4.3 μ m zenith radiance data indicates that it is a manifestation of OH airglow related mechanism OH \rightarrow N₂ for producing CO₂ 4.3 μ m and LWIR emission. A columnar transfer of $0.12 \pm .025$ ergs/cm²sec. of vibration energy from OH to N₂ is required to explain the feature. Although, to date, there has been no experiment directly aimed at simultaneous measurement of all the parameters (temperature, OH emission, CO₂ 4.3 μ m and LWIR emissions) that are pertinent to the OH airglow mechanism for CO₂ 4.3 μ m and LWIR emission, still there is considerable evidence (Kumer, 1976; Kumer et al 1978, this report, etc.) for the existence of the mechanism. Detailed verification and quantization of the mechanism could be achieved for example by carefully planned experiment utilizing rocket-borne measurements of OH emission and CO₂ 4.3 and 15 μ m zenith radiance coordinated with simultaneous and independent measurements of atmospheric temperature up to 90 km altitude (by ASL sounding rockets, Nimbus 6 PMR atmospheric temperature sounder and ground-based OH rotational temperature measurements for example).

The mechanisms aurora, airglow, and sunlight fluorescence, for pumping CO₂ emissions in LWIR earthlimb window were addressed. These mechanisms are important in the natural background and have nuclear analogues. Estimated synthetic spectra produced by these mechanisms were generated for tangent altitudes 80, 90, and 100 km at a CVF-like resolution of .01 λ in the 10 to 14.5 μ m region and in the 16.5 to 20 μ m region, and also with 0.5 cm⁻¹ HIRIS-like resolution in the region of the Q branches of selected bands.

In many cases the estimated spectral radiances were well above realizable sensor NESRs.

A major uncertainty in these estimates is that they were calculated on the assumption that the sub levels in a given complex of CO_2 levels $2 \nu_1 + \nu_2$ are populated according to local thermodynamic equilibrium (LTE). This is probably not the actual case, more research is needed to determine the spectral distribution within a given complex of levels under atmospheric conditions near 100 km altitude since this determines the spectral distribution of the CO_2 LWIR limb radiance.

The analysis of $4.3\mu\text{m}$ auroral zenith radiance data obtained 10/26/78 via a rocket borne radiometer of improved sensitivity indicated, for the first time, the presence of a relatively weak mechanism for prompt auroral emission at $4.3\mu\text{m}$. The apparent energy efficiency for the mechanism is $\epsilon \approx 0.3\%$ (or $1.1 \times 10^{-10} \text{ w/cm}^2 \text{ ster at } 4.3\mu\text{m per kR at } 4278 \text{ \AA}$) for altitude $Z \approx 115 \text{ km}$. The data indicate that the effective value of ϵ decreases rapidly with decreasing altitude in the region $100 < Z < 115 \text{ km}$, thus suggesting a strong quenching effect in this altitude region.

An important goal of future field experiments and data evaluation is to attempt to confirm and to identify the mechanism for the "prompt" $4.3\mu\text{m}$ aurora so that it may be included in nuclear IR predictive codes such as ROSCOE. Future rocket borne auroral experiments should employ high spectral resolution to identify the emitting specie, and should be designed to provide information on the altitude dependence of the effective $4.3\mu\text{m}$ fluorescent efficiency. The ground based support should be designed to complement the rocket data in

achieving this latter goal as well as to provide input for a reasonably accurate determination of the time response of the nearly prompt mechanism. Calibrated ground based all sky red (6300 \AA) and blue (4278 \AA) filtered TV data is ideal for this purpose.

We also suggest that detailed radiation transport analysis in application to the 25 February 1974 side looking radiometer data may reveal confirming evidence for the existence of a nearly prompt mechanism. It is possible that a 2 dimensional analysis of the 25 February 1974 side looking data might also distinguish the contribution of the dominant slow CO_2 $4.3\mu\text{m}$ aurora from that of the nearly "prompt" mechanism.

9.0 REFERENCES

Baker, D. J., G. D. Frodsham, J. B. Kumer, A. T. Stair, Jr., J. C. Ulwick, "Rocketborne Measurements of Infrared Aurora and Airglow Emissions at $4.3\mu\text{m}$ ", EOS 60, 328, 1979

Baker, D. J., T. Conley, and A. T. Stair, On the Altitude of the OH Airglow, EOS 58, No. 6, 460, 1977

Billingsley, II, F., Chem. Phys. Lett. 23, 160, 1973

Blank, C. A., T. Baurer, M. H. Bortner, and A. A. Feryok, A Pocket Manual of the Physical and Chemical Characteristics of the Earth's Atmosphere, Handbook DNA 3467H, 1974

Charters, P. E., R. G. MacDonald, and J. C. Polanyi, Appl. Optics, 10, 1747, 1971

Good, R. E., Determination of Atomic Oxygen Density from Rocketborne Measurement of Hydroxyl Airglow, Planet. Space. Sci. 34, 389, 1976

Gardietz, B. F., M. N. Markov and L. A. Shelekin, "IR Radiation of the Upper Atmosphere", Planet. Space Sci. 26, 933, 1978

Groves, G. V., Atmospheric Models, Air Force Cambridge Research Laboratories Technical Report, AFCRL-TR-70-1261, 1970

Kumer, J. B., "Approximate and Exact Technique for multidimensional Radiation Transport in a Plan Parallel Atmosphere; Application to the $4.3\mu\text{m}$ Auroral Arc", J. Quant. Spectrosc. Radiat. Transfer 19, 649, 1978

Kumer, J. B., Theory of the CO_2 $4.3\mu\text{m}$ Aurora and Related Phenomena, J. Geophys. Res. 82, 2203, 1977a

Kumer, J. B., CO_2 and N_2 Vibrational Temperatures, 40 to 140 km, J. Geophys. Res. 82, 2195, 1977b

Kumer, J. B., Further Evaluation of ICECAP Auroral 4.3 μ m Zenith Radiance, HAES Report No. 57, Final Report on Contract No. DNA001-76-C-0015, 1976

Kumer, J. B., Analysis of 4.3 μ m ICECAP Data, Air Force Cambridge Research Laboratories Technical Report, AFCRL-TR-74-0334, 1974

Kumer, J. B., D. J. Baker, G. D. F. Frodsham, A. T. Stair, Jr., J. C. Ulwick, "Analysis for Measurements of 4.3 μ m Airglow and Aurora; Evidence for a Prompt 4.3 μ m Auroral Component", to be submitted to J. Geophys. Res., Oct. 1979

Kumer, J. B., A. T. Stair, Jr., Ned Whiller, K. D. Baker and D. J. Baker, "Evidence For an OH γ^v N₂ γ^v CO₂(v_3) \rightarrow CO₂ + h ν (4.3 μ m) Mechanism for 4.3 μ m Airglow", J. Geophys. Res. 83, 4743, 1978

Kumer, J. B. and T. C. James, "Atmospheric Infrared Background Study: Experimental Confirmation of 2.7 to 4.3 μ m Fluorescence; Modeling of 4.3 μ m Spectral Structure", HAES Report No. 70, DNA 4409F, 1977

Kumer, J. B. and A. E. Roche, "Arc Overfly Nadir Radiance Experiment for the Multi II Lockheed Technical Brief, LMSC D457106, May 1975

Kumer, J. B., and T. C. James, CO₂(001) and N₂ Vibrational Temperatures in the 50 < z < 130 km Altitude Range, J. Geophys. Res. 79, 638, 1974

Mies, F. H., J. Mol Spectry, 53, 150, 1974, "Calculated Vibrational Transition Probabilities of OH(X² π)"

Murphy, R. E., J. Chem. Phys. 54, 4852, 1971

Noxon, J. F., "Effect of Internal Gravity Waves Upon Night Airglow Temperatures", Geophys. Res. Lett. 5, 25, 1978

Olsen, R. O., private communication of meteorological rocket data on atmospheric temperature and density for the 25 February 1974, 11 April 1974, 6 March 1975, and 12 March 1975 events, June 1976

Rogers, J. W., R. E. Murphy, A. T. Stair, Jr., J. C. Ulwick, K. D. Baker and L. L. Jensen, J. Geophys. Res. 78, 7023, 1973

Smith et al, NASA Number 5 Users Guide, 1972

Stair, A. T., Jr., J. W. Rogers and W. R. Williamson, "HIRIS Experiment, Quick Look Data Report", AFGL-OP-TM-02, 15 April 1976

Stair, A. T., Jr., J. C. Ulwick, K. D. Baker, and D. J. Baker, Rocketborne Observations of Atmospheric Infrared Emissions in the Auroral Zone, Atmospheres of the Earth and Planets, B. M. McCormac (Ed.), D. Reidel Publ. Co., Dordrecht-Holland, 335-346, 1975

Stair, A. T., Jr., N. B. Wheeler, D. J. Baker, and C. L. Wyatt, Cryogenic IR Spectrometers for rocketborne measurements, IEEE/NEREM Part 3, Infrared, 1973

Streit, G. E., and H. S. Johnston, J. Chem. Phys. 64, 95, 1976

Tarr, P. W., D. H. Archer and N. G. Utterback, "Studies of Auroral Simulation", Tech. Report DNA 3297F, April 1974

Ware, G. A., private communication of OH airglow rotational temperatures determined interferometer data obtained 4/9/74 and 4/13/74 near the PKR site, Feb. 1978

Ware, G. A., and D. J. Baker, OH Rotational Temperatures at Auroral Latitudes, EOS 57, 301, 1976

Westenberg, A. A., N. DeHass and J. M. Roscoe, Radical Reactions in Electron Spin Resonance, J. phys. Chem. 74, pp. 3431-3438, 1970

Wheeler, N. B., A. T. Stair, Jr., G. Frodsham, and D. J. Baker, Rocketborne Spectral Measurements of Atmospheric Infrared Emissions During Quiet Conditions in the Auroral Zone, AFGL-TR-76-0252, HAES Report No. 32, Air Force Geophysics Laboratory, Hanscom AFB, Mass., 1976

Wyatt, C. L. and D. J. Frodsham, "Short Wavelength Rocketborne IR Spectrometer", SPIE 124, Aug. 1977

Appendix A: The Approximate 3D Formulation

Here we give the 3-dimensional formulation for CO₂ 4.3 μm excitation in the earth's upper atmosphere. The application for other problems involves an appropriate change in the form of the Green's function H_b. The formulation is

$$S_{3D}(\sigma N, x, y) = S_0(\sigma N, x, y) + \sigma \int dN' dx' dy' \Omega(N') S_{3D}(\sigma N', x', y') H_{3D}(|N-N'|, |x-x'|, |y-y'|), \quad (a1)$$

where

$$H_{3D} = H_b(\sigma N) / 4\pi (|\vec{r} - \vec{r}'|^2) \quad (a2)$$

Approximate forms are

$$S_{1D}(\sigma N, x, y) = S_0(\sigma N, x, y) + \sigma \int dN' \Omega(N') S_{1D}(\sigma N', x, y) \int dx' dy' H_{3D}(|N-N'|, |x-x'|, |y-y'|) \quad (a3)$$

and

$$S_{3D}^A(\sigma N, x, y) = S_0^A(\sigma N, x, y) + \sigma \int dx' dy' \Omega(N) S_{3D}^A(\sigma N, x', y') \int dN' H_{3D}(|N-N'|, |x-x'|, |y-y'|), \quad (a4)$$

where

$$S_0^A = S_{1D}(1 - \Omega(1-E)).$$

Useful identities are

$$\int dx dy S_{3D} = \int dx dy S_{3D}^A = \int dx dy S_{1D} \quad (a5)$$

and

$$\sigma \int dN S_{3D} = \sigma \int dN S_{3D}^A. \quad (a6)$$

Appendix B: Nominal Arc Model

The nominal arc was assumed to move out of the north at $V_A = 3 \text{ km/min.}$ and it was assumed to have stopped and stabilized its motion for two minutes prior to the time for which the calculations on Figure 2-1 apply. The nominal arc spatial structure is modeled on the basis of structure observed in the 3/27/73 arc in the ICECAP measurements program. In Fig. B1 we show the deposition at arc center $q_H(z)$ and at the point of rocket penetration $q_{up}(z)$ for the March 27, 1973 BB73 rocket measurement of $4.3 \mu\text{m}$ auroral zenith radiance. The brightness of the 3914 \AA aurora is 95 and 15 kR respectively for these two deposition profiles. The deposition shapes q_H and q_{up} are discussed in more detail by Kumer in AFCRL-TR-74-0334. In order to form a nominal aurora of 30 kR 3914 \AA brightness, 105 km altitude peak in deposition, and 15 km width, we utilize

$$q(z, 0) = \frac{30}{95} q_H(z + 5)$$

and

$$q(z, x_1) = \frac{30}{95} q_{up}(z - 5)$$

where $x_1 = 7 \text{ km} \times \sqrt{\ln(95/15)} = 9.5 \text{ km}$. The deposition then in the arc at altitude z and position x is given by

$$q(z, x) = q(z, 0) e^{-(x/\alpha(z))^2}$$

where $\alpha(z) = x_1 / \sqrt{\ln(q_H(z)/q_{up}(z))}$.

Arc motion and winds are accounted for as follows

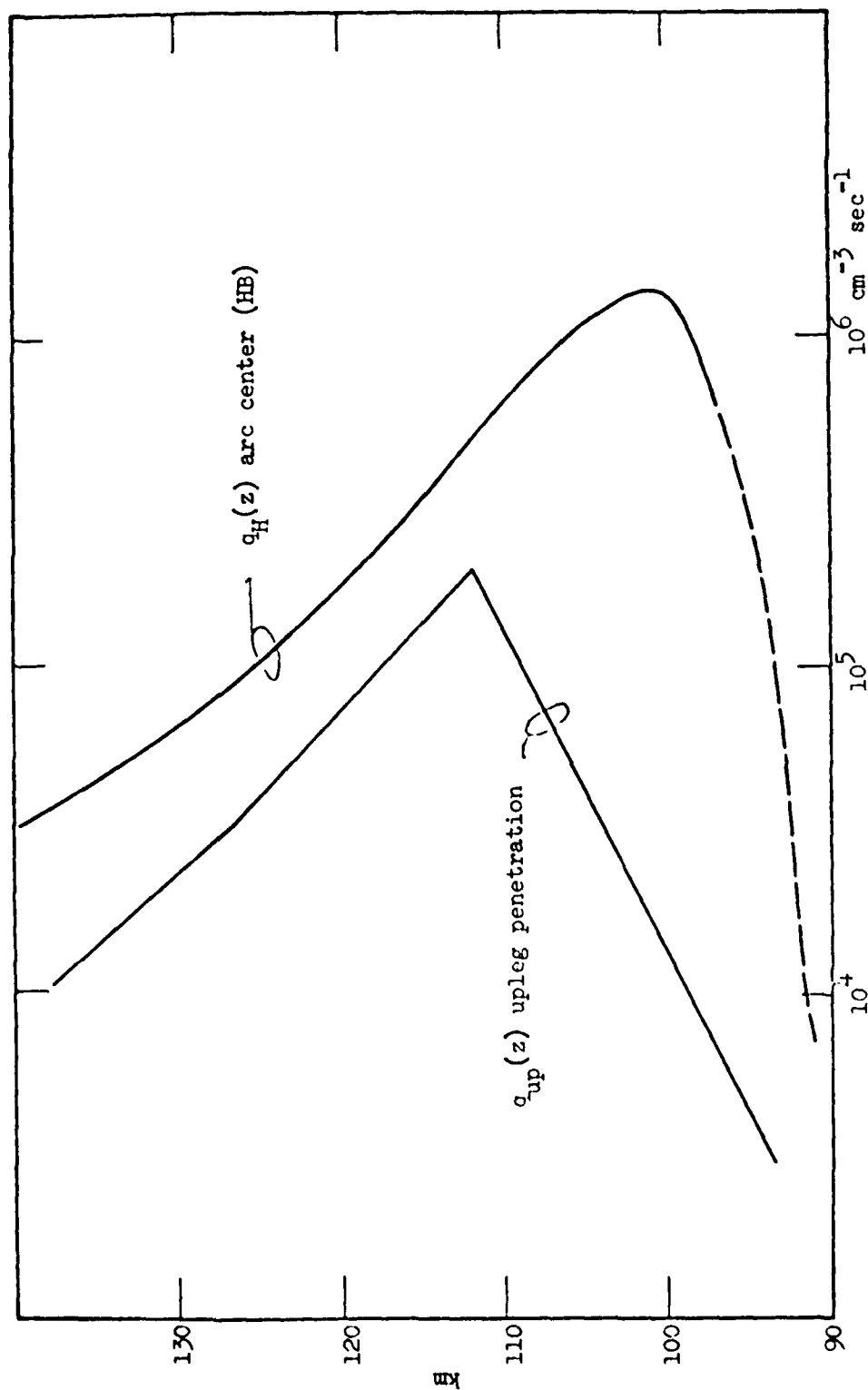


Figure B1. Models for $q(z)$ at the upleg penetration point $q_{\text{up}}(z)$ and at arc center $q_H(z)$ for the March 27, 1973 BB73 rocket shot (see AFRL-TR-74-0334 for more discussion of q_{up} and q_H).

$$q(z, x') = q(z, 0)e^{-(x'/\alpha(z))^2}$$

where

$$x' = x - (V_A - V_W(z))(t+2)$$

for $t < -2$ min. before stabilization time and

$x' = x + V_W^{(z)}(t+2)$ after arc stabilization time. The wind fields $V_W(z)$ measured by tracking a TMA release on the 3/23/73 date by Faire and Bettinger (private communication, 1976) are shown on Figure B2.

The $S_0(\sigma N, x)$ that are shown on Figure 2-1 in the text are calculated by the STDA method (Kumer, Equation (7) in AFCRL-TR-74-0334, 1974)

$$S_0(\sigma N, x) = \epsilon f(z) \int_{-\infty}^0 \tau^{-1} dt e^{t/\tau} q(z, x')$$

where $\tau(z)$ is the CO_2 4.3 μm relaxation time given by the curve EFA, Q_W that is shown in Figure 1 of the publication theory of the CO_2 4.3 μm aurora and "Related Phenomena" by Kumer (1977a) and where ϵ and $f(z)$ are defined in the report AFCRL-TR-74-0334. Here we used $\epsilon = 10$ N_2 vibration quanta/ion pair.

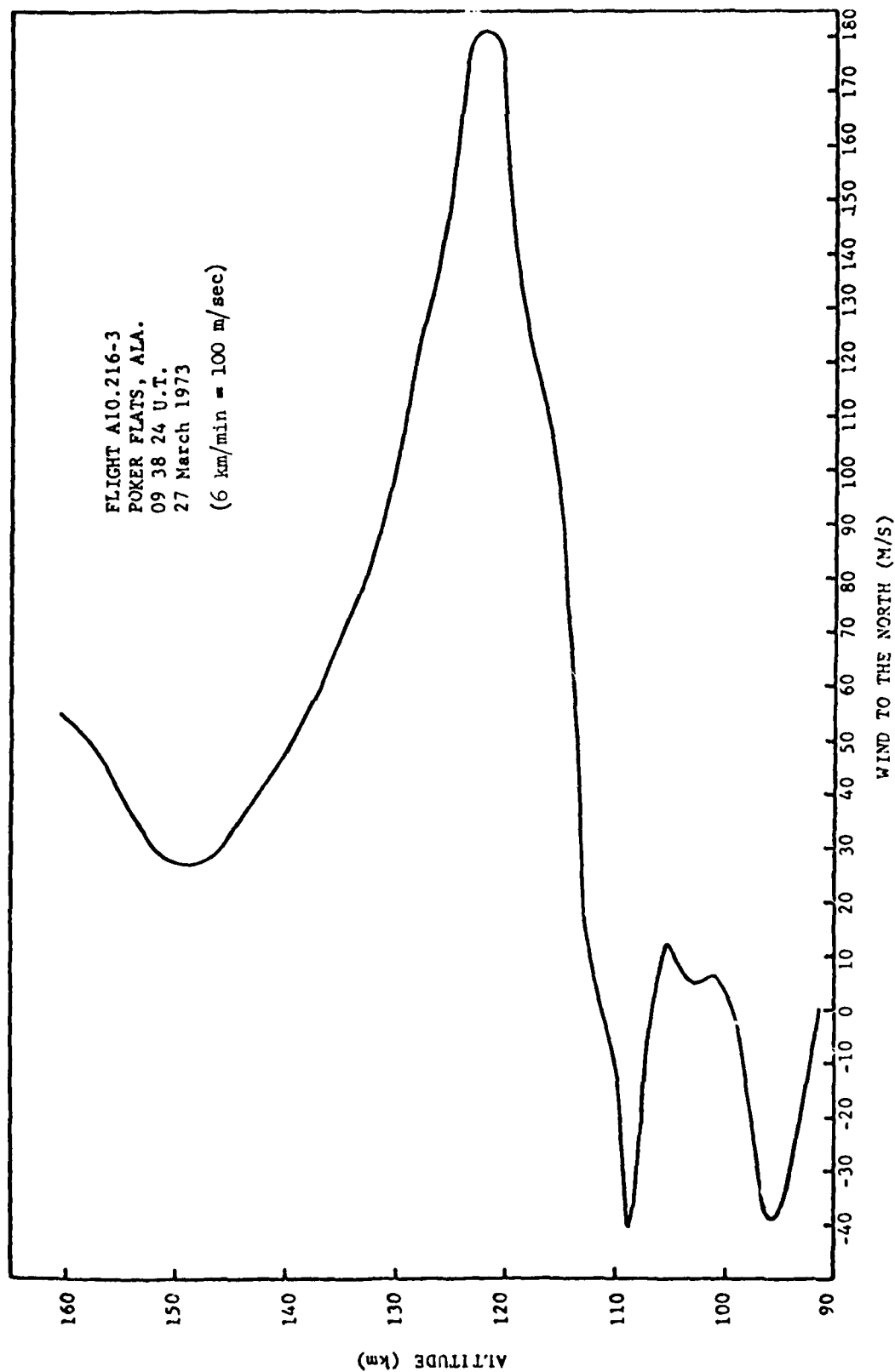


Figure B2. Preliminary wind speed data kindly provided by Faire, Bettinger, et al.

Appendix C: Procedure for Rapid Convergence

Equations such as eq.(2-1) must be discretized to a matrix formulation (see KJ) in order to obtain a solution. The matrix formulation of eq. (2-1)

$$S = S_0 + HS \quad (C1)$$

or

$$(1-H)S = S_0. \quad (C2)$$

The solution is then

$$S = GS_0 \quad (C3)$$

where

$$G = (1-H)^{-1}. \quad (C4)$$

If there are too many mesh points, it is not practical to solve for G. In this case, we must use an iterative technique. We use a trial solution

$S' = S + \delta$ where S and δ are unknown. After n iterations of eq. (C1), we get

$$S_n = S + H^n \delta. \quad (C5)$$

For any physically realistic radiation transport H,

$$H^n \rightarrow 0 \text{ as } n \rightarrow \infty. \quad (C6)$$

Thus, satisfactory convergence is achieved if we iterate enough times.

If $H^n \rightarrow 0$ quite slowly as n increases, it could be expedient to attempt an iteration scheme which provides more rapid convergence with increasing n.

For example, we may use an approximate inverse matrix G' given by

$$G' = G - K, \quad (C7)$$

where G and K are unknown, and go through the iteration scheme

AD-A084 940

LOCKHEED MISSILES AND SPACE CO INC PALO ALTO CA PALO --ETC F/8 17/5
MULTIDIMENSIONAL TIME-DEPENDENT STRUCTURE AND MECHANISMS FOR NO--ETC(U)
AUG 79 J B KUMER F19628-76-C-0209

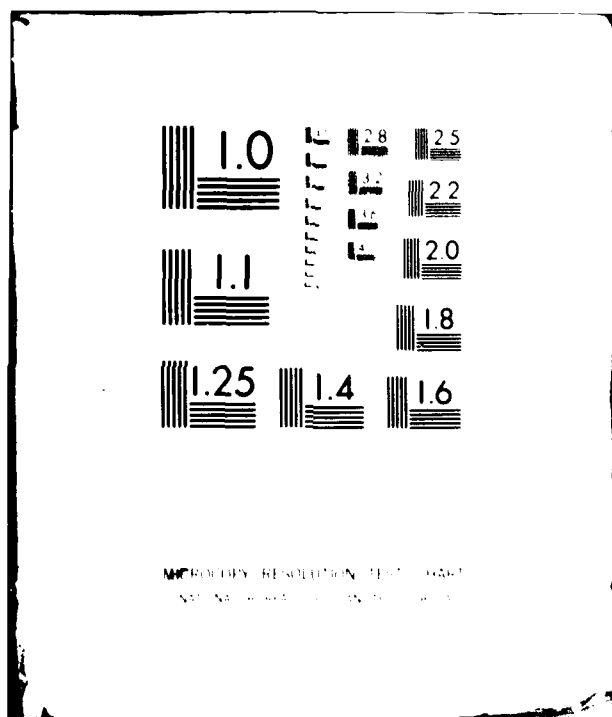
UNCLASSIFIED

AF6L -TR-79-0224

NL

2 2
A-1
A-11-101

END
DATE
FILMED
7-80
DTIC



$$S_F = S_O + HS' = S + F\delta, \quad (C8)$$

$$(1-H)\delta = S' - S_F, \quad (C9)$$

$$S_1 = S' - G'(1 - H)\delta$$

$$S_1 = S + K\delta, \quad (C10)$$

and then, after n iterations,

$$S_n = S + K^n \delta. \quad (C11)$$

If $K^n \rightarrow 0$ appreciably faster than $H^n \rightarrow 0$ with increasing n , then more rapid convergence is achieved if we use the iteration scheme given by eq. (C7) through (C11) rather than simple iteration of eq. (C1).

For the solution of equation (2-1), we found the approximation

$$G' = 1/(1-H_{11})$$

to be effective for achieving rapid convergence via the interaction scheme of eqns. (C7) through (C11). With this approximation for G' , 30 iterations of eq. (C7) through (C11) were required to achieve satisfactory convergence. However, 130 simple iterations of eq. (C1) were required to attain comparable convergence. The trial solution $S^O = S_{2D}^A$ was used in both cases. The scheme of eqns. (C7) through (C11) saved in computer time a factor 0.23 over simple iteration of eq. (C1).

In order to achieve satisfactory convergence, we required that

$$\delta_n \equiv |S_{n+1} - S_n| \leq 10^{-5} \times S_{0 \max}$$

holds for all elements δ_n where $S_{0 \max}$ is the largest element of the inhomogeneous vector S_0 . This is reasonable when one considers that $\int dx \delta_n \equiv \int dx (K^n \text{ or } H^n) \delta = 0$ is an identity if the initial trial solution is given by S_{2D}^A . This is true since $\delta = S_{2D}^A - S$ so that $\int dx \delta = 0$ [by the identity(2-5) in the text]. The quantities H^n and K^n must be functions of $|x - x'|$. Next, we consider that $\int dx dx' g(|x - x'|) \delta(x') = G \int dx' \delta(x') = 0$ where $G = \int dx g(|x - x'|)$ and, therefore, $\frac{d}{dx} G = 0$. Hence $\int dx H^n \delta = \int dx K^n \delta = 0 = \int dx (S_n - S)$.

APPENDIX D

CALCULATIONS FOR SPATIAL EXCEED

Introduction: In this section we provide the details of our calculation of estimates R^I , R^{II} and R_{NO+} that are shown in table 4-1 of the text.

Problem Definition for CO₂ Emission: The radiation transport problem is essentially 3 dimensional (3D). As yet we have not developed calculational facility to deal with 3D problem, however, for this study we used a version of the 3D approximation as described in our paper "Approximate and Exact Technique for Multidimensional Radiation Transport in a Plane Parallel Atmosphere; Application to the 4.3 μ m Auroral Arc" (Kumer, J. Quant. Spectrosc. and Radiat. Transfer 19, 649, 1978).

We approximated the deposition by the rectangular geometry described in chapter 4. Next we generated time dependent 1D solutions S_{1D} (see Appendix A) for initial electron gun induced vibrational excitation of CO₂ (call it S_{1D}^I) and for initial excitation of N₂ (call it S_{1D}^{II}) by methods described in our paper "Theory of the CO₂ 4.3 μ m Aurora and Related Phenomena" (Kumer, J. Geophy. Res. 82, 2203, 1977a). The inhomogeneous terms which are required to generate S_{1D}^I (these are defined in the paper just cited) were

$$\eta_1 = \frac{120 \text{ kw} \times (1 \text{ ev}/1.6 \text{ E-22 kw})(10 \text{ quanta/ionization})}{(7\text{E3 cm} \times 2 \text{ E3 cm} \times 1 \text{ cm})(35 \text{ ev/ionization})(N_2)}$$

on the interval $90 < z < 90.0 \text{ km}$, and $\eta_1 = 0$ elsewhere, $\eta_{N_2} = 0$ everywhere. The time dependence of $\eta_1(x, z)$ is given by $\eta_1(z) \neq 0$ for $-10 \text{ m} < vt < 10 \text{ m}$ where x measures horizontal distance perpendicular to the magnetic field and $v = 0.6 \text{ km/sec}$. In order to compute S^{II} it is merely necessary to interchange the identities of η_1 and η_{N_2} . Thus we are assuming that the electron gun excitation efficiency of N_2^+ and $CO_2(v_3)$ are identical (i.e., $\epsilon_{N_2} = \epsilon_{CO_2}$). This is legitimate for the purpose of estimating the EXCEDE signature for these 2 mechanisms. Performance of the experiment should ideally result in the actual determination of the absolute excitation efficiencies for both species.

Some representative solutions S_{1D}^I and S_{1D}^{II} are shown in table D.1. These solutions show that S_{1D}^{II} forms a DC trail in the predosed region (PR) just as expected, and that emission due to S_{1D}^I is essentially prompt, again as is expected.

In addition in the predosed region radiation transport produces a signal in the 70 m altitude region which is directly below the 70 m predosed region. This transport signal is reduced by about a factor 10 from that in the predosed region itself. We will show below that the transport signal is comparable with the ambient radiance level one expects at 90 km. In addition there is a noticeable gradient across this 70 m transport region.

Three Dimensional Transport Effects: Since emission in the dosed and predosed regions is essentially the first emission for a given quantum, the effects of 3D multiple absorption and emission (scattering) in the dosed and predosed regions will be negligible. These effects will be substantial in the transport region, however, since emission in this region results from one or more scatterings. Just vertical radiation transport is accounted for in the calculation of S_{1D} , however, it is shown in appendix A that

$$\int dx dy (S_{1D} - S_{3D}) = 0$$

where S_{3D} is the exact 3D radiation transport solution. Radiance values $R(z,x)$ viewing from the side are computed from the source function $S(z,x,y)$ via an integral along the y direction (y to both the magnetic field and the velocity)

Table D.1a. One dimensional solution $S_{1D}^I(z, x)$ for mechanism I. Radiance R^I in units watts/cm²sr given by $R^I \approx \sigma [CO_2] S^I$. Also, we note here that in order to perform the calculation it was numerically convenient to use $z = 89.97$ km rather than $z = 90$ km as the lower boundary of the deposition region. However, throughout the rest of the text $z = 90$ km is taken as the lower boundary.

| z (km) | $x = 0$ | $- 6$ m | $- 26$ m, | $- 1.5$ km, | $- 167$ km |
|----------|----------|----------|-----------|-------------|------------|
| 140.00 | .1945-09 | .3204-09 | .1978-09 | .1569-08 | .3852-09 |
| 107.28 | .2428-09 | .4079-09 | .2641-09 | .2043-08 | .5042-09 |
| 98.88 | .3820-09 | .6552-09 | .4418-09 | .3383-08 | .8701-09 |
| 95.12 | .6458-09 | .1069-04 | .6262-09 | .5297-08 | .1384-08 |
| 92.57 | .1265-04 | .1905-04 | .7623-09 | .8149-08 | .1944-08 |
| 91.02 | .2896-04 | .3817-04 | .8247-09 | .1247-07 | .2419-08 |
| 90.23 | .7290-04 | .8481-04 | .8255-09 | .1912-07 | .2783-08 |
| 90.04 | .8815-03 | .8967-03 | .8297-09 | .5875-07 | .3942-08 |
| 90.02 | .8939-03 | .9093-03 | .8299-09 | .6023-07 | .3966-08 |
| 89.99 | .9041-03 | .9199-03 | .8294-09 | .6173-07 | .3982-08 |
| 89.95 | .1226-03 | .1360-03 | .8170-09 | .2500-07 | .2986-08 |
| 89.92 | .1077-03 | .1207-03 | .8131-09 | .2367-07 | .2941-08 |
| 89.90 | .1008-03 | .1137-03 | .8104-09 | .2304-07 | .2919-08 |
| 88.10 | .1016-04 | .1473-04 | .5333-09 | .1081-07 | .2503-08 |
| 83.81 | .6394-06 | .1033-05 | .5778-06 | .2409-08 | .1470-08 |
| 80.21 | .9932-07 | .1512-06 | .6809-07 | .5822-09 | .6845-09 |
| 77.67 | .2913-07 | .4203-07 | .1573-07 | .2149-09 | .3466-09 |
| 76.05 | .1342-07 | .1882-07 | .6415-08 | .1162-09 | .2180-09 |
| 75.20 | .8964-08 | .1241-07 | .4072-08 | .8539-10 | .1759-09 |
| 71.34 | .1533-08 | .2039-08 | .5948-09 | .2199-10 | .4292-10 |
| 62.98 | .7115-10 | .9215-10 | .2575-10 | .2653-11 | .3731-11 |
| 57.21 | .9267-11 | .1197-10 | .3548-11 | .6905-12 | .5126-12 |
| 53.63 | .2564-11 | .3320-11 | .1065-11 | .2967-12 | .1358-12 |
| 51.42 | .1173-11 | .1524-11 | .5230-12 | .1774-12 | .5839-13 |
| 50.26 | .7916-12 | .1030-11 | .3686-12 | .1372-12 | .3592-13 |
| 50.00 | .7209-12 | .9384-12 | .3364-12 | .1031-12 | .6808-14 |

Table D.16. One dimensional solution $S_{1p}^{II}(z,x)$ for mechanism II.
Radiance R^{II} is given as units watts/cm² sr by $k_{WR}^{II} = \sigma[CO_2]S^{II}$.

| z(km) | x = 0, | - 6 m, | - 26 m, | -1.5 km, | - 167 km |
|--------|----------|----------|----------|----------|----------|
| 140.00 | .4746=06 | .1337=09 | .9513=09 | .6769=09 | .1472=09 |
| 107.28 | .5797=06 | .1670=09 | .7118=09 | .8807=09 | .1923=09 |
| 98.88 | .8914=06 | .2628=09 | .1158=04 | .1441=04 | .3265=09 |
| 95.12 | .1937=05 | .4413=05 | .1818=04 | .2204=04 | .5177=09 |
| 92.57 | .3225=05 | .8565=05 | .2960=04 | .3384=04 | .7531=05 |
| 91.02 | .8317=05 | .1944=04 | .5334=04 | .5713=04 | .1014=04 |
| 90.23 | .2421=04 | .5071=04 | .1093=03 | .1115=03 | .1331=04 |
| 90.04 | .4201=03 | .7147=03 | .1075=02 | .1048=02 | .4051=04 |
| 90.02 | .4262=03 | .7258=03 | .1094=02 | .1065=02 | .4062=04 |
| 89.99 | .4322=03 | .7365=03 | .1111=02 | .1081=02 | .4052=04 |
| 89.95 | .4350=04 | .8688=04 | .1706=03 | .1711=03 | .1590=04 |
| 89.92 | .3748=04 | .7581=04 | .1523=03 | .1533=03 | .1524=04 |
| 89.90 | .3474=04 | .7074=04 | .1438=03 | .1450=03 | .1492=04 |
| 89.10 | .2714=05 | .6906=05 | .2241=04 | .2571=04 | .2930=05 |
| 83.81 | .1564=06 | .4375=06 | .1733=05 | .2252=05 | .4379=05 |
| 80.21 | .2573=07 | .6763=07 | .2408=06 | .3240=06 | .1795=05 |
| 77.67 | .8319=08 | .1961=07 | .6443=07 | .8971=07 | .8542=06 |
| 76.05 | .3431=08 | .9368=08 | .2833=07 | .4112=07 | .5212=06 |
| 75.20 | .1853=08 | .6564=08 | .1856=07 | .2776=07 | .4141=06 |
| 71.34 | .3375=09 | .1208=08 | .2966=08 | .5004=08 | .1010=06 |
| 62.98 | .1931=10 | .5680=10 | .1329=09 | .3670=09 | .9334=08 |
| 57.21 | .2798=11 | .6826=11 | .1740=10 | .7829=10 | .1434=08 |
| 53.63 | .8291=12 | .1921=11 | .4876=11 | .3103=10 | .4063=09 |
| 51.42 | .3819=12 | .8777=12 | .2254=11 | .1797=10 | .1800=09 |
| 50.26 | .2597=12 | .5868=12 | .1533=11 | .1372=10 | .1120=09 |
| 50.00 | .2400=12 | .5230=12 | .1392=11 | .1154=10 | .2138=10 |

$$4\pi R_{3D} = \int_y^\infty \sigma [CO_2] dy' \Omega(z) T(\sigma[CO_2] |y-y'|) S_{3D}$$

so that in the case of S_{1D}^{II} where $\frac{\partial}{\partial x} S_{1D} \approx 0$ for $x < - .01$ km we therefore, expect that $R_{1D}^{II} \approx R_{3D}^{II}$ for $x < - .01$ km. On the other hand since S_{1D}^I is concentrated in the instantaneous deposition region (IDR) we expect that $R_{1D}^I > R_{3D}^I$ for $- .01 < x < .01$ km and that $R_{1D}^I < R_{3D}^I$ on the rest of the x axis.

In order to quantitatively estimate these effects we attempted to calculate the approximate 3D solution S_{3D}^A which is defined in Appendix A. Unfortunately the scope of the effort did not permit the development of a working computer program for the calculation of S_{3D}^A for application to EXCEDE planning.

We did , however, develop a working computer program which uses a diffusive approach to the problem. This approach is less accurate but easier to implement than is calculation of S_{3D}^A by solution of the lateral 2D radiative transport integral equation (a4) in appendix A. In order to calculate S_{3D}^{AD} the diffusion approximation solution, we perform the following calculation

$$S_{3D}^{AD}(x,y) = \int_{-\infty}^{x_0} dx' \int_{-\infty}^{\infty} dy' G_D(\xi,t) S_{1D}(x') \delta(y')$$

where

$$x_0 = .01 \text{ km},$$

$$G_D = \frac{1}{4\pi a t} e^{-\zeta^2/4at},$$

$$\zeta^2 = (x-x')^2 + y^2,$$

$$t \approx (x_0 - x')/v.$$

The value $a \approx .41 \text{ km}^2/\text{sec}$ is the radiative diffusion coefficient appropriate for 90 km altitude. The derivation of this value is given in the report (Kumer, J. B., "Theoretical Estimates for the Lateral Structure in the $4.3 \text{ } \mu\text{m}$ Auroral Arc," Draft Report in Utah State University Subcontract SC-75-019, Authorized by Government Contract F19628-73-C-0048; February, 1976). This approximation conserves the identity

$$\int dx dy S_{3D} = \int dx dy S_{1D} = \int dx dy S_{3D}^{AD}.$$

Results for CO_2 and $\text{N}_2 \rightarrow \text{CO}_2$ Radiances: A plot of the radiance component $R^I(x)$ which results from direct electron beam excitation of $\text{CO}_2(v_3)$ (mechanism I) is shown on fig. D-1. The approximate radiance calculations R_{3D}^{IAD} and R_{1D}^I are shown. These are computed from the approximate solutions S_{3D}^{IAD} and S_{1D}^I respectively. Radiance values for $z = 20 \text{ m}$ above and below $z = 90 \text{ km}$ (which is the lower boundary of deposition) are shown on fig. D-1.

The estimates R_{3D}^{IAD} are shown by solid curves and R_{1D}^I by dashed curves. The label A designates the case where $z = 90 \text{ km} = + 20 \text{ m}$ and B the case where $z = 90 \text{ km} = - 20 \text{ m}$.

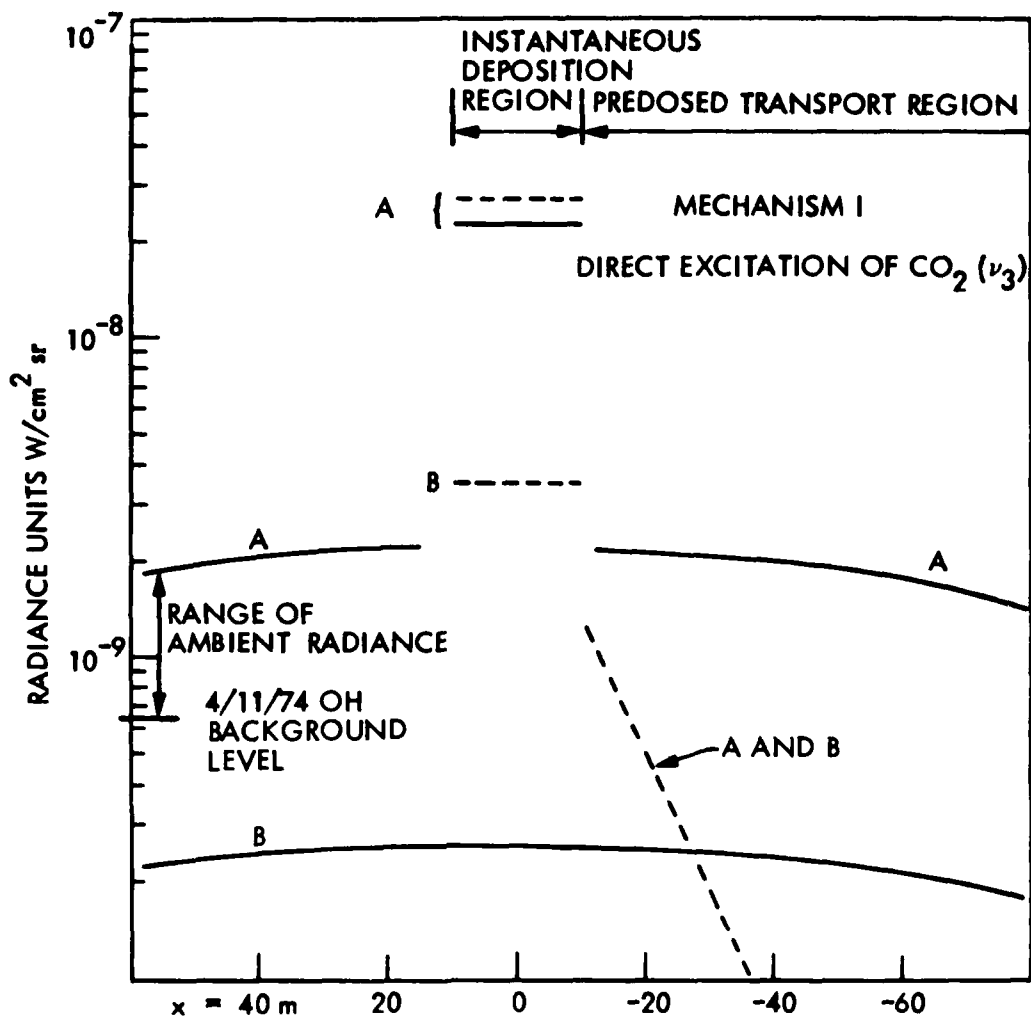


Figure D-1 The Solid Curves are our Estimates for the Mechanism I Component of Lateral $4.3\mu m$ the Radiance Profiles R^{13D}_{AD} Taken 20 m Above (Case A) and 20 m Below (Case B) the Boundary of the Dosed and Predosed Regions. The dashed curves are lateral radiance profiles R^{1}_{iD} for the Same Circumstances. These curves apply for deposition at 90 km. The difference in Cases A and B in the transport regions (which are $x > 10 m$ and $x < -10 m$) is an artifact of our approximate solution S^{AD}_{3D} as is explained in the text. We expect $R^I \approx 10^{-9}$ watts is probably fairly close to the actual value which should obtain in the transport regions.

We note that $R_{1D}^I > R_{3D}^{IAD}$ in the region IDR, just as expected on the basis of our earlier discussion. In the PDR we see that transport dominates over pre-dosing in generating R^I . Next we note a large disparity in the value of R_{3D}^{IAD} in the region ATR and PTR as compared to that in the region LTR. Intuitively we know this disparity exists in the calculations because use of the S_{3D}^{IAD} approximation does not allow for a direct contribution via the integral in equation 2-1 to S_{3D}^{IAD} in the region LTR from the initial emission which occurs in the region IDR. However, since we know $\int dN(S_{3D}^{AD} - S_{3D}) = 0$ is an identity, it seems reasonable that we take $R_{3D}^I \approx (2 \times 10^{-9} + 2 \times 10^{-10})/2 \text{ watts/cm}^2 \text{ sr} \approx 10^{-9} \text{ watts/cm}^2 \text{ sr}$ to obtain near to the region IDR in all the transport regions, PTR, ATR and LTR.

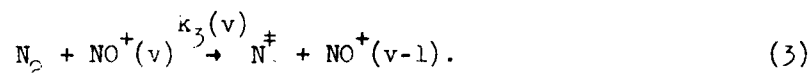
The $OH^\dagger + N_2 \rightarrow N_2^\dagger$; $N_2^\dagger + CO_2 \rightarrow CO_2(v_3)$ generated ambient $4.3 \mu\text{m}$ radiance level for horizontal viewing at 90 km, as inferred from the $4.3 \mu\text{m}$ zenith radiance data set which was obtained on 4/11/74, is also shown on fig. D-1. 4/11/74 ambient 90 km horizontal $4.3 \mu\text{m}$ radiance thus shown is probably somewhat smaller than would be expected on the average.

It could conceivably be greater by a factor 5 as is indicated on fig. D-1. However, we can in principle launch the EXCEDE experiment on an evening for which the ground based OH airglow is observed to be lower than average, and hopefully in this way, select an evening for which the ambient $4.3 \mu\text{m}$ radiance is lower than usual, as was the case on the evening of 4/11/74. In this case R^I in the transport regions will be comparable to or larger than ambient. We shall see below however, that it will probably not be possible to distinguish R^I from a much larger component R^{II} in the transport regions.

Next consider fig. D-2. Results for R^{II} are shown on fig. D-2. These results are analogous to those for R^I which are shown on fig. D-1 in that they are horizontal profiles R_{3D}^{IIAD} and R_{1D}^{II} at $z - 90 \text{ km} = \pm 20 \text{ m}$. Obviously predosing dominates in the region PR. Transport dominates the regions LTR and ATR. Near to the region IDR, but inside the regions LTR and ATR, we expect, on the basis of the same arguments that are applied to R^I in the transport regions that $R^{II} \approx 4.5 \times 10^{-9} \text{ watts/cm}^2 \text{ sr}$ should probably be close to the actual value which obtains in these transport regions. The R^{II} in the transport regions is considerably larger than R^I and is also considerably larger than the maximum expected ambient horizontal radiance value.

On figures D-3 & D-4 we show vertical cuts at $x = 26, 0$ and -26 m of R_{3D}^{IIAD} and R_{3D}^{IIAD} . These show that we can expect a variation of the order 0.5 to $1.5 \times 10^{-9} \text{ watts/cm}^2 \text{ sr}$ on the interval $0 > (z - 90 \text{ km}) > -70 \text{ m}$. It may be possible to detect a gradient of this magnitude.

Results for $\text{NO}^+(v)$ Radiance: We expect $\text{NO}^+(v)$ will be strongly quenched by



From Gordietz et al. ("Theoretical Study...Mechanisms," Mockba, 1976) we get a rate constant $k_3(1) = 4.9 \times 10^{-15} \text{ T}^{3/2}$ for reactions (2). From Tarr and Archer (DNA 3297F) we get

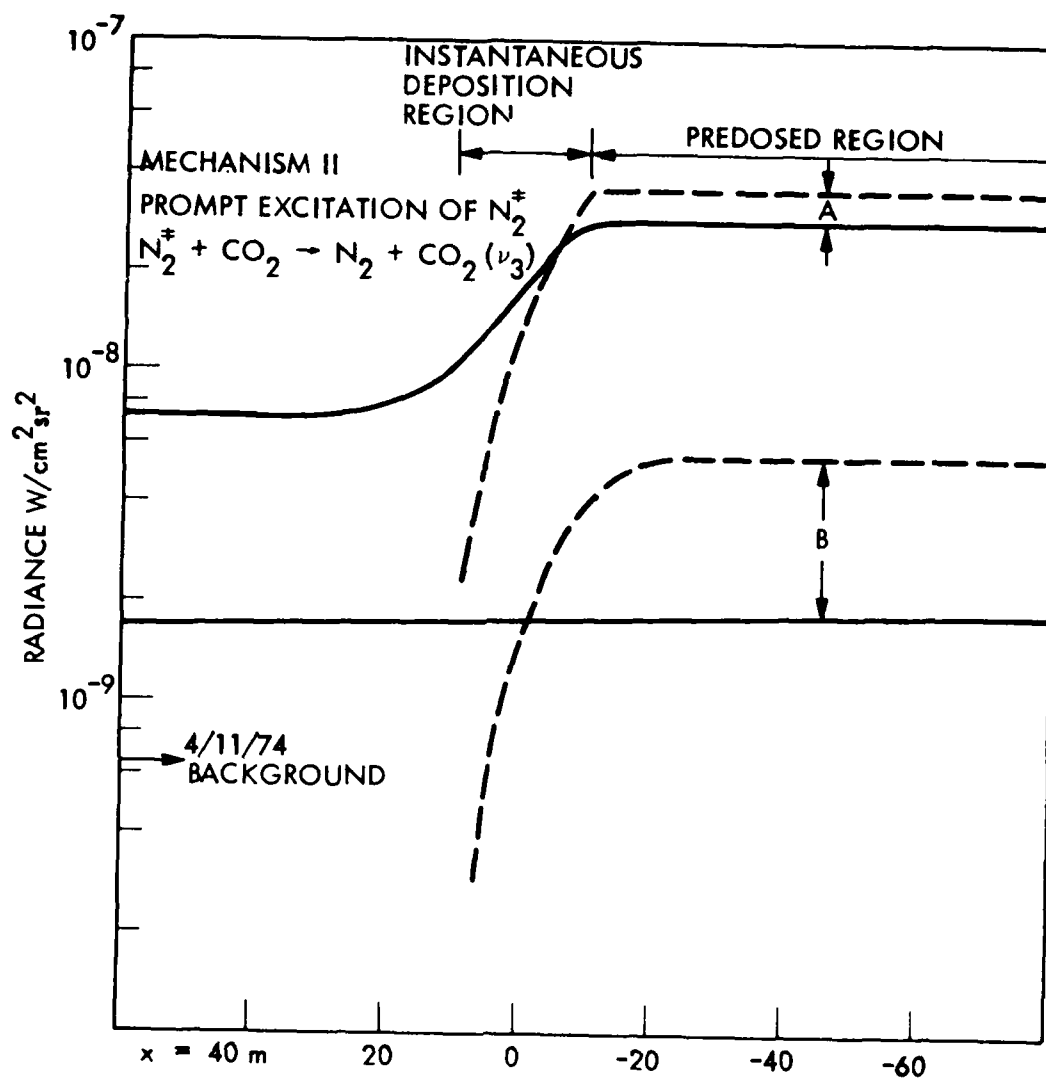


Figure D-2 Same as Figure D-1 Except in This Case the $4.3\mu m$ Radiance Components R^{II} are due to the Mechanism II, Prompt Electron Beam Induced Excitation of N_2^+ Followed by $N_2^+ + CO_2 \rightarrow N_2 + CO_2(\nu_3)$. Again, Cases A and B for R^{II} in the transport region ($x > 10 \text{ m}$) represent upper and lower limits, the actual value will be $\approx 4.5 \times 10^{-9} \text{ watts/cm}^2\text{sr}$.

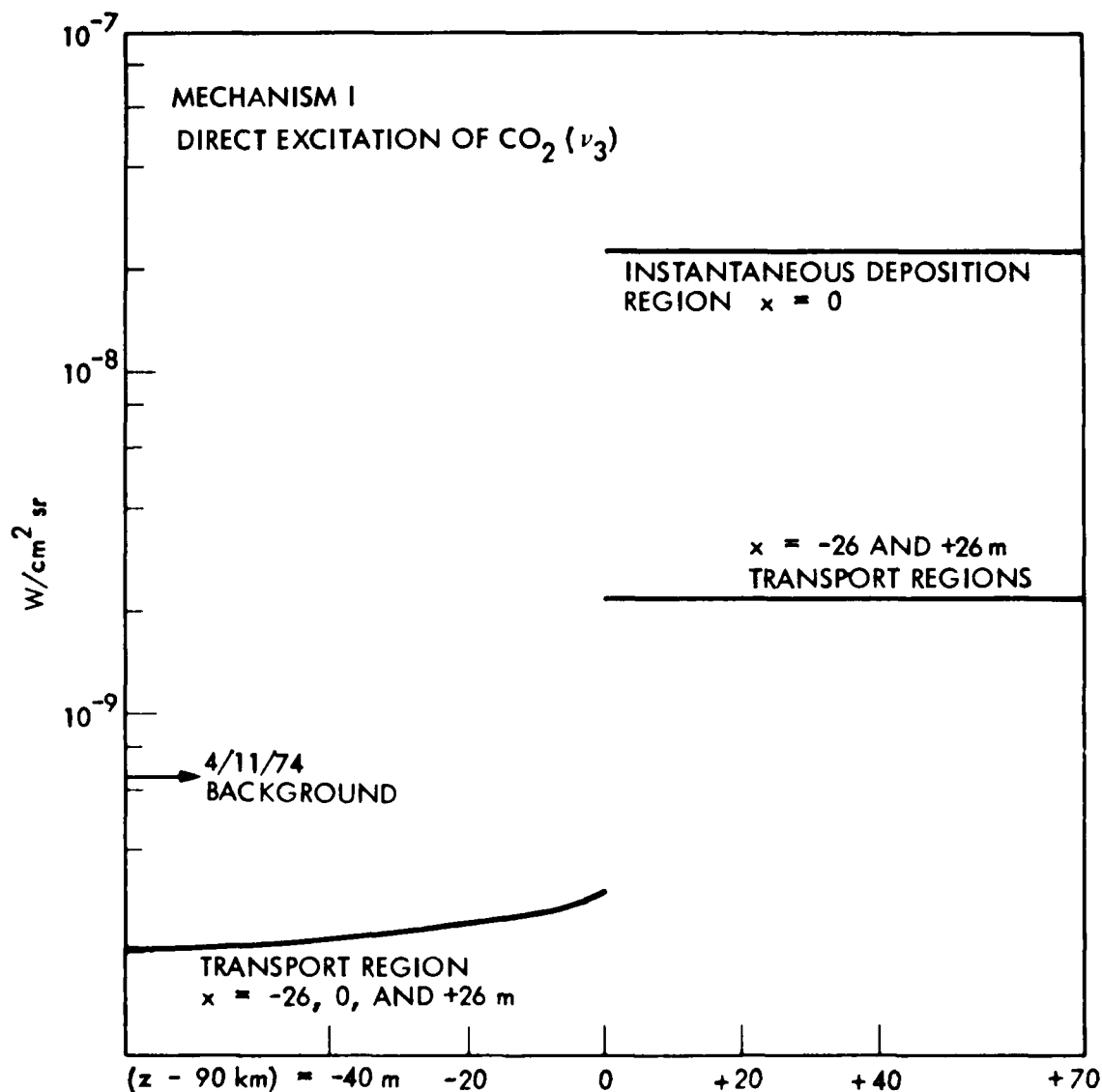


Figure D-3 Estimates R_{3D}^{IAD} for the Component of the $4.3\mu\text{m}$ Radiance Vertical Profiles Which are due to the Mechanism I. These vertical cuts are for $x = -26, 0$ and 26 m. For $z < 90$ km there is essentially no x variation in $R_{3D}^{IAD}(z)$. The large variation of R_{3D}^{IAD} in the transport region where $z - 90 \text{ km} > 0$ with respect to R_{3D}^{IAD} in the transport region where $z - 90 \text{ km} < 0$ is an artifact of the approximate method which is used in the calculation of S_{3D} . We expect 10^{-9} watts/cm²sr should be representative of the actual value of R^I which should obtain in both transport regions.

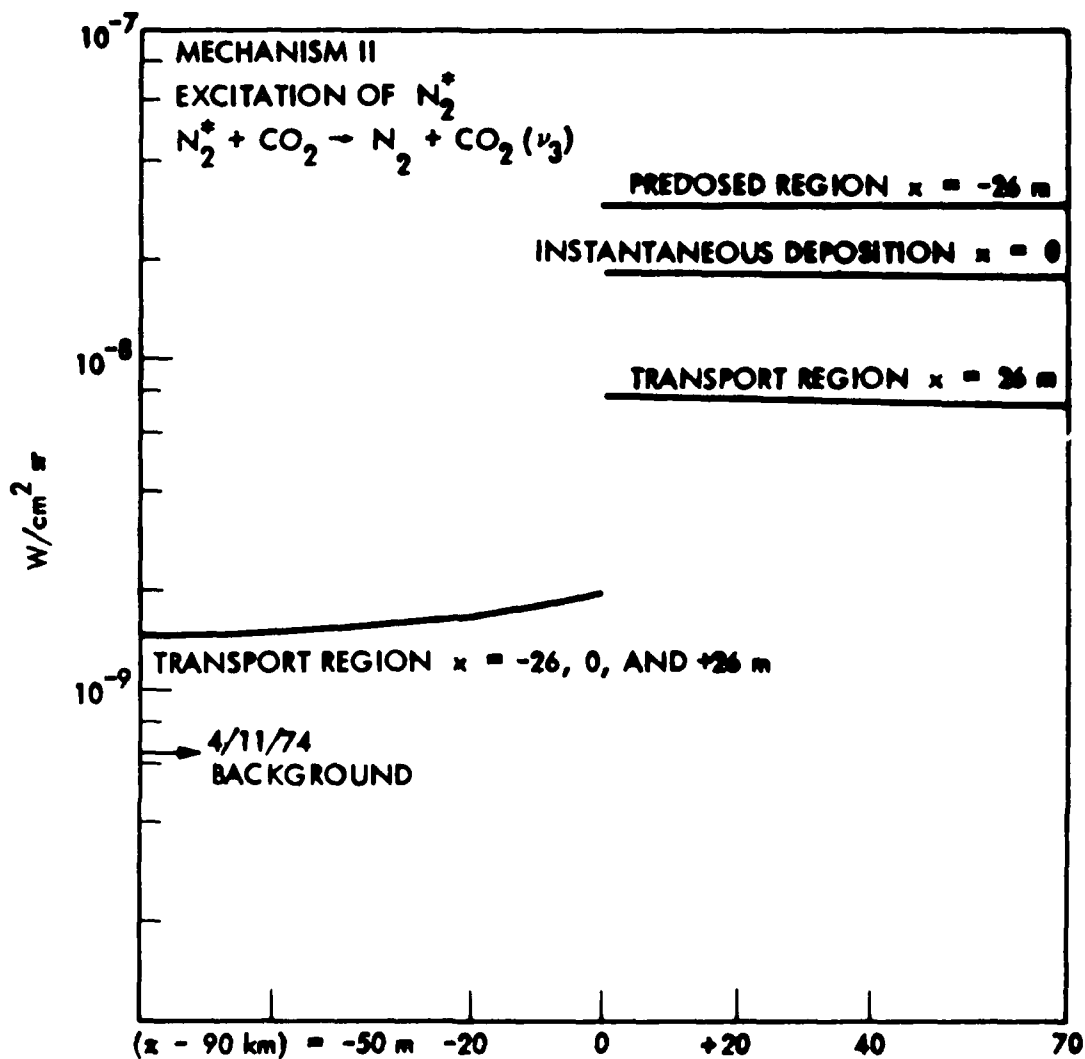


Figure D-4 Estimates R_{3D}^{IIAD} for the Component of $4.3\mu\text{m}$ Vertical Radiance Profiles Which are Due to Mechanism II, Excitation of N_2 ; $N_2 + CO_2 \rightarrow N_2 + CO_2(\nu_3)$. These vertical cuts are for $x = -26, 0$ and 26 m . The large variation of R_{3D}^{IIAD} in the transport region associated with $z - 90 \text{ km} > 0$ as compared to R_{3D}^{IIAD} in the transport region where $z - 90 \text{ km} < 0$ is an artifact of the method by which the approximate solution S_{3D}^{IIAD} is calculated. We expect $R_{3D}^{IIAD} \approx 4.5 \times 10^{-9} \text{ watts/cm}^2 \text{ watts/cm}^2 \text{ sr}$ should be near the actual radiance value in the transport region.

| $k_3(v)/k_3(1)$ | v |
|-----------------|-----|
| 1.77 | 2 |
| 1.27 | 3 |
| 0.91 | 4 |
| 0.59 | 5 |
| 0.36 | 6 |
| 0.22 | 7 |
| 0.13 | 8 |
| 0.074 | 9 |
| 0.043 | 10. |

We also get from DNA 3297F an efficiency estimate of 5 NO^+ vibrational quanta formed per ionization event. Equivalently, $\epsilon_{\text{NO}^+} = .05$ is the fraction of the deposition energy converted into NO^+ vibrational excitation. Finally, from DNA 3297F we estimate that just the NO^+ bands $3 \rightarrow 2$, $2 \rightarrow 1$ and $1 \rightarrow 0$ may be expected to contribute radiation which is overlapped with CO_2 radiation in the 4.1 to 4.4 μm region. The fraction $F_{\bar{3}}$ of the total $\text{NO}^+(v)$ emission spectrum contained in these bands is $F_{\bar{3}} \simeq 0.5$ (DNA 3297F).

From Billingsleys calculation we get $A_0^1 = 13.5/\text{sec}$ and that $A_1^2 \simeq 2A_0^1$, we assume $A_2^3 \simeq 3A_0^1$ may not be too bad an approximation. The branching ratio $B_{e/q}$ for emission rather than quenching is

$$B_{e/q} \simeq \frac{3 A_0^1}{A_0^1 + k_3(1) [N_2]}$$

and with $k_3(1) = 4.9 \text{ E-15} \times (220)^{3/2} = 1.6 \text{ E-11 cm}^3/\text{sec}$ and $[N_2] = 10^{13.747} \text{ cm}^{-3}$ at $z = 90 \text{ km}$ we get

$$B_{e/q} \approx .045$$

So finally we get

$$R_{NO^+} = \frac{1}{4\pi} \epsilon_{NO^+} F \frac{120 \text{ kw}}{DL} B_{e/q}$$

$$R_{NO^+} \approx 8 \times 10^{-7} \text{ watts/cm}^2 \text{sr.}$$

This is the value R_{NO^+} that will obtain in the region IDR. Since $k_3(1)[N_2] \approx 900/\text{sec}$ the value of R_{NO^+} will rapidly decay in the region PR such that $R_{NO^+} < R^{II}$ for $x < -14.5 \text{ m}$. Only molecular diffusion will contribute to R_{NO^+} in the transport regions, we have not as yet included molecular diffusive effects into our calculation.

Finally we emphasize that our estimate for R_{NO^+} is based on data (ϵ_{NO^+} and $k_3(v)/k_3(1)$ from DNA 3297F, $k_3(1)$ from Gordietz and A_{v-1}^v from Billingsley) which are in some cases unconfirmed. Major discrepancies in this data base could induce proportionate discrepancy in our estimate for R_{NO^+} . Indeed, analysis by Herb Mitchell of previous rocket borne electron gun induced atmospheric emissions indicates our estimate of R_{NO^+} which is based on the data base cited above, is probably too large. This point was discussed above in somewhat more detail.

In our study we did not consider in detail quenching due to $NO^+(v) + e \rightarrow N + O$ but if we take $\alpha = 3 \times 10^{-7} \text{ cm}^3/\text{sec}$ at $z = 90 \text{ km}$ we get $\alpha[e] = 540/\text{sec}$. This is comparable to $k_3(1)[N_2] = 900/\text{sec}$ so apparently recombinative quenching of $NO^+(v)$ will be important for interpreting the EXCEDE experimental $4.3 \mu\text{m}$ data. Also, we expect $\alpha(v)$ may actually be quite a bit larger than $3 \times 10^{-7} \text{ cm}^3/\text{sec}$, thus increasing the importance of recombinative quenching. Recombinative quenching is not important for the auroral case however, since the volume

ionizations rate is down by about six orders in that case, hence $\alpha[e]$ is reduced by three orders of magnitude.

Summary of Results, Discussion: The results are summarized in table 4-1.

Clearly R_{NO^+} dominates the region IDR and R^{II} dominates the transport regions and the region PR. From the data in IDR we can get ϵ_{NO^+} since $\epsilon_{NO^+} \propto R_{NO^+}$. From data in the region PR we can get ϵ_{N_2} , the efficiency for prompt high energetic electron collision induced excitation of N^+ by means other than vv transfer from $NO^+(v)$ since $\epsilon_{N_2} + \epsilon_{NO^+} \propto R^{II}$. Finally we may get some information on ϵ_{CO_2} , the prompt high energetic electron collision induced efficiency for prompt electron beam excitation of $CO_2(v_2)$ from data in the transport region since in these regions $R^I/R^{II} \approx 0.1$ based on the efficiencies we have assumed in order to generate these preliminary estimates.

Data in the region PR will help to confirm that our 1 dimensional CO_2 4.3 μm time dependent radiation transport can be applied with confidence to the nuclear case (nearly uniform x-ray patch). Data in the transport regions can guide us so that we can develop a numerically effective CO_2 4.3 μm 5 dimensional radiation transport facility for application to the nuclear case (highly structured 3 deposition region).

Finally, we need to upgrade our calculations in application to EXCEER as follows:

- Generate calculations for altitudes other than 20 km.
- Develop capability to calculate S_{3D}^A rather than the less accurate radiative diffusion approximation S_{3D}^{AD} .
- If S_{3D}^A and S_{3D}^{AD} prove to be similar we can develop a diffusive approximation

S_{3D}^D that will effectively wipe out the present disparity in our calculations for R_{3D}^{II} and R_{3D}^I in the region LTR as compared to the region ATR. Such an approximation S_{3D}^D may be necessary to adequately account for structure in the B patch.

- Utilize a more realistic geometry for the deposition.
- Account for molecular diffusion.

Finally we briefly comment on what we expect to be the major differences in the 80 and 100 km cases in comparison with the 90 km case that we have treated here. At 80 km most of the CO_2 $4.3 \mu m$ signal we see will be dominated by radiation transport effects, the region IDR will be just 7 m in length, R_{NO+} will be significantly depressed, the ambient radiance will be increasingly bothersome. At 100 km radiation transport effects will be very weak as will the ambient radiance, R_{NO+} will become much stronger.

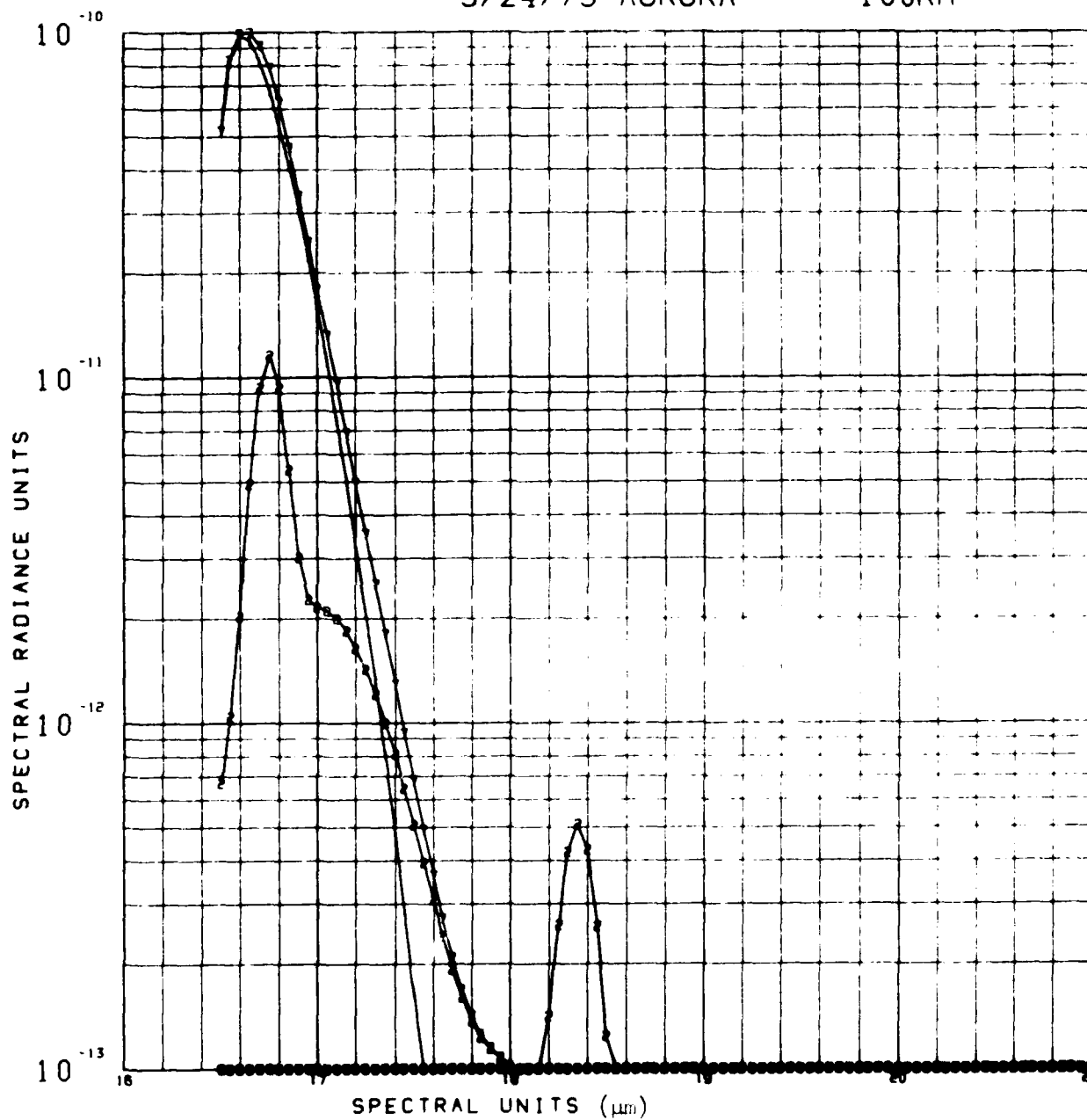
Appendix E
ESTIMATED SYNTHETIC SPECTRA

Spectral radiance $R_{\lambda n}$ denoted by the symbol $n = 1$ to 6 on the figures is due to lines in the band complex n as defined above. The symbol $n = 7$ designates the sum of spectral radiance $\sum_{n=1}^6 R_{\lambda n}$ over all band complexes.

3/24/73 AURORA

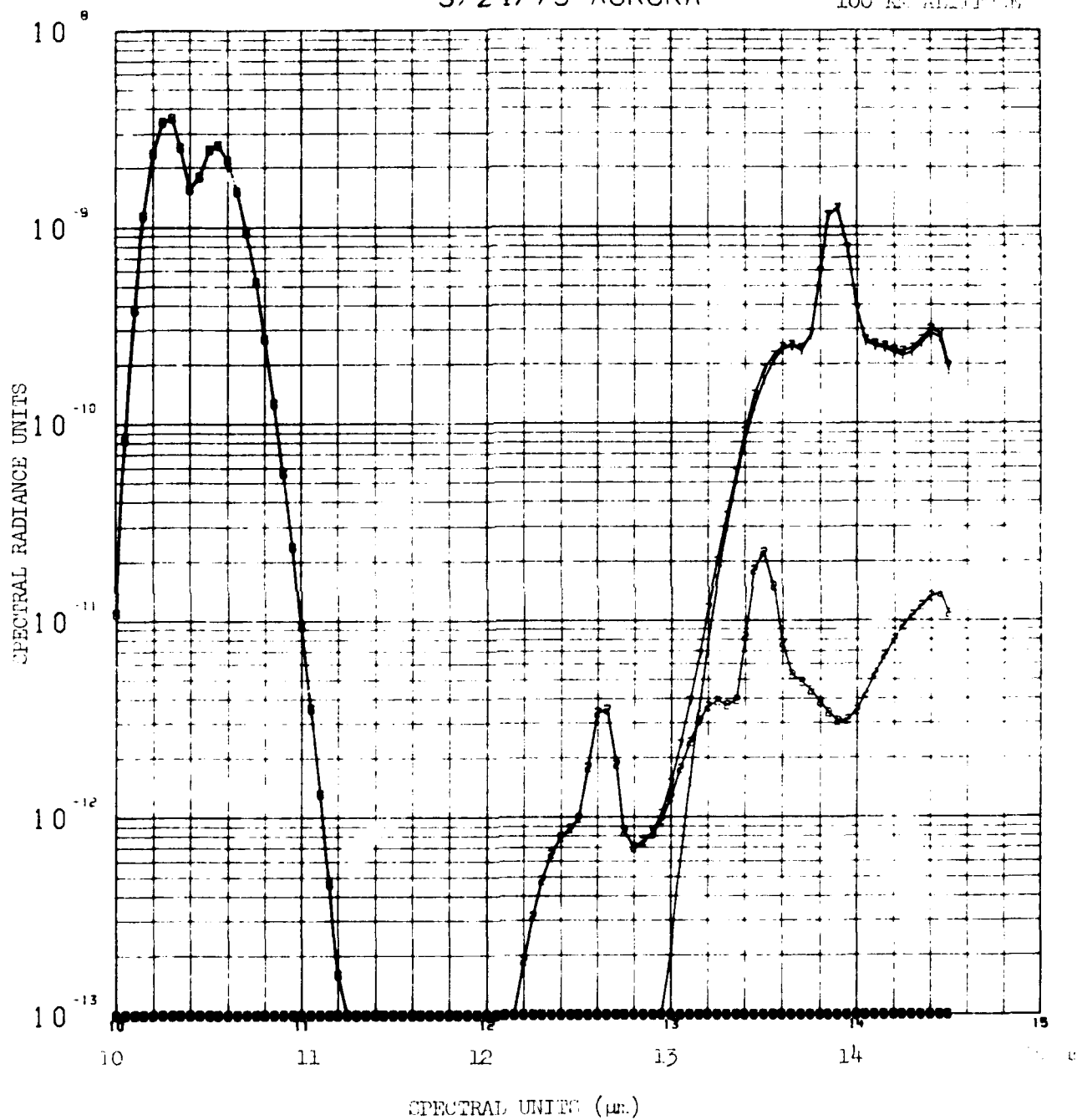
100KM

01108/SC-020
0000 0027



3/24/73 AURORA

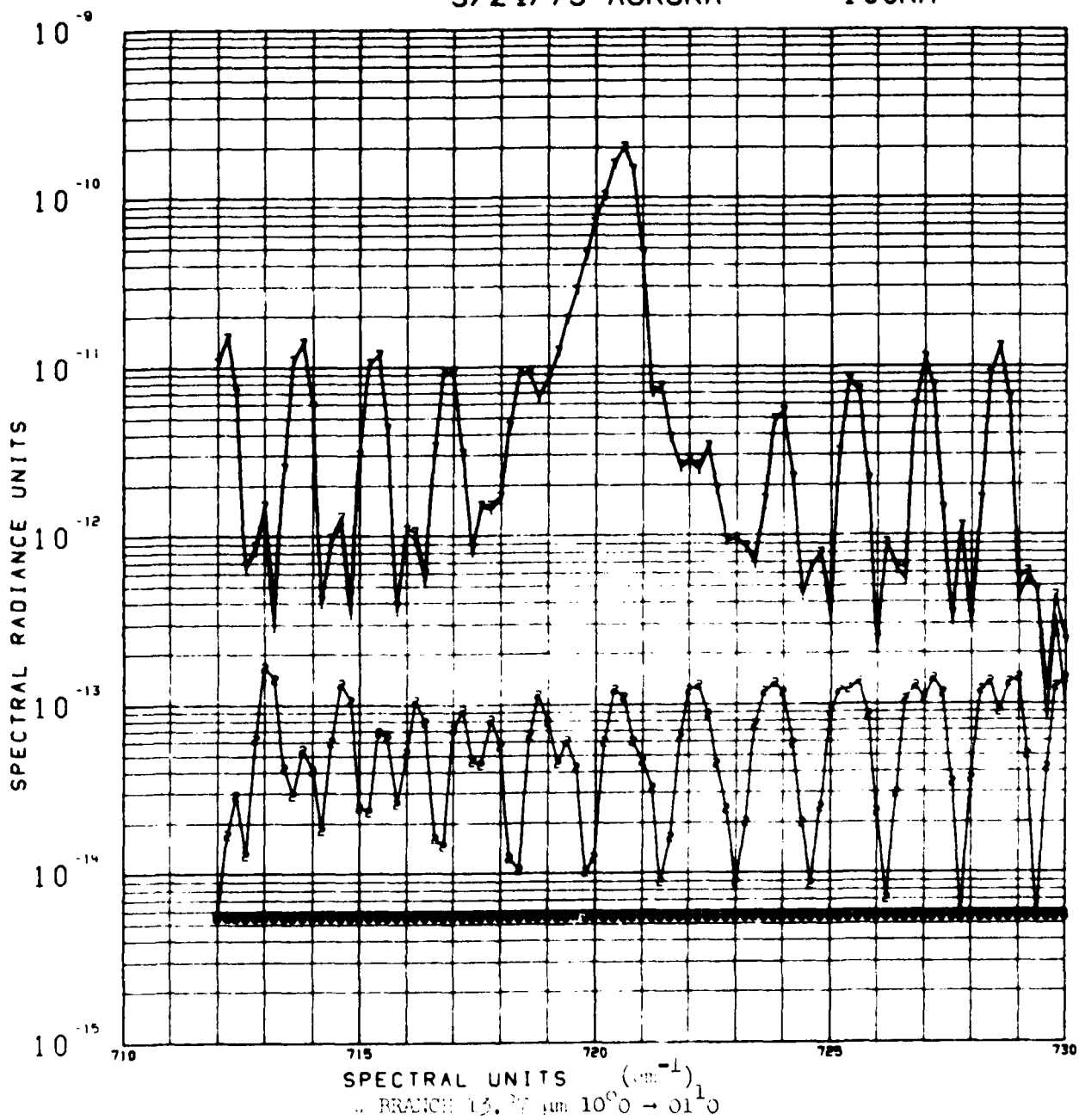
100 KM ALTITUDE



3/24/73 AURORA

100KM

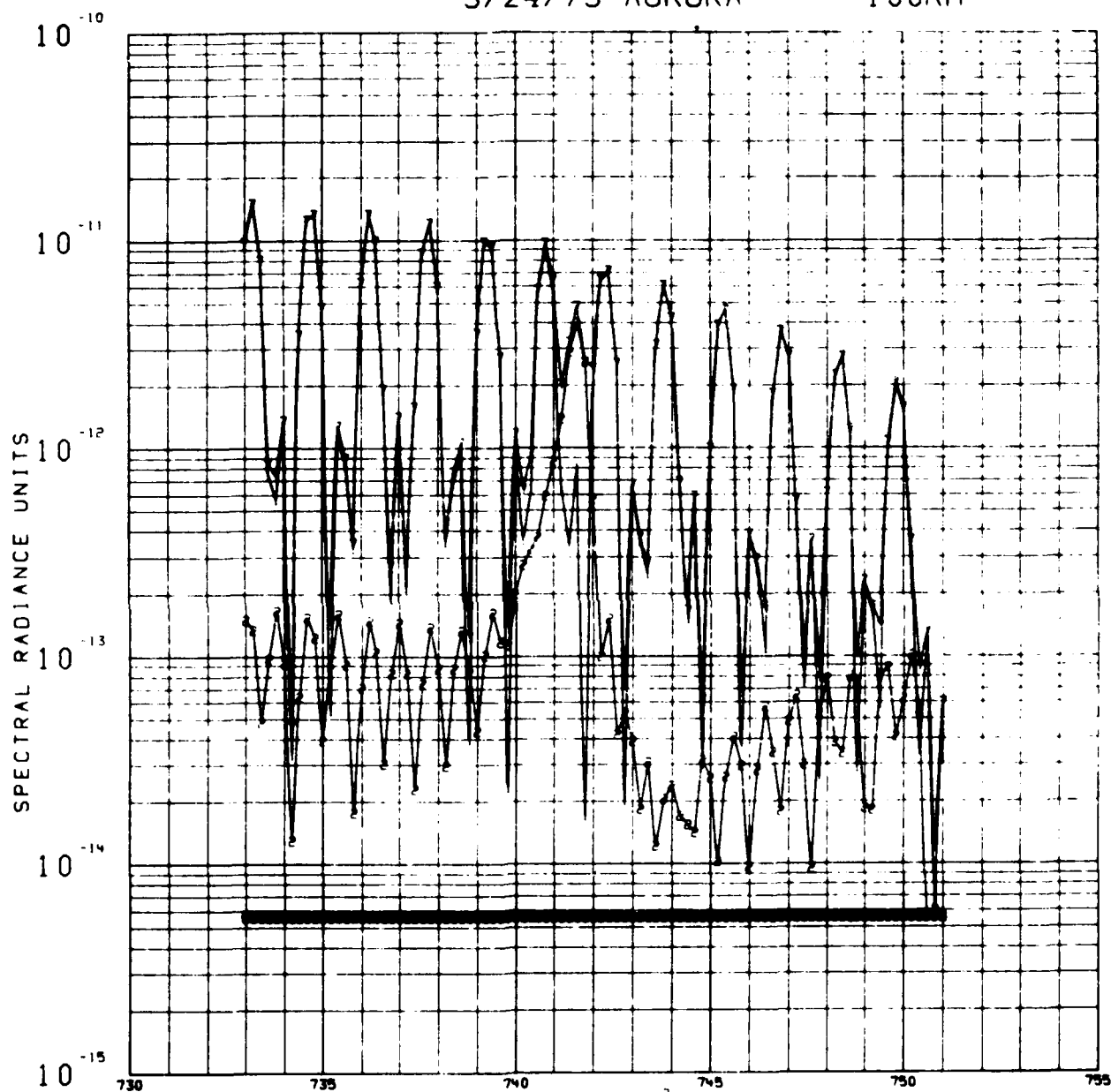
U1108/SCN020
0000 0020



3/24/73 AURORA

100KM

0008/SC-020
0002 0029



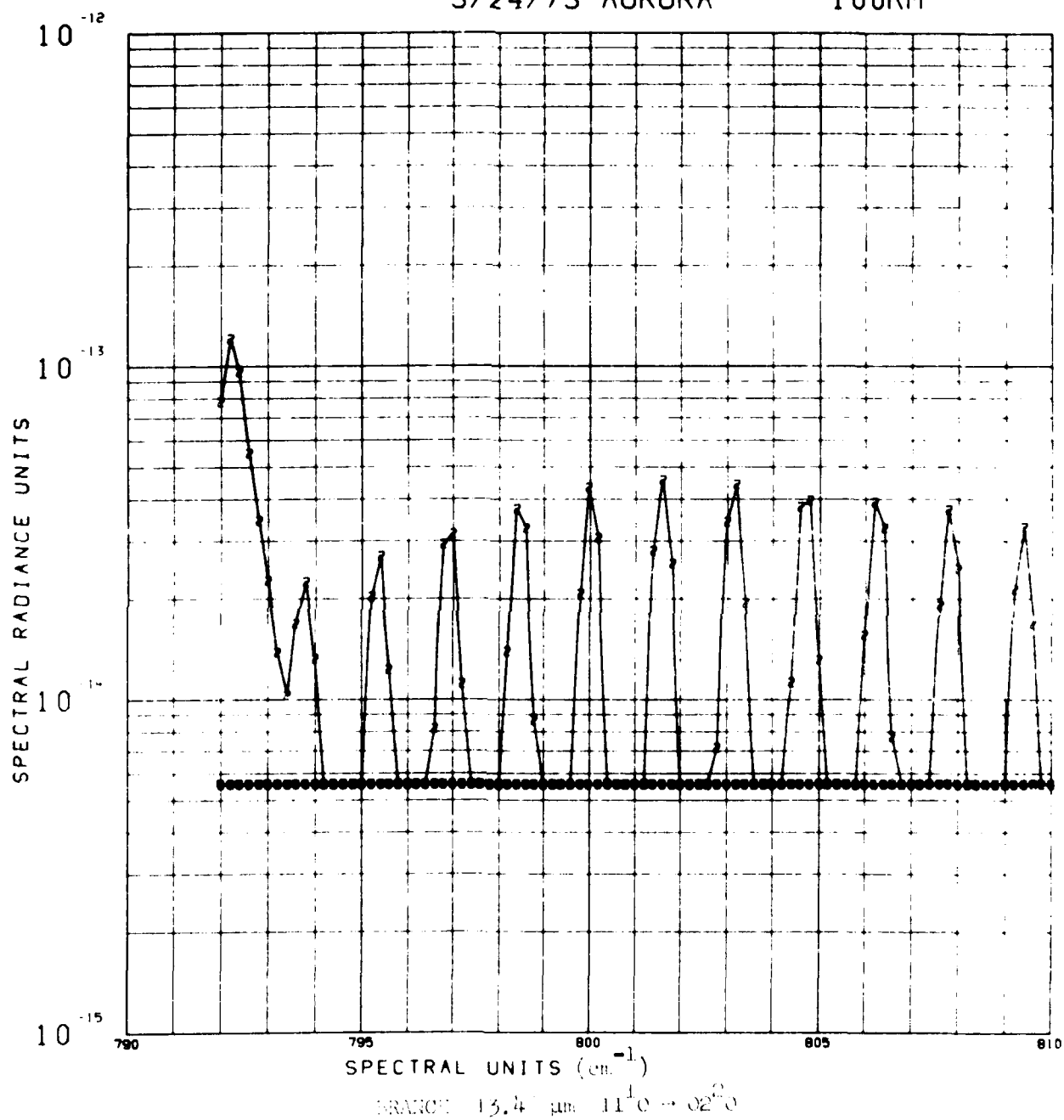
SPECTRAL UNITS (cm^{-1})

Q BRANCH $13.43 \mu\text{m}$ $11^1_0 \rightarrow 02^2_0$

3/24/73 AURORA

100KM

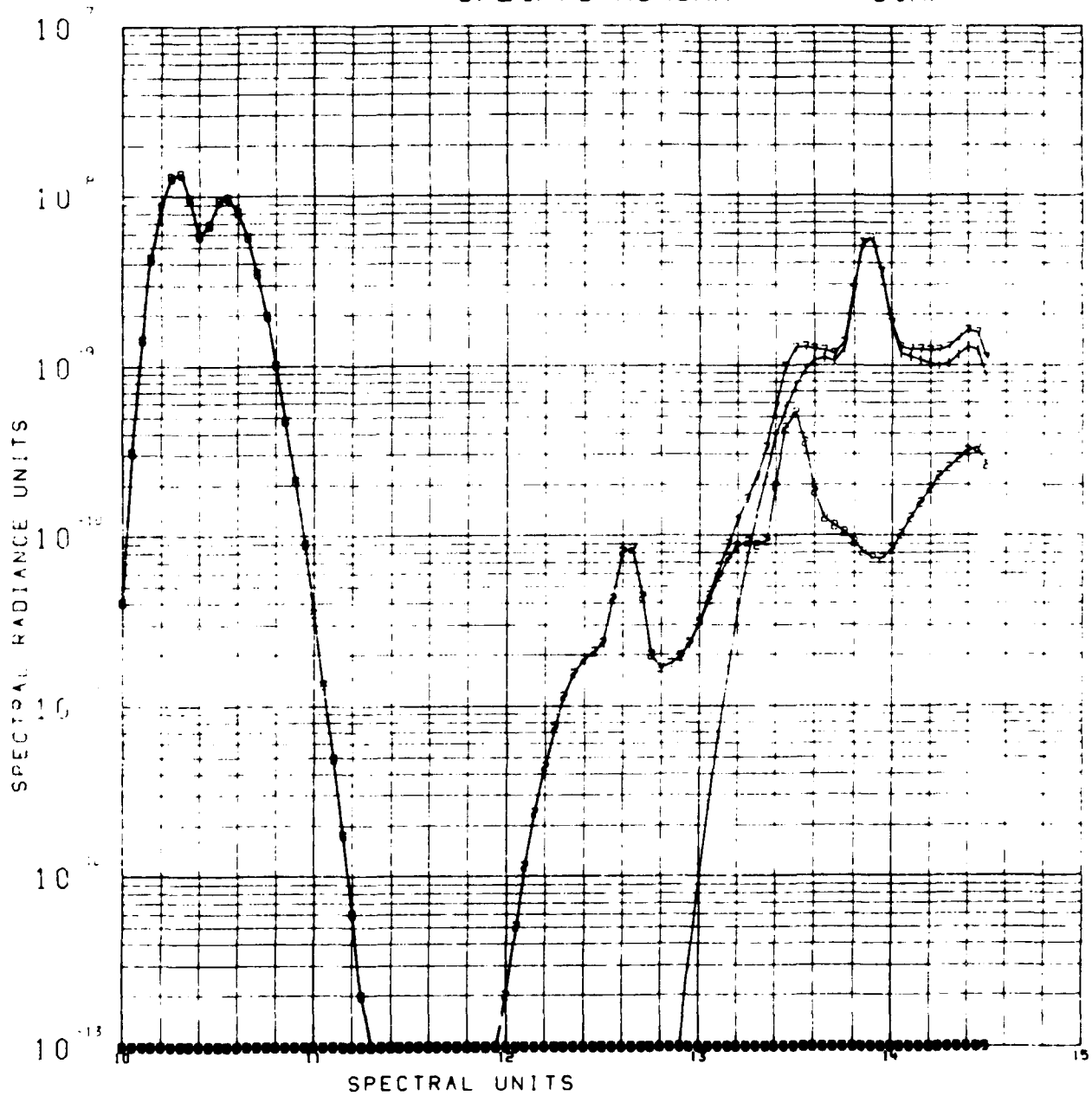
011061SC-020
0000 0030



3/24/73 AURORA

90KM

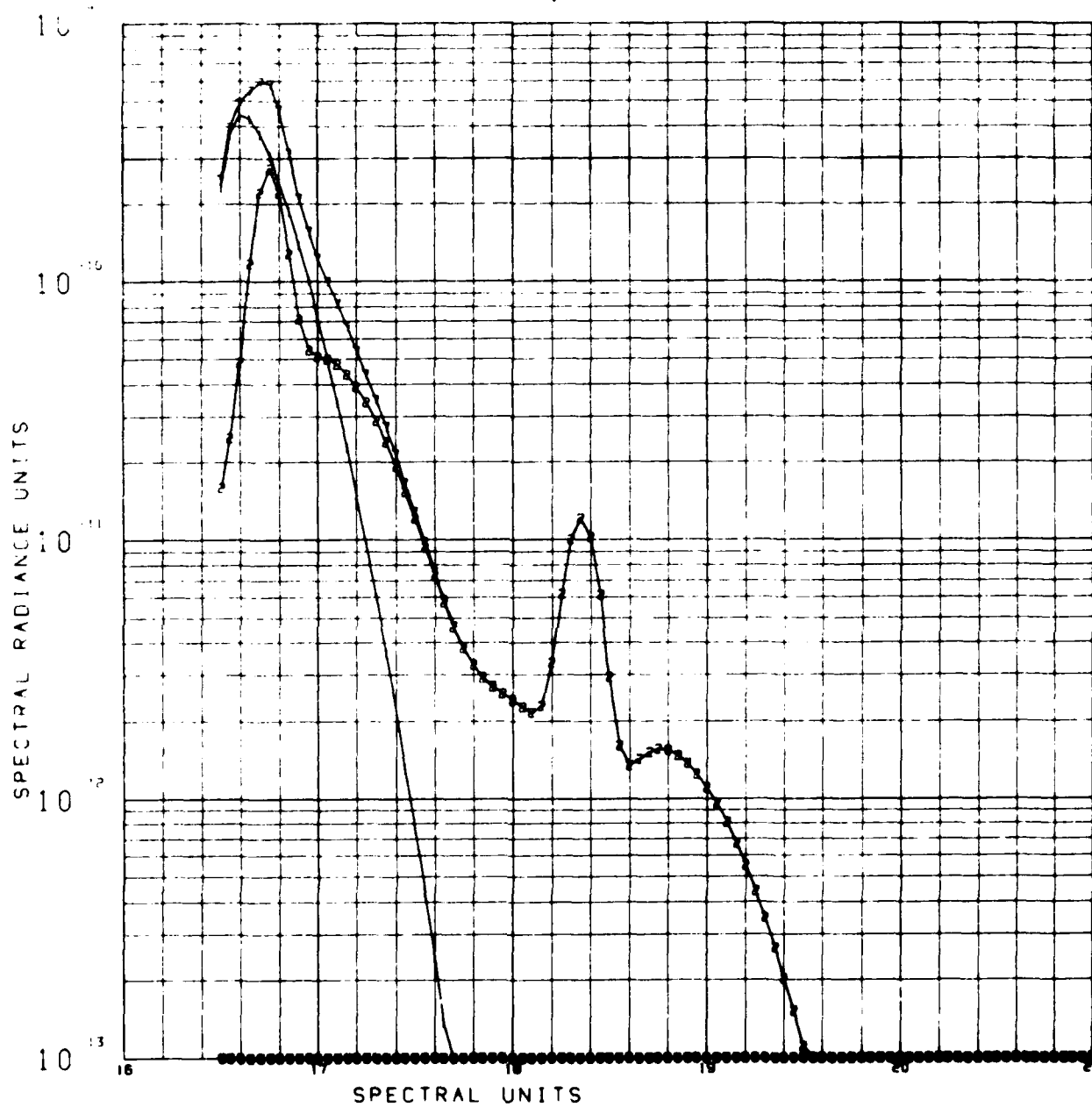
01108/504220
0000 0016



3/24/73 AURORA

90KM

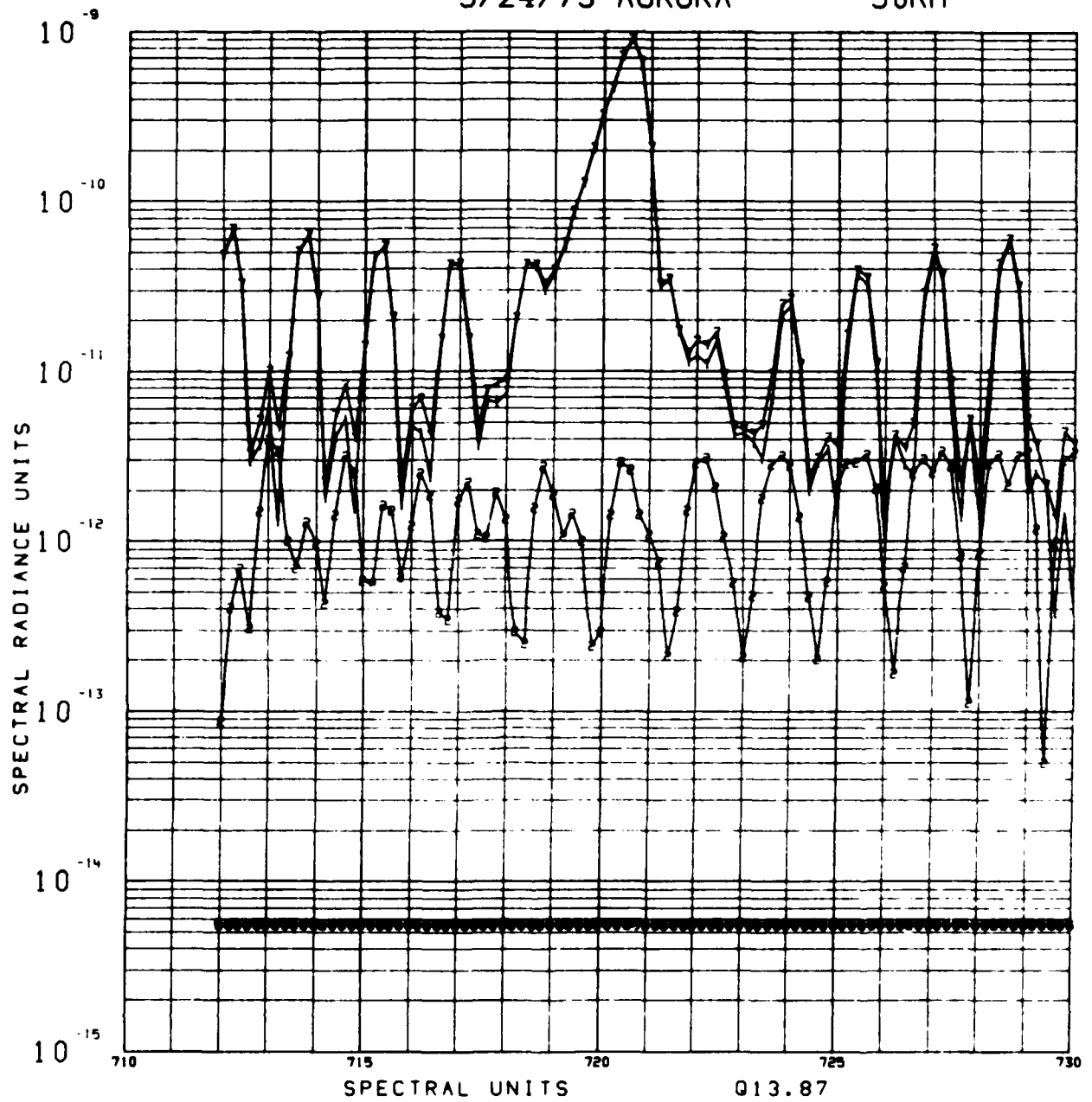
U1108/SC-020
0000 0017



3/24/73 AURORA

90KM

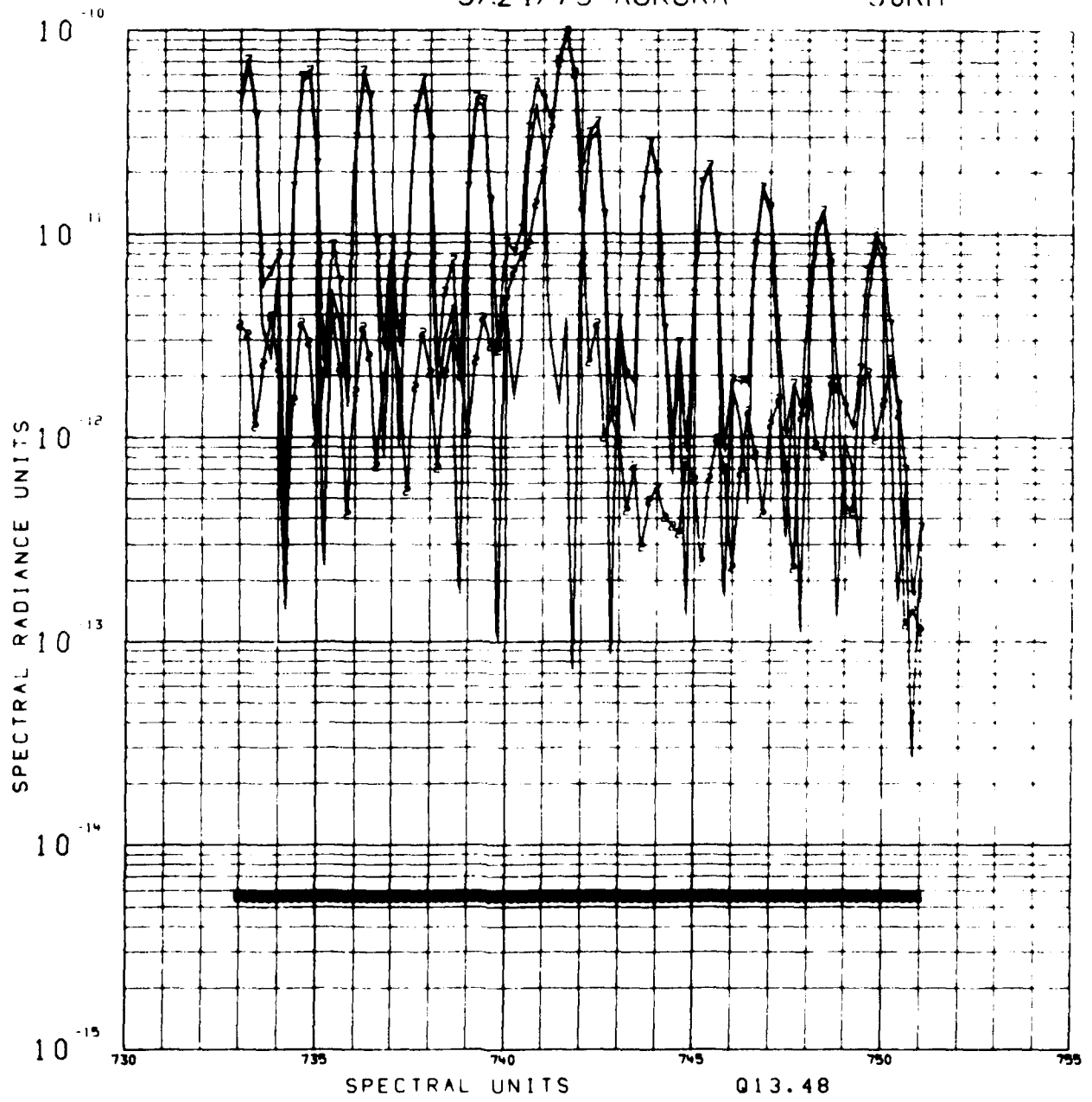
01100/SC-0201
0000 0010



3/24/73 AURORA

90KM

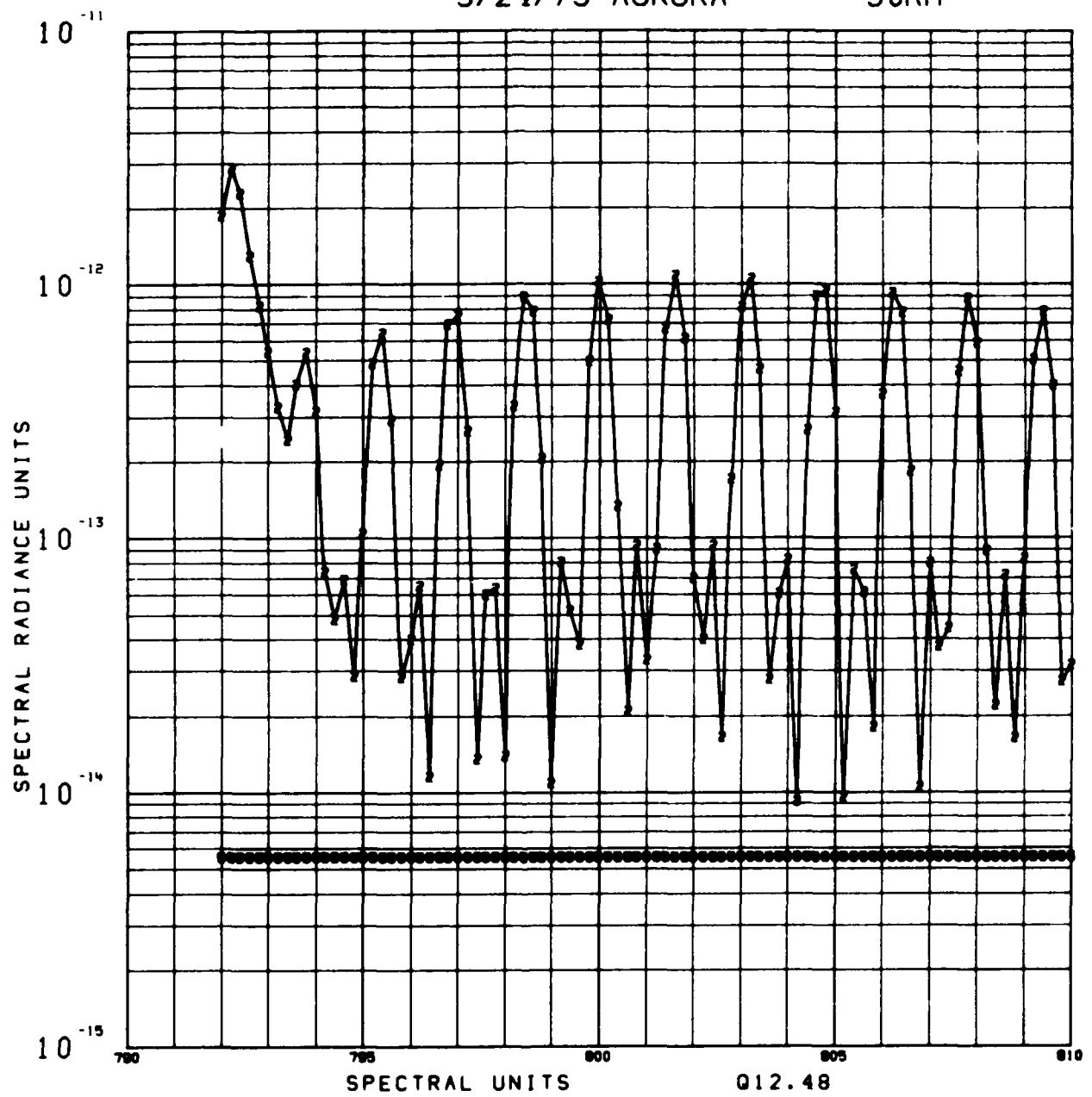
08/50/020
0017 1000



3/24/73 AURORA

90KM

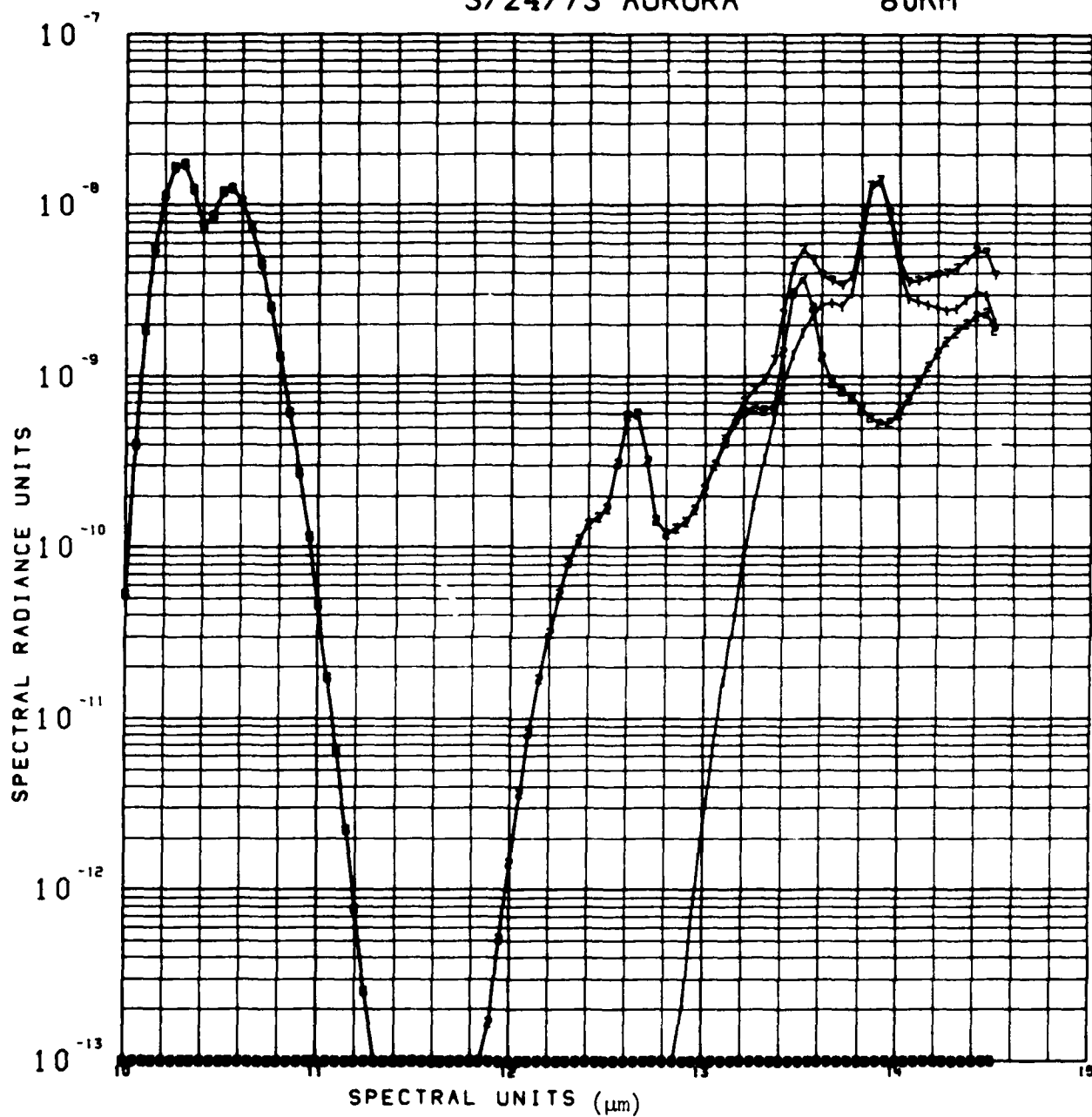
0000 0000



3/24/73 AURORA

80KM

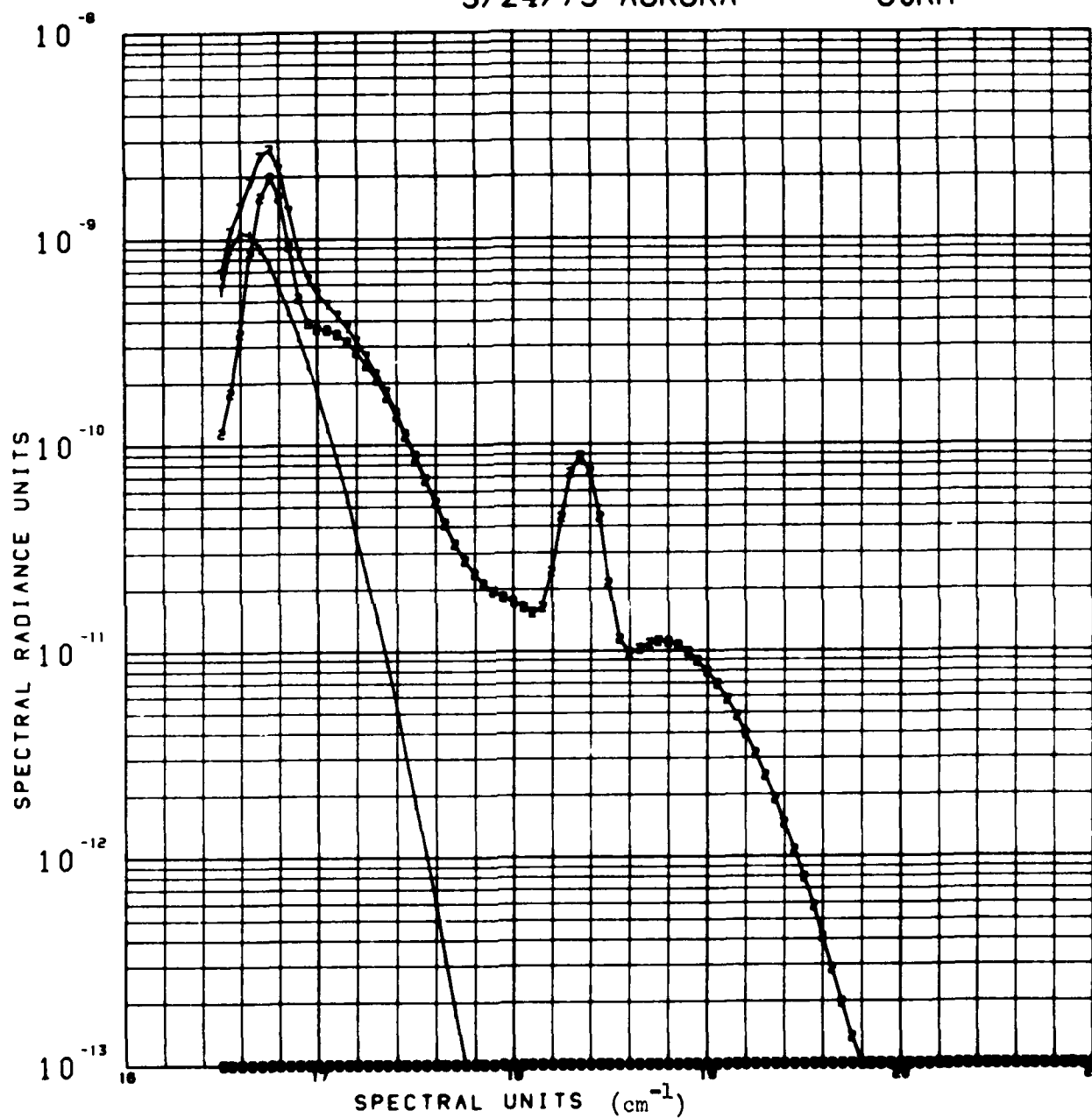
U1100/SC-020
0000 0021



3/24/73 AURORA

80KM

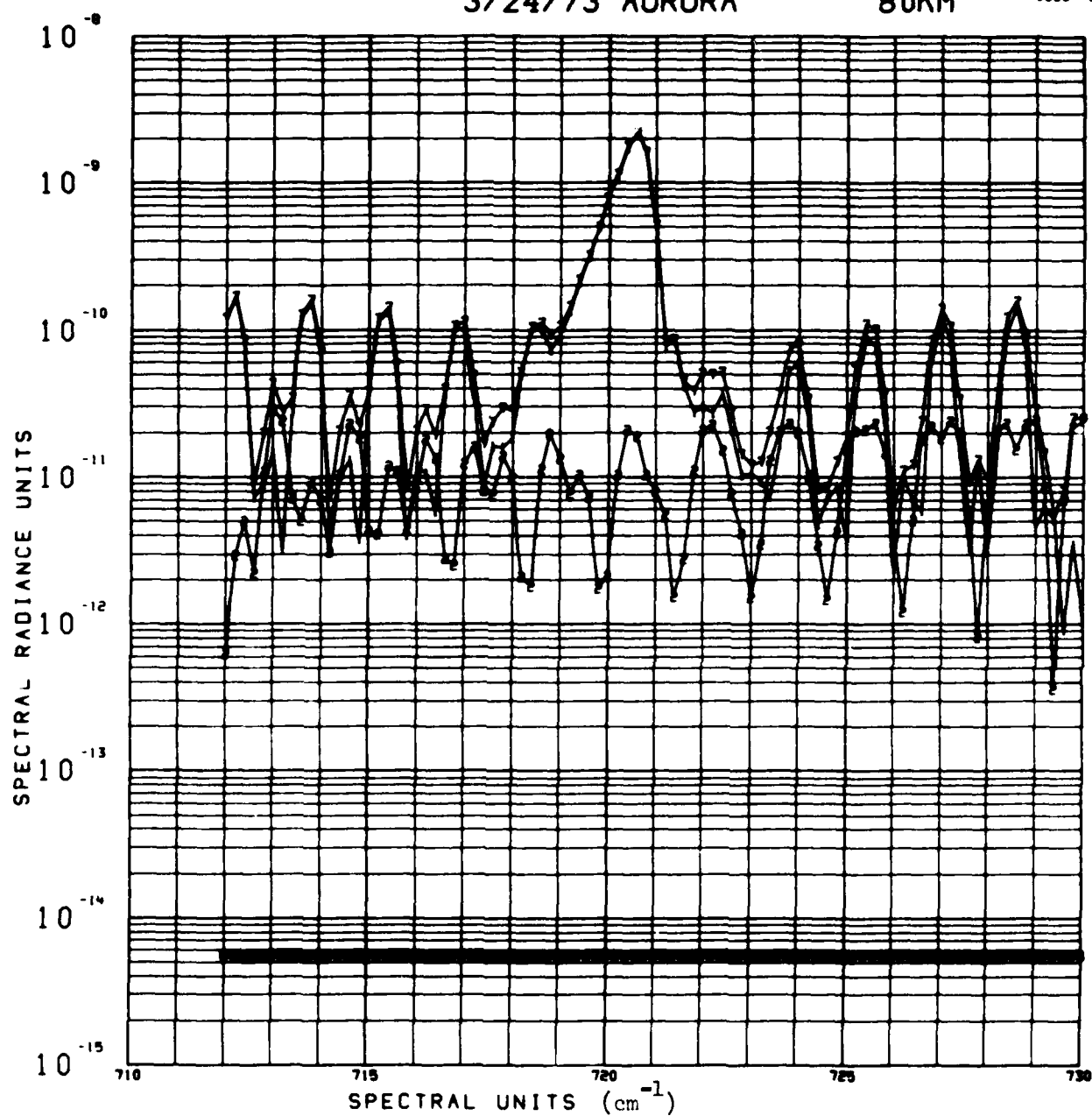
U1108/SC-020
0000 0022



3/24/73 AURORA

80KM

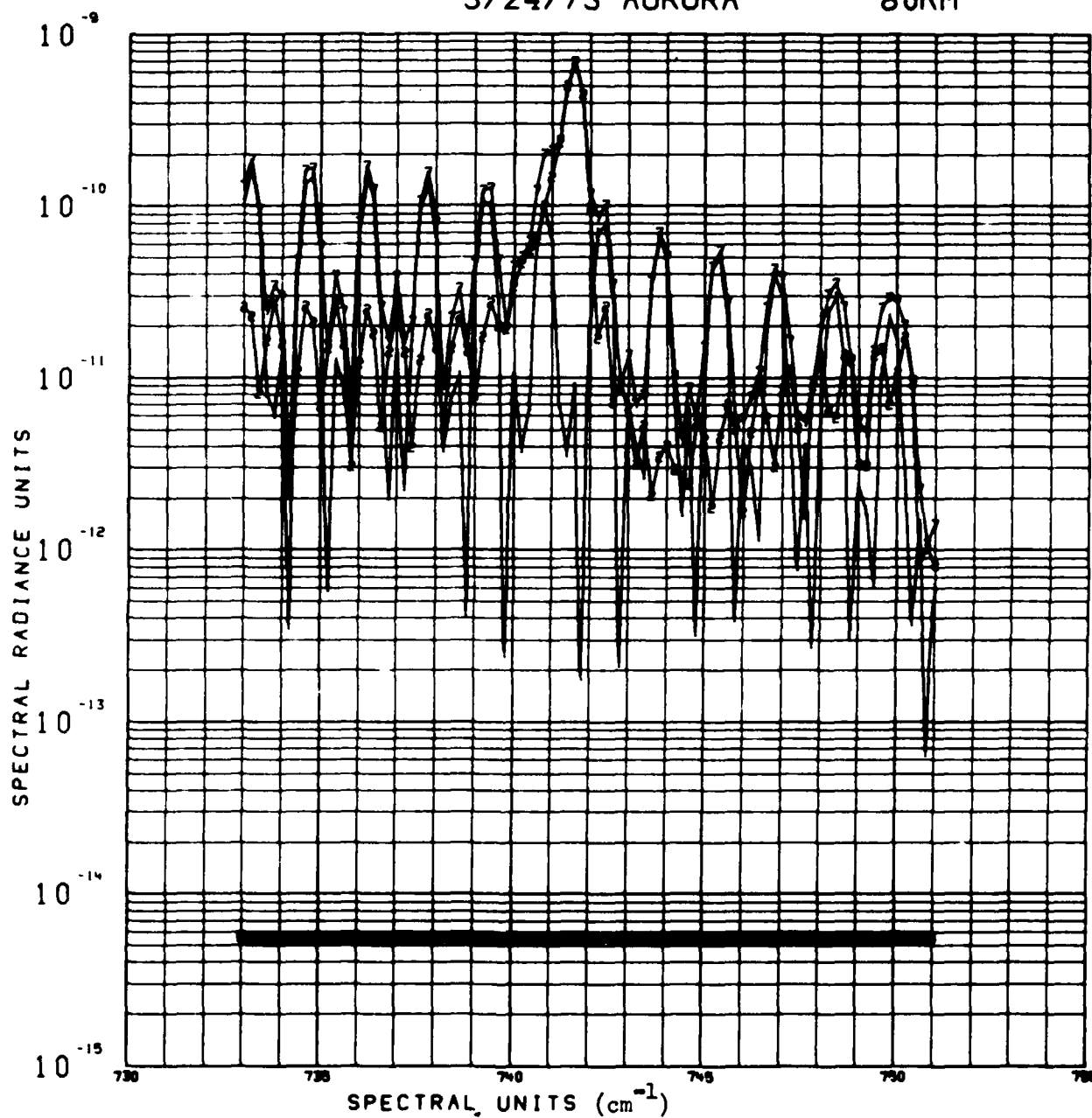
U1189/SC-828
0000 0023



3/24/73 AURORA

80KM

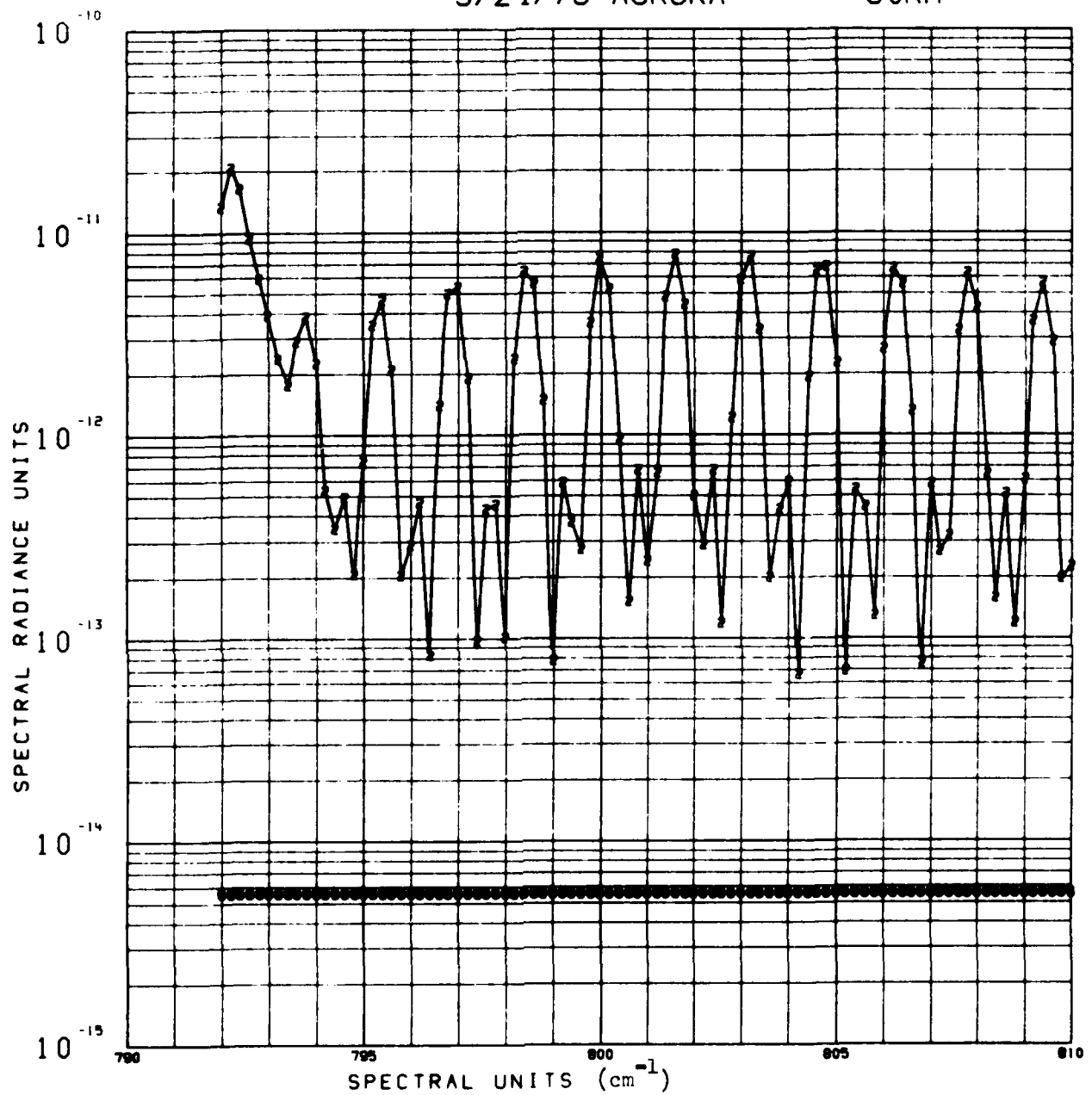
U1100/SC-020
0000 0024



3/24/73 AURORA

80KM

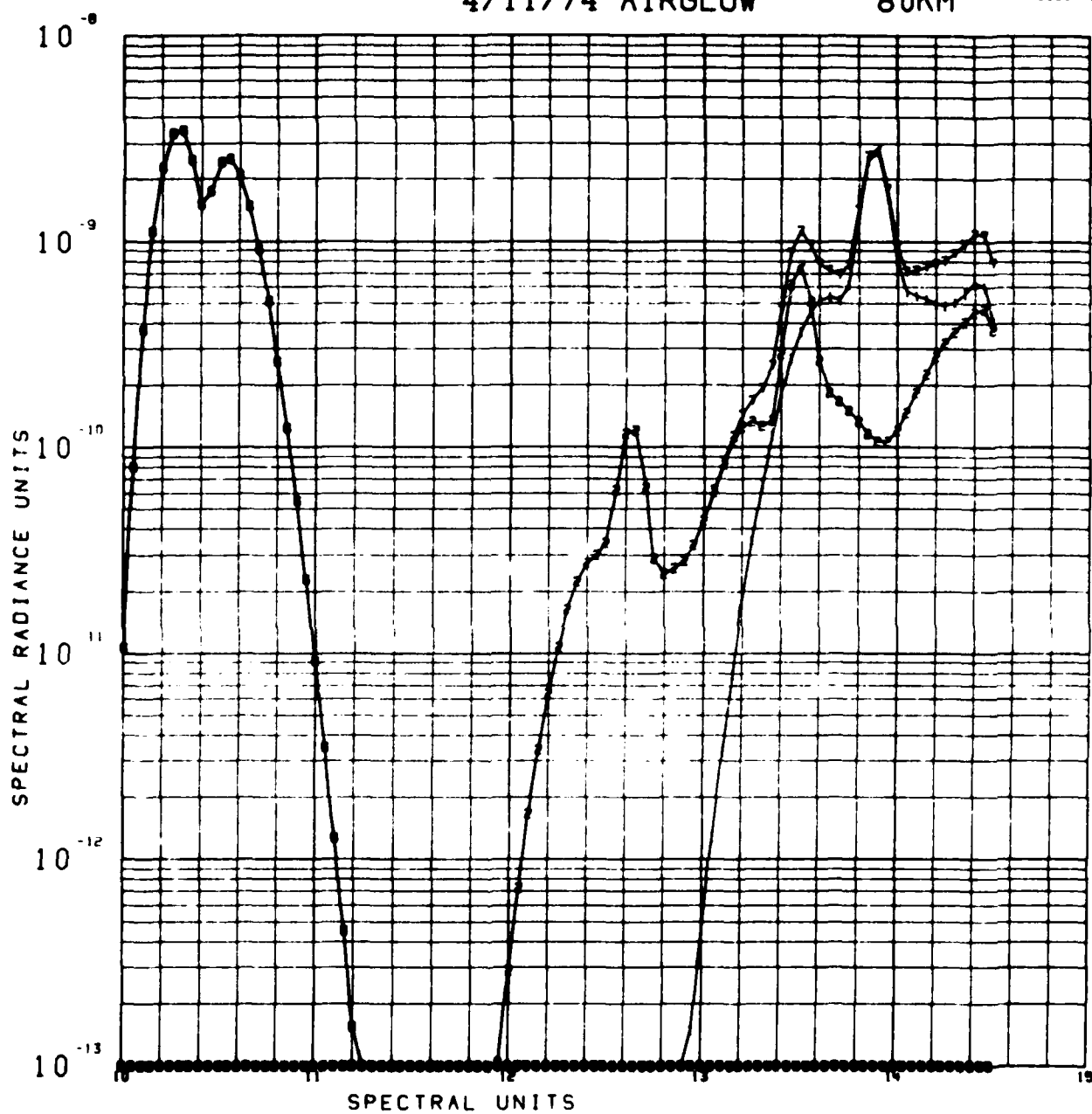
0110M/SL4020
0000 0025



4/11/74 AIRGLOW

80KM

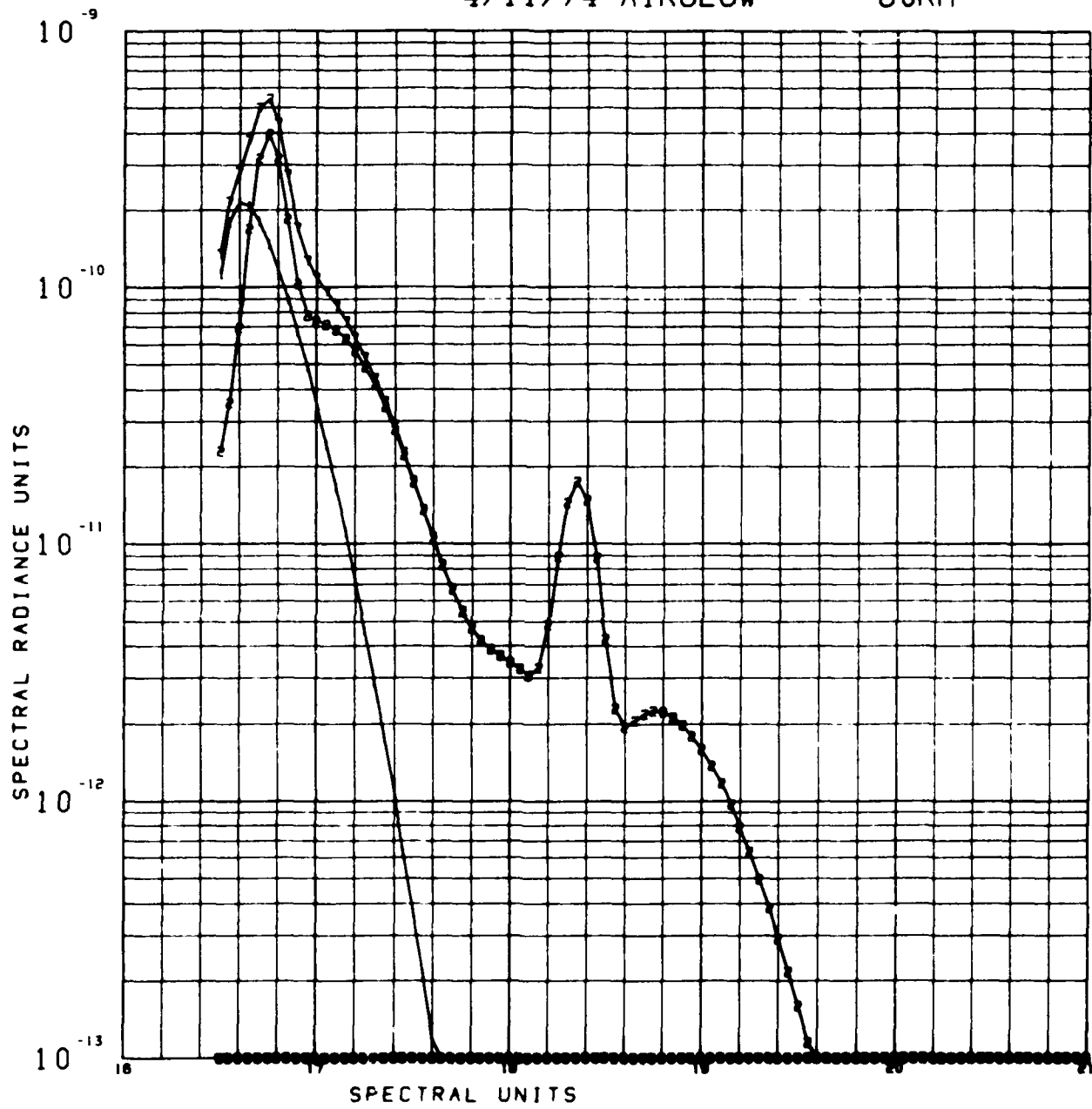
U1108/SC4020
0000 0001



4/11/74 AIRGLOW

80KM

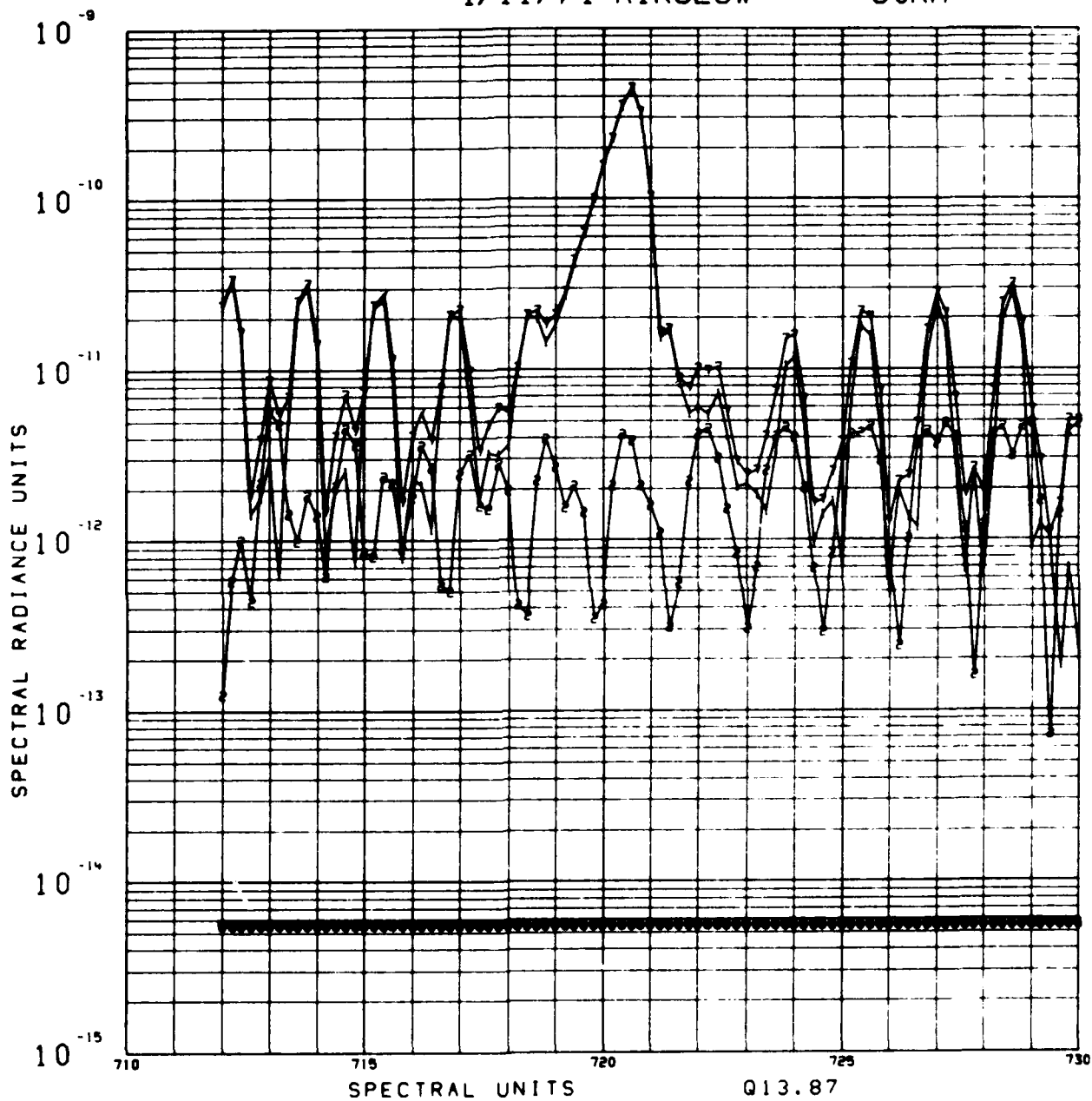
U1108/SCN020
0000 0002



4/11/74 AIRGLOW

80KM

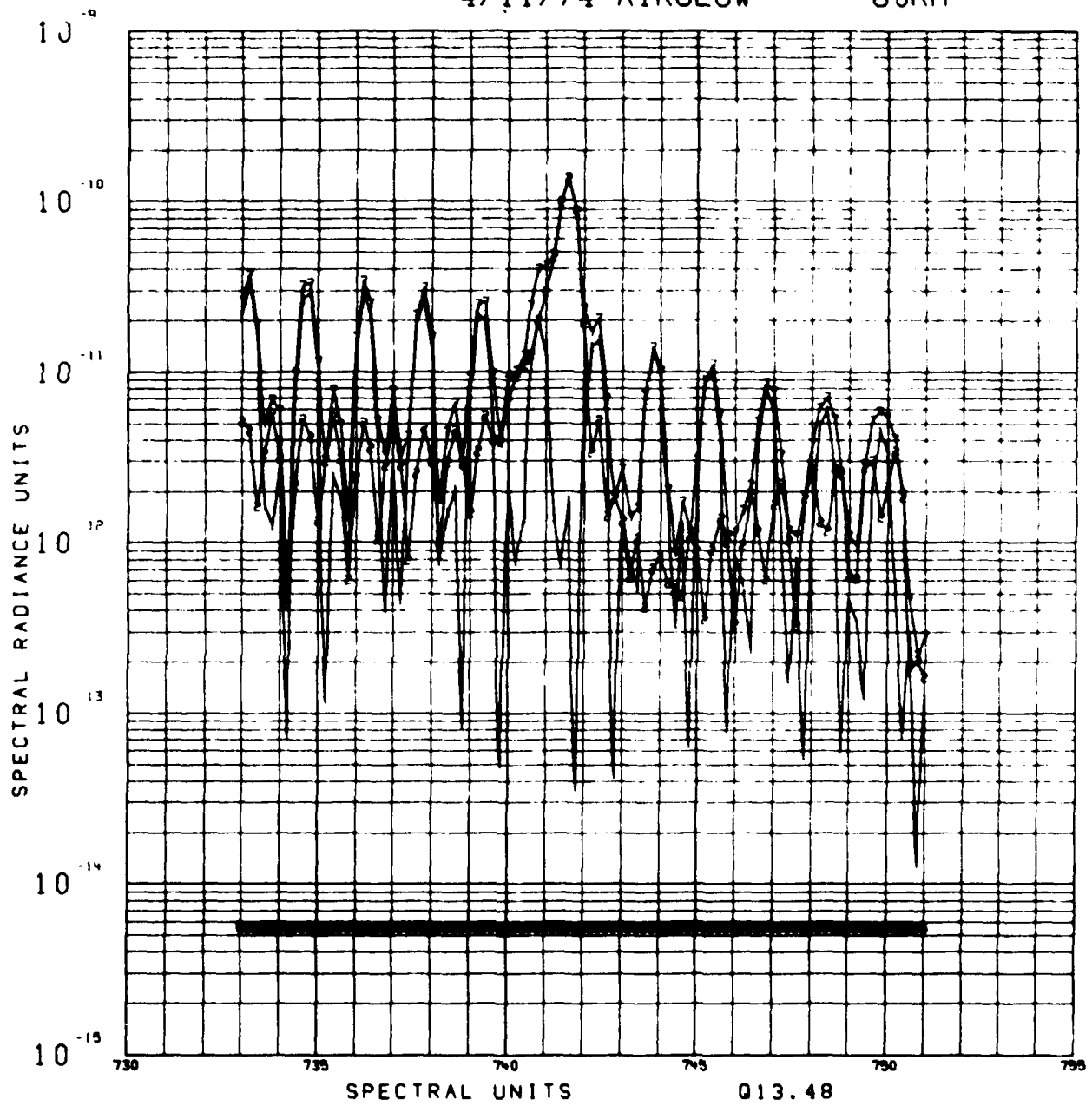
01100/SC-020
0000 0003



4/11/74 AIRGLOW

80KM

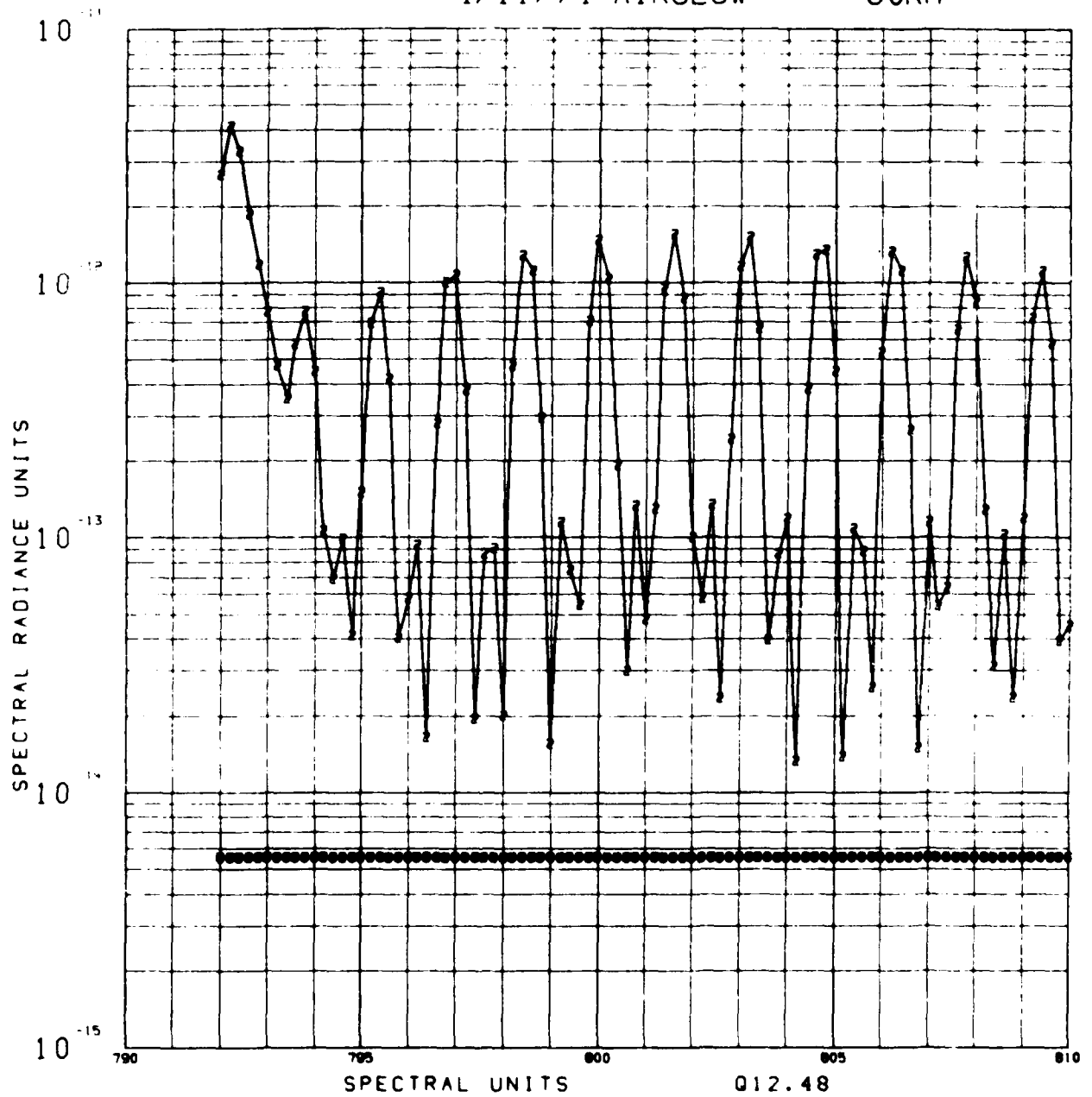
0000 000



4/11/74 AIRGLOW

80KM

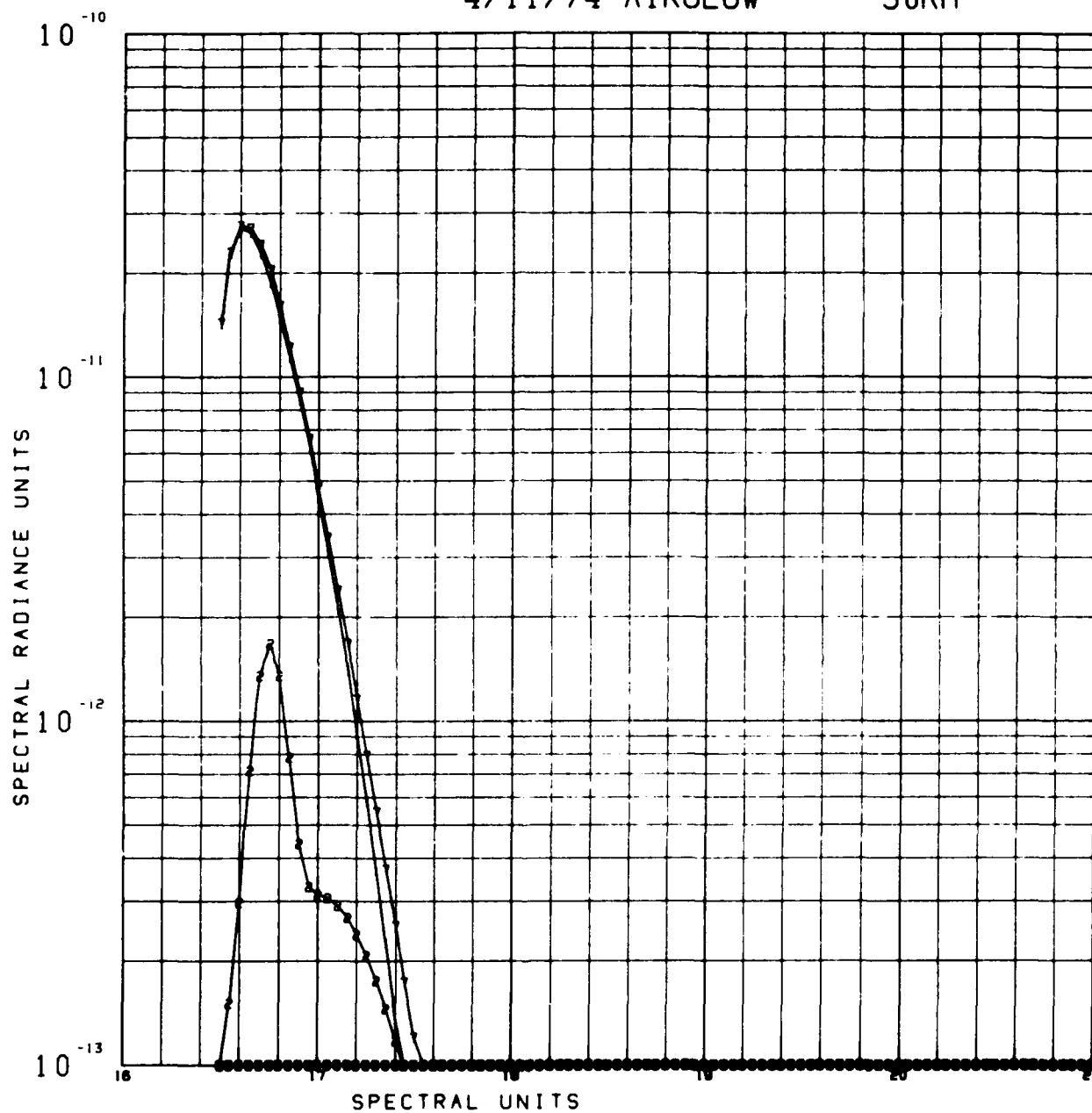
01108 SC40201
0000 0005



4/11/74 AIRGLOW

90KM

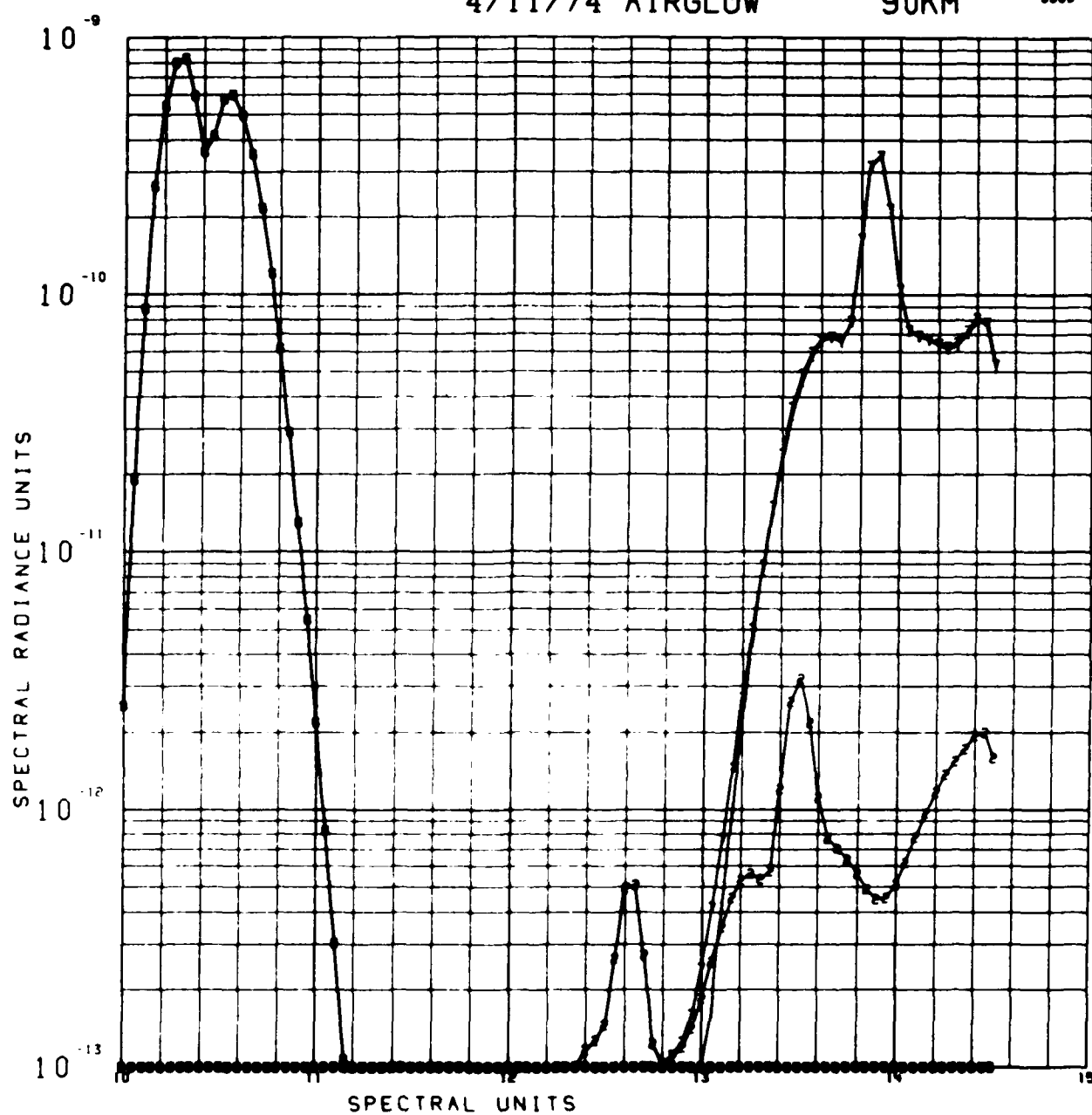
U1108/SC40204
0000 0007



4/11/74 AIRGLOW

90KM

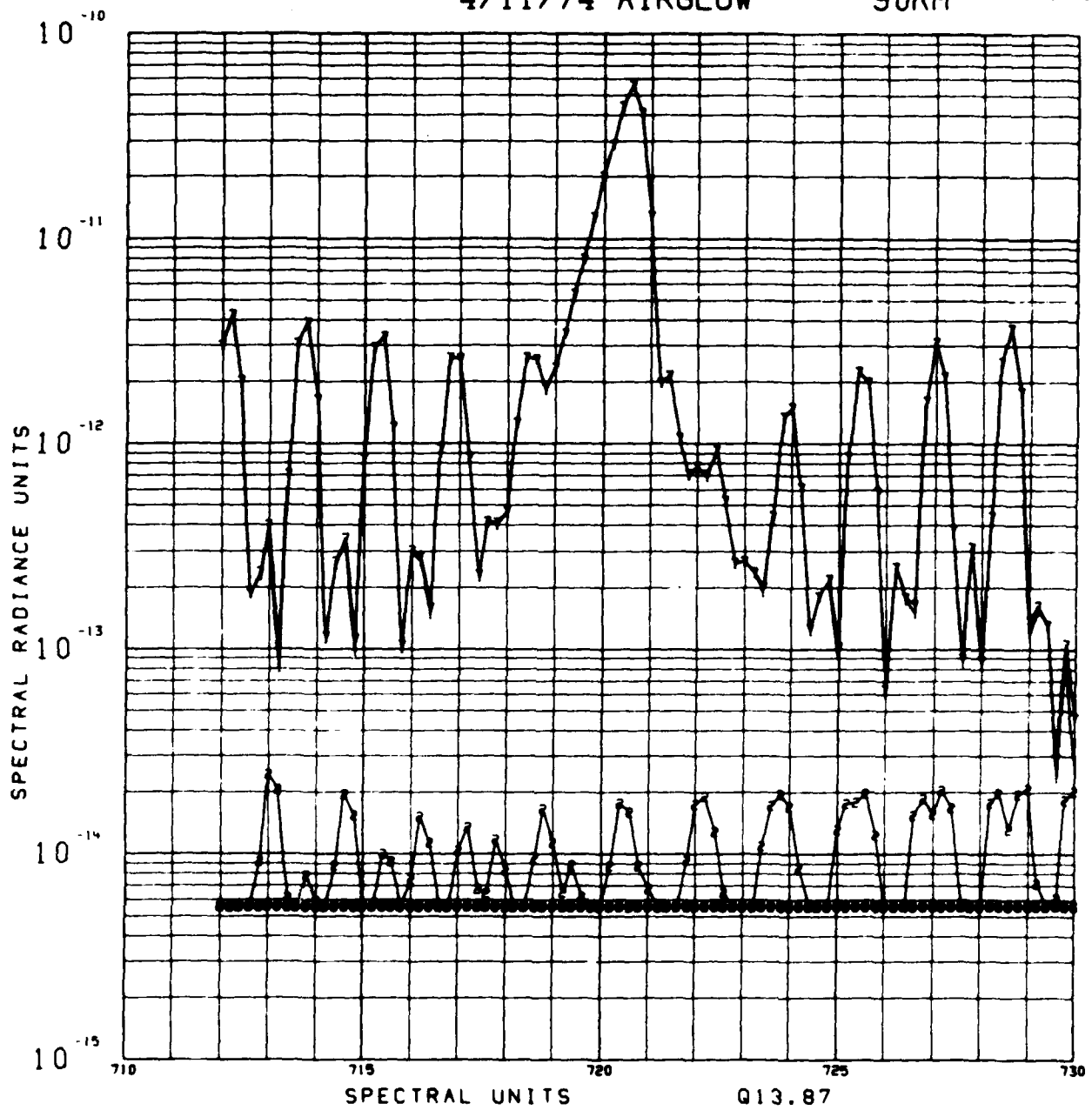
U1100/SC-020
0000 0006



4/11/74 AIRGLOW

90KM

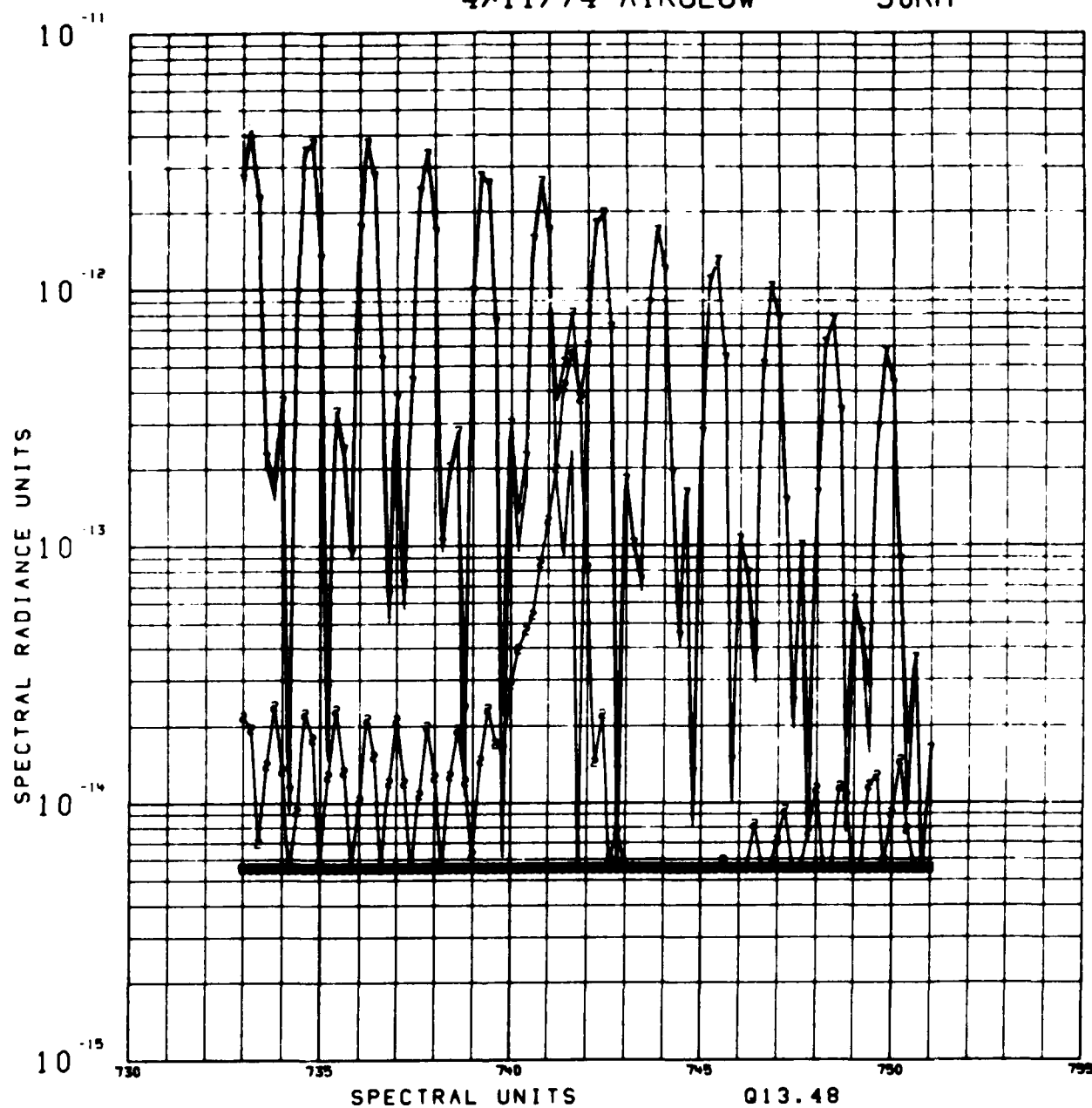
U1108/SC4020
0000 0000



4/11/74 AIRGLOW

90KM

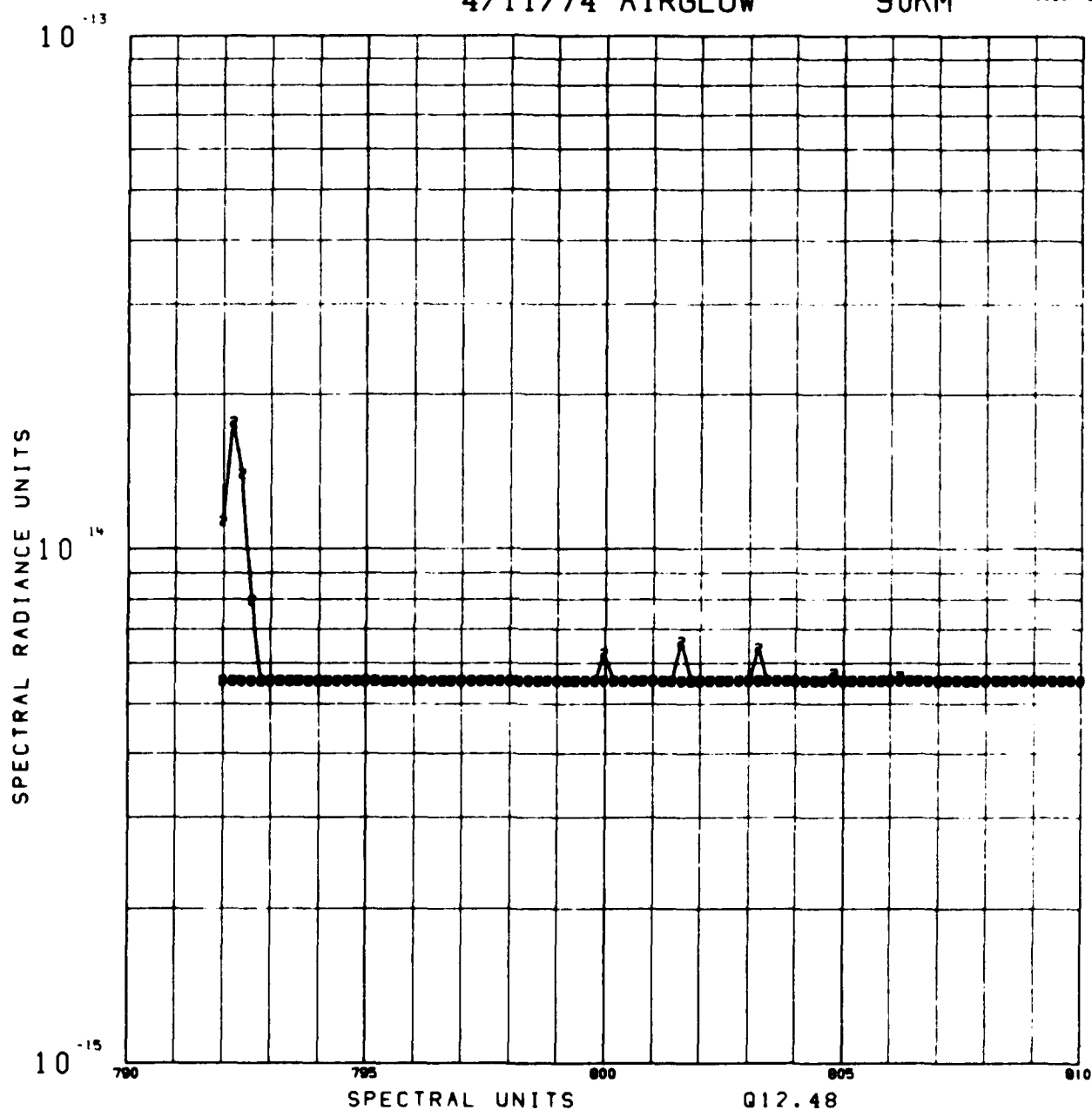
U1108/SC4020
0000 0009



4/11/74 AIRGLOW

90KM

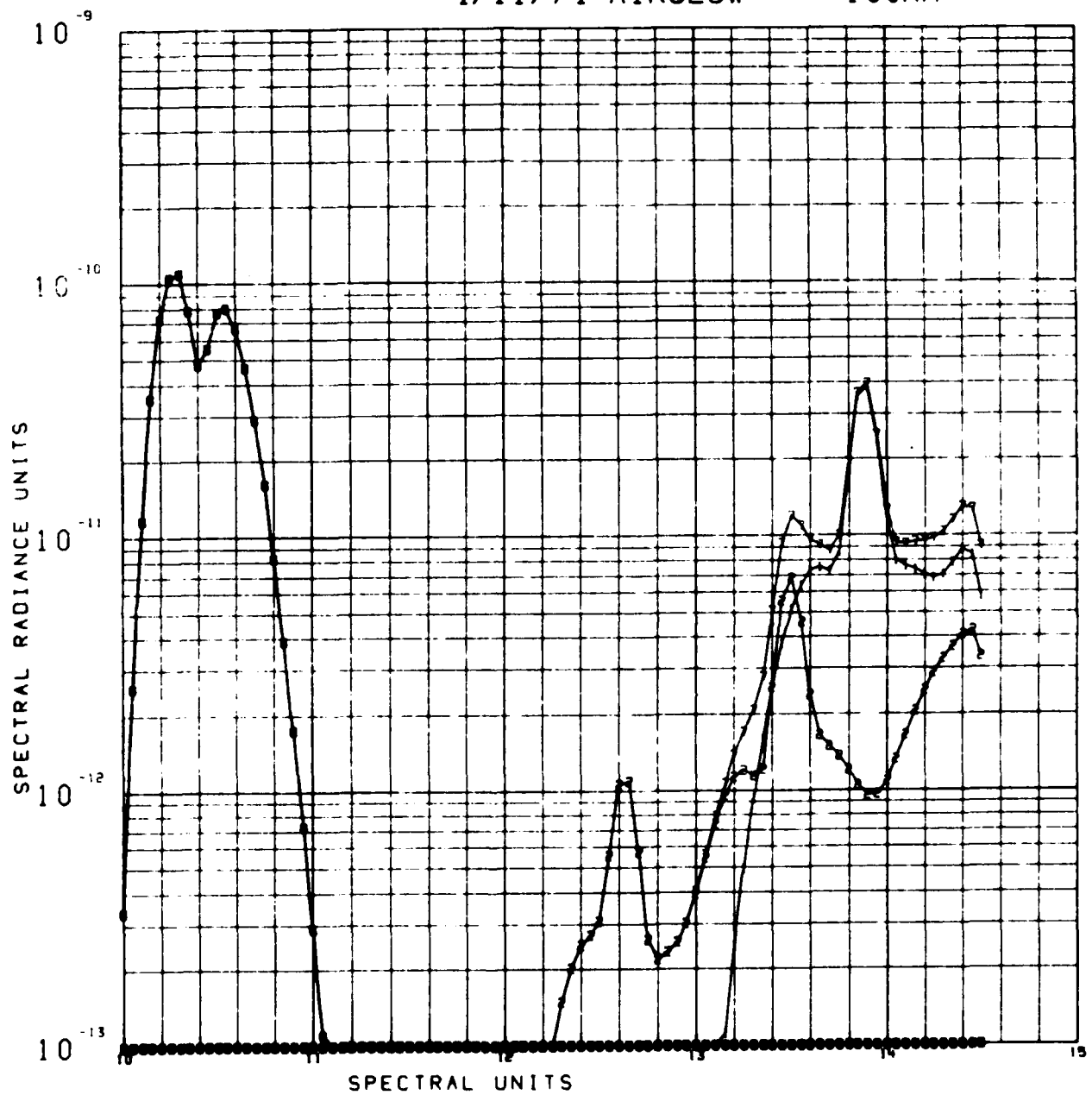
U1108/SC-020
0000 0010



4/11/74 AIRGLOW

100KM

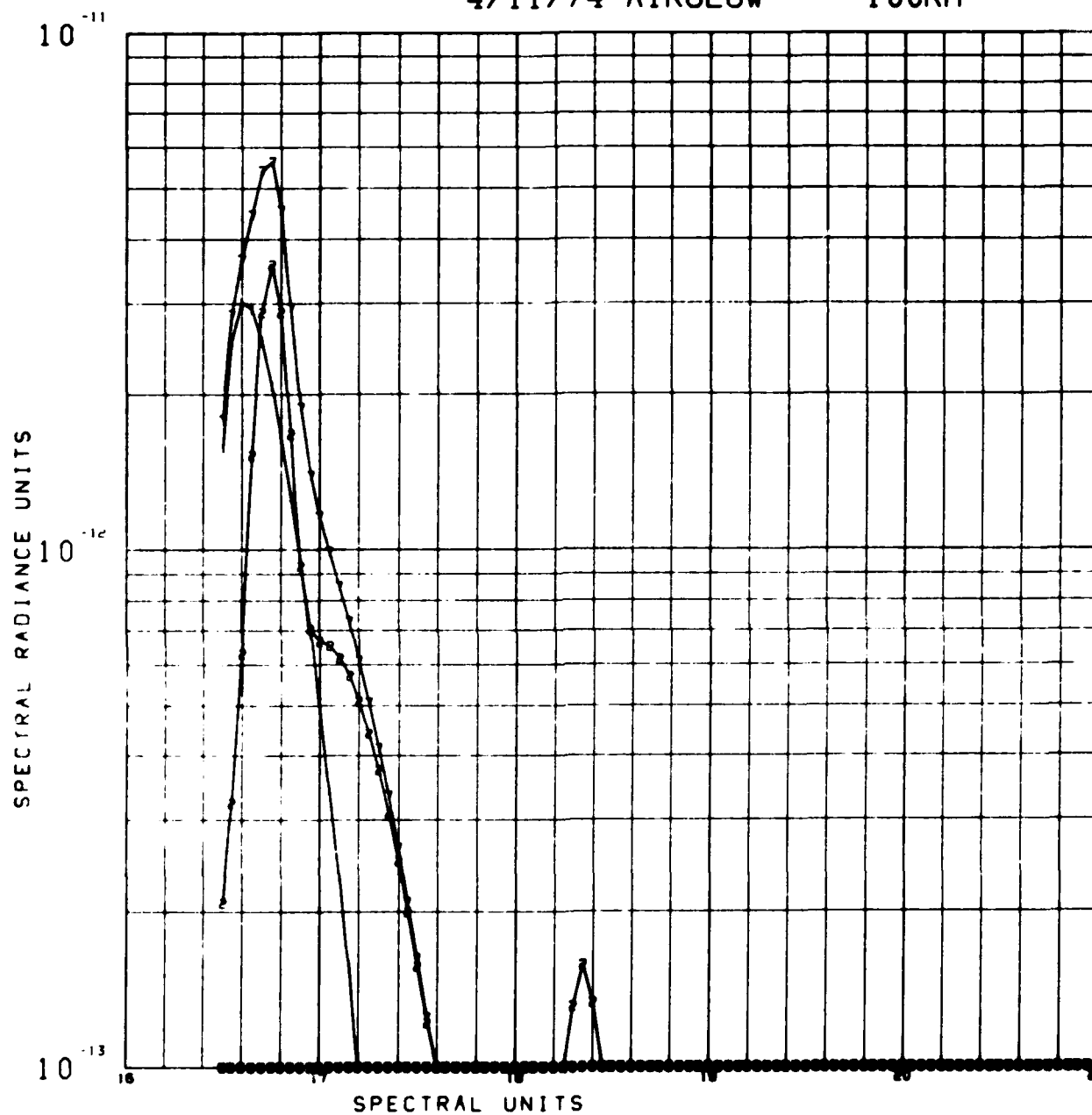
U. 108/SC4020
0000 0011



4/11/74 AIRGLOW

100KM

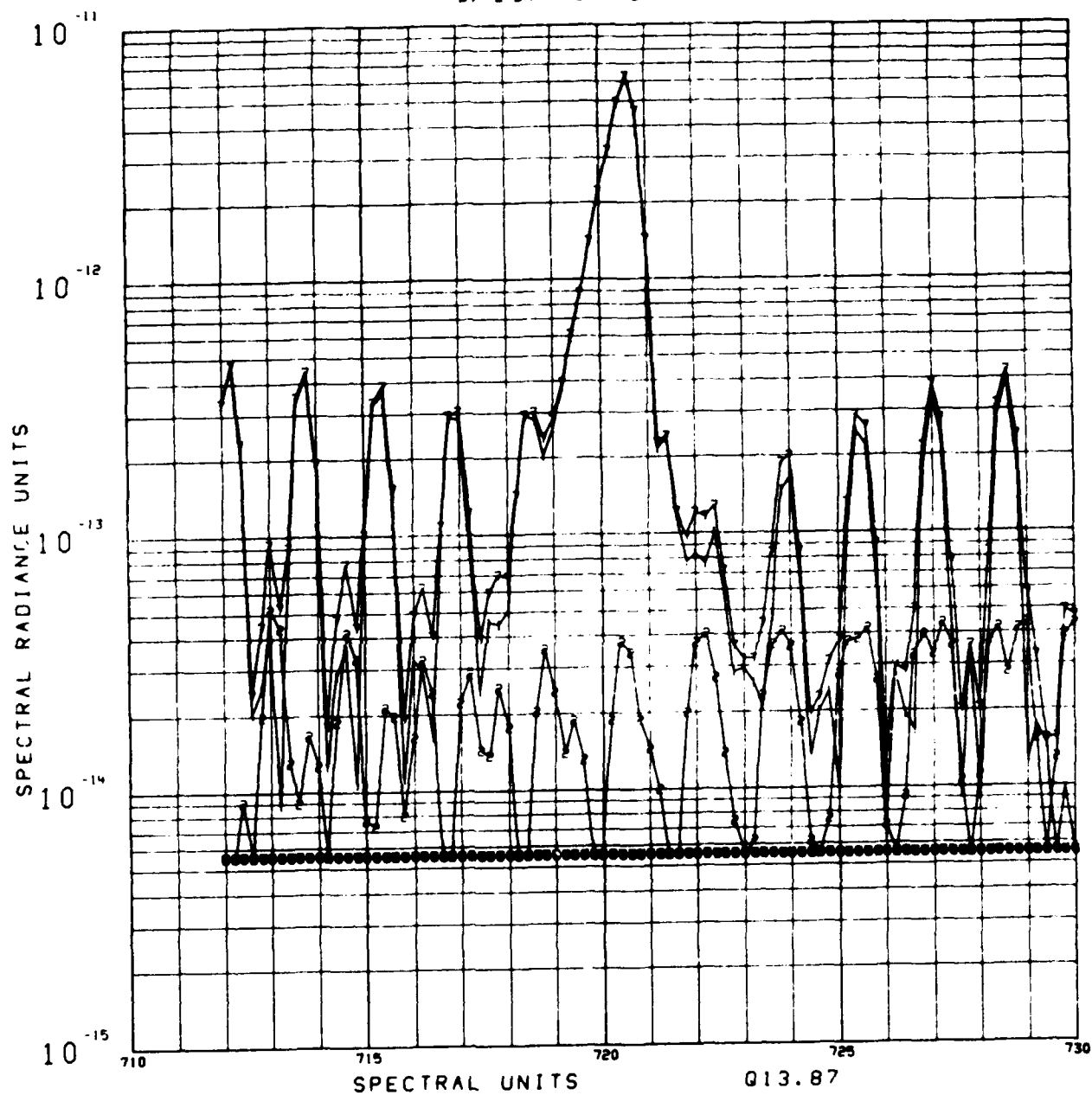
U1108/SC4020
0000 0012



4/11/74 AIRGLOW

100KM

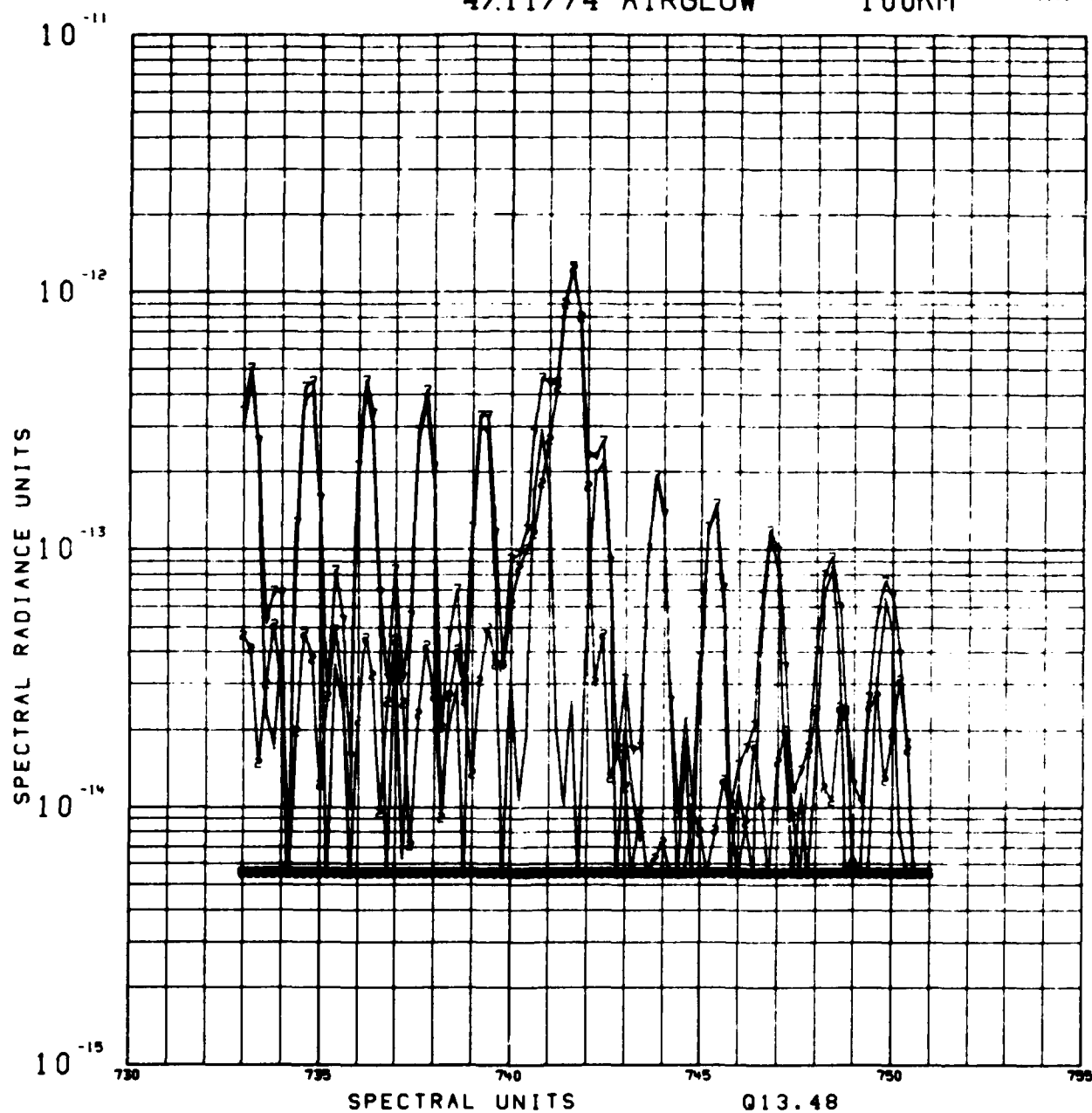
01100/SC4020
0000 0013



4/11/74 AIRGLOW

100KM

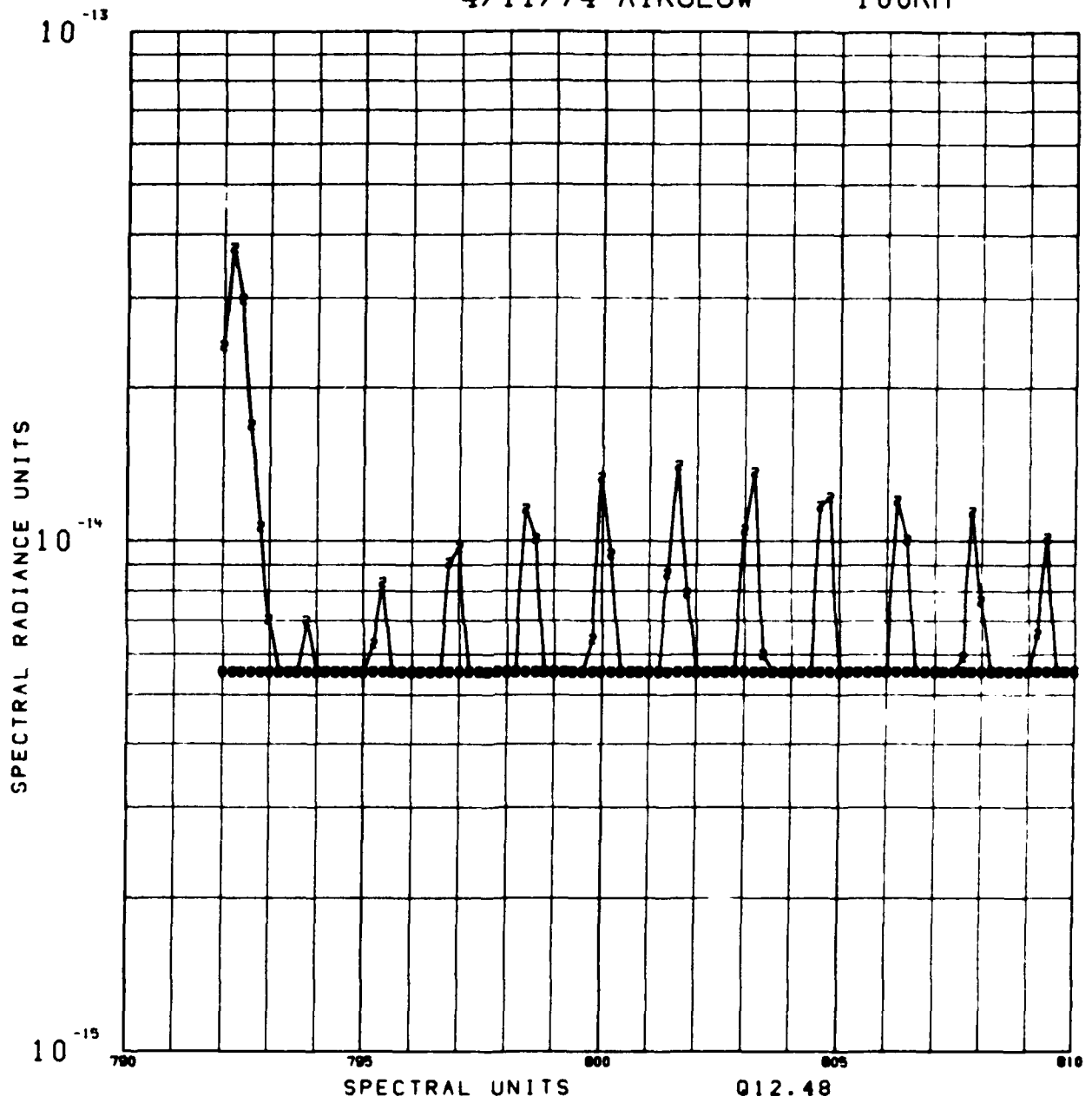
U1100/SC4020
0000 0014



4/11/74 AIRGLOW

100KM

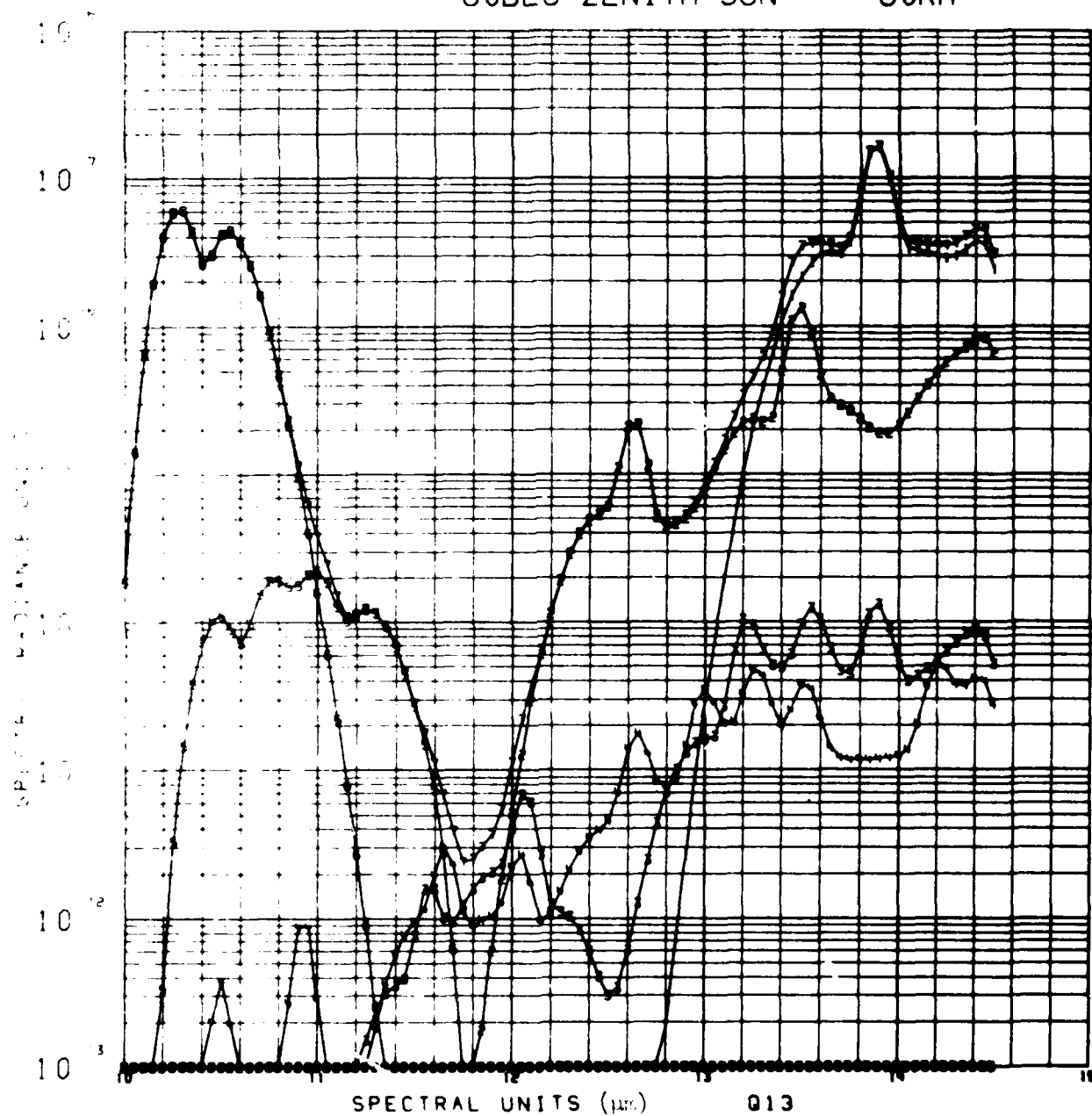
U1108/SC-020-
0000 0015



60DEG ZENITH SUN

80KM

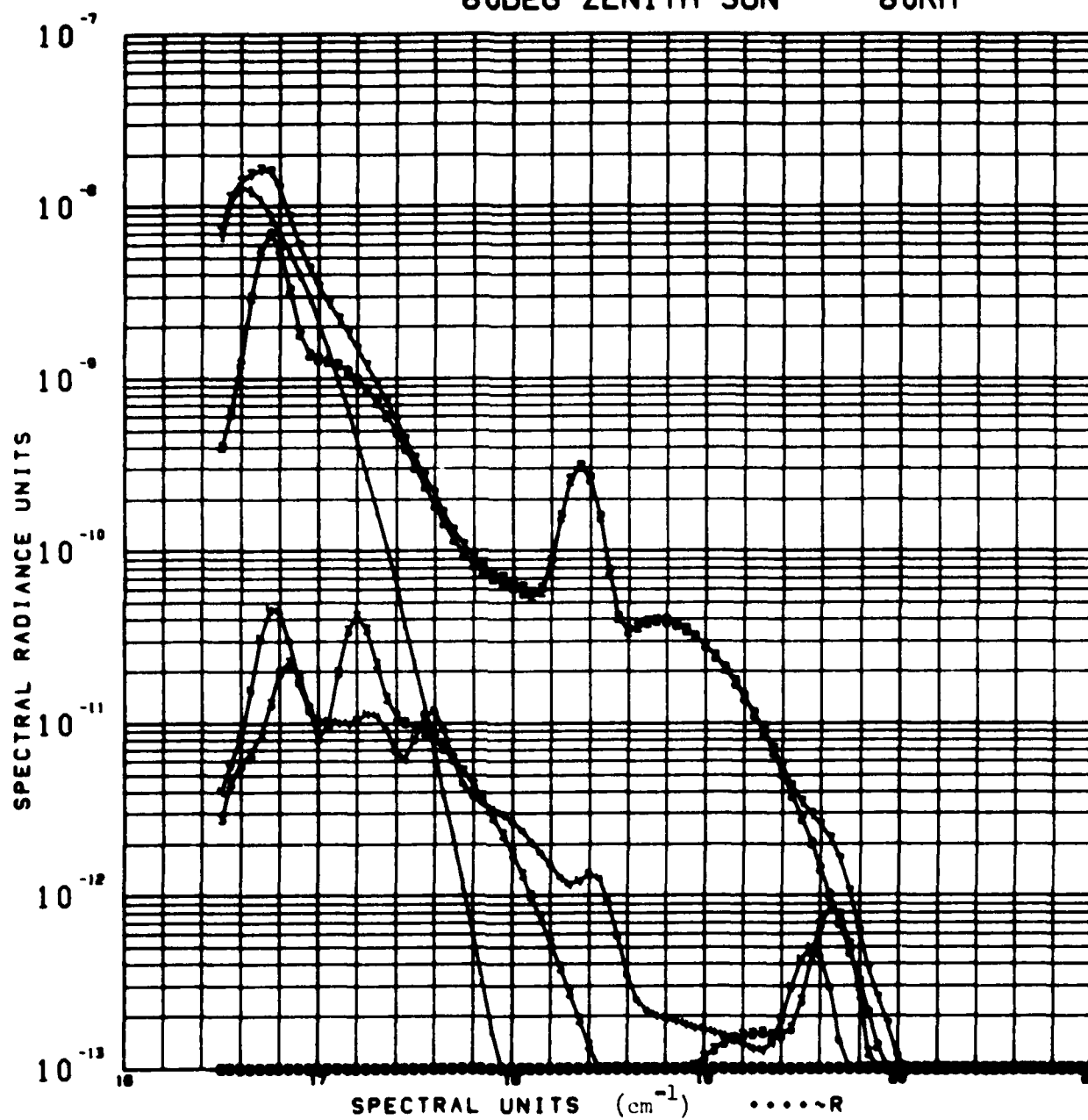
01100/SC-0P0
0000 0001



60DEG ZENITH SUN

80KM

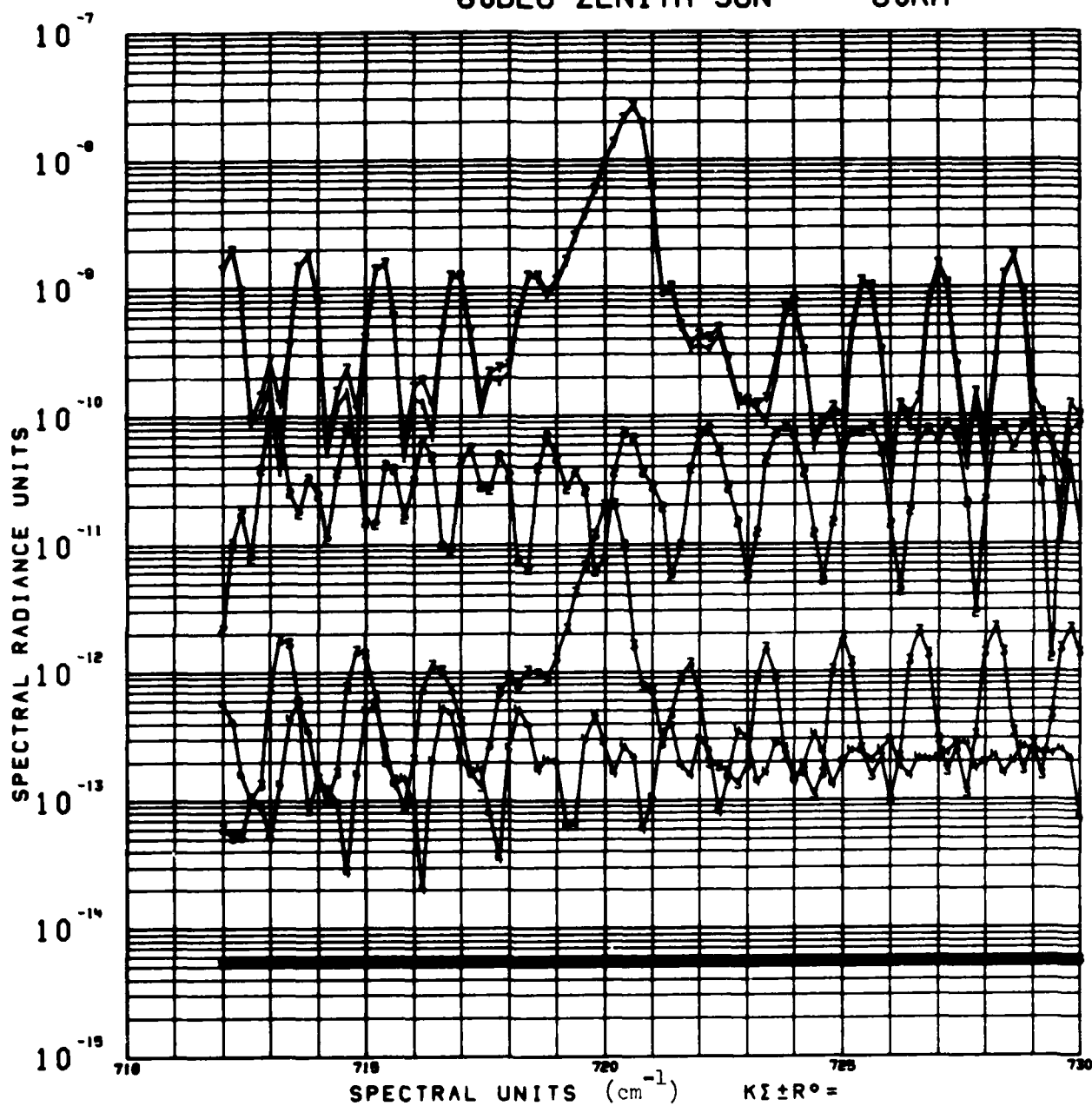
U1188/SC-000
0000 0000



60DEG ZENITH SUN

80KM

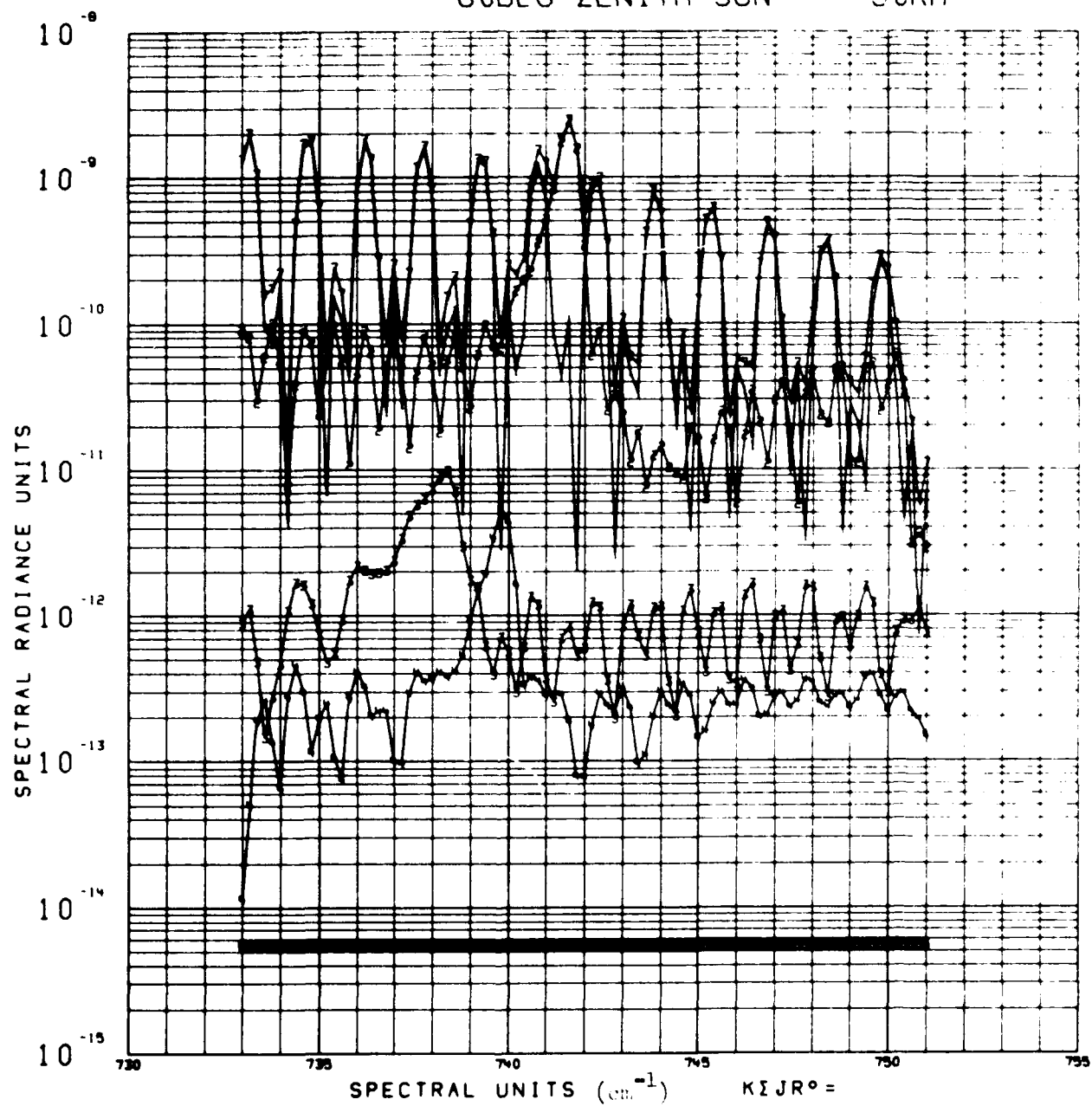
U1108/SC4088
0000 0003



60 DEG ZENITH SUN

80KM

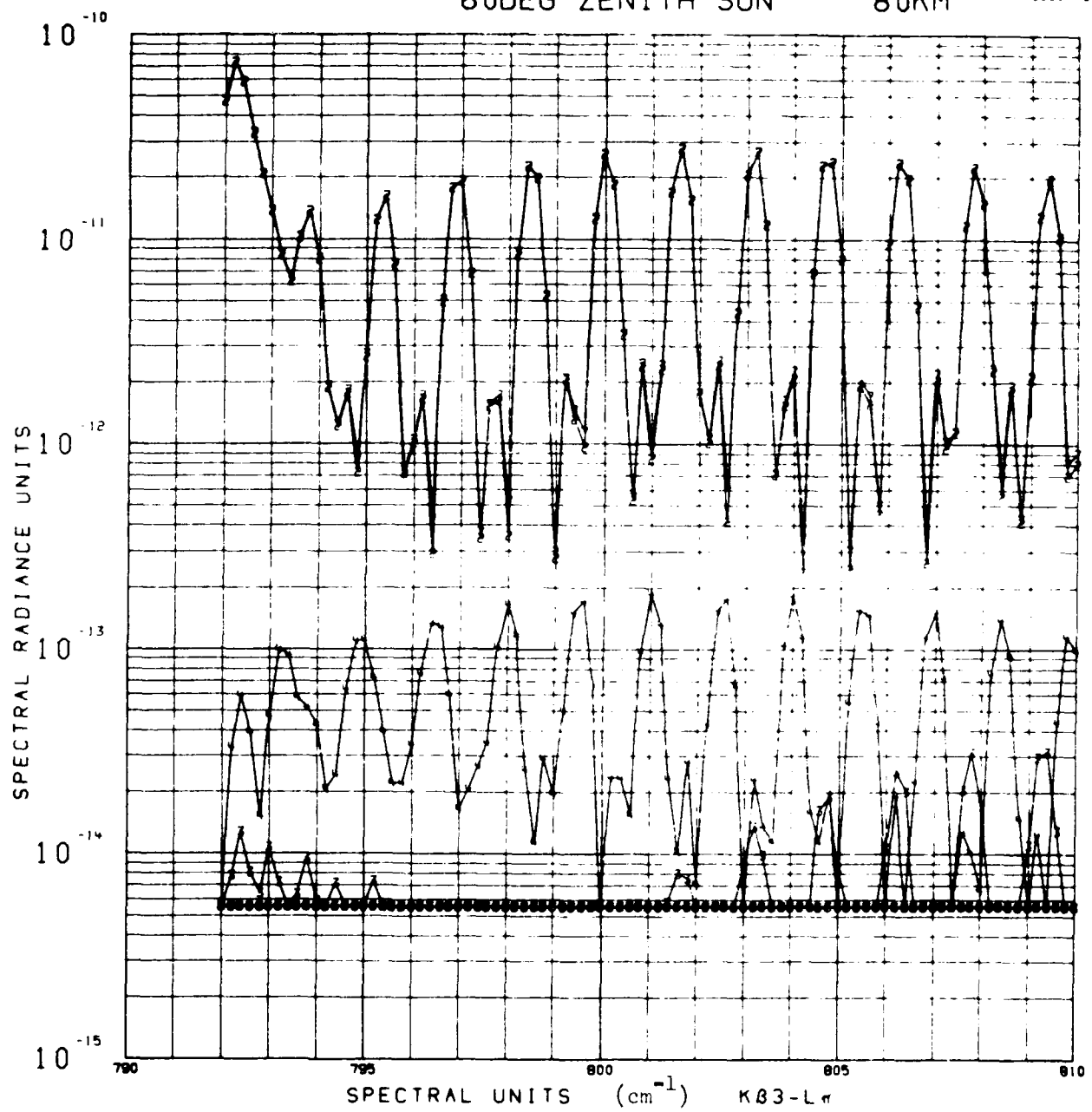
1106 50-020
0000 0004



60DEG ZENITH SUN

80KM

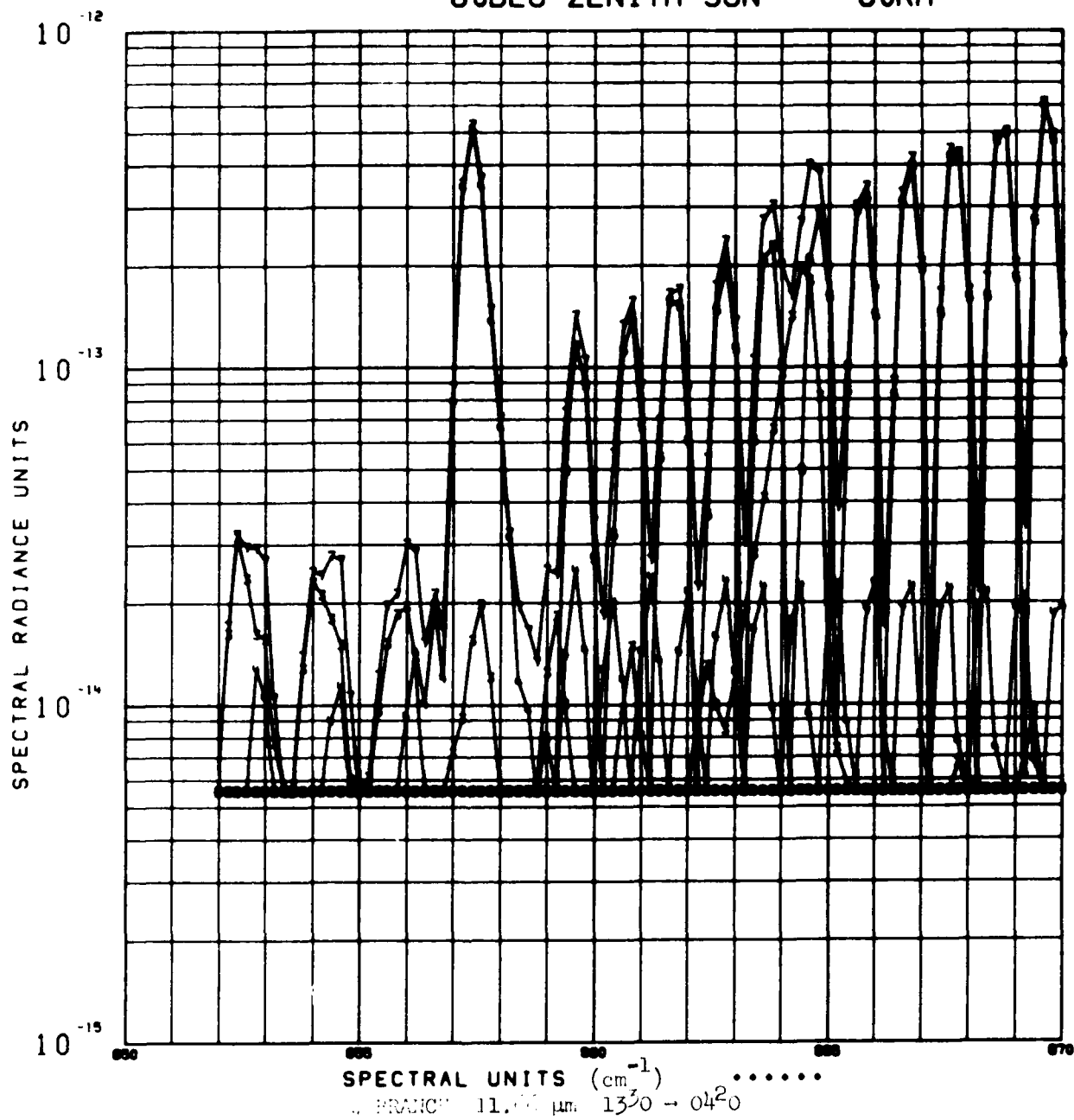
01100/5C-020
0000 0005



60 DEG ZENITH SUN

80KM

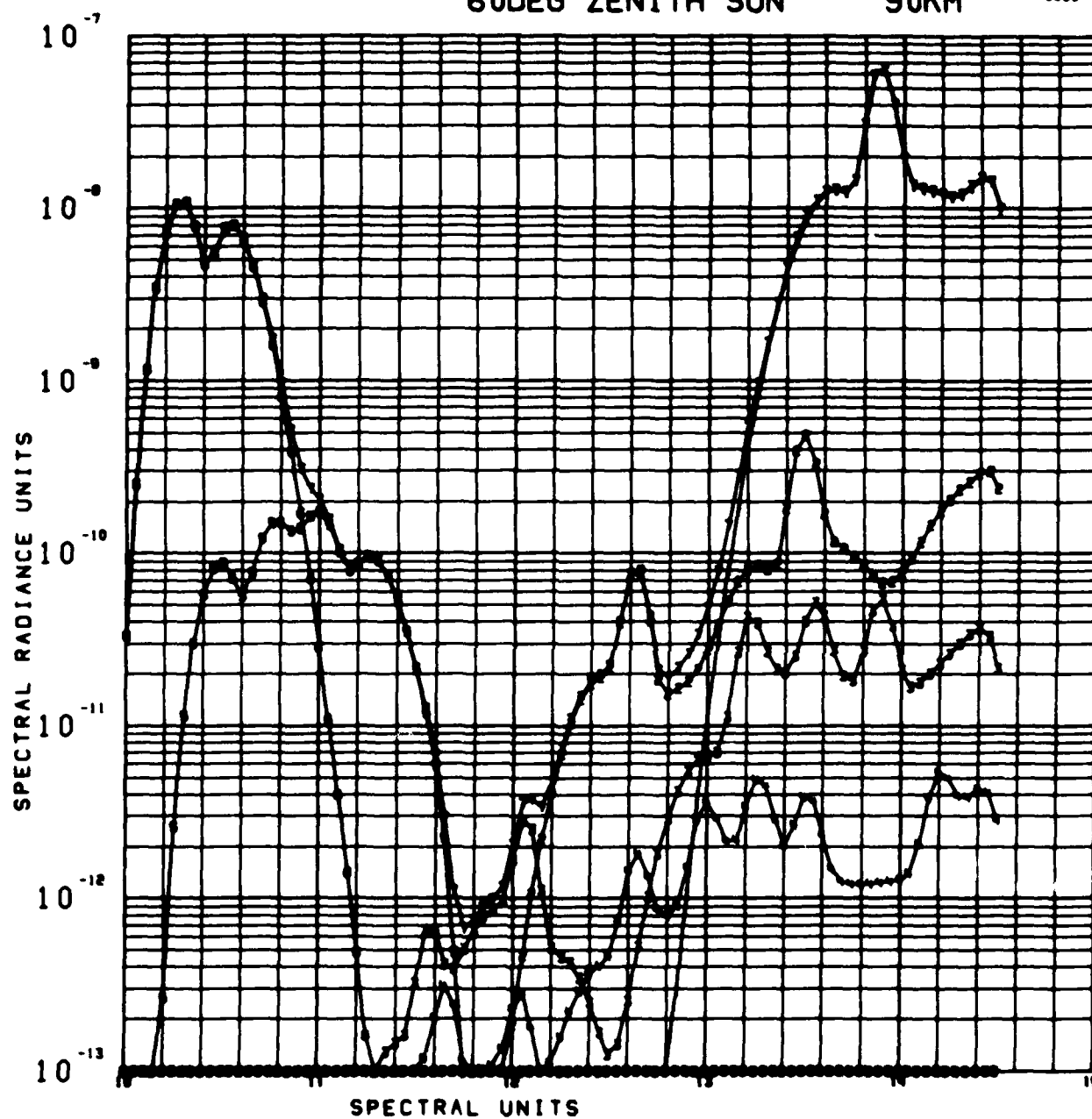
U1100/SC-000
0000 0000



60DEG ZENITH SUN

90KM

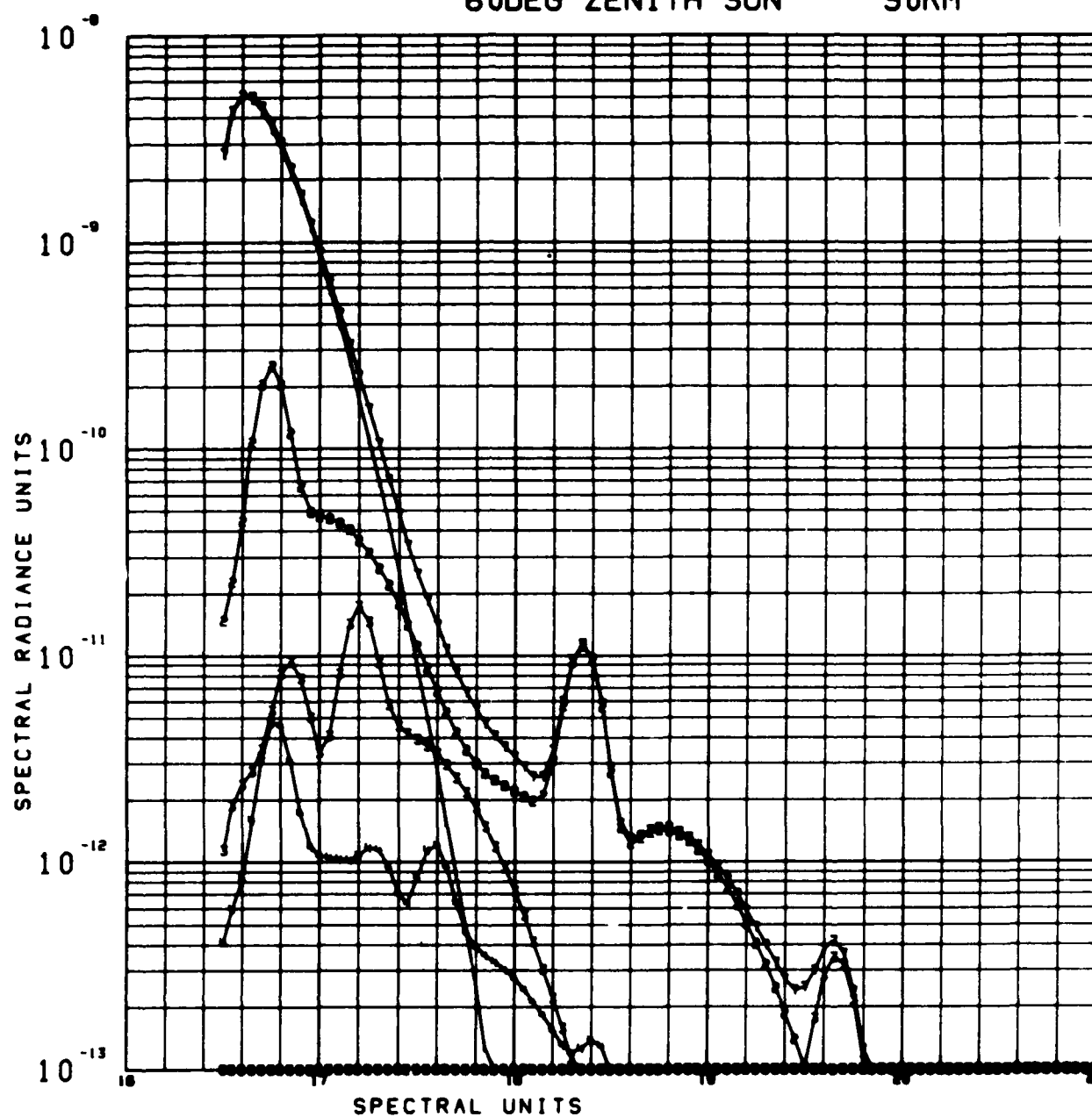
U1102/SC-028
0004 0007



60DEG ZENITH SUN

90KM

U1108/SC-020
0000 0000

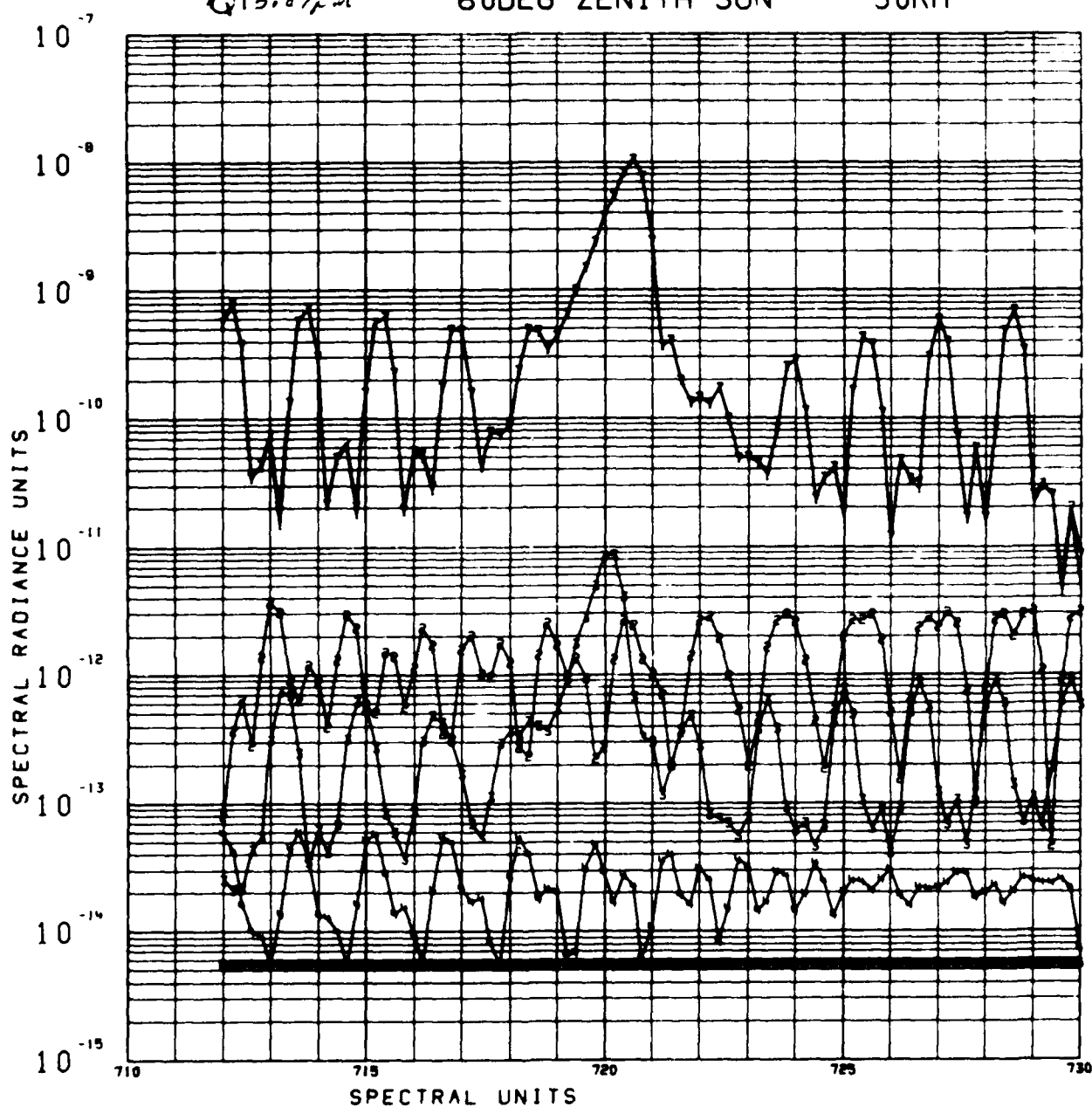


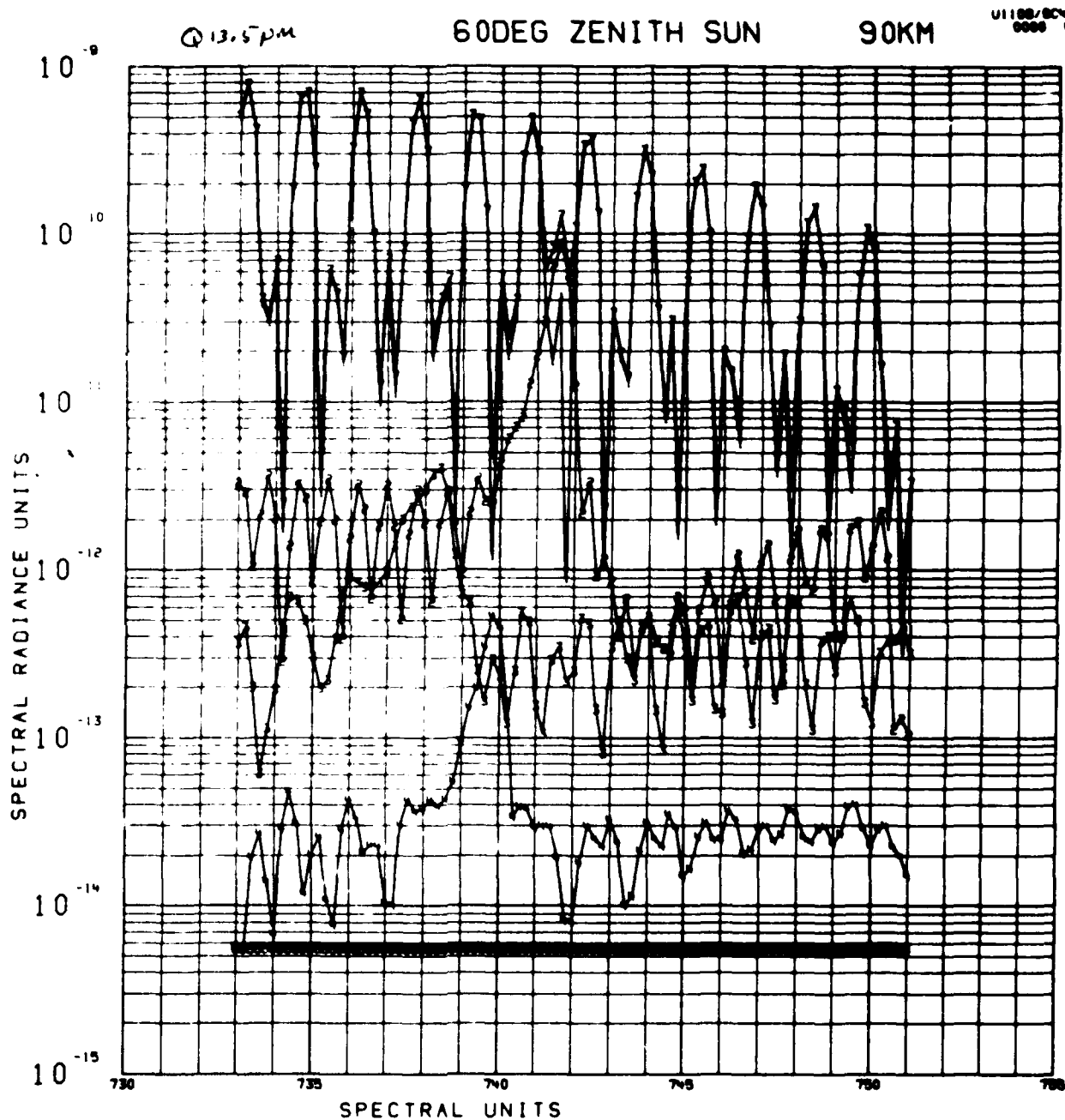
Q13.87 μ m

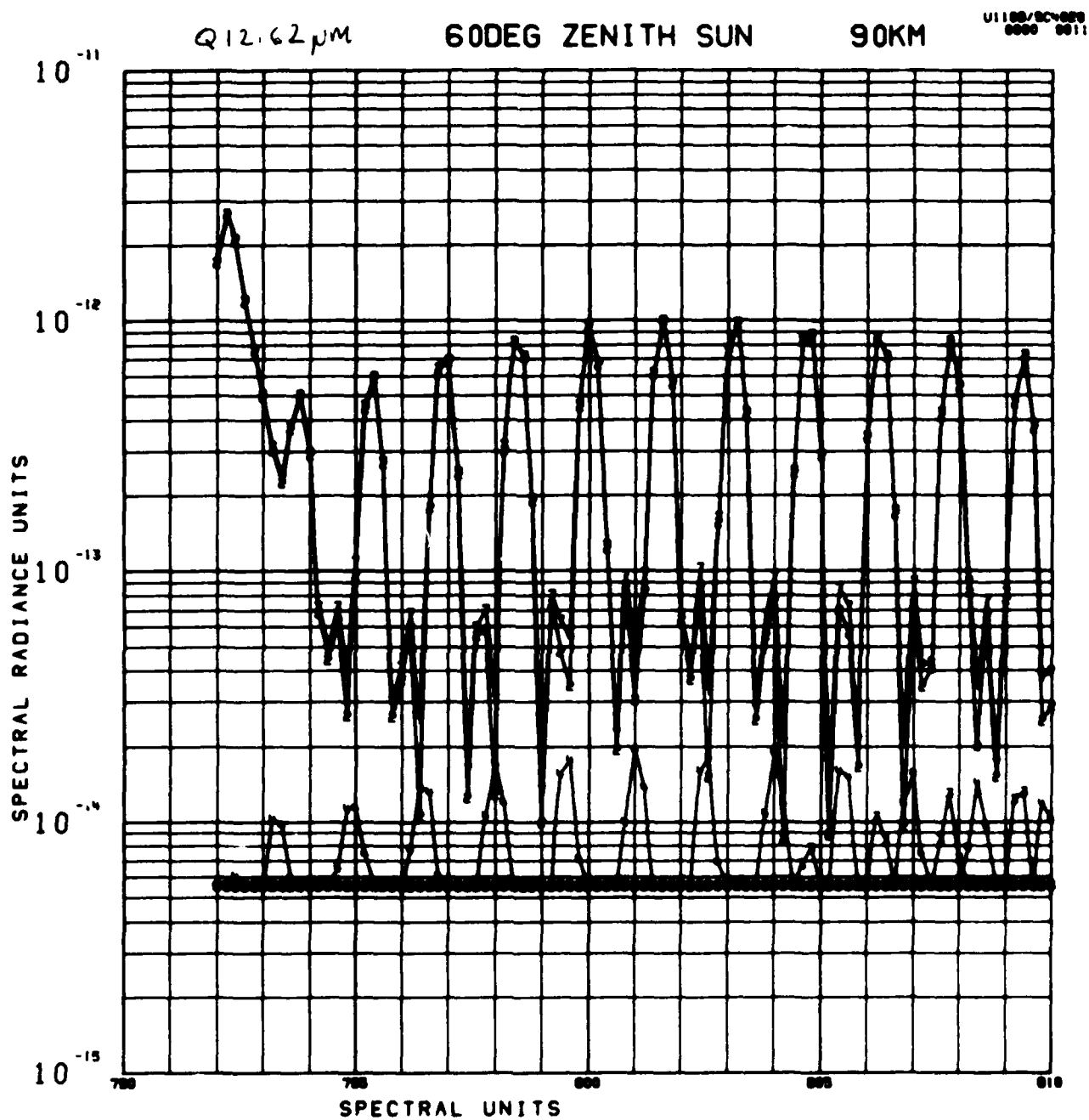
60 DEG ZENITH SUN

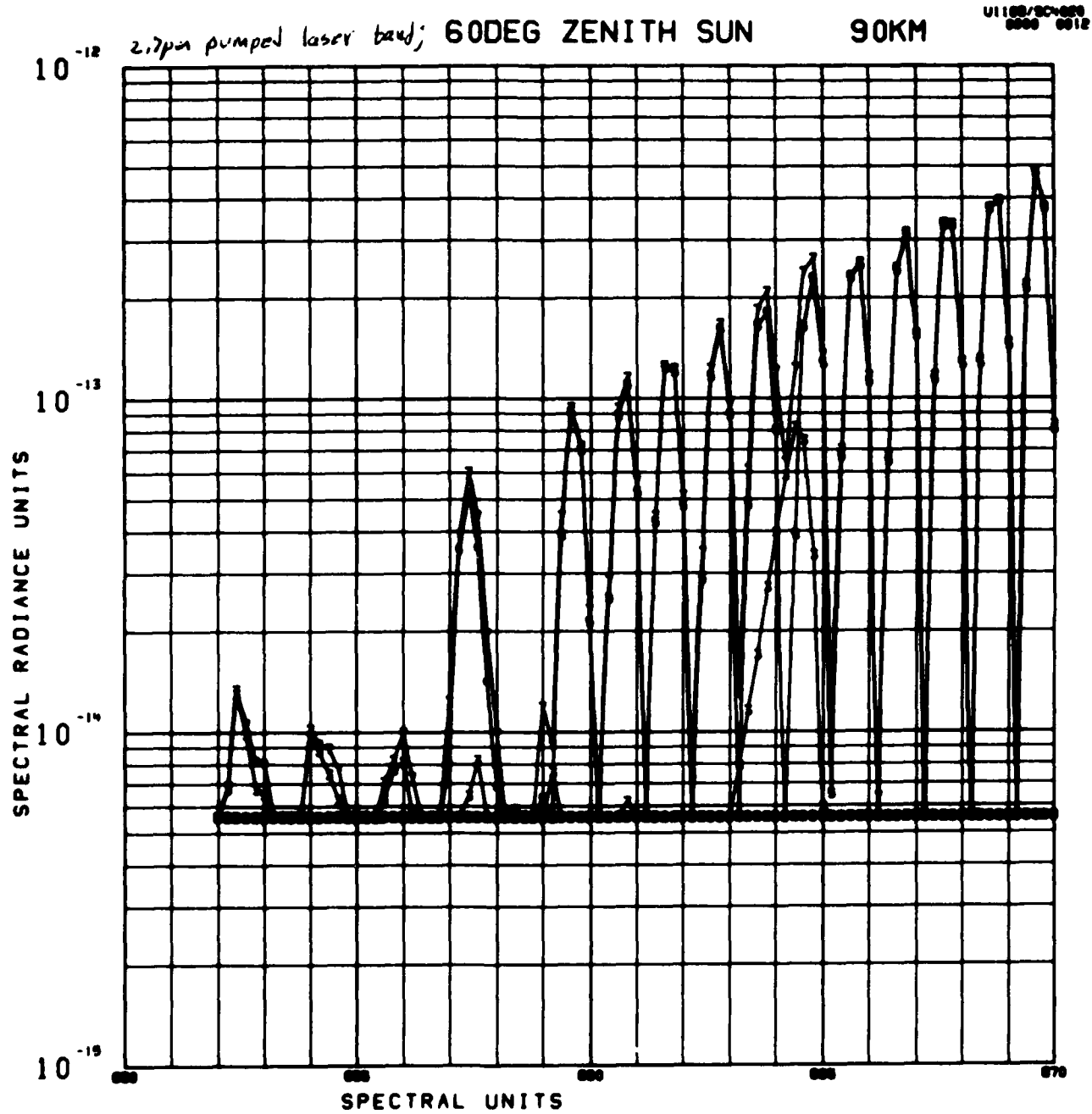
90KM

01108/SC-020
0000 0009





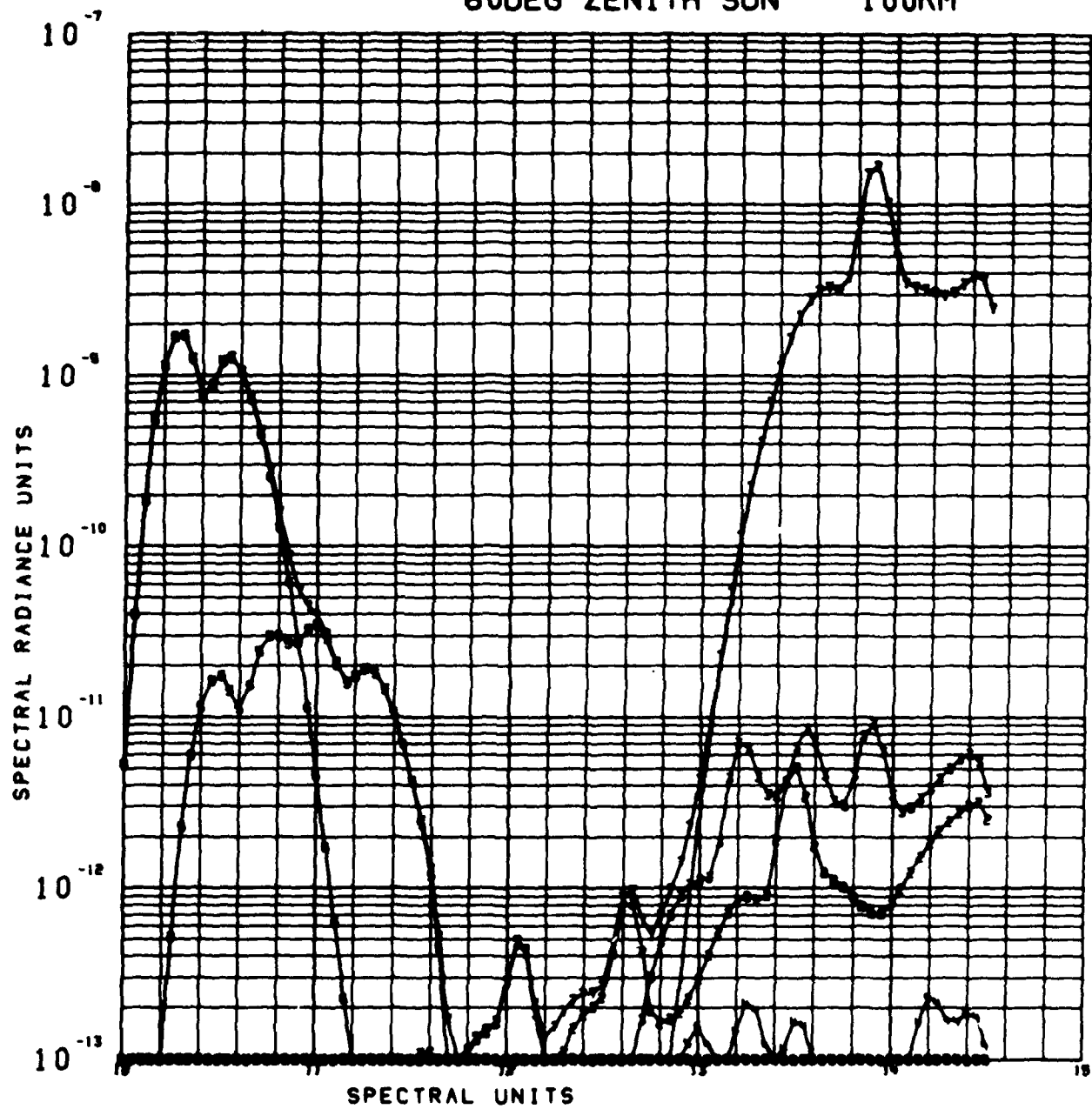




60 DEG ZENITH SUN

100KM

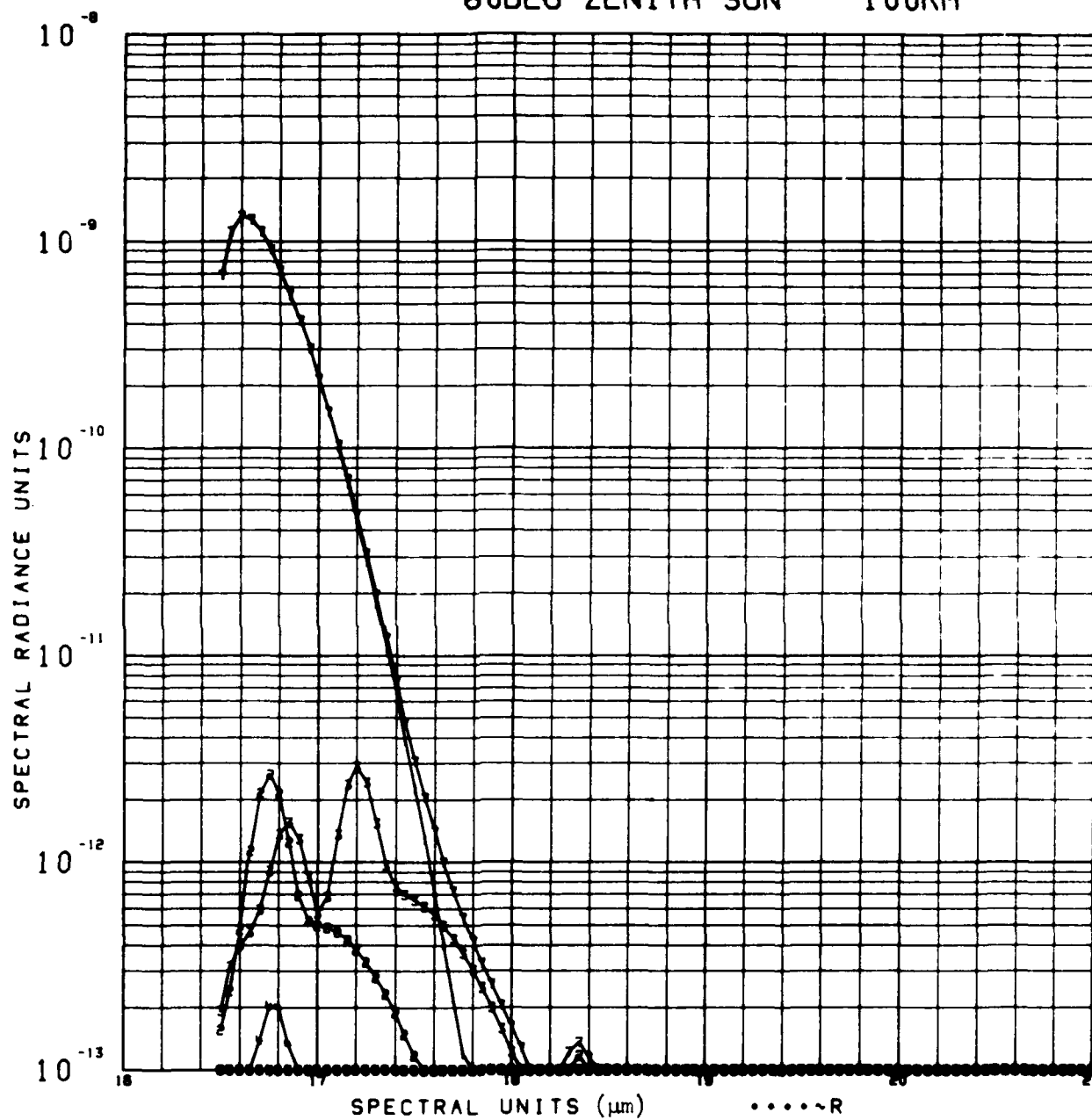
U1108/SC-029
0000 0013



60DEG ZENITH SUN

100KM

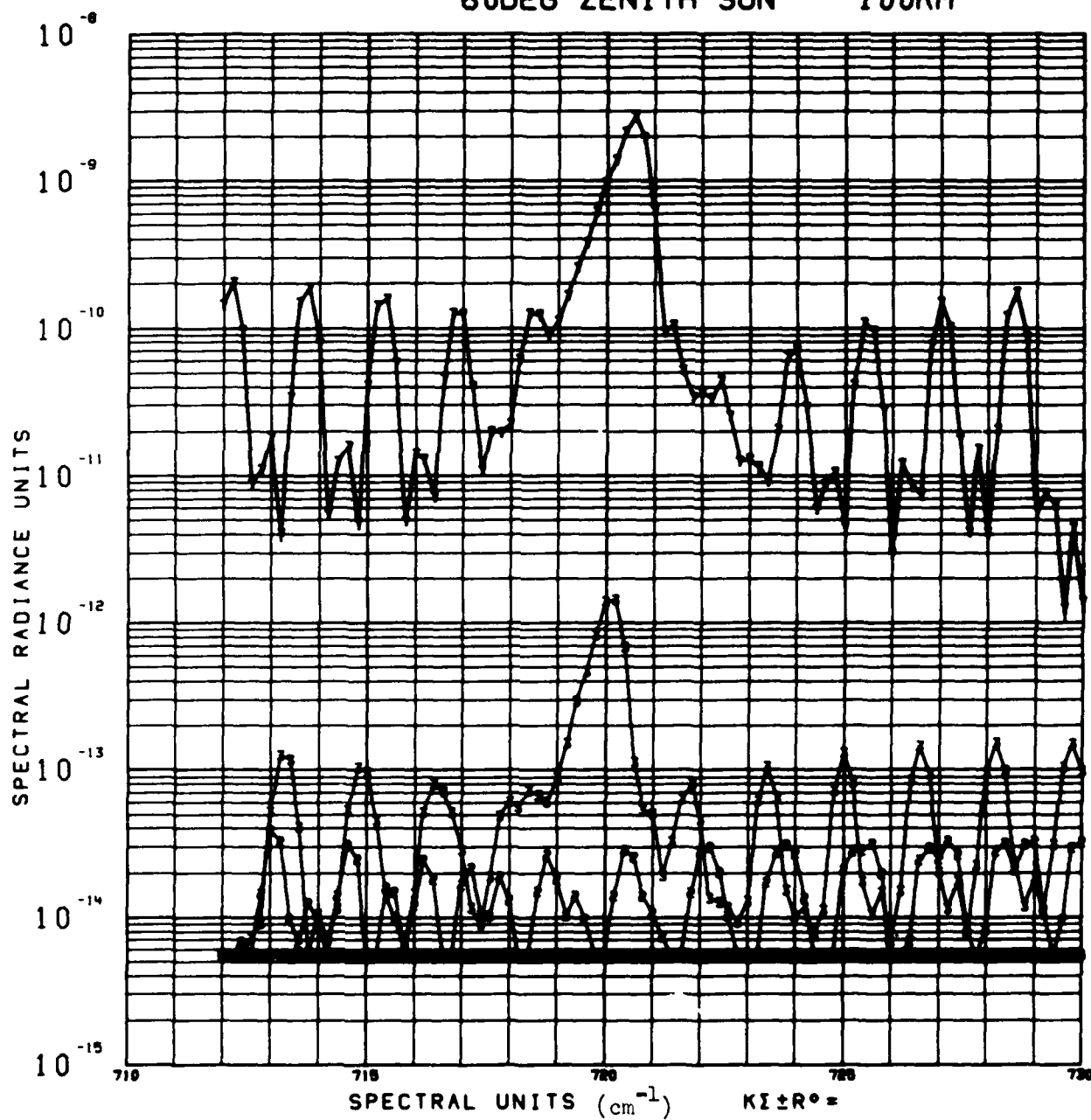
U1108/SC4020
0000 0014



60 DEG ZENITH SUN

100KM

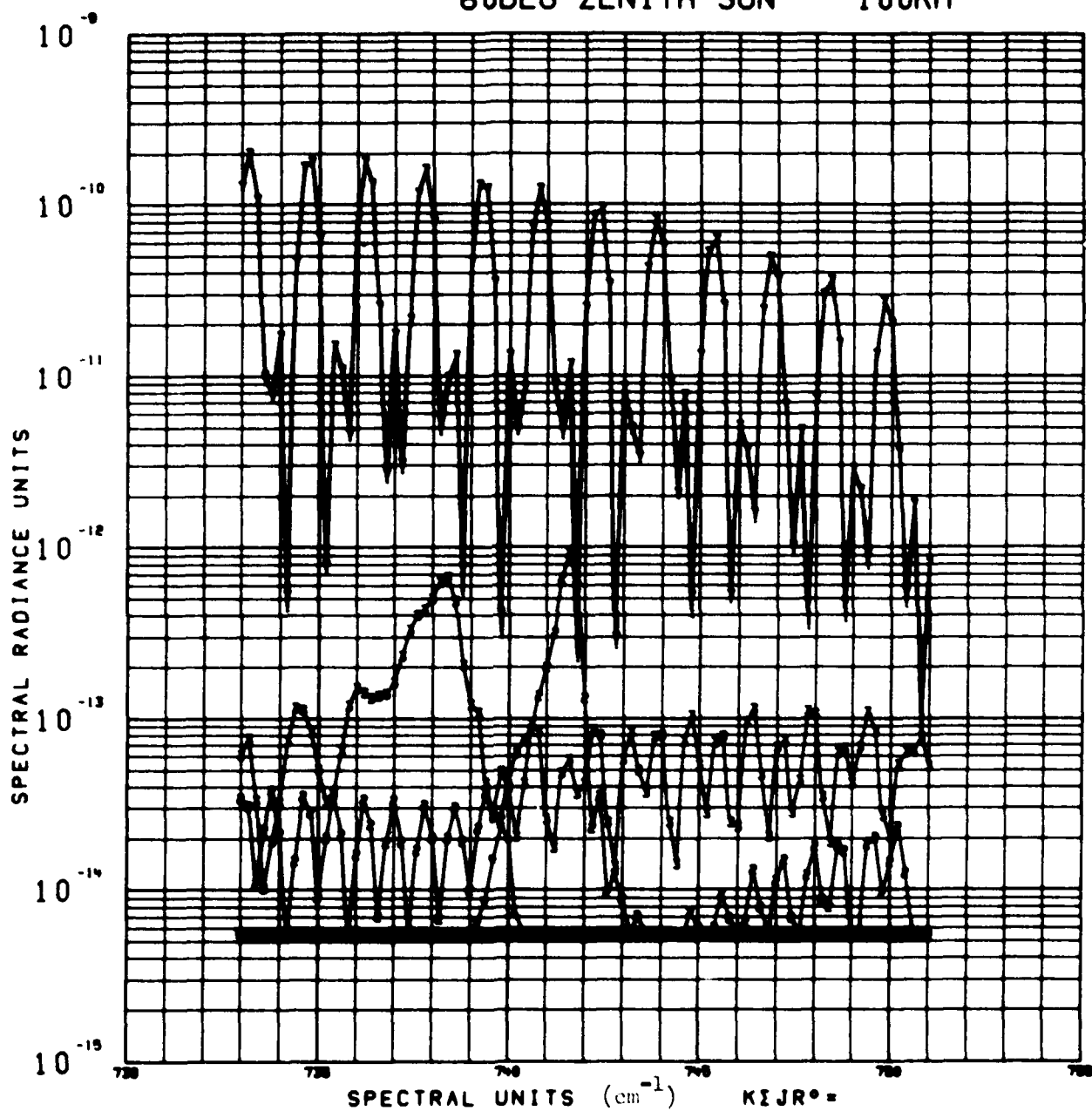
U1100/SC-000
0000 0010



60DEG ZENITH SUN

100KM

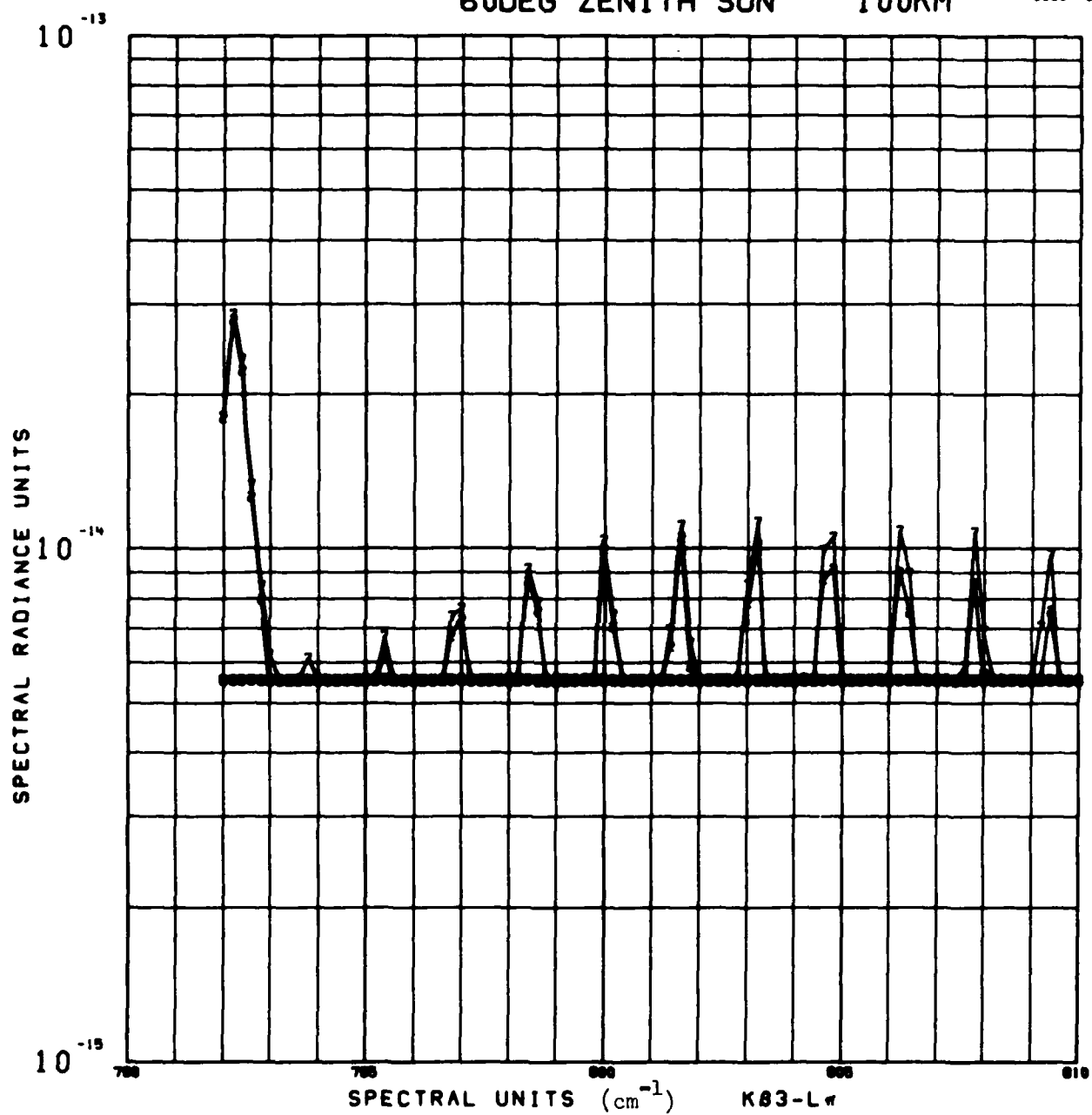
U1100/SC-000
0000 0010



60 DEG ZENITH SUN

100KM

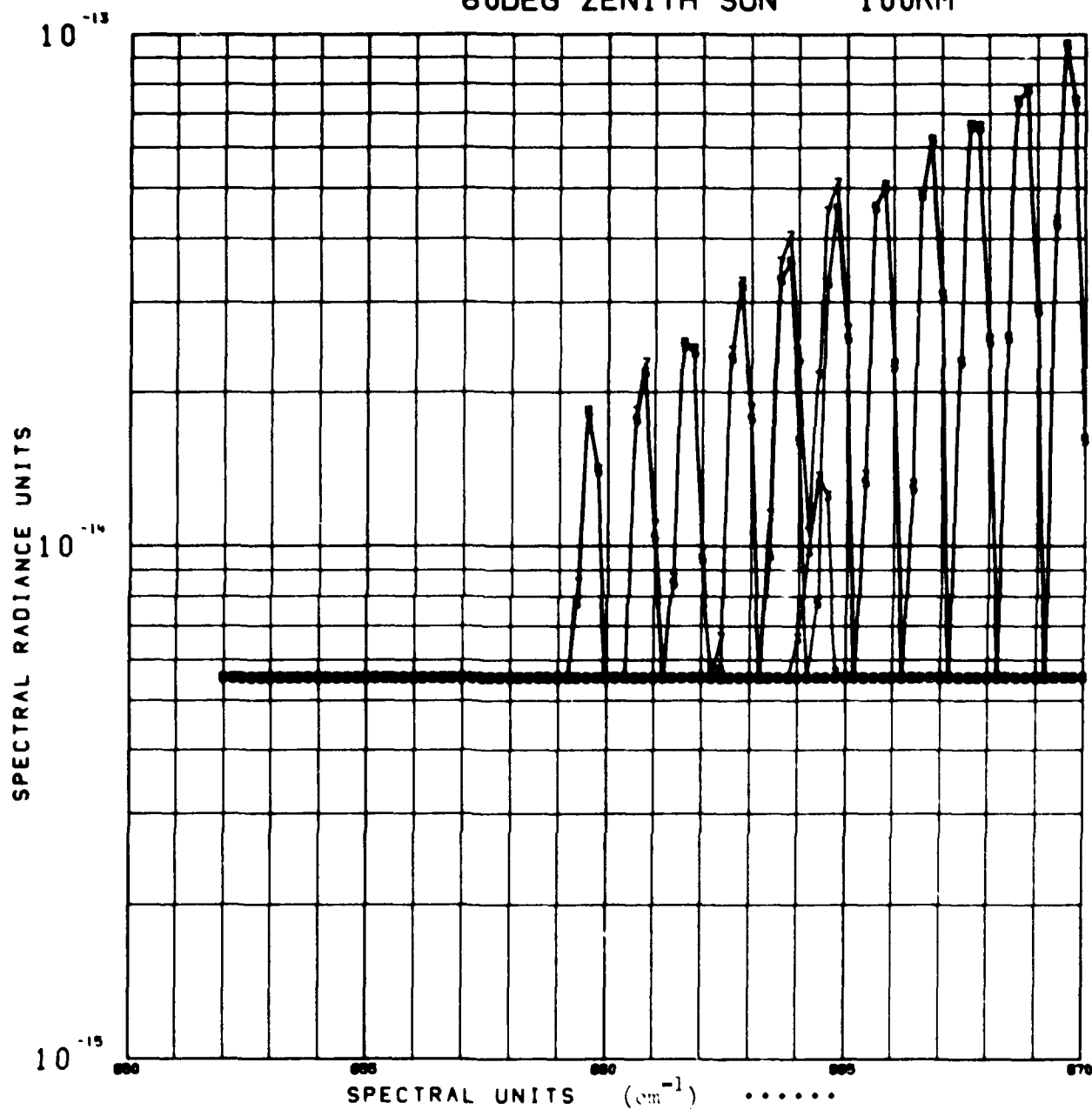
U1108/SC-826
0000 0017



60DEG ZENITH SUN

100KM

U1188/SC-889-
0000 0018



Appendix F: Vufoils Shown at the 1979 Spring
Meeting of the A.G.U.

LOCKHEED

ANALYSIS FOR 26 OCT 1978 ROCKETBORNE MEASUREMENTS OF
4.3- μ m AURORA AND AIRGLOW

- REVIEW CO₂ 4.3 μ m EMISSION MECHANISM
- APPLICATION TO 26 OCT 1978 DATA
- CONCLUSIONS:
 - (1) CO₂ AIRGLOW AND AURORA AS EXPECTED
 - (2) EVIDENCE FOR "PROMPT" AURORAL EMISSION

CO₂ 4.3 μm EMISSION MECHANISMS

N₂⁺ PRODUCED BY AURORA OR TRANSFER FROM OH(V)

$$P(N_2^+) = eq(z, t)$$

$$N_2^+ + CO_2(j) \rightleftharpoons N_2 + CO_2(j\nu_3) \quad ; \quad k_2$$

$$CO_2(j\nu_3) \rightleftharpoons CO_2(j) + h\nu$$

$$\begin{array}{l} N_2^+ + O \rightleftharpoons N_2 + O \quad ; \quad \frac{k_{10}}{k_{ell}} \\ N_2^+ + O_2 \rightleftharpoons N_2 + O_2^+ \\ CO_2(j\nu_3) + M \rightleftharpoons CO_2(j\nu_1\nu_2) + M \quad ; \quad \frac{k_1}{k_{ell}} \end{array}$$

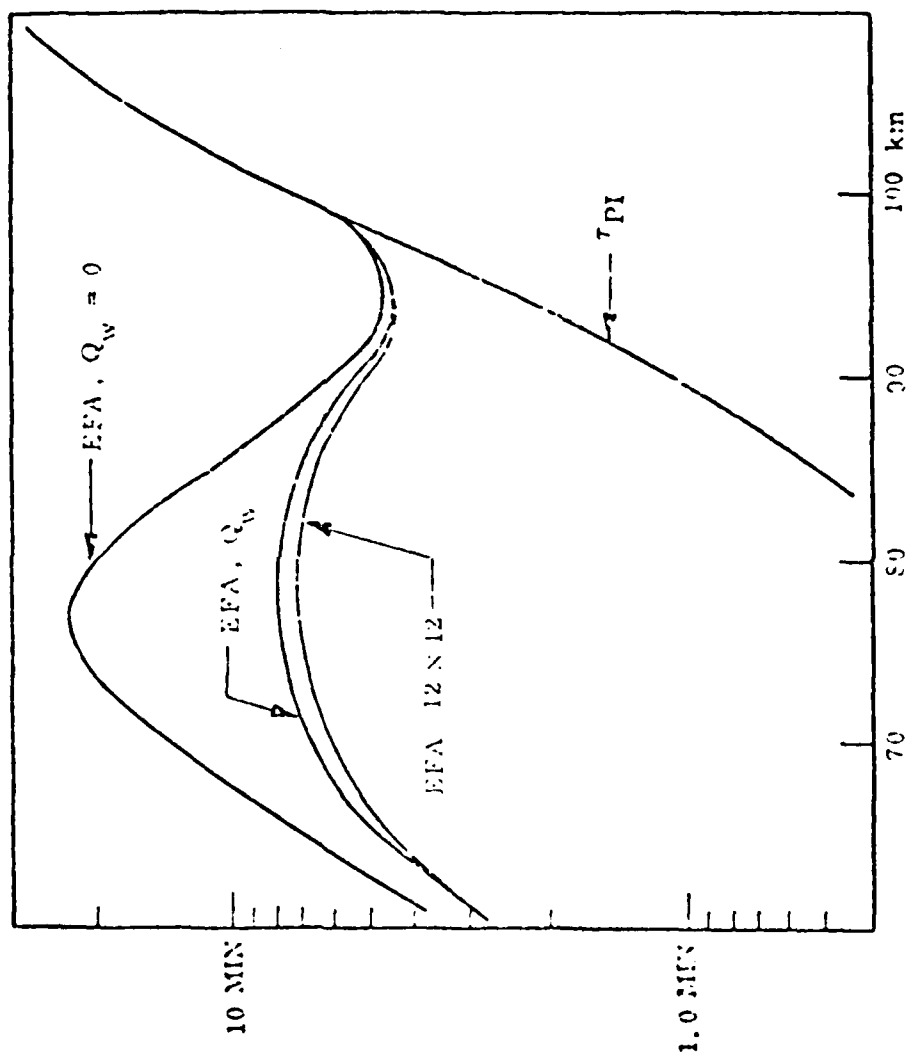
See JGR 72 638 (1974) for notation definition

Table I. THE WEAK CO_2 ν_3 BANDS

| j | $\text{CO}_2(j\nu_3) \rightarrow (j)$ | Isotope |
|----|---------------------------------------|---------|
| | Transition | |
| 2 | $00^0_1 \rightarrow 00^0_0$ | 636 |
| 3 | $00^0_1 \rightarrow 00^0_0$ | 628 |
| 4 | $00^0_1 \rightarrow 00^0_0$ | 627 |
| 5 | $01^1_1 \rightarrow 01^1_0$ | 626 |
| 6 | $01^1_1 \rightarrow 01^1_0$ | 636 |
| 7 | $01^1_1 \rightarrow 01^1_0$ | 628 |
| 8 | $01^1_1 \rightarrow 01^1_0$ | 627 |
| 9 | $02^2_1 \rightarrow 02^2_0$ | 626 |
| 10 | $02^0_1 \rightarrow 02^0_0$ | 626 |
| 11 | $10^0_1 \rightarrow 10^0_0$ | 626 |

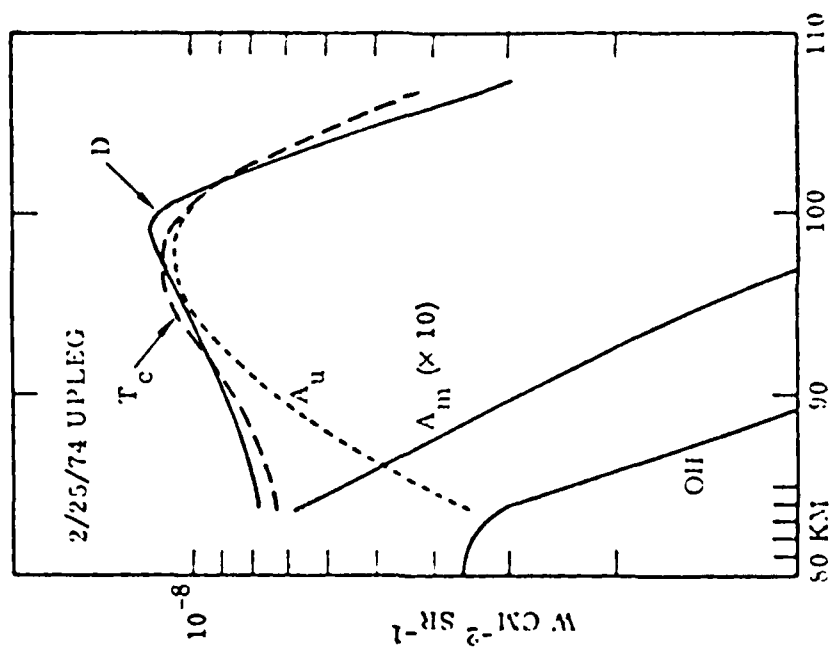
LOCKHEED

RESPONSE TIME FOR CO₂ 4.3 μ m "AURORA"



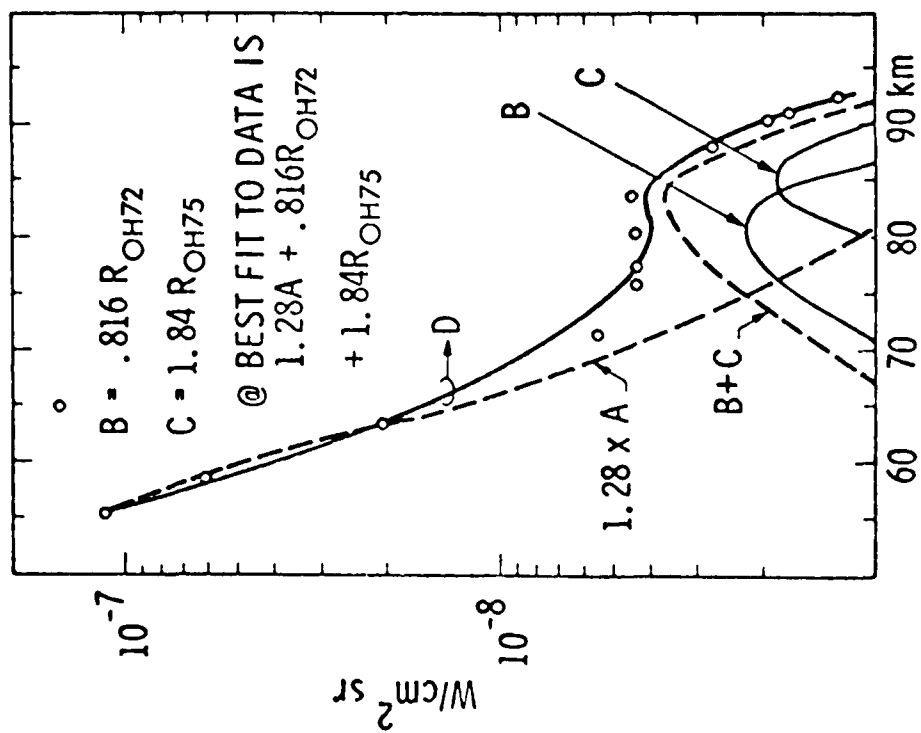
LOCKHEED

4.3 μm DATA ANALYSIS



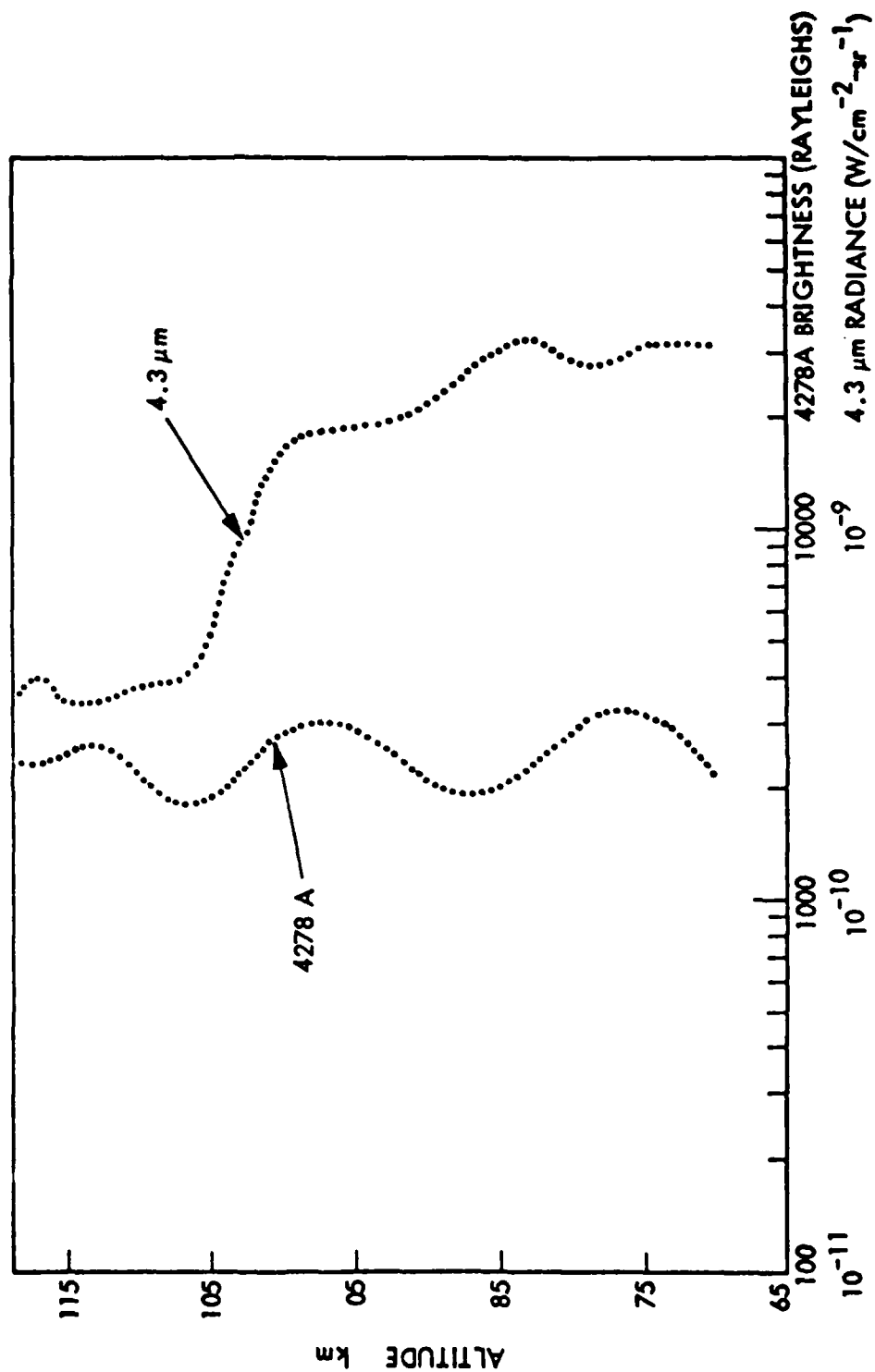
LOCKHEED

4/11/74 4.3 μm DATA, QUIET NIGHT CONDITIONS



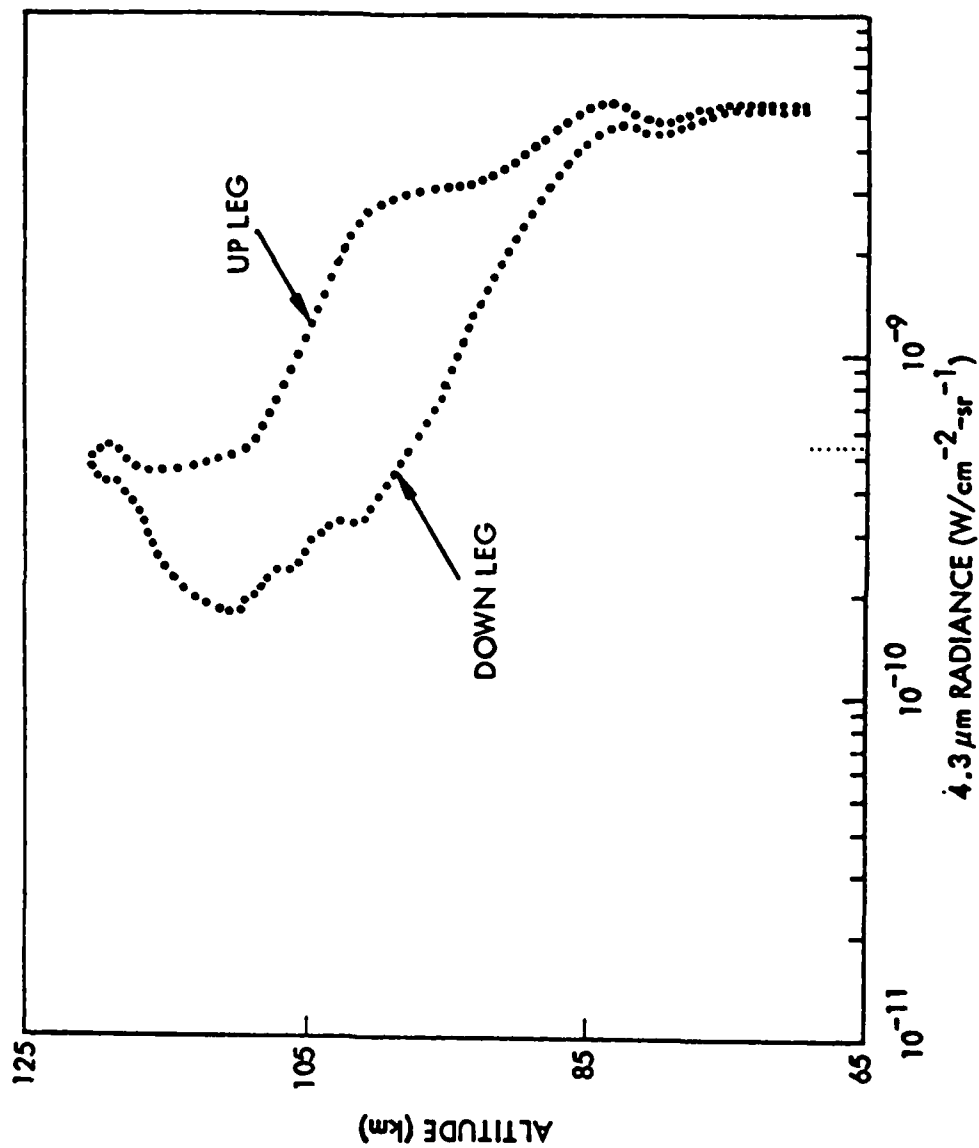
LOCKHEED

ROCKET ASCOUT



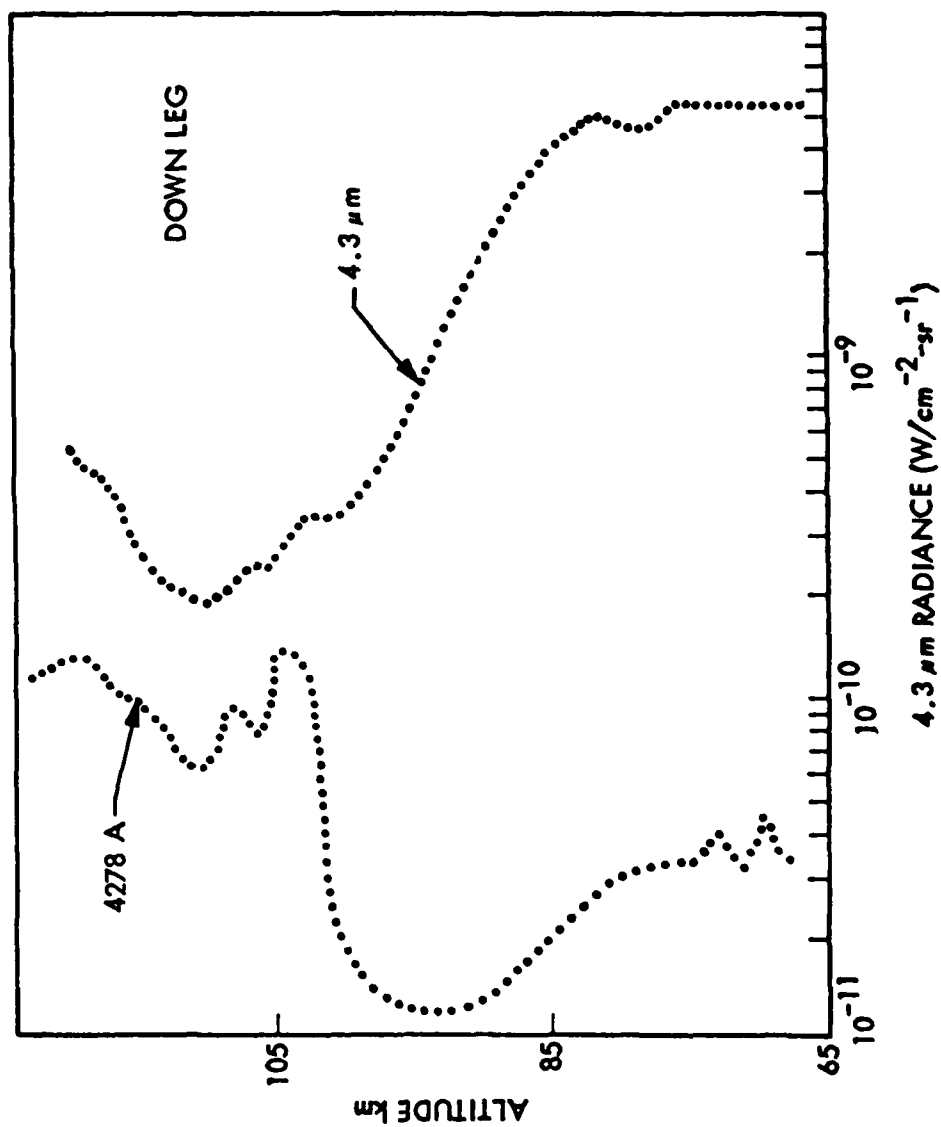
LOCKHEED

NR4-C-1 4.3-MICRON RADIOMETER



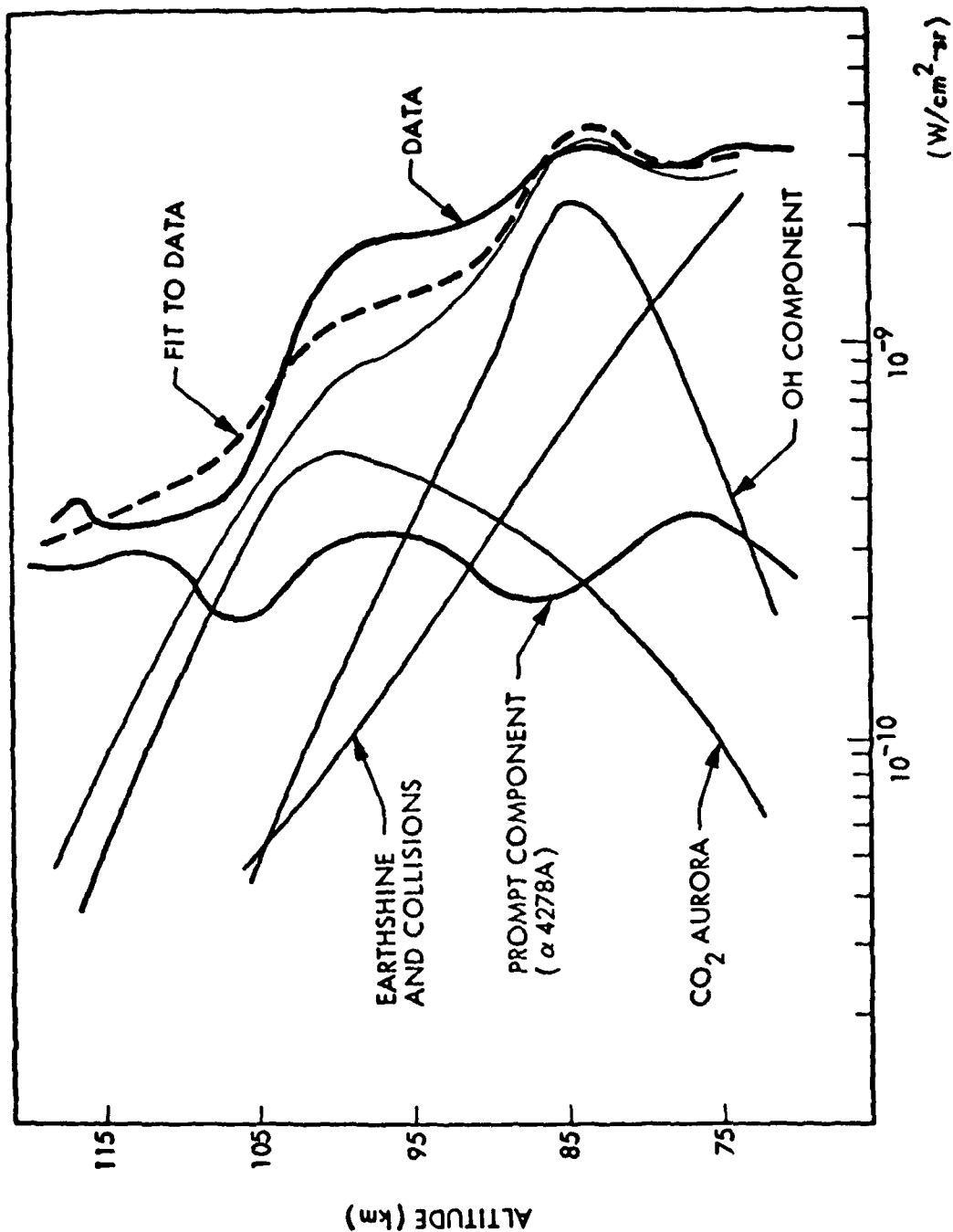
LOCKHEED

NR4-C-1 2.7- μ m RADIOMETER



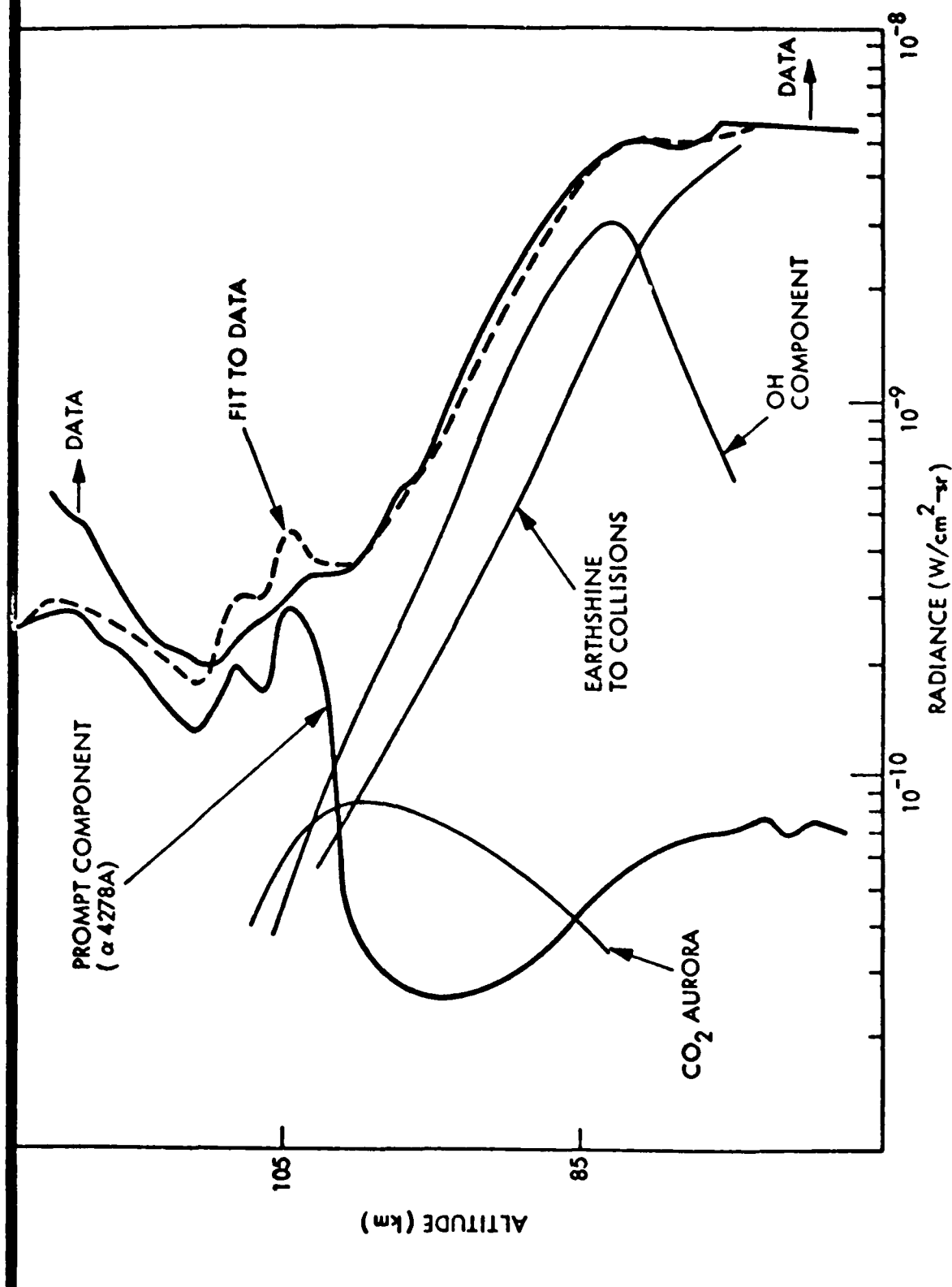
LOCARNEE

MODELING THE 10/26/78 UPLEG DATA



LOCKHEED

MODELING THE DOWNLEG 10/26/78 DATA

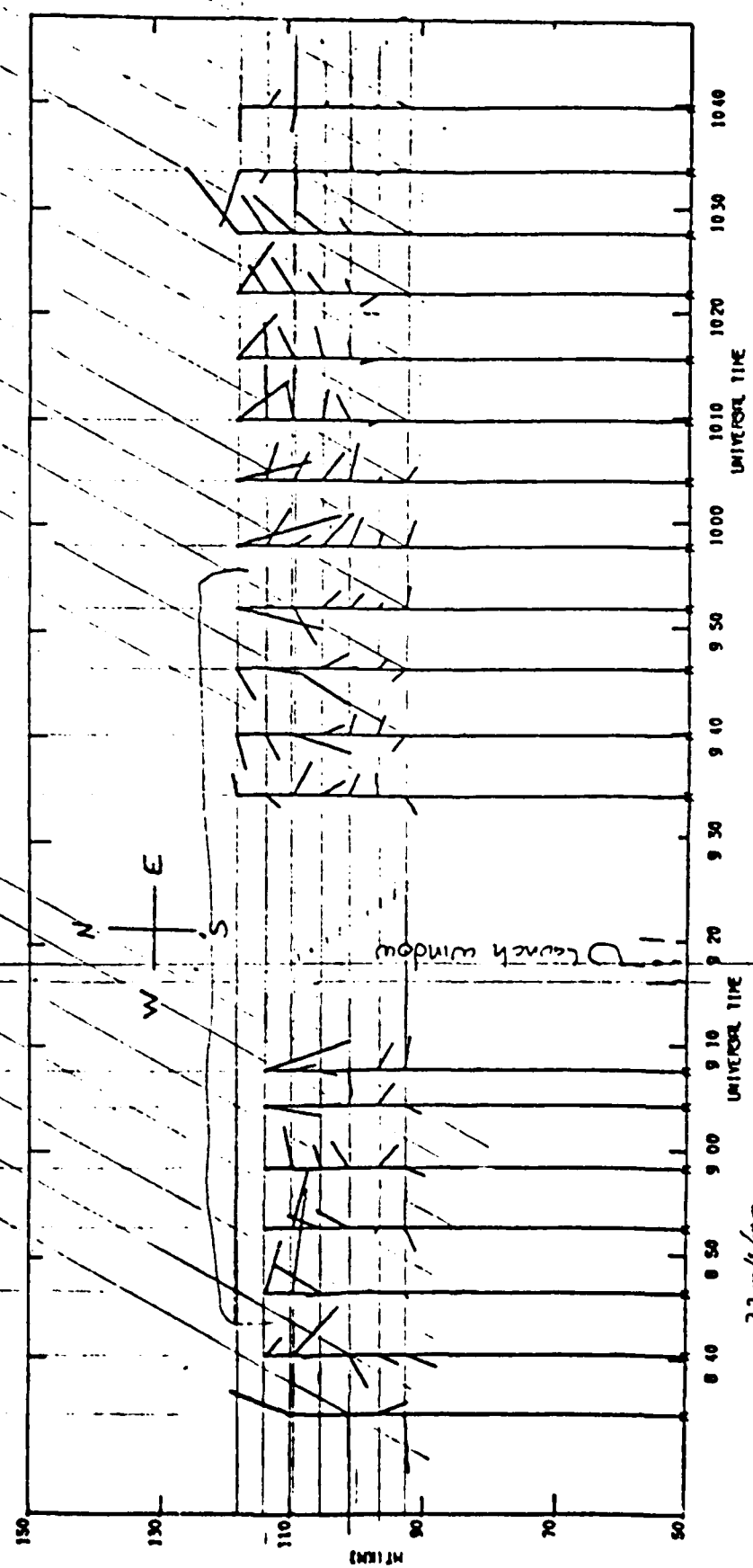


CONCLUSIONS

- A PROMPT MECHANISM IS INDICATED
 - 0.3 % ENERGY EFFICIENCY FOR $Z \gtrsim 115$ km
 - $\tau \gtrsim$ SEVERAL SECONDS
- CO₂ AIRGLOW AND AURORA AS EXPECTED

Launch 9:16.52
 9:15.52

Preliminary Chat. Radar wind
 data, courtesy of M. Baron



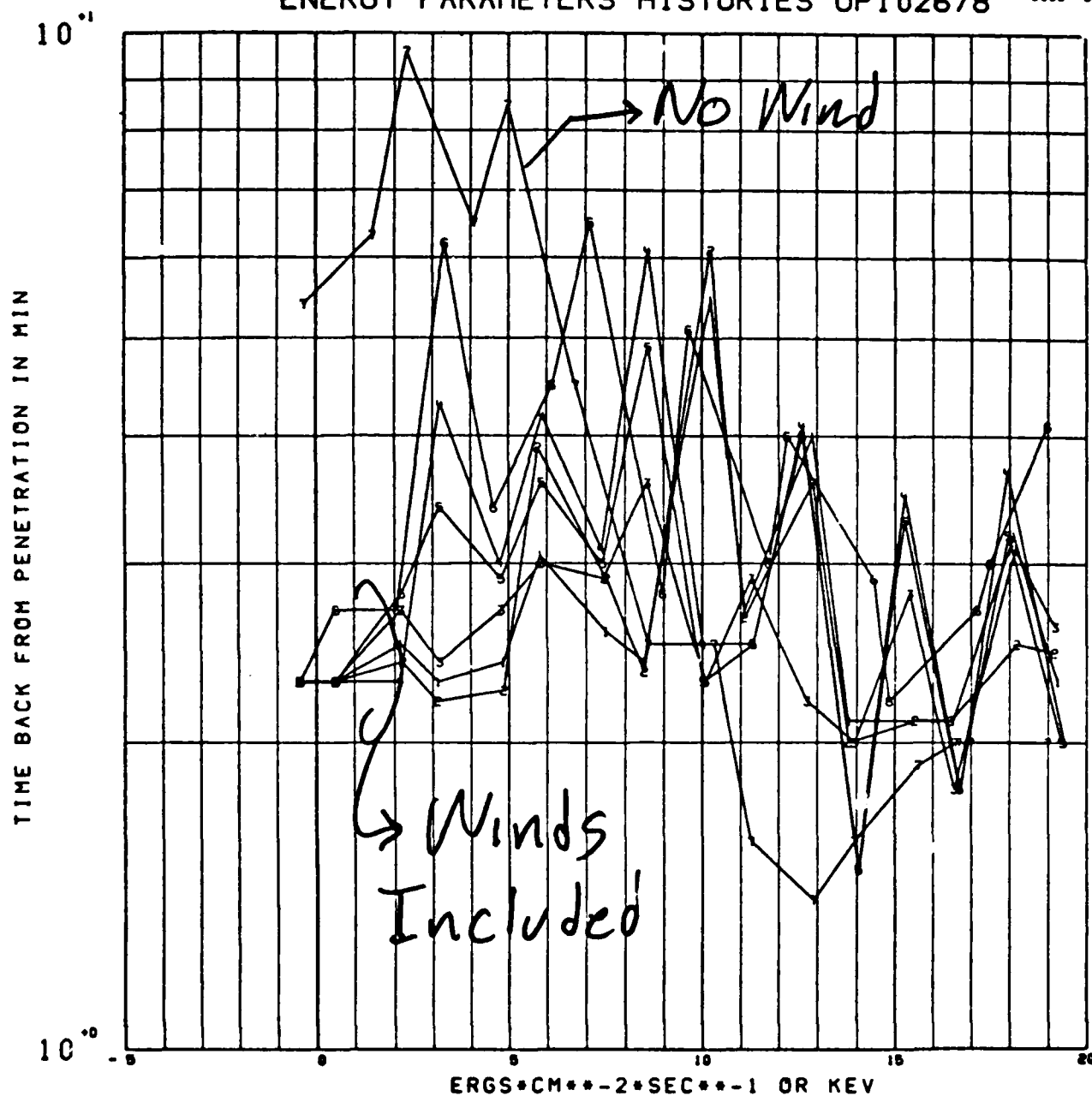
32 m/s/mm
 500 m/s

Neutral Winds

Figure 9

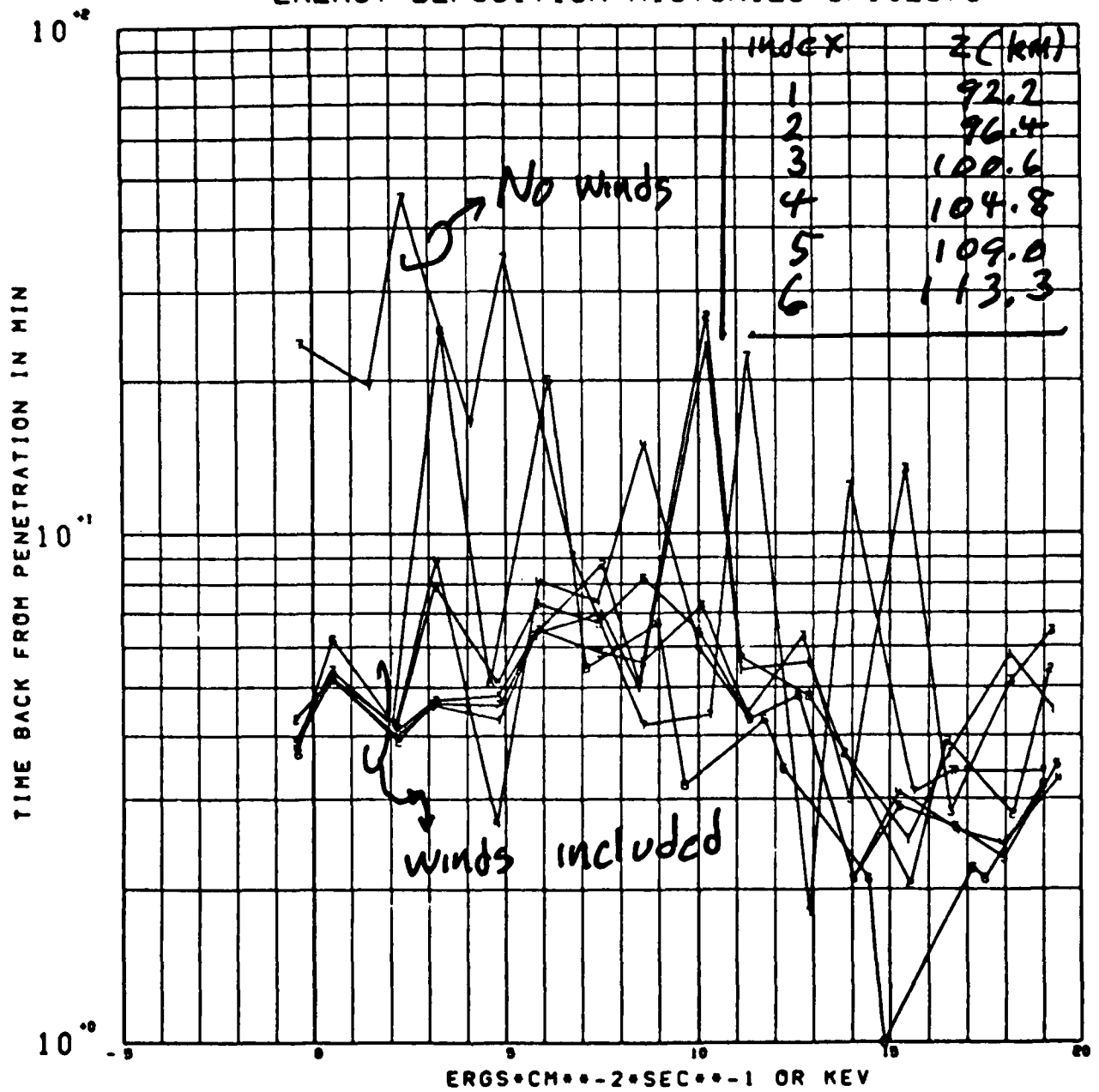
ENERGY PARAMETERS HISTORIES UP102678

U1108/SCN020
0000 0002



ENERGY DEPOSITION HISTORIES UP102678

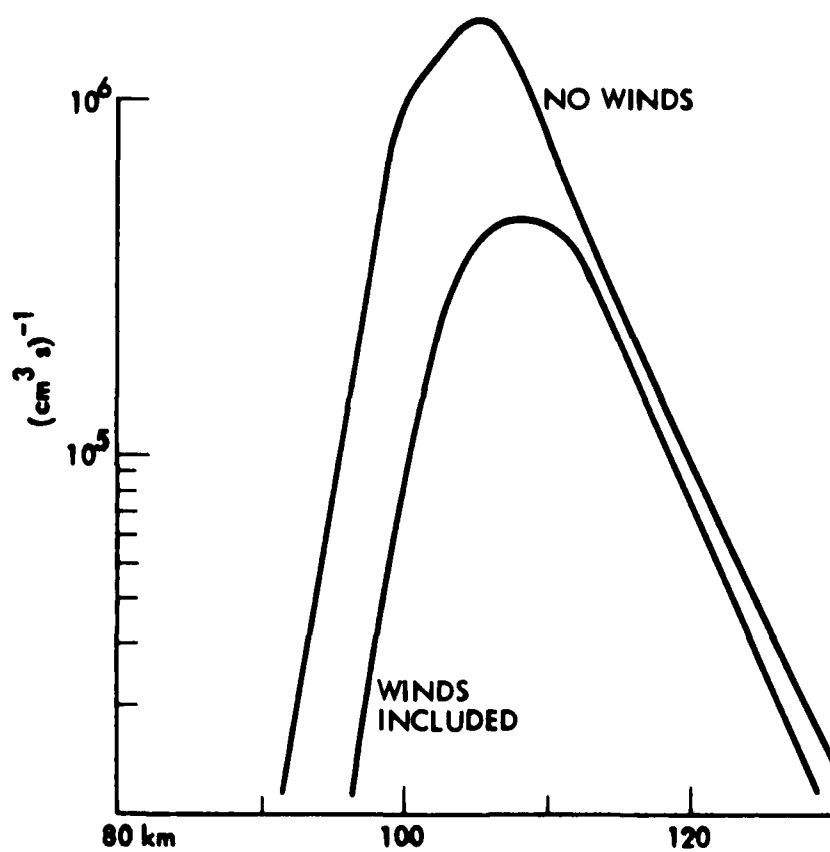
U1100/SC4020
0000 0001



4.3 μm RADIOMETER PASS BAND



UP 10/26/78 QUASI STATIONARY CO₂ (001) PRODUCTION RATE



Appendix G: Calculation of Cell Wheel Interchange Weighting Functions

In this appendix we discuss calculations of cell interchange weighting functions W^{ij} for an absorption cell wheel filtered radiometer that are analogous to those given on Fig. 5-9 in the article "The Infrared Temperature Profile Radiometer (ITPR) Experiment" by Smith et al., which appears in the NASA Nimbus 5 User's Guide, 1972. A weighting function may be generated to calculate the change in signal R^{ij} that is observed on replacing absorption cell i by cell j . The form of the weighting function $W^{ij}(\sigma N)$ then is

$$W^{ij} = \int \frac{dx}{\sqrt{\pi}} b \varphi(a, bx) \sum_m \sum_B s_{Bm} g_m e^{-\tau_{Bm}(z,x)} (e^{-\tau_{Bm}^i(x)} - e^{-\tau_{Bm}^j(x)}). \quad (G-1)$$

The quantity $b = b(z) = \sqrt{T(z_L)/T(z)}$ accounts for the temperature dependent altitude variation in the Doppler line width. A reference altitude $z_L = 40\text{km}$ is utilized in the calculation, $T(z_L)$ and $T(z)$ are the atmospheric temperatures at z_L and z respectively. The Lorentz parameter $a = a(z) = (\gamma_0 c \sqrt{273^\circ\text{K}/T(z)} p(z)) / (v_D b(z))$ accounts for pressure and temperature dependent altitude variation in the collisional contribution to the line shape. We will take the $\gamma_0 = .067 \text{ cm}^{-1} \text{ atm}^{-1}$ as is recommended by Ludwig et. al., NASA SP-3080, 1972. The quantity $p(z)$ is the atmospheric pressure in atm at z , c is the speed of light and v_D is $1/2$ the e fold Doppler line width calculated for the temperature $T(z_L)$. The quantity $\varphi(a(z), b(z)x)$ is the Voigt absorption line profile at z . The quantity s_{Bm} is the normalized line strength; it may be calculated for the branches $B = P, Q$ and R by formulas (9) through (12) given by McClatchey et. al., on page 13 of their report AFCRL-TR-73-0096. The sum $\sum_B s_{Bm} = 1$. The line index no. m is defined on page 11 of AFCRL-TR-73-0096. The quantity $g_m = g_m(z)$ is the fractional population of the rotational ground state corresponding to index m , i.e.

$$g_m(z) \approx (2m+1) \exp(-hc B m(m+1)/kT(z)) / (wkT(z)/2hc B \sqrt{\pi}) \quad (G-2)$$

where $hc/k \cong 1.439 \text{ cm}^{\circ}/\text{k}$ and the CO_2 rotation constant $B \cong 0.390218 \text{ cm}^{-1}$.

The quantity $\tau_{Bm}(x, z)$ is the atmospheric CO_2 optical depth above z at x dimensionless frequency units from the center of the line designated by Bm .

The quantity $x = (\nu_{Bm} - \nu)/\nu_D$ where ν_{Bm} is the Bm line center frequency. The quantity $w = 1/2$ for the 626 001 \rightarrow 000 band. The quantity τ_{Bm} is given by

$$\tau_{Bm}(z, x) = \sigma \int_z^{\infty} dz' [\text{CO}_2]_z \cdot b(z') \varphi(a(z'), b(z')x) s_{Bm} g_m(z'). \quad (\text{G-3})$$

The quantities $\tau_{Bm}^i(x)$ and $\tau_{Bm}^j(x)$ are the optical depths across the i th and j th cells at frequency x from the center of the Bm line. They are given by

$$\tau_{Bm}^i(x) = \sigma N^i b^i \varphi(a^i, b^i x) s_{Bm} g_m^i \quad (\text{G-4})$$

where N^i is the CO_2 column density across the i th cell, $b^i = \sqrt{T(z_L)/T^i}$ where T^i is the temperature of the i th cell, a^i is the Lorentz parameter for the i th cell which is determined by T^i , $[\text{CO}_2]^i$ and $[B]^i$ where $[\text{CO}_2]^i$ and $[B]^i$ are the number densities of CO_2 and a possible broadener gas B in the i th cell, g_m^i is determined by T^i via equation (G-2) above.

The change in nadir radiance R^{ij} which occurs when cell i is replaced by cell j is given by

$$4\pi R^{ij} = \int_0^{N_L} dN' w^{ij}(\sigma N') \Omega(N') S(\sigma N') \quad (\text{G-5})$$

where $\Omega(N') S(\sigma N')$ is defined in the paper by Kumer and James (J. Geophys. Res. 79, 638, 1974), it is proportional to the atmospheric CO_2 626 001 \rightarrow 000 $4.3 \mu\text{m}$ volume emission rate. Implementation of eqns. (G-1) through (G-5) resulted in the calculations the cell interchange weighting functions w^{ij} and the corresponding cell interchange nadir auroral signals R_A^{ij} that are shown on Figures 3-6 and 3-7 respectively in the main text.

Appendix H: Arc Overfly Nadir Viewing HIRIS NESR Calc.

- o $\Delta\nu_c = 60 \text{ cm}^{-1}$ cold filter width, 80% transmission
- o Resolution $\Delta\nu = 0.5 \text{ cm}^{-1}$ achieved by stroke of Michelson
- o Aperture $\approx 2.54 \text{ cm}$ (diameter)
- o $\text{FOV } \alpha_m = (2/(2347 \text{ cm}^{-1}/.5 \text{ cm}^{-1}))^{1/2} = 2.07 \times 10^{-2} \approx 20.7 \text{ mrad}$
- o Fill up FOV with 250°K black body earth
- o $B_\nu(250^\circ, 2347 \text{ cm}^{-1}) = 3.742^{-12} (\nu^3/\pi)(e^{T_0/250}-1)^{-1} = 2.1 \times 10^{-8} \text{ w/cm}^2 \text{ str cm}^{-1}$ where $\nu = 2347 \text{ cm}^{-1}$ and $T_0 = 1.439\nu$
- o HIRIS throughput $\phi_H = [\pi \times (2.54/2) \times (21 \times 10^{-3}/2)]^2 \times 0.4 = 7 \times 10^{-4}$ (assume 0.4 optics transmission)
- o Photon energy $h\nu = 4.66 \times 10^{-20} \text{ Joule}$
- o $\Delta f = 120 \text{ Hz} = N(\# \text{ of resolution elements})$
- o Quantum efficiency $\eta = 0.2$ at $4.3\mu\text{m}$ for $A_s : S_i$
- o $\text{NER} = (B\nu \Delta\nu_c \phi_H \Delta f / \eta h\nu)^{1/2} (\frac{2 h\nu}{\phi_H}) = 4.5 \times 10^{-10} \text{ w/cm}^2 \text{ str (PC formula)}$
- o $\text{NESR} = \text{NER}/\Delta\nu \approx 9 \times 10^{-10} \text{ w/cm}^2 \text{ str cm}^{-1}$

This NESR is achieved in 1 sec. of integration time. Note that use of a field widened interferometer would decrease the NER as computed above by the ratio of the improvement in α_m . Other significant improvements by use of the field widened interferometer could be achieved by use of an In:Sb PV detector rather than the $A_s : S_i$ PC detector.

Appendix I: Contractually Supported Publications

Kumer, J. B., "Lateral Structure in the 4.3 μ m Arc", EOS 58, 460, 1977

Kumer, J. B., "Approximate and Exact Technique for Multidimensional Radiation Transport in a Plane Parallel Atmosphere; Application to the 4.3 μ m Auroral Arc", J. Quant. Spectrosc. Radiat. Transfer 19, 649, 1978

Kumer, J. B., A. T. Stair, Jr., Ned Whiller, K. D. Baker and D. J. Baker, "Evidence For an OH γ^V N₂ γ^V CO₂(ν_3) \rightarrow CO₂ + hv (4.3 μ m) Mechanism for 4.3 μ m Airglow", J. Geophys. Res. 83, 4743, 1978

Baker, D. J., G. D. Frodsham, J. B. Kumer, A. T. Stair, Jr., J. C. Ulwick, "Rocketborne Measurements of Infrared Aurora and Airglow Emissions at 4.3 μ m", EOS 60, 328, 1979

Kumer, J. B., D. J. Baker, G. D. F. Frodsham, A. T. Stair, Jr., J. C. Ulwick, "Analysis for Measurements of 4.3 μ m Airglow and Aurora; Evidence for a Prompt 4.3 μ m Auroral Component", to be submitted to J. Geophys. Res., Oct. 1979

DISTRIBUTION LIST

DEPARTMENT OF DEFENSE

Director
Defense Advanced Rsch. Proj. Agency
Attn: LTC W.A. Whitaker

Defense Documentation Center
Attn: TC (2 Copies)

Director
Defense Nuclear Agency
Attn: TITL Tech. Library (3 Copies)
Attn: TISI Archives
Attn: RAEV Harold C. Fitz, Jr.
Attn: RAAZ Maj. J. Mayo
Attn: RAAE G. Soper
Attn: RAAE Maj. R. Bigoni

Dir. of Defense Rsch. & Engineering
Department of Defense
Attn: DD/S&SS(OS) Daniel Brockway

Commander
Field Command
Defense Nuclear Agency
Attn: FCPR

Chief Livermore Division
FLD Command DNA
Attn: FCPRL

DEPARTMENT OF THE ARMY

Commander/Director
Atmospheric Sciences Laboratory
U.S. Army Electronics Command
Attn: DRSEL-BL-SY-A.F. Niles
Attn: H. Ballard

Commander
Harry Diamond Laboratories
Attn: DRXDO-NP, F.H. Wiminetz
(2 Copies)

Commander
U.S. Army Nuclear Agency
Attn: Mona-We

Director
RMD Advanced Technical Center
Attn: ATC-T, M. Capps
Attn: ATC-O, W. Davies

Dep. Chief of Staff for Rsch, Dev & Acct
Department of the Army
Attn: MCB Division
Attn: DAMA-CSZ-C
Attn: DAMA-WSZC

Director
U.S. Army Ballistic Rsch. Labs.
Attn: John Mester
Attn: Tech. Library

Commander
U.S. Army Electronics Command
Attn: Inst. for Expl. Research
Attn: Weapons Effects Section

Commander
CORADCOM
Attn: PP-Library

DEPARTMENT OF THE NAVY

Commander
Naval Oceans Systems Center
Attn: Code 2200 William Moler

Director
Naval Research Laboratory
Attn: Code 7712 D.P. McNut
Attn: Code 6701 J.D. Brown
Attn: Code 2600 Tech. Library
Attn: Code 7173J C.Y. Johnson
Attn: Code 6700 T.P. Coffey
Attn: Code 7709 Wahab Ali
Attn: Code 6780 D.F. Strobel
Attn: Code 6780 P. Julienne
Attn: Code 67800 J. Fedder
Attn: Code 6780 S. Ossakow
Attn: Code 6707 J. Davis

Commander
Naval Surface Weapons Center
Attn: Code WA 501 Navy NUC
Prgrms. Off.
Attn: Technical Library

Superintendent
Naval Post Graduate School
Attn: Rech Rpts Librarian

Commander
Naval Intelligence Support Ctr
Attn: Document Control

DEPARTMENT OF THE AIR FORCE

AF Geophysics Laboratory, AFSC
Attn: LKB, K.S.W. Champion
Attn: OPR, A.T. Stair, Jr.
Attn: OPR, P.G. Doyle
Attn: OPR, R. Murphy
Attn: LKO, R. Huffman

AF Weapons Laboratory, AFSC
Attn: Maj. Gary Ganong, DES

Commander
ASD
Attn: ASD-YH-EX-LTC R. Leverette

SAMSO/AW
Attn: SZJ Lt. Col. Doan

SAMSO/YN
Attn: Maj. P. Sivgals

AFTAC
Attn: Tech Library
Attn: TD

HQ
Air Force Systems Command
Attn: DLS
Attn: Tech Library
Attn: DLCAE
Attn: DLTW
Attn: DLXP
Attn: SDR
Attn: RDQ

U.S. ENERGY RESEARCH AND DEV. ADMIN.

Division of Military Application
U.S. Energy Resch & Dev Admin
Attn: Doc. Con.

Los Alamos Scientific Laboratory
Attn: DOC CON for H.V. Argo
Attn: DOC CON for M.B. Pongratz
ATTN: DOC CON for R. Brownlee
Attn: Broup AP-4, MS 567
Attn: DOC CON for J. Zinn

University of California
Los Alamos Scientific Laboratory
Attn: Librarian MS 362

Sandia Laboratories
Attn: DOC CON for W.B. Brown,
Org. 1353
Attn: Tech Library Org. 3141

Argonne National Laboratory
Records Control
Attn: Doc Con for D.W. Green
Attn: Doc Con for LIR SVCS Rpts
Sec
Attn: Doc Con for G.T. Reedy

University of California
Lawrence Livermore Laboratory
Attn: W.H. Duewer, L-262
Attn: J. Chang, L-71

U.S. Energy Resch & Dev Admin
Division of Headquarters Services,
Library Branch
Attn: Doc Con for Class. Tech.
Lib.

OTHER GOVERNMENT

Department of Transportation
Office of the Secretary
Attn: S.C. Coroniti

NASA
Goddard Space Flight Center
Attn: Code 6801 A. Temkin
Attn: Tech. Library
Attn: Code 900 J. Siry

NASA
Langley Station
Attn: Tech. Library

NASA
Ames Research Center
Attn: N-245-3 R. Whitten

Department of the Army
Bal. Miss. Def. Adv. Tech. Ctr.
Attn: W.O. Davies

Federal Aviation Administration
Attn: HAPP/AEQ-10/ James W. Rogers

Central Intelligence Agency
Attn: ED/SI RM 5G48 HQ Bldg.
Attn: NED/OS I-2G4R HQS

Department of Commerce
National Bureau of Standards
Attn: Sec. Officer for M. Krauss
Attn: Sec. Officer for L.H. Gevantman

National Oceanic & Atmospheric Admin.
Environmental Research Laboratories
Department of Commerce
Attn: G. Reid
Attn: E. Ferguson
Attn: F. Fehsenfeld

DEPARTMENT OF DEFENSE CONTRACTORS

Science Applications Inc.
Attn: D.G. Hopper

Aero-Chem Research Laboratories, Inc.
Attn: A. Fontign
Attn: H. Pergament

Aerodyne Research, Inc.
Attn: F. Bien
Attn: M. Camac

Aerospace Corporation
Attn: N. Cohen
Attn: H. Mayer
Attn: R.J. McNeal
Attn: T.D. Taylor
Attn: J. Reinheimer
Attn: R.D. Rawcliffe

AVCO-Everett Research Laboratory Inc.
Attn: Tech. Library
Attn: C.W. Von Rosenberg, Jr.

Battelle Memorial Institute
Attn: H.L. LaMuth
Attn: STOIAC

Brown Engineering Company, Inc.
Attn: N. Passino

General Research Corporation
Attn: D. Jones

California At Riverside, University of
Attn: J.N. Pitts, Jr

California At San Diego, University of
Attn: S.C. Lin

California University of Berkeley
Attn: Sec. Officer for H. Johnston
Attn: Sec. Officer for Dept of Chem.
H.L. Strauss

Calspan Corporation
Attn: C.E. Treanor
Attn: J.M. Grace
Attn: M.G. Dunn
Attn: W. Wruster

University of Colorado
Astro-Geophysics
Attn: J.B. Pearch

Colorado, University of
Office of Contracts and Grants
Attn: G.M. Lawrence, LASP

Concord Sciences
Attn: E.A. Sutton

University of Denver
Space Science Laboratory
Attn: B. Van Zyl

University of Denver
Denver Research Laboratory
Attn: Sec. Officer for D. Murcray

General Electric Company
Tempo-Center for Advanced Studies
Attn: DASAIC
Attn: W.S. Knapp
Attn: T. Stephens
Attn: D. Chandler
Attn: V.R. Strull

**General Electric Company
Space Division**

Attn: M.H. Bortner, Space Sci Lab
Attn: J. Burns
Attn: F. Alyea
Attn: P. Zavitsands
Attn: R.H. Edsall
Attn: T. Baurer

**General Research Corporation
Attn: J. Ise, Jr.**

**Geophysical Institute
University of Alaska
Attn: J.S. Wagner
Attn: M. Brown**

**Lowell University of
Center for Atmospheric Research
Attn: G.T. Best**

**Lockheed Missiles and Space Company
Attn: J. Kumer, Dept. 52-54
Attn: J.B. Cladis, Dept 52-12, B202
Attn: B.M. McCormac, Dept. 52-54
Attn: T. James, Dept. 52-54
Attn: M. Walt, Dept. 52-10
Attn: R.D. Sears, Dept. 52-54**

**Institute for Defense Analysis
Attn: E. Bauer
Attn: H. Wolfhard**

**Mission Research Corporation
Attn: D. Archer
Attn: D. Fischer
Attn: M. Scheibe
Attn: D. Sappenfield
Attn: D. Sowle**

**Photometrics, Inc.
Attn: I.L. Kofsky**

**Berkeley Research Associates
Attn: J.B. Workman**

**Physical Dynamics Inc.
Attn: A. Thompson**

**Physical Sciences, Inc.
Attn: K. Wray
Attn: R.L. Taylor
Attn: G. Caledonia**

**Physics International Company
Attn: Doc Con for Tech Library**

**Pittsburgh, University of the Commonwealth
System of Higher Education
Attn: W.L. Fite
Attn: M.A. Biondi
Attn: F. Kaufman**

**R & D Associates
Attn: R. Latter
Attn: R.G. Lindgren
Attn: B. Gabbard
Attn: R. Lelevier
Attn: A.L. Latter
Attn: F. Gilmore
Attn: H.J. Mitchell**

**Rand Corporation
Attn: C. Crain**

**Science Applications, Inc.
Attn: D.A. Hamlin
Attn: D. Sachs**

**Stanford Research Institute International
Attn: M. Baron
Attn: W.G. Chesnut**

**Technology International Corporation
Attn: W.P. Boquist**

**United Technologies Corporation
Attn: H. Michels
Attn: R.H. Bullis**

**Utah State University
Attn: D. Baker
Attn: K. Baker
Attn: C. Wyatt
Attn: A. Steed**

**Visidyne, Inc.
Attn: H. Smith
Attn: J.W. Carpenter
Attn: T.C. Degges
Attn: C. Humphrey**

**Wayne State University
Attn: R.H. Kummel
Attn: W.E. Kaupplia**

Commander
Rome Air Development Center
Attn: OSCA, J.J. Simons

Stewart Radiance Laboratory
Attn: R. Huppi

Boston College
Space Data Analysis Laboratory
Attn: E.R. Hegblom
Attn: W.F. Grieder

Forrestial Campus Library
Princeton University
Attn: Librarian